A Thesis Submitted for the Degree of PhD at the University of Warwick

White dwarfs: perfect laboratories for understanding non-radial pulsations and revealing secrets on the single degenerate pathway towards Supernova type Ia

by

Odette Toloza Castillo

Thesis

Submitted to the University of Warwick

for the degree of PhD

Doctor of Philosophy

Department of Physics

March 2018

THE UNIVERSITY OF
WARWICK

Contents

Acknowledgments **iv**

Declarations **v**

Abstract **vi**

Abbreviations **viii**

Chapter 1 Introduction **1**

- 1.1 White dwarfs . . . 1
  - 1.1.1 Forming white dwarfs . . . 1
  - 1.1.2 Fundamental properties of white dwarfs . . . 6
  - 1.1.3 Pulsating white dwarfs . . . 15
- 1.2 White dwarfs in binary systems: Cataclysmic Variables . . . 19
  - 1.2.1 Geometry of a binary . . . 21
  - 1.2.2 Evolution of CVs: the initial stages . . . 24
  - 1.2.3 Orbital period distribution . . . 27
  - 1.2.4 CV sub-classes . . . 30
  - 1.2.5 Dwarf Novae . . . 31
  - 1.2.6 Shell burning on white dwarfs . . . 33

Chapter 2 Hubble Space Telescope **39**

- 2.1 The Cosmic Origins Spectrograph . . . 39
- 2.2 Space Telescope Imaging Spectrograph . . . 44
- 2.3 Time-tagged data manipulation . . . 47
  - 2.3.1 Ultraviolet light curves . . . 48
  - 2.3.2 Spectra from selected time intervals: Peaks & troughs . . . 51
  - 2.3.3 Radial velocity corrections for the eclipsing binary QS Vir . . . 52
  - 2.3.4 Reducing the effects of airglow . . . 53

2.4 Side Projects: Analysis of light curves 54
  2.4.1 Spectroscopy from *HST*/COS of the southern nova-like BB Doradus in an intermediate state, Godon et al. 2016, APJ, 833, 146) 54
  2.4.2 The composition of a disrupted extrasolar planetesimal at SDSS J0845+2257, Wilson et al. 2015, MNRAS, 451, 3237 56

Chapter 3 Fitting HST spectroscopy of white dwarfs 60

3.1 White dwarf model atmospheres 60
  3.1.1 White dwarf atmospheric structure: ATM and TLUSTY 61
  3.1.2 Synthetic emergent spectrum: SYN and SYNSPEC 61
3.2 Markov Chain Monte Carlo ensemble sampler 62
  3.2.1 Example: white dwarf radial velocity of QS Vir 64
3.3 White dwarf $T_{\rm eff}$ and $\log g$ from fits to ultraviolet spectroscopy: the need for constraints 67
  3.3.1 Distance as a prior 68
  3.3.2 Constraints from optical photometry 71
3.4 Side projects 72
  3.4.1 The intermediate polar CC Sculptoris, Szkody et al. 2017, AJ, 153, 123 73
  3.4.2 The ultraviolet spectrum of the radio pulsar AR Sco Marsh et al. 2016, Nature, 537, 374 75

Chapter 4 G29-38: a pulsating white dwarf with metal pollution 78

4.1 Introduction 78
  4.1.1 Previous studies 79
4.2 Flux variations due to the non-radial pulsations 84
4.3 COS time-tagged spectroscopy 85
4.4 Ultraviolet pulsation periods 86
4.5 Spectral fits 90
  4.5.1 Grid of white dwarf models 90
  4.5.2 Average spectrum 91
  4.5.3 Five spectra 94
4.6 Surface gravity of G29-38 from the lowest flux spectrum 1 97
4.7 Chemical abundances 99
  4.7.1 Average abundances on the white dwarf 103
  4.7.2 Abundances in a heated spot 105
4.8 Conclusions 107

Chapter 5 GW Librae: a cataclysmic variable with a pulsating white dwarf 109
5.1 Introduction 109
5.2 Observations 112
5.2.1 Ultraviolet spectroscopy 112
5.2.2 Variability 113
5.3 Spectral fitting 116
5.3.1 2002, 2010, and 2011 observations 116
5.3.2 2013 observation 119
5.4 Discussion 122
5.4.1 Possible scenarios explaining the change in flux of the white dwarf . 122
5.4.2 Nature of the second component 129
5.5 Conclusions 129

Chapter 6 Cataclysmic Variables with nuclear evolved donors 131
6.1 Introduction 131
6.1.1 White dwarf masses in CVs 133
6.1.2 Low C/N ultraviolet emission line flux ratio as a signature of supersoft X-rays source descendants 134
6.2 HS0218+3229 & QZ Ser, two failed SNIa 135
6.3 COS spectroscopy 136
6.4 Spectral fits 136
6.4.1 Results 139
6.5 Stellar evolution of the evolved companion with MESA 142
6.5.1 Physical inputs 142
6.5.2 Procedure for the evolution of the donor star in the CV 143
6.5.3 Evolutionary tracks for the donor 145
6.5.4 Results 146
6.6 Discussion 153
6.6.1 Observable signatures of the He/H ratio 153
6.6.2 Side project: TYC6760-497-1, the first pre-supersoft X-rays source, (Parsons et al., 2015, MNRAS, 452, 1754) 155
6.7 Conclusions 157

Chapter 7 Concluding summary 159

Acknowledgments

I come from the place with the clearest skies where the view of the beautiful band of the Milky Way stretching above us, inspired me to pursue the pathway that today comes to the end of a chapter. If you are reading, let me tell you that the greatest achievement is not to get to the goal, but all the experiences learnt during the journey. Along my universal evolution, I am very grateful to everyone who somehow shared my successes and failures, from the Big Bang (my pillars, dad & mum, and my best partners, my siblings, who continuously prodded and encouraged me), trough the reionization era (Lissete, Nadia, Lili & Nicolle who have taught me how meaningful friendship is) until the present day in Warwick. Here, I need to do a special mention to whom has been the key in this journey, my supervisor Boris who was always willing to support and share valuable advices, and undoubtedly can say that I could not have ask for better supervisor.

A further big thank you goes to Danny and Stuart, who donate part of their precious time to read my work, who provided the final bricks to give good shape to this thesis.

Finally, a huge thanks to the ones that join later: the climbing Tim and Mediloza School who always shared a good laugh and endless conversations, and to all my fellows and friends that I have been honoured to meet.

While unexplored worlds are beyond that darkness in the sky, what I can explore is the beauty of this world and its people that make that every single day I can learn wonderful things.

Declarations

This thesis is submitted to the University of Warwick in support of my application for the degree of Doctor of Philosophy. The analysis and work presented within this thesis were completed mainly by the author, except the models of the g-mode splitting due to fast rotation presented in Chapter 5 that were made by Dean Townsley, the ULTRACAM data presented in Chapter 4 was reduced and analysed by Boris Gänsicke, and the Xshooter spectrum of KT Eri shown in Figure 7.2 was reduced by N. Gentile Fusillo.

The work presented within Chapter 5 is based on a paper published by the journal Monthly Notices of the Royal Astronomical Society (MNRAS): *GW Librae: a unique laboratory for pulsations in an accreting white dwarf*.

The data within this thesis is mainly spectroscopy taken with the HST. The HST data of WD1919+145 used to explain the method in Chapter 3 is from program ID 14077 (PI: Gänsicke). Further HST data of QS Virginis was used in order to explain Markov Chain Monte Carlo technique in Chapters 2 and 3, was kindly provided by the PI, Jeremy Drake (ID:13754). G29-38 HST data used in Chapter 4 is publicly available (PI: Jura, ID:12290) and the ULTRACAM data of G29-30 was obtained by J. Farihi and S. Parsons. GW Librae (Chapter 5), QZ Serpenties (Chapter 6), and HS0218+3229 (Chapter 6) spectroscopic data was taken with *HST* under the program ID:12870 (PI: Gänsicke).

The codes used in this work are mainly public: EMCEE (Foreman-Mackey et al., 2013), Period04 (Lenz & Breger, 2005), MESA (Paxton et al., 2011, 2013, 2015), and TLUSTY/SYNSPEC (Hubeny & Lanz, 1995), except the white dwarf atmosphere code ATM/SYN written by prof. Detlev (Koester, 2010), that was kindly provided by himself.

Abstract

White dwarfs are elderly stars that represent the endpoint of stars with masses lower than $\simeq 9\,\mathrm{M}_\odot$, which comprise 95%–98% of all stars in our Galaxy, including our Sun. Hence, the motivation of their study is to reveal important insight about the future of our Solar system. In this thesis I present three main projects that are linked because the analysed systems host white dwarfs. I begin by introducing in Chapter 1 the evolution and properties of single white dwarfs and in cataclysmic variables. Most of the light emitted by the white dwarf is detected in the ultraviolet, therefore the spectrographs mounted in the Hubble Space Telescope are ideal for the white dwarf science. In this thesis I performed the analysis of spectroscopic data taken with the Cosmic Origins Spectrograph and the Space Telescope Imaging Spectrograph, therefore I explain their performance and capabilities in Chapter 2. The analysis of the Hubble spectroscopy consists mainly in determining the white dwarf atmospheric parameters. The technique used in this thesis is fitting the data with synthetic white dwarf atmospheres using the Markov Chain Monte Carlo for Bayesian inference, which I explain in Chapter 3. G29-38 is a non-radial pulsating white dwarf that shows infrared excess due to a dusty debris disc that formed from the tidal disruption of a planetesimal. The ongoing accretion from this debris disc pollutes the atmosphere of G29-38. The analysis of the photospheric contamination provides a direct measurement of the bulk composition of the disrupted planetesimal. However, the geometry and the process of the accretion from the debris disc onto the white dwarf are not yet well understood. In Chapter 4, I make use of the pulsations as a spotlight to investigate the metal distribution across the white dwarf surface which provides constraints on the geometry of the accretion process. In Chapter 5 I present my work on the dwarf nova GW Librae in which the white dwarf drives non-radial pulsations. GW Librae stands out by having a well-established observational record of three independent pulsation modes that disappeared when the white dwarf temperature rose dramatically following its 2007 outburst. Therefore, GW Librae offers the opportunity to investigate the response of these modes to changes in the white dwarf temperature. Here I report the presence of a high-amplitude variability on a $\simeq 4.4\,\mathrm{h}$ time-scale, which I demonstrate to be the result of an increase of the temperature of a relatively small region on the white dwarf surface. Cataclysmic variables undergoing thermal time scale mass transfer are known as super-soft X-rays sources which provide a pathway towards Supernova type Ia through the single degenerate channel. The study of these systems is very difficult due to the small number of systems known, moreover the extremely hot white dwarfs outshine their companions. In Chapter 6 I present the analysis of HS0218+3229 and QZ Ser which present low abundance ratios of carbon to nitrogen which is the signature seen in descendants of super-soft X-rays sources. I also present MESA simulations that constrain the parameter space for the formation of these failed supernova type Ia. Finally, I present the concluding remarks of this thesis in Chapter 7.

★ ★ ★

Abbreviations

AGB	Asymptotic Giant Branch
BOA	Bright Object Aperture
C	Carbon
CNO	Carbon-Nitrogen-Oxygen
COS	Cosmic Origins Spectrograph
CV	Cataclysmic Variable
CVs	Cataclysmic Variables
E-AGB	Early Asymptotic Giant Branch
FCA	Flat-Field Calibration Aperture
FUV	Far-ultraviolet
GB	Giant Branch
GTI	Good Time Intervals
H	Hydrogen
HB	Horizontal Branch
He	Helium
HST	Hubble Space Telescope
HRD	Hetzsprung-Rusell diagram
IP	Intermediate polar
IR	Infrared
IMF	Initial Mass Function
MAMA	Multi-Anode Micro-channel Array

MCMC	Markov Chain Monte Carlo
MS	Main Sequence
NUV	Near-ultraviolet
Ne	Neon
N	Nitrogen
O	Oxygen
OSM1	Optics Select Mechanism 1
PHA	pulse height amplitude
PN	Planetary Nebula
PP	Proton-Proton
PSA	Primary Science Aperture
Post-AGB	Post-Asymptotic Giant Branch
PCEB	Post Common Envelope Binary
RG	Red Giant
RGB	Red Giant Branch
SED	Spectral Energy Distribution
SDSS	Sloan Digital Sky Survey
SGB	Subgiant branch
Si	Silicon
SNIa	Supernovae type Ia
SSSs	Supersoft X-rays sources
STIS	Space Telescope Imaging Spectrograph
TP-AGB	Thermal Pulse Asymptotic Giant Branch
WCA	Wavelength Calibration Aperture
XDL	Large format Cross Delay Line
ZAMS	Zero Age Main Sequence

Chapter 1

Introduction

1.1 White dwarfs

White dwarfs are the remnants of the evolution of main sequence stars with masses $\lesssim 9\,\mathrm{M}_\odot$ (e.g. Iben et al., 1997). In this section I will explain the formation of white dwarfs from early phases, their defining properties, including effective temperatures, surface gravities, chemical abundances, and the characteristic mass – radius relationship of these degenerate stars. I will also introduce a subclass of white dwarfs which drive pulsations.

1.1.1 Forming white dwarfs

The formation of stars occurs in molecular clouds when their hydrostatic equilibrium is affected by external perturbations (e.g. shock waves resulting from a Supernova explosion), causing the cloud to fragment. If these fragments exceeds the so-called Jeans mass (Jeans, 1902), they will proceed to collapse, becoming opaque to their own radiation, and protostars are formed. Therefore, the nascent stars are likely bound gravitationally with their nearby companions, forming binaries or triples. The contraction continues until the central temperature is high enough to ignite nuclear reactions in the central core. However, if the mass of the collapsing protostar is below the critical mass limit ($\sim 0.08\,\mathrm{M}_\odot$), the core will never reach the critical density and temperature needed to fuse nuclear reactions. These failed stars are known as brown dwarfs and their fate is just to cool down. In contrast, if the collapsing protostar exceeds the minimum stellar mass limit, Hydrogen (H) fusion does ignite in the core. The nascent stars evolve aiming to find a hydrostatic and thermal equilibrium and join the Zero Age Main Sequence (ZAMS) in the Hetzsprung-Rusell diagram (HRD). The distribution of the initial masses of the stars is described by the Initial Mass Function (IMF). This function is $\propto \mathrm{M}^{-\alpha}$, with α=2.35 according to Salpeter (1955). For more details see Kroupa (2001), where the index decreases for smaller masses (α=0.3 for $0.01\,M_\odot \leqslant \mathrm{M} < 0.08\,M_\odot$,

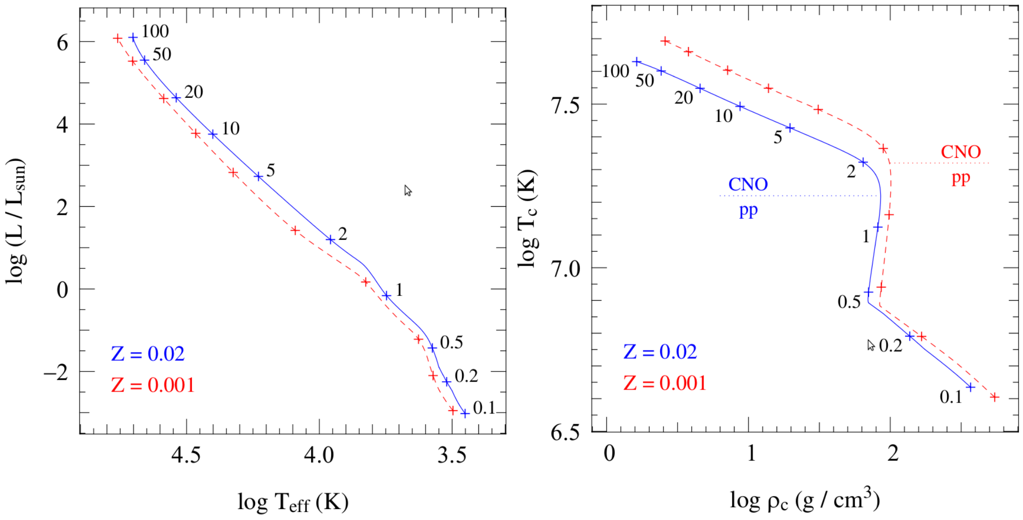

Figure 1.1: The blue line is a ZAMS model for a hydrogen mass fraction of X=0.7, and metallicity of Z=0.02, and the red line corresponds to X=0.757 and Z=0.001. The plus symbols indicate the mass in solar units. *Left:* ZAMS in the HRD, low-mass stars at lower metallicities are less luminous. *Right:* central temperature versus central density, dotted lines represent the border between CNO and PP energy production mechanisms. Figures taken from Kippenhahn et al. (2012)

α=1.3 for 0.08 $M_\odot \leqslant$M<0.5 $M_\odot$, α=2.3 for 1.0 $M_\odot \leqslant$M). This empirical power law dictates that the number of stars in each mass range decreases while increasing the mass. The mass is the main parameter that determines the subsequent evolution of the star. The stars spend most of their lifetime on the Main Sequence (MS), balancing the gravitational contraction with (thermal) pressure generated by nuclear fusion (Hurley et al., 2000). In other words, stars consume themselves to survive the pull of gravity by converting H into Helium (He) in their cores.

Energy Production

The stars on the MS are powered by either the Proton-Proton (PP) chain or the Carbon-Nitrogen-Oxygen (CNO) cycle, and what nuclear reaction dominates depends on the conditions in the core, primarily the central temperature. The right panel in Figure 1.1 shows detailed ZAMS models of the core for different masses. The CNO regime dominates at higher central temperatures ($T_c \simeq 1.7{\times}10^7$ K, for solar composition), which stars with masses higher than $\simeq 1.3\,M_\odot$ can reach. Therefore low mass stars fuel themselves by the PP chain. The abrupt change in the slope of the density is related to the change of the energy transport in the core: fully convective ($M < 0.35\,M_\odot$), radiative core+convective envelope ($0.35\,M_\odot < M < 1.2\,M_\odot$), or convective core plus radiative envelope ($M > 1.2\,M_\odot$).

The lifetime of a star on the MS depends upon the fuel it has available (total mass of the star), and how fast it is burnt (luminosity), i.e. $\tau_{\rm MS} \propto$ M/L. As illustrated in Figure 1.2, the luminosity is a function of the mass (Kuiper, 1938), i.e. L$\propto$M$^{\alpha}$, with $\alpha \sim$ 3–4 for MS stars. In conclusion, the lifetime on the MS is dramatically shorter for higher mass stars than for low-mass stars ($\tau_{\rm MS} \propto$ M$^{1-\alpha}$).

Post-main sequence evolution

With the H content depleting, the core generates less thermal energy, and to maintain hydrostatic equilibrium the core begins to contract. The main factor that drives the evolution onwards is the mass, which defines four qualitative pathways:

1. very-low-mass stars ($\sim$ 0.1–0.7 M$_\odot$) He never ignites. The envelope of the star is ejected into the interstellar medium, and the stellar remnant left behind is a $\lesssim$ 0.4 M$_\odot$-mass core He white dwarf. However, the MS lifetime of these stars exceeds the age of our Galaxy. Therefore, He white dwarfs can not have not formed yet unless binary interactions force an early end of the core H burning (a formation channel which will be explained in Section 1.2.2)
2. low-mass stars ($\sim$ 0.7–2 M$_\odot$) develop a degenerate He core, and evolve onto a relatively long-lived Red Giant Branch (RGB). They eventually experience a thermonuclear runaway in the core called *He flash*.
3. intermediate-mass stars ($\sim$ 2–8 M$_\odot$) fuse steadily He into Carbon (C) and Oxygen (O) in a non-degenerate core resulting in CO white dwarfs.
4. massive stars (> 8 M$_\odot$) are at the boundary that defines two radically different fates of the star. A narrow range of masses between $\simeq$8–10 $M_\odot$ can form either $\sim$1.4 $M_\odot$ neutron stars due to collapse of the core or lead to O-Neon (Ne) white dwarfs, but the details of stellar evolution in this mass regime remains unclear (Heger et al., 2003). For masses beyond 10 M$_\odot$ the fate of these stars is to end as either neutron stars or black holes, which are beyond the interest of this thesis.

The extreme pathways of low-mass stars and massive stars are beyond the interest of this thesis. To understand the pathways of low-mass and intermediate-mass stars throughout the HRD, I will explain the evolution of two stellar models for stars with 1 M$_\odot$ and 5 M$_\odot$ in more detail (Figure 1.2). The evolution of 1 M$_\odot$ and 5 M$_\odot$ stars differs significantly once the stars leave the MS, and until they reach the Asymptotic Giant Branch (AGB).

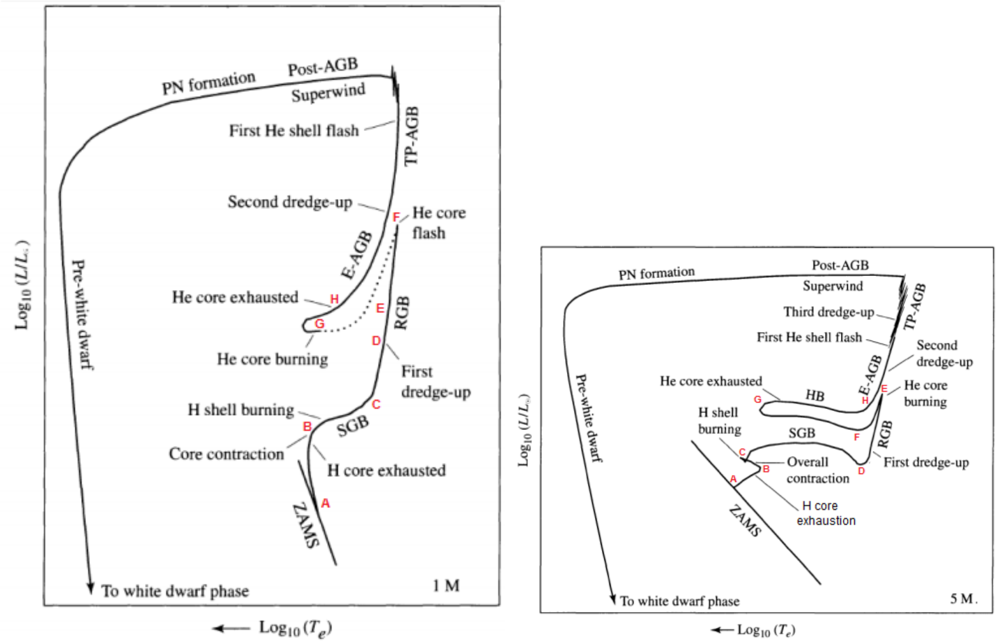

Figure 1.2: Schematic diagram showing the evolution of a low-mass star (1 M$_\odot$; left) and an intermediate-mass star (5 M$_\odot$; right). The dotted line represents an ultra fast phase in the evolution, the Hertzsprung gap. Labels are: zero age main sequence (ZAMS), subgiant branch (SGB), Red Giant Branch (RGB), Horizontal Branch (HB), Early Asymptotic Giant Branch (E-AGB), Thermal Pulse Asymptotic Giant Branch (TP-AGB), Post-Asymptotic Giant Branch (Post-AGB) and Planetary Nebula (PN) formation. Figures taken from Carroll & Ostlie (2006)

	1 M$_\odot$	5 M$_\odot$
A-B	MS, H fusion takes place in the core. At **B** the overall contraction starts.	
B-C	H into He fusion occurs in a shell. The core grows in mass and contracts while the envelope expands during the Subgiant branch (SGB) phase. At **C** the core has become degenerate and the envelope is largely convective. The star is now at the base of the RGB.	While contracting the star fuses the last reservoir of H in the core, exhausting at **C**.

C-D	The electron degeneracy dominates the pressure in the core, sustaining the contraction. Therefore, the star maintains the hydrostatic and thermal equilibrium during the H shell burning, hence the star does not exhibit the Hertzsprung gap. The core grows slowly because of the mass added by the H burning shell. The envelope continues its expansion, becoming convective.	On the SGB the temperature and density gradients between the core and the envelope are shallow, hence H burning continues in a shell which adds more He to the core, increasing its mass. Therefore the core contraction speeds up while the envelope expands faster, steepening the temperature and density gradients. As a result, the thickness of this burning H shell decreases, so the temperature decreases and the energy produced by the burning shell is absorbed by the envelope, resulting in a decrease of the luminosity, and the star migrates towards the RGB. This phase is very short, diminishing the number of stars that can be observed in this state, therefore it is known as the Hertzsprung gap in the HRD.
D-E	The core contracts faster and the radius and luminosity increase. The Red Giant (RG) has a very convective envelope, reaching the steepest extent, penetrating into layers were H was processed, producing the first dredge up at **D**. At **E** the burning shell has reached the deepest extent of the convective envelope, hence it is enriched with additional H, resulting in a little decrease of the luminosity, which is not visible on the scale of the HRD.	Because of the expansion of the envelope, the effective temperature decreases and hence the opacity increases. The energy transport via radiation becomes inefficient, and becomes dominated by convection. The RG with a deep convective envelope dredges up some of the material processed in the core. At **E** the burning H layer has contributed sufficient He to the core such that He ignites, fusing into CO.
E-H	The core continues growing until He is ignited at **F**. The temperature in the degenerate core increases to very high values ($\sim 10^8$ K), He is ignited, but the process is unstable, resulting in the thermonuclear runaway He flash. A series of smaller flashes occur before degeneracy is finally lifted at **G**, and He is stably burnt in the core between **G** and **H**, fully exhausting at **H**.	A loop is prescribed during the He burning, known as blue loop. The envelope contracts while turning radiative (fully radiative at **F**) moving away from the RGB. The effective temperature increases, reaching its highest value at **G**. While He is being exhausted, the envelope starts its expansion moving through the Horizontal Branch (HB) and returning back to the branch at point **H**, referred now as AGB. To loop or not to loop depends on a series of factors, but is quite sensitive on the chemical composition and the mass of He core relative to the envelope.

At point H, with He fully exhausted in the core, the AGB phase begins. The evolution for both stars continues qualitatively similar. There are two well defined stages during the evolution through the AGB phase: The Early Asymptotic Giant Branch (E-AGB) and the Thermal Pulse Asymptotic Giant Branch (TP-AGB). During the E-AGB the He burning sits in a shell around a contracting core composed mainly of CO. The He burning shell adds CO mass to the core, which becomes increasingly electron degenerate. The star contains two active burning shells, with the He shell being the one that generates more energy. The envelope expands to giant dimensions and due to the depth of the convection zone a second dredge up occurs. The TP-AGB starts when He starts to run out in the He burning shell, generating periodic thermal pulses. Therefore, the H burning shell becomes the main source of energy, adding more He and eventually the He shell ignites explosively which is called He shell flash. As a response the star expands and cools, causing the H shell burning to halt and the region between the shells becomes deeply convective (in intermediate-mass stars it causes a third dredge up). When the He shell burning and the base of the H shell are closer, the temperature increases, reigniting the fusion in the H shell and the cycle begins again. As the star climbs the AGB, the envelope develops a superwind that blows the convective outer layers into space. Therefore, the star moves away from the AGB, forming a planetary nebulae. With the envelope gone, the H shell finally is extinguishing, allowing one last late thermal pulse to happen, which may remove all residual H resulting in He rich atmosphere remnant (an important point that can lead to a He rich white dwarf atmosphere, as explained later in Section 1.1.2). The luminosity decreases, and the cooling remnants become white dwarfs (Iben, 1991).

Without nuclear fusion, the white dwarf cannot support gravitational contraction through thermal pressure, instead it finds a stable configuration due to electron degeneracy. According to the Pauli exclusion principle, only two electrons, with opposite spins, can occupy the same quantum-mechanical state. Because of the contraction of the core, electrons are pushed together and forced to occupy higher energy levels, generating an outward pressure, which stops the gravitational contraction.

1.1.2 Fundamental properties of white dwarfs

Temperature and surface gravity

The white dwarfs emerging from the planetary nebulae are extremely hot due to the gravitational energy released during contraction of the pre-white dwarf stellar core, which has just finished nuclear fusion of the last available fuel. The initial cooling stage is due to the energy losses by large quantities of neutrinos that escape from the white dwarf. At some point the neutrino luminosity falls below the photon luminosity, and thereby thermal cooling takes over (Fontaine et al., 2001). As the temperature is decreasing, the white dwarf continues its contraction, resulting in a fully electron degenerate core balancing gravity (Koester, 2013). Henceforth, the evolution of the white dwarf is mainly driven by its cooling, resulting eventually in the processes of crystallization, convection and the formation of opaque layers.

Once the temperature drops sufficiently, the opacity in the outer layers increases due to recombination of the elements. Therefore, the thin H and He layers (Althaus et al., 2013; Wood, 1995) play an important role in the cooling process since they regulate the energy flow.

As white dwarfs cool, they reach the effective temperature regime at which they experience pulsational instabilities. These are mainly driven by changes in the opacities caused by ionisation instabilities. This latter process will be discussed in more detail later in Section 1.1.3.

The steep temperature gradient in the envelope causes convective motions. The depth of this convective zone will increase as the white dwarf cools, until it reaches the isothermal core (Althaus et al., 2010). The extent of the convection zone also depends on the chemical composition and the thickness of the envelope layer, e.g. Figure 1.3 shows the location of the convection zone for a $0.6\,M_{\odot}$ white dwarf for H and He envelopes. Convection is largely efficient for thin layers ($\Delta M/M_{\star}$=10^{-11}) of H composition when $T_{\rm eff} < 11\,000$ K (Dufour et al., 2007), or for He dominated composition when $T_{\rm eff} < 25\,000$ K (Bergeron et al., 2011). This so-called convective coupling speeds up the cooling significantly, since the core's energy can now effectively be transported to the outer atmosphere where it is radiated away.

At late stages of the cooling, the particles will form a highly organized solid structure, a crystal. The crystallization process starts in the center, therefore asteroseismological observations of pulsating white dwarfs provide potential tests of the crystallization process (Winget, 1995). Eventually, the white dwarf will become a black dwarf, which is a crystallised, very low-temperature degenerate remnant.

Another important parameter besides temperature is the surface gravity, log g, typically expressed as a logarithm with g in cgs units of cm/s^2 (e.g. Earth log $g_{\oplus} \simeq 3$). The large gravity stratifies the chemical composition according to the atomic weight. The bulk of white dwarf stars have very high surface gravities, with a mean close to log $g \simeq 8$ as shown

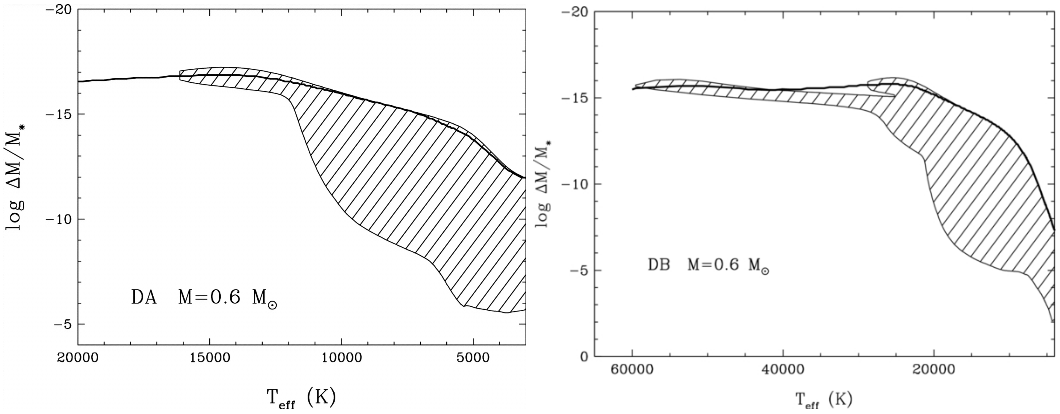

Figure 1.3: Location of the convection zone (hatched area) as function of $T_{\rm eff}$ for a $0.6\,{\rm M}_{\odot}$ white dwarf with a hydrogen envelope (*left*) and with a helium envelope (*right*). The y-axis represents in logarithmic scale the fractional mass above a certain point of interest respect to the total mass of the star. Figures taken from Bergeron et al. (2011) and Dufour et al. (2007), respectively. Solid line represents the location of the photosphere.

in left panel in Figure 1.4 (Liebert et al., 2005; Gianninas et al., 2006; Kleinman et al., 2013).

The temperature and surface gravity of a single white dwarf cannot be measured directly. One method to estimate them is the comparison with stellar atmosphere models (see Section 3.1). Hence, this approach relies on high-quality spectroscopic data and an adequate understanding of the relevant physics of the white dwarf structure, their atmospheres, and the cooling process.

The most commonly used method to determine both of these parameters relies on fitting spectroscopic data of the Balmer absorption lines, which result from the excitation of the electrons in atoms of H. They are present in the spectra of most white dwarfs (Section 1.1.2). The shape and width of the Balmer lines are sensitive to the temperature and surface gravity (Bergeron et al., 1991; Gianninas et al., 2011; Giammichele et al., 2012a).

Understanding the cooling process can constrain the white dwarf ages, which can be used as independent age estimators of the population they reside in e.g. the local neighbourhood, open clusters, or the Galactic disc and halo (Wood, 1992; Renzini et al., 1996; Hansen et al., 2004, 2013; Tremblay et al., 2014).

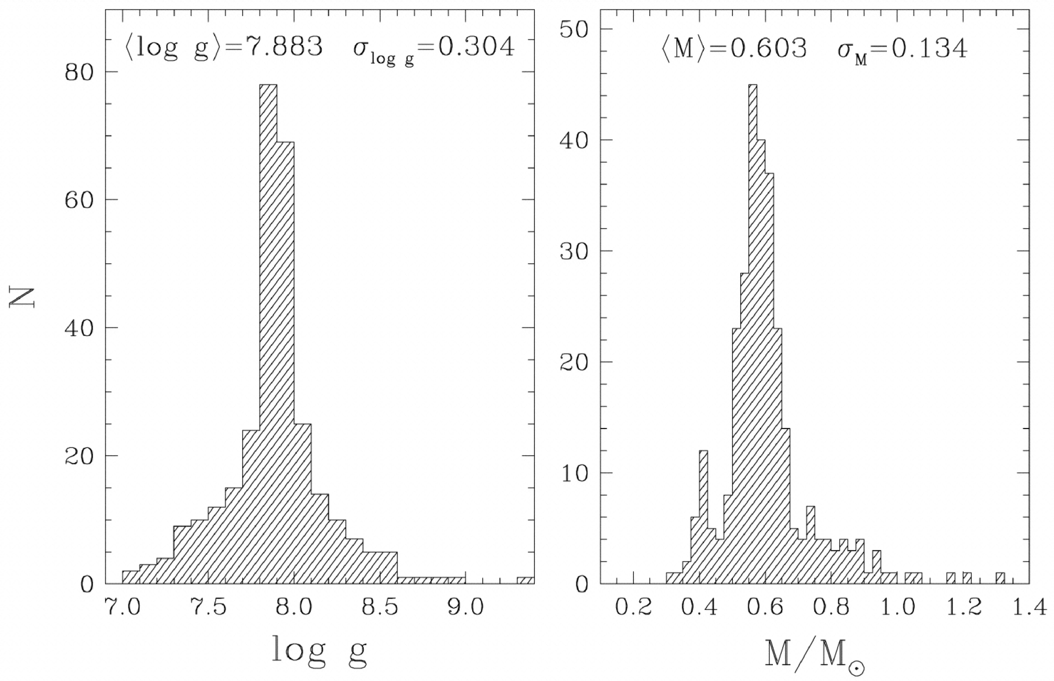

Figure 1.4: Histograms of surface gravities (log g, *left*) and masses (*right*) of a spectroscopic sample consisting of 298 white dwarfs from the Palomar Green Survey with effective temperatures $T_{\rm eff} > 13000$ K and with H-rich atmospheres (Liebert et al., 2005).

Masses and Radii

The mass and the radius of a star are connected via the equation of state of the stellar interior, which in the ideal situation can be modelled with polytropes. A polytrope is a self-gravitating gaseous sphere. Throughout the sphere, a polytrope is described by an equation of state $P \propto \rho^{1+\frac{1}{n}}$, where P and ρ are the pressure and density, respectively and n is called the polytropic index. The well-known Lane-Emden equation combines the equation of state and the equation of hydrostatic equilibrium:

$$\frac{1}{\xi^2}\frac{d}{d\xi}\left(\xi^2\frac{d\theta}{d\xi}\right) = -\theta^n \tag{1.1}$$

where ξ is a dimensionless variable representing the stellar radius and θ is a dimensionless variable relating the density to the central density through $\rho = \rho_c\theta^n$. White dwarfs are dense enough to be dominated by non-relativistic electron degeneracy pressure, and can be accurately described by a polytrope with index $n = 3/2$. Hence, the solution of the Lane-Emden equation reduces to a mass – radius relation where

$$R \propto M^{-1/3} \tag{1.2}$$

(see for example Prialnik, 2000; Kippenhahn & Weigert, 1990). The relation shows that more massive white dwarfs have smaller radii. In the extreme case where the electron degenerate gas is fully relativistic, the star is properly described by a polytrope with index $n = 3$. The solution is independent of the radius, resulting in the well-known upper mass limit for white dwarf stars, the Chandrasekhar mass limit of $M_{\mathrm{Ch}} \simeq 1.4\,\mathrm{M}_{\odot}$ (Chandrasekhar, 1931). If the star exceeds this mass limit, a thermonuclear runaway is triggered resulting in a very violent explosion: a supernova.

The relation in Eq. 1.2 has been known for a long time, however is has been very difficult to determine exact mass – radius relations (Wood, 1995; Benvenuto & Althaus, 1998; Althaus et al., 2013). Some complications come from the fact that the relations differ for white dwarfs with different core compositions. Additionally, they are sensitive to the temperature, because a white dwarf with a non-zero temperature becomes 'bloated' due to thermal pressure, with the outer non-degenerate layers of the star being more affected. Therefore, testing and improving theoretical mass – radius relations, empirical data of the masses and radii are essential. There are several methods available to accomplish these measurements.

The radius of a white dwarf (R_{WD}) for which the distance (D) is known (e.g. from a trigonometric parallax), can be obtained by modelling the observed flux. The flux emitted depends on the radius and the effective temperature [$F_{\mathrm{obs}} = 4\pi(R_{\mathrm{WD}}/D)^2 \times F_{\mathrm{WD}}(T_{\mathrm{eff}}, \log g)$]. It is worth to note that this method does not depend on any mass–radius relation, though still relies on synthetic models to obtain the temperature by fitting the spectroscopic data (Holberg et al., 2012).

The mass can be inferred using asteroseismology (Metcalfe, 2001). This technique relies on modelling the pulsation periods of pulsating white dwarfs. The models usually assume a core composition and depend upon the temperature, the He layer mass and the total mass (which, given enough independent pulsation modes, can also be measured). For example, the mass of G29-38, a pulsating white dwarf of special emphasis in this thesis (Chapter 4), has been constrained to ~0.6–0.8 $\mathrm{M}_{\odot}$ (Castanheira & Kepler, 2009; Romero et al., 2012; Chen & Li, 2013).

An additional method to measure masses is through gravitational redshift. The gravitational redshift is the effect that the photons reduce their frequency (i.e. move towards longer wavelengths) so to compensate the energy they need to escape from the gravitational potential of white dwarf. The gravitational redshift v_g depends on the white dwarf's mass and radius, i.e. $v_g = G\,M_{\rm WD}/R_{\rm WD}\,c$, where c is the speed of light and G the gravitational constant. Therefore, with accurate measurements of the wavelength of (red)shifted absorption lines in spectroscopic data of white dwarfs (usually Balmer lines), plus the mass–radius relation from evolutionary models, the mass (and radius) can be calculated. However, spectral features are in addition redshifted or blueshifted as the white dwarf has a radial velocity with respect to the Earth. Therefore, the gravitational redshift technique can only be applied if the radial velocity can be determined, such as in common-proper motion systems or in open clusters (Koester, 1987; Reid, 1996). Alternatively, in a sufficiently large sample of white dwarfs in the thin disc of the Milky Way, the radial velocities are assumed to cancel out on average. Using the SPY white dwarf sample (Koester et al., 2009), a statistical analysis results in a mean gravitational redshift of v_g=32.57±1.17 km s^{-1}, which translates into a mean mass of $0.647^{+0.013}_{-0.014}\,\rm M_\odot$ (Falcon et al., 2010). Note that this approach requires the use of a theoretical mass–radius relation in order to measure the mass and the radius of a white dwarf. Thus, it does not provide an independent test for the mass–radius relation.

Masses *and* radii can be measured for white dwarfs in nearby and wide binaries. The masses can be derived in spatially resolved binaries from the visible orbital motion as projected on the plane of the sky and radii can be obtained from parallax observations and using effective temperatures from spectroscopic observations, as mentioned above (Shipman et al., 1997; Holberg et al., 1998; Provencal et al., 1998, 2002). The best white dwarf to test this technique is the brightest and closest one, Sirius B, however the mass and radius estimates from Balmer line fitting, gravitational redshift and astrometry of the binary are in significant disagreement (Barstow et al., 2017).

Masses *and* radii can also be measured for white dwarfs in unresolved eclipsing binaries. The mass is obtained from the radial velocity measurements of both stellar components, measured from high time series spectroscopy. The radius is measured from high speed photometry using the duration of the ingress and egress of the primary and secondary eclipses (Parsons et al., 2010a, 2012, 2017).

Another approach to determine masses involves evolutionary models combined with temperatures and surface gravities obtained from fitting model spectra to spectroscopic data. This method has provided large samples of white dwarf masses, e.g. the distribution of white dwarf masses with $T_{\rm eff}$ > 13000 K determined by Liebert et al. (2005), is shown in Figure 1.4. The cooler white dwarfs are excluded from this sample to avoid the effects of convection (Tassoul et al., 1990). The histogram shows a central component at a mass close to 0.6 $\rm M_\odot$ (which agrees with the average mass measurements from gravitational redshifts), corresponding to the bulk of the white dwarf remnants, mainly with CO cores. There is also a sharp, smaller peak at ~ 0.4 $M_{\odot}$, and a broad contribution of white dwarfs with masses > 0.8 $M_{\odot}$. These sub-distributions correspond to the He core and ONe core white dwarfs, respectively. This sample is magnitude-limited, and thereby it is biased towards low-mass white dwarfs due to their larger radii and larger surface area. Indeed, if the mass distribution is corrected for the volume searched, it shows a more prominent component at higher white dwarf masses (see Figure 1.4 right panel). However, the spectroscopic approach requires the use of a theoretical mass-radius relation, and therefore can not provide independent tests.

Chemical composition

The high surface gravity of white dwarfs stratifies the chemical constituents, settling them according to their atomic weights. Therefore, the core is mainly composed by the heavier elements of the white dwarf, i.e. the ashes of nuclear burning, while light elements such as He and H remain in the outer layers of the envelope and atmosphere.

The study of the interiors of white dwarfs has been possible thanks to seismic analysis (see for example Kawaler & Bradley, 1994; Costa et al., 2008; Aerts et al., 2010; Córsico et al., 2012; Giammichele et al., 2017). However, the majority of white dwarfs do not pulsate, and therefore their core and envelope composition are assumed depending on their mass (the atmosphere's composition can be observed as I will explain later). Usually, the core composition is thought to be either He, a CO mixture, or an ONe mixture for low-mass (~ 0.4 $M_{\odot}$), canonical (~ 0.6 $M_{\odot}$) and high-mass (~ 0.8 $M_{\odot}$) white dwarfs, respectively. The latter two categories are surrounded by both a He and H layer, whereas for the former, the He core white dwarfs, it is believed that their atmospheres are composed of H. Typical masses for these layers are assumed to be 10^{-2} M_{WD} for the He layer, and 10^{-4} M_{WD} for the H layer (Althaus et al., 2013; Wood, 1995), although very low-mass white dwarfs can have substantially thicker H envelopes of $\sim 10^{-2}$ $M_{\odot}$ (Istrate et al., 2014). Figure 1.5 shows the chemical profiles for canonical white dwarfs with a H-rich (top) and He-rich atmosphere (bottom). The x-axes indicates the negative of the logarithmic mass-fraction, from the core of the white dwarf at 0 out to the outer envelope at 3 and above.

Observationally, only the outermost layer of a white dwarf can be directly studied in great detail via high-quality spectroscopy. Therefore, the spectral classification of white dwarfs is based on their atmospheric composition. In roughly 70% of all white dwarfs, the photospheres are dominated by H and their spectra will show H absorption lines. If only H is detected in the spectrum, the star will be classified as a DA white dwarf. If all H has been lost during the pre-white dwarf evolutionary phases (late shell flash, as explained in

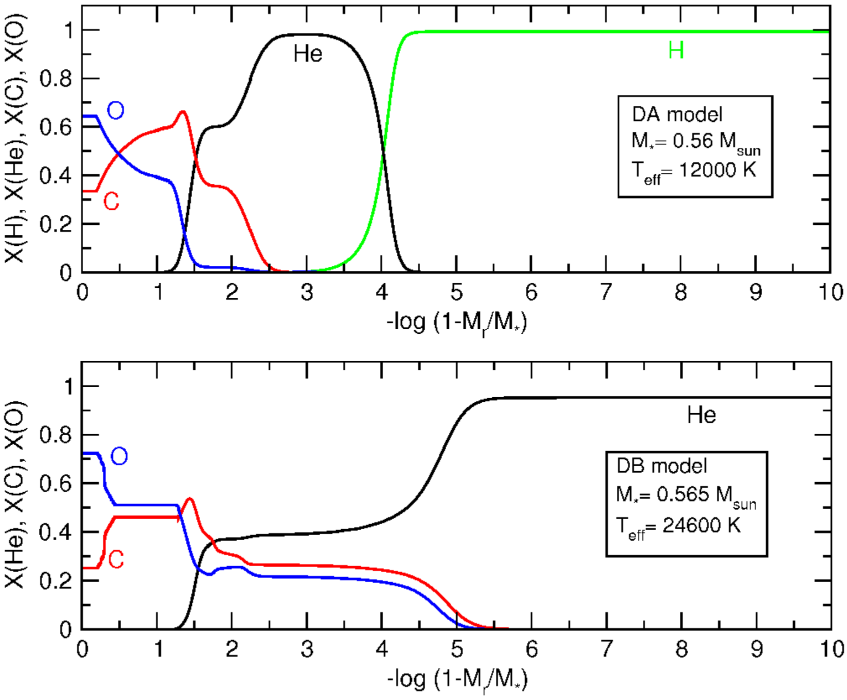

Figure 1.5: Cross-section showing the relative mass fractions X of O, C, He and H in a DA (*top panel*) and DB (*bottom panel*) white dwarf with a CO core of mass $M_\star$ and temperature $T_{\rm eff}$, from (from Althaus et al., 2010). The horizontal axes indicate the mass fraction contained in the star beyond radius r. The centre of the white dwarf is at the left and the outer atmosphere is off the figures towards the right. The part of the atmosphere directly available to observations typically has a mass fraction $< 10^{-15}$, which corresponds to $-\log(1-M_r/M_\star) > 15$.

Section 1.1.1), He will dominate the outer atmosphere, and for $T_{\rm eff} \gtrsim 10000$ K, the spectrum will show He absorption lines and the star will be classified as a DB white dwarf. Examples of spectra of a DA and DB white dwarf are shown in Figure 1.6.

With increasing amounts of spectroscopic data on white dwarfs emerged the need to define more categories for non-DA and non-DB stars. A basic classification is listed in Table 1.2, and includes several subclasses besides the DA and DB white dwarfs. Among them are DC white dwarfs which show no deep absorption lines at all, DO white dwarfs that show strong He ɪɪ lines and weak He ɪ or H lines, DZ white dwarfs which show metal lines but no H or He lines, and because of deep convective envelopes, dredging up C from the core, DQ white dwarfs show C features. Different spectral classes can also be combined, e.g. when a white dwarf has a H enriched enriched with metals, it will be classified as DAZ white dwarf. For pulsating white dwarfs a V (for variability) is often added to the

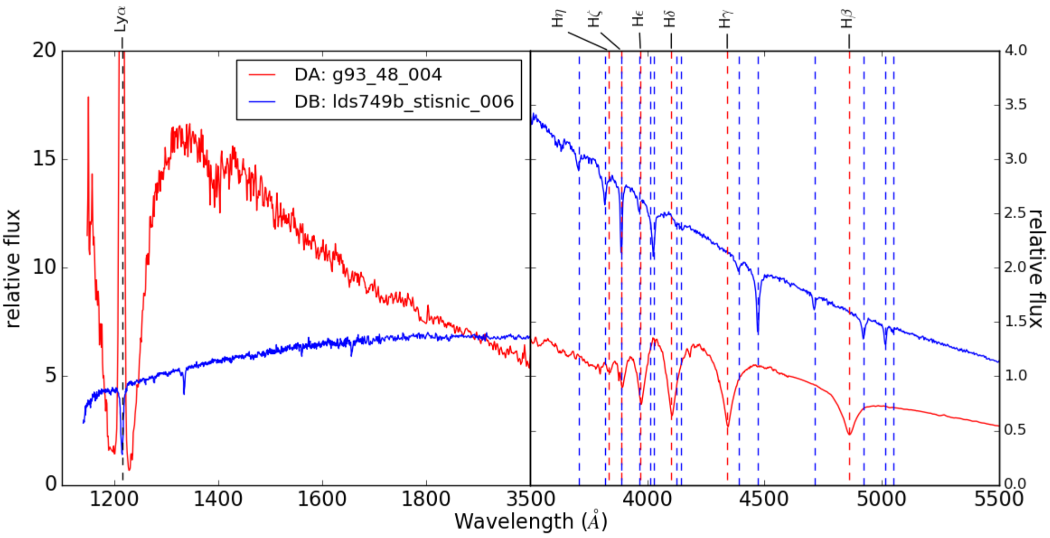

Figure 1.6: Spectra of a DA (red) and DB (blue) white dwarfs, from the *HST* calibration database as seen in the ultraviolet (*left*) and optical (*right*). The positions of H (dashed red) and He (dashed blue) spectral lines are indicated.

classification. Some white dwarfs have a strong magnetic fields, which can be detected through Zeeman splitting of the absorption lines. In these cases, the letter m or H is added to the spectral classification. A few additional but rare classes exist, see for example the review by Koester (2013) for more details.

As mentioned above, the elements sink due to the high gravity. This process occurs on time scales that are much shorter than the white dwarf's cooling age (Paquette et al., 1986; Koester, 2009). Therefore, heavier elements than He should not be detected in their atmospheres. However, metals have been observed in several white dwarfs (Zuckerman & Reid, 1998; Zuckerman et al., 2003; Koester et al., 2014). At temperatures above ~25000 K, the heavier elements in the atmosphere are partially ionised and have larger cross-sections absorbing effectively the photons coming from the deeper layer, and therefore they are lifted towards the photosphere. This process, known as radiative levitation, can sustain detectable abundances of some ions (see Chayer et al., 1995a,b, for a detailed discussion). In contrast, for temperatures below ≃20000 K radiative levitation is negligible and can not explain the heavy elements. At lower temperatures the metal abundances seen can be explained by ongoing or recent accretion of material, or have recently accreted, material from an external source (e.g. the tidal disruption of a planetesimal), and the sinking process is slowed by turbulences of the fluid. The convection zone acts as a reservoir, where the evolution of the mass fraction of a metal is a strong function of the diffusion velocity at the bottom of

Table 1.2: White dwarf spectral classes.

classification	spectroscopic signature
DA	H lines, no Heor metals present
DB	He I lines, no H or metals present
DC	no lines deeper than 5% present
DO	strong He II lines, some He I or H may be present
DZ	metal lines only, no H or He lines
DQ	carbon features present
V	photometric variability
m or H	magnetic

the convection zone. Thus, if the accretion stops, the metal abundances decay according to their different diffusion time scales.

1.1.3 Pulsating white dwarfs

As mentioned before, as white dwarfs cool, they will reach effective temperatures at which oscillations are driven mainly by changes in the opacity in the envelope. Three types of pulsating white dwarfs are known, classified according the composition of their atmosphere: the ZZ Ceti, GW Vir, and V777 Her stars. Theoretically, a fourth class of pulsating white dwarfs has been proposed having C-dominated atmospheres, DQV, however the cause of their variability is still under discussion.

ZZ Ceti (or DAVs, see Landolt 1968; Gianninas et al. 2011) are H atmosphere white dwarfs located in an instability strip that spans ≃10 000–12 300 K. Their effective temperatures are slightly correlated with their surface gravities e.g. the higher the surface gravity, the hotter the white dwarf.

GW Vir (or DOV stars, McGraw et al. 1979) are hot white dwarf pulsators, with $T_{\rm eff}$=75 000–170 000 K. The most intensely studied example of this class is the prototype PG 1119-035.

V777 Her (or DBV, see for example Winget et al. 1982; Provencal et al. 2009; Østensen et al. 2011) are He-rich atmospheres which have temperatures ~22000–28000 K (Fontaine & Brassard, 2008) that lie between the previous two classes. The prototype is GD358 (Winget et al., 1982).

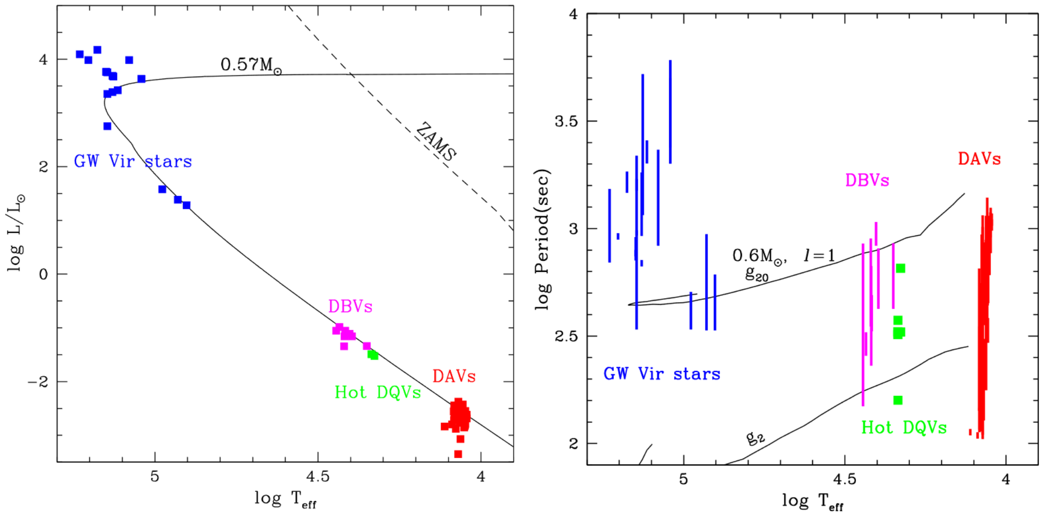

Figure 1.7: *Left:* HRD of the three (plus a questionable fourth) classes of pulsating white dwarfs together with the evolutionary track of a 0.57 M$_\odot$ white dwarf. *Right:* Range of periods observed in the different classes of white dwarf pulsators plotted against the effective temperature: ≃300–5000 s for GW Vir, ≃200–1000 s for DBVs, and ≃100–1000 for DAVs. Cooling models for a 0.6 M$_\odot$ white dwarf for dipole mode pulsations (l=1) are shown (see Section 1.1.3). Figures taken from Saio (2013).

Finally, somewhat peculiar, white dwarfs with C-rich atmospheres (DQV, see Montgomery et al. 2008a; Dufour et al. 2008a) may represent a fourth class, which have effectives temperatures within the range 18 000–24 000 K (Dufour et al., 2008a). As mentioned above, it is yet uncertain if they drive pulsations. For example its prototype, SDSS J142625.71+575218.3 (Dufour et al., 2008b), could also be a white dwarf in an ultra-compact binary (a AM CVn, see Section 1.2.3) that is accreting C (Montgomery et al., 2008a). Addionally, the discovery of a hot DQ showing a period of 2.110±0.045 days rules out the possibility of pulsations as the source of photometric variations in this star since the bulk of pulsating white dwarfs have modes shorter than 2000 s (e.g Winget & Kepler, 2008). A few of the DQV present a second periodicity detected in the ultraviolet and optical, but it is associated with the harmonic of the dominant period (Dufour et al., 2011). In addition the fact that a large fraction (~70%) of them present strong magnetic fields (~1 MG, Dufour et al. 2011, 2013), suggests that the photometric variations may be due to varying levels of Zeeman splitting as function of rotation phase.

The locations of these three classes plus the (uncertain) fourth class of pulsating white dwarfs in the HRD are shown in the left panel in Figure 1.7.

Usually pulsations are identified as radial or non-radial. The radial pulsation is just a simplified case of the non-radial pulsation where the star swells and contracts around its equilibrium state. The time scales of radial pulsations are set by the dynamical time scale ($T_{\rm dyn} \simeq (R^3/GM)^{1/2}$, Shapley 1914), which is only a few seconds for white dwarfs, which complicates their detection within the available instrumentation. However, pulsating white dwarfs have periods on the order of a few to tens of minutes (right panel in Figure 1.7). They are non-radial g-mode pulsations because the dominant restoring force is gravity[1].

In this thesis, the class of interest are the ZZ Ceti, which is by far the largest known group of pulsating white dwarfs, comprising over 100 members.

ZZ Ceti pulsations and the κ-mechanism

For pulsating white dwarfs with H-rich atmospheres, ZZ Cetis, the observed pulsations are g-modes, driven by the ionisation of H. The range of surface gravities and effective temperatures that satisfy the driving conditions define an instability strip in the $T_{\rm eff}$/log g parameter space (Figure 1.8). Empirically, this strip spans effective temperatures between $\rm T_{eff}$ = 12000 K (for high-mass white dwarfs, log $g \simeq 8$) and $\rm T_{eff}$ = 9500 K (for extremely low-mass white dwarfs, log $g \simeq 6.5$, Gianninas et al. 2014). The instability strip is consistent with theoretical models of white dwarf envelopes (Van Grootel et al., 2012, 2013).

The driving mechanism of the pulsations is related to the opacity, thus it is known as the κ-mechanism. In the H and He the ionization layers a small increase in density produces an increase in opacity, which blocks the radiation. Therefore, the gas heats and the pressure increases causing an expansion of the layer. As it moves outwards the ionization layer expands, becoming more transparent to radiation, and hence allows radiation flows through, and the gas cools. As a consequence, the pressure drops, and can no longer support the weight of the overlying layers starting its contraction to the initial equilibrium point. This effect causes an oscillation and the outer layers of the star pulsate. During the contraction, H (or He) recombines and therefore flux is absorbed. Hence, the condition for a heat engine is present: the layer gains heat on compression.

The period of the oscillation must be similar to the thermal time scale in the driving zone. If the oscillation period is much longer than the thermal time scale, then the driving

---

[1] Another group of pulsations is also believed to exist, the non-radial p-mode pulsations, where the restoring force is the pressure. However, oscillations with typical p-mode periods and amplitudes have not been detected yet, partly due to the fact that they are likely to occur on time scales of only a few seconds, as well as with significantly lower amplitudes than the g-mode pulsations (Winget & Kepler, 2008)

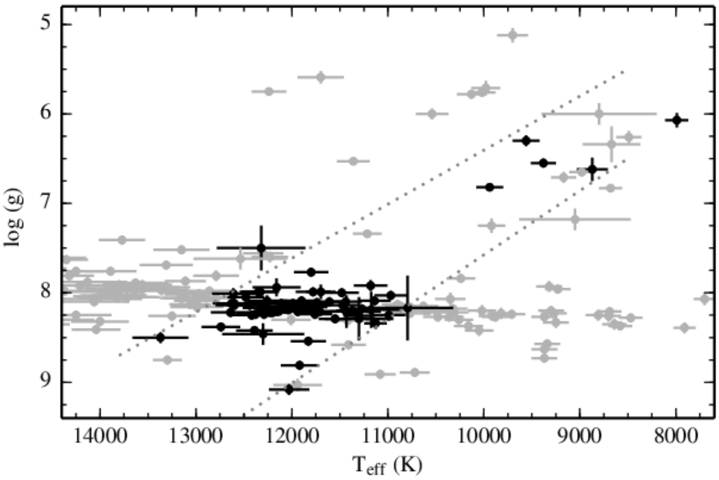

Figure 1.8: Instability strip for white dwarfs with H-rich atmospheres as a function of surface gravity and effective temperature. Shown in black are confirmed pulsating white dwarfs (ZZ Cetis) and in grey non-pulsating white dwarfs. The dotted lines follow the empirical instability strip as in Gianninas et al. (2014).

layer will remain in thermal equilibrium and not be able to excite the mode.

Modelling the pulsations

3D oscillations are described with spherical coordinates: r is the distance to the centre, θ represents the co-latitude which is measured from the pulsation pole, and ϕ is the longitude. The pulsations have displacements in the (r, θ, ϕ) directions given by:

$$\xi_r(r,\theta,\phi,t) = a(r)\, Y_l^m(\theta,\phi)\exp(-\mathrm{i}2\pi\mu t), \tag{1.3}$$

$$\xi_\theta(r,\theta,\phi,t) = b(r)\,\frac{\partial Y_l^m(\theta,\phi)}{\partial\theta}\exp(-\mathrm{i}2\pi\mu t), \tag{1.4}$$

$$\xi_\phi(r,\theta,\phi,t) = \frac{b(r)}{\sin\theta}\,\frac{\partial Y_l^m(\theta,\phi)}{\partial\phi}\exp(-\mathrm{i}2\pi\mu t), \tag{1.5}$$

$a(r)$ and $b(r)$ are the radial amplitudes, μ is the frequency of the oscillation, and Y_i^m are the spherical harmonics. Therefore there are three quantum numbers to specify the modes in 3D stars: n which represents the radial nodes, l is the degree of the mode which corresponds to the number of surface nodes, and m is the azimuthal order of the mode where $|m|$ specifies the number of longitudinal lines. Therefore l-$|m|$ corresponds to lines of co-latitude (Figure 1.9).

If $l = 0$ the modes are radial, and the simplest case is the fundamental radial mode, where the star expands and contracts symmetrically with the core as the node and the surface as the displacement antinode. The first overtone will have a concentric shell within the star, this static shell will be the node and the material moves above and below this node in antiphase. For example Cepheid variables, RR Lyrae and δ Scuti stars pulsate in the fundamental and first overtone radial modes.

If $l > 0$ the mode is non-radial, and the simplest case corresponds to the dipole mode with $l = 1$, $m = 0$. The equator is the node ($P_1^0(\cos\theta) = \cos\theta$), and the northern hemisphere contracts while the southern expands, then vice versa. However the centre of mass need to be fixed implying that non-radial modes occur when $n \geq 1$, then for $l = 1$, there is at least one radial node within the star and therefore while the outer shell moves upwards, the inner shell displaces downwards. Examples of dipoles are the rapidly oscillating Ap stars. The situation complicates more if l increases, e.g a quadrupole ($l = 2$, $m = 0$), the nodes are at 35 degrees ($P_2^0(\cos\theta) = (3\cos^2\theta - 1)/2$), and both poles swell up while the equator contracts.

Those are the simplest cases of l degrees considering always $m = 0$, however there are $2l+1$ possible solutions for a given l degree. Figure 1.9 shows the case for an octupole ($l = 3$) and m=0,1,2,3, but also includes the inclination which adds another factor of complication. Therefore, we are not yet capable to detect the nodal lines such that we can resolve the stellar surface for any star but the Sun.

Until now the fundamental properties of single white dwarfs have been explained, but white dwarfs can be part of binary systems. I will explain the evolution of binary systems containing a white dwarf, which special emphasis on Cataclysmic Variables (CVs).

1.2 White dwarfs in binary systems: Cataclysmic Variables

As introduced in Section 1.1.1, the nascent stars from a collapsing cloud are likely to have nearby companions. Most of the stars are born in binary systems (Boss & Myhill, 1992), which which are gravitationally bound to closed orbits around each other other, and the evolution of these systems depends strongly on their separations. If the orbit is very wide the two stars do not influence each other and evolve in the same way as single stars. However, in this thesis the focus is on close binary systems containing a white dwarf as the primary component. These systems are called cataclysmic variables (CVs), due to the dramatic variations in their brightness. They are systems comprising white dwarfs that accrete material from low-mass companions. Here, I will explain the evolutionary path

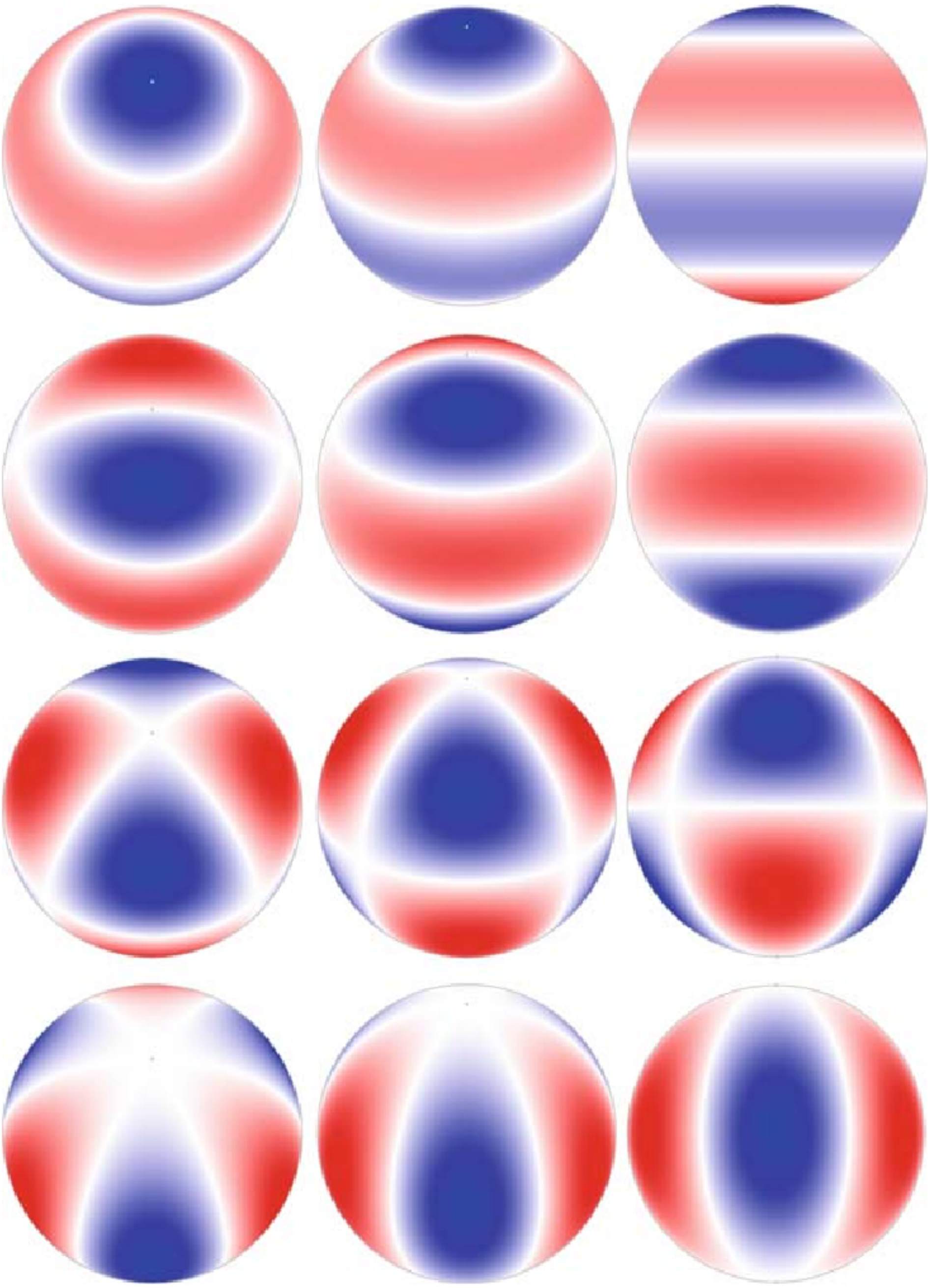

Figure 1.9: Octupole with $l = 3$. The columns varies the inclination for 30°, 60°, and 90° (from left to right). The white bands show the positions of the surface modes. Material moving outward and inward are represented in blue and red, respectively. The top row shows $m = 0$ where the nodes lie at latitudes ±51° and 0°. $m = \pm 1$, $m = \pm 2$ and $m = \pm 3$ are shown in the second, third and fourth rows, respectively. The sign of m distinguishes the rotation.

towards these types of binaries. However, it is necessary to define few concepts related with the geometry of a binary system and the equations that govern the evolution of the binary configuration.

1.2.1 Geometry of a binary

In a binary configuration having a primary star with mass M_1 (primary stands usually for the more massive star in the binary), a secondary star with mass M_2, and a separation a, the gravity of these stars defines equipotential surfaces, which are a function of their masses and the separation. The Roche geometry defines the gravitational potential in the corotating frame of the binary, as illustrated in Fig 1.10. The Roche lobes are the largest closed equipotential surfaces that enclose each of the stars. The Roche lobes of both stars meet at the Lagrange point L_1. The equivalent radius ($R_{\rm RL}$) of a Roche lobe is defined by setting the Roche lobe's volume equal to a sphere occupying the same volume. In the case for the secondary star, its Roche lobe is given by Eggleton's expression (Eggleton, 1983),

$$\frac{R_{\rm RL}}{a} = \frac{0.49q^{2/3}}{0.6q^{2/3} + \ln(1 + q^{1/3})}, \tag{1.6}$$

where $q = M_2/M_1$ is the mass ratio. Equation 1.6 is an updated version of the simpler analytical approximation of Paczyński (1971),

$$\frac{R_{\rm RL}}{a} = 0.462\left(\frac{q}{1+q}\right)^{1/3}, \qquad (q < 0.8) \tag{1.7}$$

The binary configuration is classified according to whether one, none, or both of the stars fill their Roche lobe. If none of the stars fills their Roche lobe the binary is called *detached* system, if only one of the star fills the Roche lobe, the binary is *semi-detached*, and if both stars are filling their Roche lobes, the system is in *contact* (Figure 1.10).

In general, the evolution of the orbital separation of a close binary is governed by the following equation,

$$\frac{\dot{a}}{a} = 2\frac{\dot{J}}{J} - 2\frac{\dot{M}_1}{M_1} - 2\frac{\dot{M}_2}{M_2} + \frac{\dot{M}}{M}, \tag{1.8}$$

with J the angular momentum, M_1 and M_2 the primary and secondary masses, $M = M_1 + M_2$ the total mass and dots representing time derivatives. It can be deduced from this equation that the evolution of the orbit can be driven by changes in angular momentum (e.g. losses via emission of gravitational waves or magnetic braking, which will be explained in more details later), or if a fraction of the total mass is lost from the binary system (e.g. ejection of mass due to nova eruptions, which are thermonuclear runaways on the white dwarf surface),

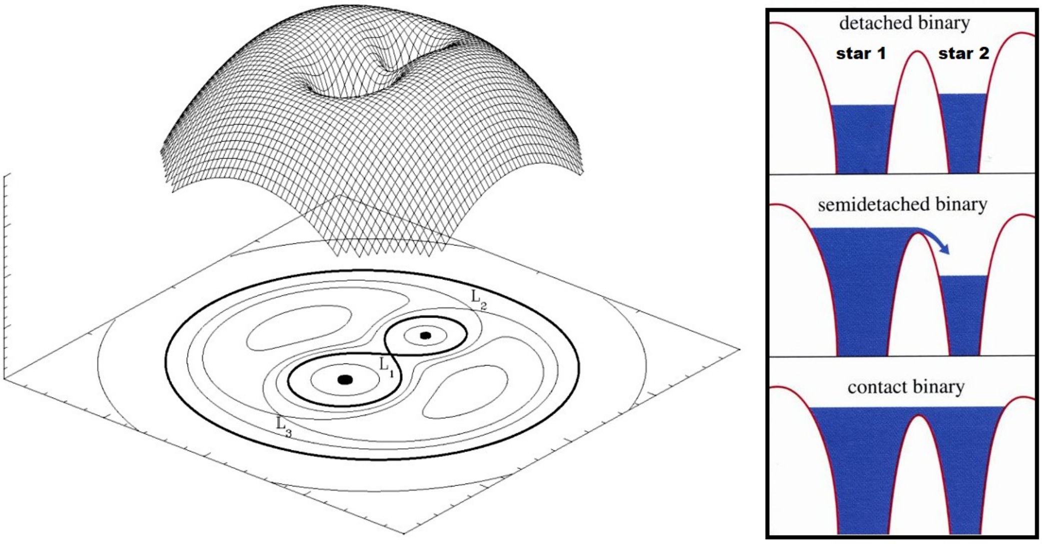

Figure 1.10: Three dimensional (and projected onto two dimensions) representation of the Roche potential in a binary with a mass ratio $q = 2$. L_1, L_2 and L_3 are Lagrange points where the gravitation of the two stars and the centrifugal potential are cancelled. The thick solid black line that crosses L_1 represents the shape of the Roche lobes. Figure taken from Postnov & Yungelson (2014). On the right side, a sketch that represents the binary configurations (top to bottom) of none, one, or both stars filling their Roche lobes.

or mass variations of one of the stars. A key example is mass transfer through the L_1 point from one star that fills its Roche lobe to the other, which is the scenario that, CVs, the systems of interest in this thesis, present.

Angular momentum losses: magnetic braking & gravitational radiation

Since this thesis focuses on CVs, I will explain the two processes that are thought to operate within the standard theory of Cataclysmic Variable (CV) evolution that lead to $\dot{J}$ in equation 1.8: magnetic braking and gravitational radiation.

Magnetic braking has its origin in the weak stellar wind of the low-mass companion. Assuming a dipole, the magnetic field lines near the rotational equator are closed, therefore the wind is mainly emitted from the poles. The ionised particles in the wind are forced by the magnetic field to corotate with the star out to the Alfvén radius. When the matter decouples from the magnetic field the particles are accelerated to high speeds leaving the companion and in this process carry away substantial amounts of angular momentum, resulting in a braking of the stellar rotation. This phenomenon has been measured indirectly by its effect on the rotation rate of single stars (Kraft, 1967; Schatzman, 1962; Reiners & Basri, 2008).

However, due to tidal forces the rotation of the companion in a CV is synchronised with the binary orbit, consequently angular momentum is extracted from the binary orbit. In the literature many descriptions have been developed in order to model magnetic braking (Verbunt & Zwaan, 1981; Rappaport et al., 1983; Mestel & Spruit, 1987; Kawaler, 1988; Andronov et al., 2003; Ivanova & Taam, 2003) and there are huge differences among them, by at least three orders of magnitude (see Knigge et al., 2011, for a review). However, within many studies Rappaport et al. (1983)'s prescription has been used due to the easy manipulation of the strength and shape by changing the γ exponent,

$$\dot{J}_{\mathrm{MB}} = -5 \times 10^{-29} k_2^2 f^{-2} \left(\frac{2\pi}{P_{\mathrm{orb}}}\right)^3 \left(\frac{M_2}{M_\odot}\right) \left(\frac{R_2}{R_\odot}\right)^4 \left(\frac{R_2}{R_\odot}\right)^{\gamma-4} . \tag{1.9}$$

k_2 is the radius of gyration of the part of the star coupled to the magnetic wind, usually ~0.1 for low-mass stars and f is a constant that lies within ~0.7–1.8 (for details see Schatzman, 1962; Huang, 1966; Mestel, 1968; Eggleton, 1976; Whyte & Eggleton, 1980; Verbunt & Zwaan, 1981). The origin of the magnetic field in low-mass stars is unclear, but it is believed that it is generated by a shell dynamo in the transition region between the radiative core and the convective envelope (Charbonneau & MacGregor, 1997; MacGregor & Charbonneau, 1997).

Another mechanism of angular momentum loss is gravitational radiation. According to the theory of general relativity, all close compact binaries warp the spacetime with ripples. These waves are gravitational radiation that is described by Einstein's quadrupole formula (Paczyński, 1967):

$$\dot{J}_{\mathrm{GR}} = \frac{-32}{5} \frac{G^{7/2}}{c^5} \frac{M_1^2 M_2^2 (M_1 + M_2)^{1/2}}{a^{7/2}} \tag{1.10}$$

with G the gravitational constant, and c the speed of light. It can be clearly deduced that when binaries have sufficiently short orbital periods, angular momentum loss through gravitational wave emission becomes very efficient, and it is a strong function of the masses of the binary. Thus, compact and dense objects such as neutrons are strong space time distorters, and their gravitational waves can be directly measured, as the two colliding neutron stars detected in 2017, GW170817 (Abbott et al., 2017).

Stability of mass transfer

In semi-detached systems with wide orbits in which all the material from the mass losing star (M_{donor}) accretes onto the accreting star (M_{acc}), i.e. the total mass of the system ($M_{\mathrm{acc}} + M_{\mathrm{donor}}$) remains constant (conservative scenario), the stability of the mass transfer is dictated by how the donor Roche lobe evolves as response to the mass transfer. The change of the Roche lobe can the obtained from differentiating the Roche lobe approximation of Paczyński (1971), given in equation 1.7,

$$\frac{\dot{R}_{\rm RL}}{R_{\rm RL}} = \frac{\dot{a}}{a} + \frac{1}{3}\frac{\dot{M}_{\rm donor}}{M_{\rm donor}}, \tag{1.11}$$

$\dot{M}_{\rm donor}$ is negative, since it is the mass losing star. In this expression, $\dot{a}/a$ can be obtained from equation 1.8, resulting in:

$$\frac{\dot{R}_{\rm RL}}{R_{\rm RL}} = 2\frac{\dot{J}}{J} - 2\frac{\dot{M}_{\rm donor}}{M_{\rm donor}}\left(\frac{5}{6} - q\right) \tag{1.12}$$

From this expression, if the angular momentum is conserved, $\dot{J} = 0$, then in situations when $q > 5/6 \sim 1$, i.e. the mass of the donor star is the largest, the Roche lobe of the donor shrinks as a consequence of its mass loss, increasing the mass transfer towards very high rates. In contrast, if $q < 5/6 \sim 1$, the Roche lobe grows, but in fact, as seen in equation 1.11, the change of the Roche lobe depends on the mass loss and the change of the orbit. Therefore, the binary will expand its orbit resulting the system to detach and therefore the accretion to stop. This fact is in contradiction with the ongoing accretion observed in CVs, which have $q < 5/6 \sim 1$ and therefore it was the empirical motivation to include the angular momentum losses in the models of CV evolution, as explained above.

1.2.2 Evolution of CVs: the initial stages

The early evolution starts with the two stars on the ZAMS, where the more massive star (primary star with mass M_1) evolves off the MS first, towards the RG phase. If, during the RG phase, the primary fills its Roche lobe, then material from the envelope starts to be transferred to the companion (secondary star with mass M_2). The mass transfer continues if the primary (donor) expands faster than its Roche lobe. For low $\dot{M}_1$ mass transfer is stable, meaning that the secondary is able to accrete (a fraction of) the transferred matter. However, if $\dot{M}_1$ increases, eventually the accretion luminosity may exceed the Eddington luminosity limit and the secondary is not able to accrete the material at the rate that is deposited. It results that the secondary is engulfed by material lost from the primary, and the system will enter a common envelope phase. The details of this stage remain poorly understood.

The classical prescription of the common envelope is based on the conservation of energy, so that the envelope is expelled extracting a fraction α of the difference of orbital energy between the initial and final configuration of the binary (Webbink, 1984; Tutukov &

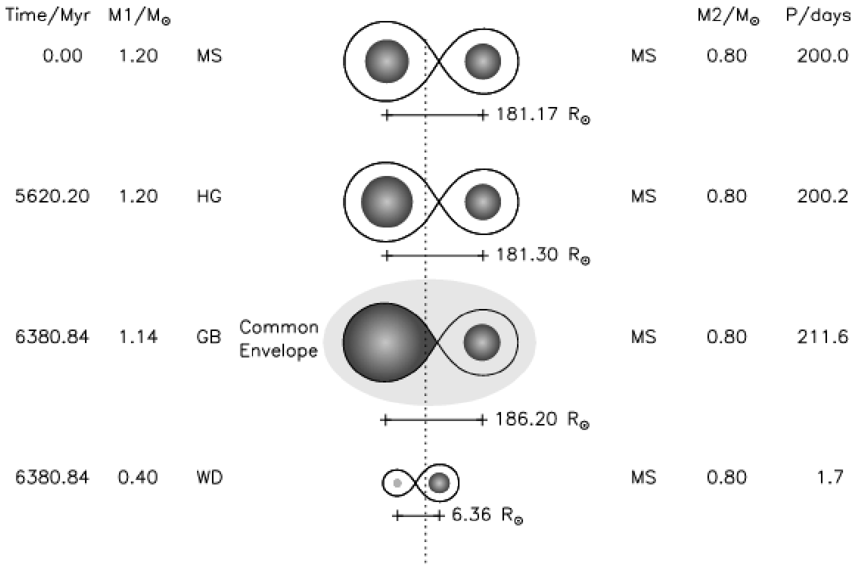

Figure 1.11: Schematic representation of the evolution resulting in the formation of a white dwarf (WD) plus main sequence (MS) post common envelope binary. HG stands for Hertzsprung gap and GB for giant branch. Figure taken from Willems & Kolb (2004).

Yungelson, 1979; van den Heuvel, 1976; Paczyński, 1967):

$$E_{\rm bind} = \alpha\, \Delta E_{\rm orb}. \tag{1.13}$$

The orbital separation needs to be highly reduced such that the envelope is ejected. However, this prescription fails to reconstruct the common envelope phase of double white dwarfs since it requires a physically unrealistic high (or even negative) efficiency, meaning that following the first common envelope the orbit shrunk significantly, that there would not be enough space for the secondary star to evolve and to produce a core as massive as the primary white dwarf (Nelemans et al., 2000). As a consequence, an alternative prescription was proposed based on conservation of angular momentum, J, in which the amount by which the binary's orbital separation decreases depends on the fraction of the mass of the envelope, $m_{\rm env}$ (Nelemans et al., 2000; Nelemans & Tout, 2005):

$$\frac{\Delta J}{J} = \gamma\, \frac{m_{\rm env}}{M_1 + M_2}\,. \tag{1.14}$$

The physics of the common envelope phase are not fully understood (e.g Toonen & Nelemans, 2013), basically because the duration of this phase is believed to be very short ($\lesssim 10^3$ yr, challenging the observations) and accordingly difficult to model dynamically. The components emerging from the common envelope phase comprise the remnant of the primary, a He or CO white dwarf (depending on the mass and evolutionary state of

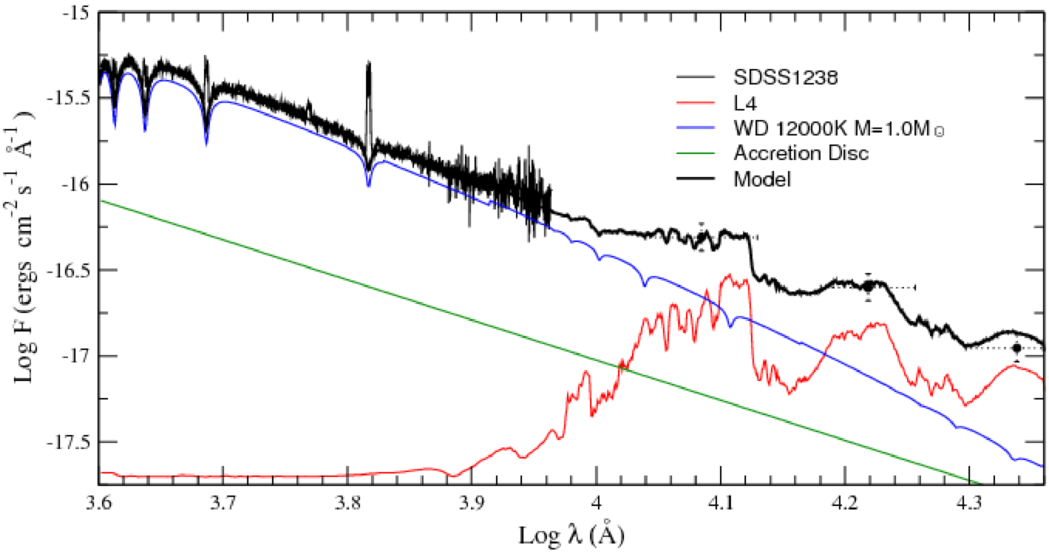

Figure 1.12: SED of SDSS1238-0339, a cataclysmic variable that has evolved beyond the period minimum (see text for details). Dots show the JHK magnitudes, L4 stands for a L4-brown dwarf. Figure taken from Aviles et al. (2010).

the progenitor), and it is usually assumed in binary population synthesis studies that the secondary remains unaffected, and is still on the MS. Figure 1.11 shows the evolution of a 1.2-$M_{\odot}$ primary plus a 0.8-$M_{\odot}$ secondary, which were initially separated by a distance of $\simeq$181 $R_{\odot}$ and shrink dramatically to $\simeq$6 $R_{\odot}$ through the common envelope. The result of ejecting the envelope leaves a detached system composed by a compact stellar remnant white dwarf in a much tighter orbit with its companion, a Post Common Envelope Binary (PCEB).

The PCEB population is dominated by systems with low-mass MS-companions and according to population synthesis studies (Yungelson, 2005) about one third of them never evolve further in the Hubble time. If following the common envelope the orbital separation of the binary is a few solar radii and the mass of the companion is lower than $\sim$1.4 $M_{\odot}$, gravitational radiation and magnetic braking bring the stars together and the secondary will eventually overflow its Roche lobe. This new configuration is a semi-detached system called as cataclysmic variable, in which the white dwarf is accreting from the low-mass MS companion.

Therefore, the Spectral Energy Distribution (SED) of a CV is composed by three components (plus one): the white dwarf which is hot and its emission dominates mainly in the ultraviolet, declining towards the optical; the companion which is cooler and contributes flux in optical towards near Infrared (IR), and the accretion disc, identified by its clearly double peaked emission lines. If the disc is bright, it can contaminate the flux of the white dwarf and the secondary, and it results very difficult to disentangle the three components. Sometimes, there is additional flux from a fourth component corresponding to a hot spot produced by the shock of the accreting material from the secondary to the disc. Figure 1.12 shows an example of the SED of a CV whose evolution was driven beyond the period minimum (which is the shortest period that CVs can reach and will be explained in more details later).

As explained in Section 1.2.1, the stability of the mass transfer in CVs depends upon the mass ratio q. For systems with $q > 1$, the mass transfer increases to rates at which the accreted material can steadily burn on the the white dwarf surface, providing a potential pathway for Supernovae type Ia (SNIa). This evolutionary channel will be explained in more detail in Section 1.2.6. Alternatively, for systems with $q < 1$ the mass transfer can only occur if the systems lose angular momentum. I will now explain the evolution of this latter case.

1.2.3 Orbital period distribution

In CVs with $q < 1$, the masses of the companions are limited to masses lower than the Chandrasekhar mass limit. And since under a Roche lobe overflow assumption, the average density of the companion is a function of the orbital period ($\overline{\rho} \propto P_{\mathrm{orb}}^{-2}$), It results that the orbital periods in these CVs are shorter than ~12 h. As explained above, the standard evolution of CVs is regulated by angular momentum losses, which reduce the orbit towards shorter periods, but it is also important to understand the response that the MS secondary has to its mass loss. Therefore, it is necessary to explain the mass-radius index, (ζ, M $\propto$R$^{\zeta}$), which is tightly related with the contraction or expansion of the secondary in response to mass loss,

$$\frac{\dot{R}_2}{R_2} = \zeta \frac{\dot{M}_2}{M_2} \tag{1.15}$$

If the mass loss timescale is longer than thermal timescale, $\tau_{\mathrm{ML}} \gg \tau_{\mathrm{KH}}$, then the secondary is in total equilibrium and the index can be obtained from the thermal equilibrium mass-radius relation of low mass MS stars, (M~R$^{\zeta}$, with $\zeta \simeq$0.8). If, in contrast, the mass loss timescale is shorter than thermal timescale, $\tau_{\mathrm{ML}} \ll \tau_{\mathrm{KH}}$, the response is adiabatic (ζ=-1/3 for low mass stars with significant convective envelopes, Paczyński 1965; Rappaport et al. 1982). The response of the secondary to mass loss is regulated by this index.

Period gap

The period gap is a strong feature in the period distribution of CVs with a dearth of systems in the range $P_{\rm orb} \simeq 2$–3 h (green band in Figure 1.13), that can be explained by the cessation of magnetic braking. During the evolution driven by angular momentum losses (mainly magnetic braking for systems with $P_{\rm orb} \gtrsim 3$ h), the timescale at which the outer layers are removed from the secondary (hereafter mass loss timescale $\tau_{\rm ML}$) is somewhat shorter than the timescale on which the companion can readjust its thermal equilibrium (thermal timescale $\tau_{\rm KH}$) by the rate of nuclear burning in its core. Hence, the CV is only a bit out of its thermal equilibrium ($\zeta \simeq 0.65$). In other words, by the removing the envelope, the gravity decreases faster than the thermal pressure and therefore the secondary inflates. Indeed, it has been found that the secondaries in CVs with $P_{\rm orb} < 6$ h are 20%–30% larger than MS stars of the same mass (Patterson et al., 2005; Knigge, 2006). During the evolution the mass-losing companion eventually reaches a stage at which it becomes fully convective ($M_2 \simeq 0.2$–$0.3\,{\rm M}_\odot$,Knigge et al. 2011) and as a consequence the magnetic field topology of the secondary is highly modified, from large, open field lines at $M_2 \gtrsim 0.2$–$0.3\,{\rm M}_\odot$ to small closed field lines at $M_2 \lesssim 0.2$–$0.3\,{\rm M}_\odot$ (Morin et al., 2010; Shulyak et al., 2017). Hence, it is thought that magnetic braking abruptly decreases, becoming very inefficient. The response of the secondary to this relaxation is to find again its thermal equilibrium, shrinking inside its Roche lobe, and stopping the mass transfer. At this stage, the orbital period of the CV is roughly 3 h, and the detached CV enters into the period gap, and the secondary recovers the mass-radius index of ≃0.8. From now on, the evolution is driven by the less effective gravitational wave radiation, which continues reducing the orbit and hence the size of the Roche lobe, until the secondary fills it again, and the mass transfer resumes at orbital periods of around 2 h. The re-emerging active CV contains a secondary in thermal equilibrium and therefore will be indistinguishable from a MS analogue (King & Kolb, 1995).

Period minimum

After the CV exits the period gap, the decreasing orbital period is limited to a minimum value ($P_{\rm min}$), then the system bounces back towards longer orbital periods. Approaching $P_{\rm min}$, the secondary is slowly running out of H in the core, progressively extinguishing the nuclear fusion. Therefore, the core evolves towards a state of non-relativistic electron degeneracy, i.e. the response of the secondary is to become adiabatic ($\zeta \longrightarrow -1/3$). The decreasing mass-radius index is responsible that the orbit stops shrinking and starts to widen. Let us look at the reason for this statement: in this regime q is very small and therefore the Roche lobe can be approximated by Paczynski's (1971) approximation given in equation 1.11, where $\dot{R}/R$ can be replaced by equation 1.15, resulting in:

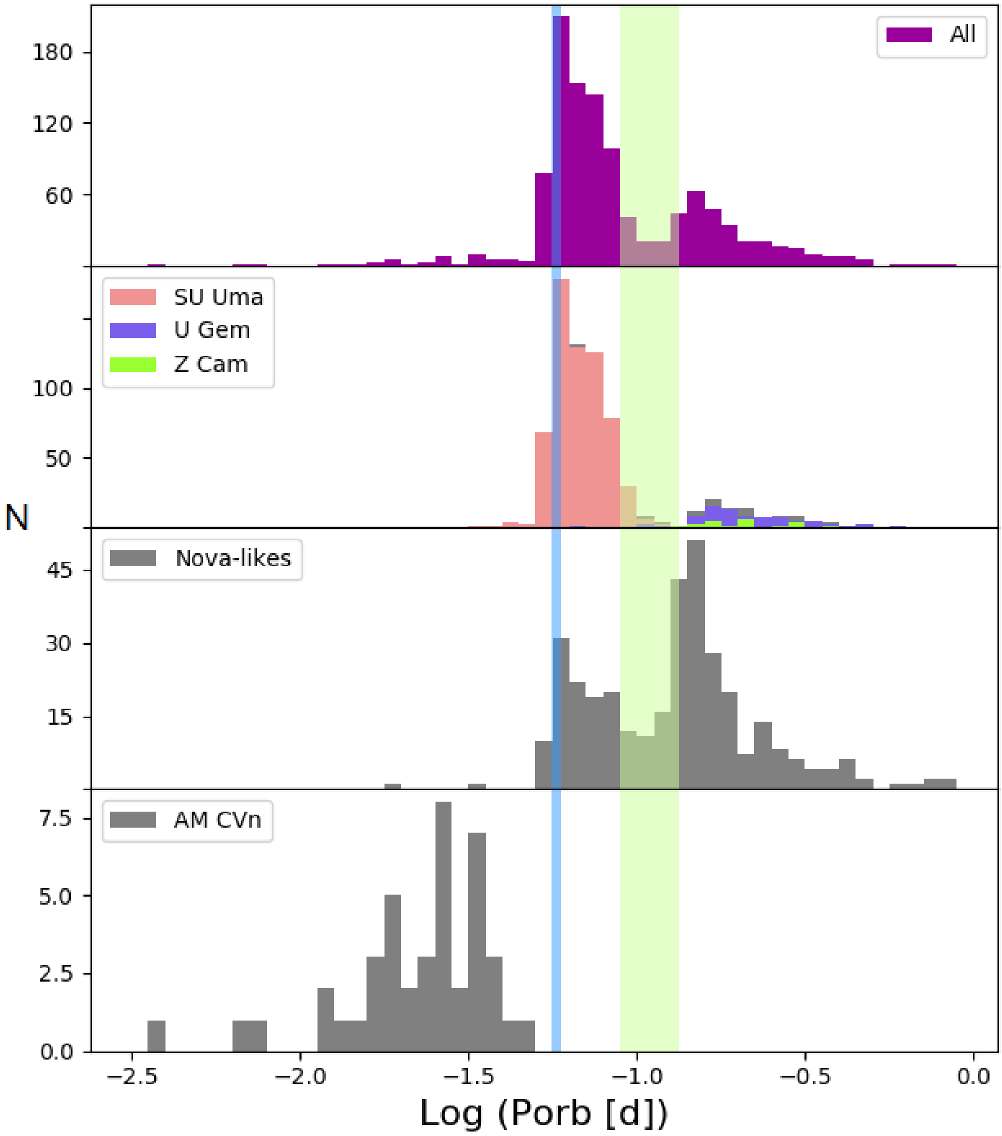

Figure 1.13: Period distribution of CVs with white dwarfs with no (or very weak) magnetic fields. The period gap (≃2–3 h) and the period minimum (≃80–86 min) are represented with green and blue bands, respectively. Data taken from Ritter & Kolb Catalogue Version 7.20.

$$\frac{\dot{a}}{a} = \left(\zeta - \frac{1}{3}\right)\frac{\dot{M}_{\rm sec}}{M_{\rm sec}}. \tag{1.16}$$

It is clear that if $\zeta < 1/3$ the orbit expands ($\dot{M}_{\rm sec}$ is negative). Therefore, it is not expected to find CVs at periods shorter than $P_{\rm min} \simeq 65$–70 min (Kolb & Baraffe, 1999; Howell et al., 2001), and the period distribution of a homogeneous sample of CVs from the

Sloan Digital Sky Survey (SDSS) shows a peak at $P_{\rm min} \simeq 80$–86 min (Gänsicke et al., 2009). The observed period minimum is marked within a blue band in Figure 1.13.

While the rare kind of AM Canum Venaticorum (AM CVn) stars are not strictly CVs, they are usually included in the zoo of CVs. They have ultra-short orbital periods, between 10 and 65 minutes (see bottom panel in Figure 1.13). The lack of H in their spectra indicates that their donors are He-dominated, and different evolutionary pathways have been proposed for their origin which will be explained in more details in Section 1.2.6

1.2.4 CV sub-classes

The broadest split into two categories depends upon the strength of the magnetic field of the white dwarf.

In magnetic systems, the field disrupts the accretion disc at the Alfvén radius (where the magnetic energy density is equal to the kinetic energy density of the gas, deflecting significantly the radial accretion), and the gas stream flows along the field lines to accrete onto the magnetic poles of the white dwarf. These systems are further subdivided into polars, where the magnetic field is sufficiently strong to prevent the formation of the disc, and intermediate polars, which have weaker fields, allowing a truncated disc. A key characteristic due to the strong magnetic field in polars is the synchronisation of the orbital period with the white dwarf spin period, whereas in intermediate polars the spin period is always shorter than the orbital period.

In non- or very weakly magnetic systems, the disc is not disrupted. They can be further classified according the mass transfer rate and orbital period. The first group are the nova-like systems, which do not undergo quasi-periodic outbursts, they contain an accretion disc in the steady hot state (high state). A second group is known as dwarf novae, which undergo recurrent outbursts, brightening ~2–5 magnitudes. These outbursts are thought to occur due to an instability in the accretion disc, which I will explain later in more detail. The period distribution of these two kinds of CVs are illustrated in Figure 1.13.

In this thesis, the study of the dwarf nova GW Lib will be presented, therefore I will provide some more details on this CV subclass .

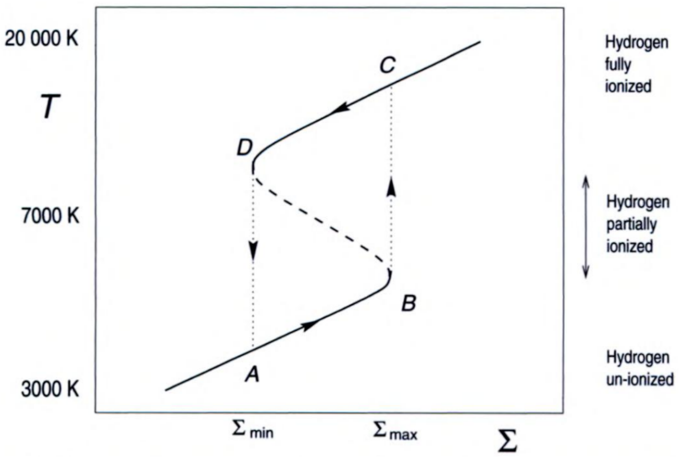

Figure 1.14: Surface density (Σ) against temperature (T) plot which illustrates the dwarf nova cycle that leads to outbursts.

1.2.5 Dwarf Novae

In the sample of observed CVs, dwarf novae represent the largest fraction, because their discoveries are based on their outbursts (see below). The recurrent outbursts last typically ≃2–20 days, and intervals between outbursts range from as short as ten days to tens of years (Warner, 1995).

Outbursts

The large amplitude of the dwarf nova outbursts suggests an increase in the luminosity of the accretion disc that is thought to be related to a thermal-viscous disc instability (Osaki, 1974; Hōshi, 1979). This instability is caused by the partial ionisation of H (Meyer & Meyer-Hofmeister, 1981). This process is represented by the well-known "S-curve" in a plot of the disc's temperature against its surface density (Σ), as shown in Figure 1.14. Material from the secondary is transferred at a rate higher than it can be transported through the disc by viscous processes (the viscosity drives the redistribution of angular momentum), and matter builds up in the disc, increasing the surface density (A⟶ B). The viscosity increases slightly, which leads to an increase in temperature to the point that H starts to ionise (B). The ionisation causes a drastic increase in opacity, and the disc cannot radiate away efficiently the released energy, causing a fast increase in temperature (B ⟶ C). In this phase the disc is thermally unstable until H is fully ionised, at which point the disc has reached a new equilibrium state (e.g. Hellier, 2001).

In this hot, ionised environment the viscosity of the disc is much higher, and hence the material can flow through the disc faster, resulting in an increase of the accretion rate onto the white dwarf. Consequently, the excess of material is drained from the disc, causing the increase in luminosity, the outburst. Since the inward material flow now exceeds the rate at which material is provided by the secondary, the surface density decreases and so the temperature drops (C $\longrightarrow$ D), initialising recombination of the ions. This instability causes the disc to evolve rapidly back to the low neutral temperature and low viscosity state (D $\longrightarrow$ A). This state is known as the quiescence. Material then begins to build up again towards a new outburst, initialising the cycle again.

Further subtypes of dwarf novae are (see Figure 1.13):

- Z Camelopardalis stars (Z Cam): their light curves show rapid outbursts, which occasionally “halt” at a roughly constant brightness below (~0.7 magnitudes) their peaks (standstills). The standstills last from days to years. It is believed that Z Cam stars are the link between dwarf novae and nova-like systems (Smak, 1983), with the mass transfer rate fluctuating above and below the critical rate, behaving as a dwarf nova or nova-like (Schreiber & Gänsicke, 2002). Their orbital periods place them above the gap.
- SU Ursae Majoris stars (SU UMa): the recurrence time of the outbursts ranges from a few weeks to hundreds of days. In addition to normal outbursts, they present less-frequent brighter and longer outbursts, superoutbursts, that will be explained below. ER Ursae Majoris (ER UMa) stars and WZ Sagittae (WZ Sge) stars belong to this subtype. ER UMa undergo superoutbursts every 20–50 days, with subsequent outbursts every few days. In contrast, WZ Sge do not present normal outbursts, instead they undergo infrequent superoutbursts every few years to decades. Their orbital periods fall below the period gap.
- U Gem stars: while they show regular outbursts identifying them as dwarf novae, these systems cannot be classified either as SU UMa nor Z Cam types. They usually have longer orbital periods, above the period gap.

Superoutbursts

The superoutbursts are ~0.7 magnitudes brighter and last ~ 5 times longer than normal outbursts. As an example, the light curve of the superoutburst of the dwarf nova GW Lib is shown in Figure 1.15. During a superoutburst, tidal interactions between the disc and the donor star cause the disc to become asymmetric. The increased viscous dissipation caused

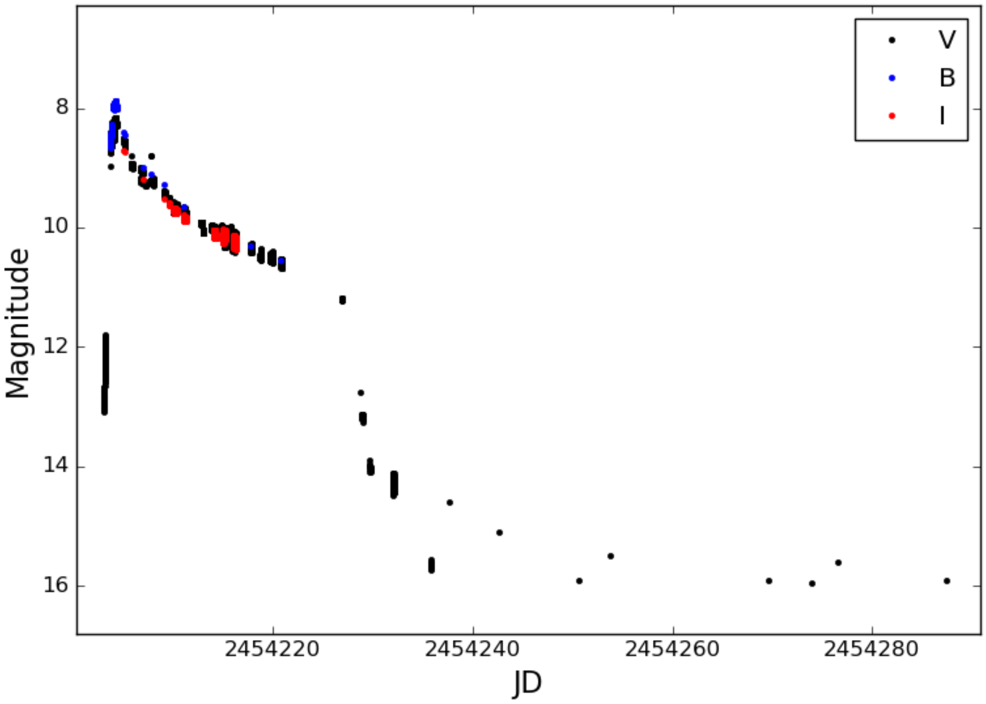

Figure 1.15: Light curve of the dwarf nova GW Lib during the outburst in 2007, where its brightness increased by ~ 8 magnitudes (data taken from AAVSO). Chapter 5 presents the study of the pulsating white dwarf in this system.

by this resonant interaction between the donor and the distorted disc leads to periodic brightness variations known as superhumps.

1.2.6 Shell burning on white dwarfs

Until now I considered the evolution of CVs where $q < 1$. For systems in which the mass of the donor is larger than that of the white dwarf accretor, $q > 1$, the evolution differs from the standard scenario of CVs.

Thermal time scale mass transfer

The stability for mass transfer from the companion depends on the radius-mass exponents (see Section 1.2.3) of the Roche lobe, $\zeta_{\rm RL} = d\ln(R_{\rm RL})/d\ln(M_{\rm MS})$, and the MS companion, $\zeta_{\rm MS} = d\ln(R_{\rm MS})/d\ln(M_{\rm MS})$. In general, the Roche lobe reduces ($\zeta_{\rm RL}$>0) when material is transferred from the donor to a less massive accretor. If the donor star has a radiative envelope, it will shrink ($\zeta_{\rm MS}$>0) in response to mass loss, but if it has a deep convective en-

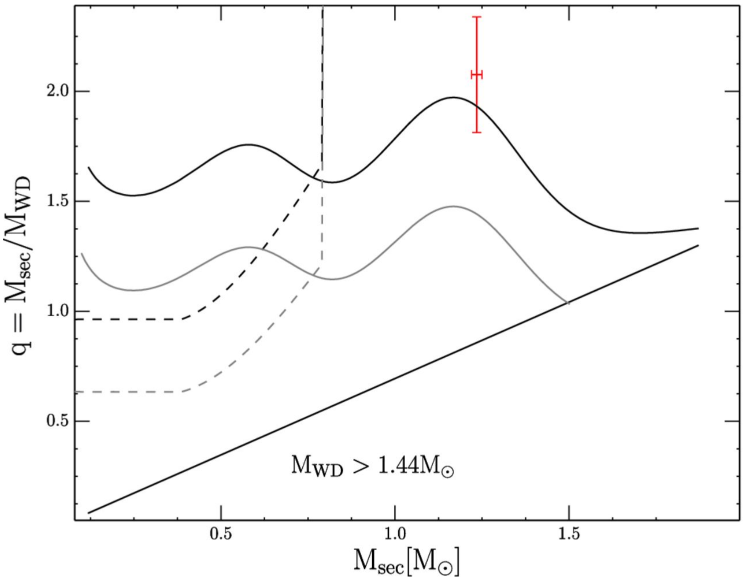

Figure 1.16: Critical mass ratio for thermal (solid) and dynamical (dashed) time scale mass transfer as a function of the mass of the main sequence donor. The mass ratio limit has been calculated assuming conservative (grey) and non-conservative (black) mass transfer. The red cross indicates the position of TYC 6760-497-1, which is a system that will undergo a phase of thermal time-scale mass transfer. Figure taken from Parsons et al. (2015).

velope, it will expand rapidly ($\zeta_{\rm MS}$<0). These parameters regulate whether the mass transfer proceeds on a dynamical or thermal time scale. If $\zeta_{\rm MS} < \zeta_{\rm RL}$ the Roche lobe radius shrinks more rapidly than the adiabatic radius, and the mass transfer proceeds on the dynamical time scale, which leads very quickly to a common envelope (Section 1.2.2). If, in contrast, $\zeta_{\rm MS} > \zeta_{\rm RL}$, the mass transfer occurs on the thermal time scale. Thermal time scale mass transfer can drive very high mass transfer rates.

The orbit shrinks faster to a point that the mass-losing star is no longer able to adjust its thermal equilibrium inside the rapidly reducing Roche lobe, resulting in a drastic increase of the rate of mass transfer. The response of the Roche lobe to the mass transfer depends on the mass ratio, whereas the response of the stellar radius of the companion to the mass transfer is a function of the mass transfer rate. The critical mass ratio for marginal stability against thermal time-scale mass transfer can be calculated by equating the mass-radius exponents of the Roche lobe and the star (Figure 1.16). Therefore, a pre-CV with a mass ratio of q=2, is likely to go through a phase of thermal time scale mass transfer. Since the average mass of the white dwarfs in pre-CVs is 0.67±0.21 $M_\odot$ (Zorotovic et al., 2011), the mass of their companions need to be as large as ~1.3 $M_\odot$ to ensure a thermal time scale mass transfer phase.

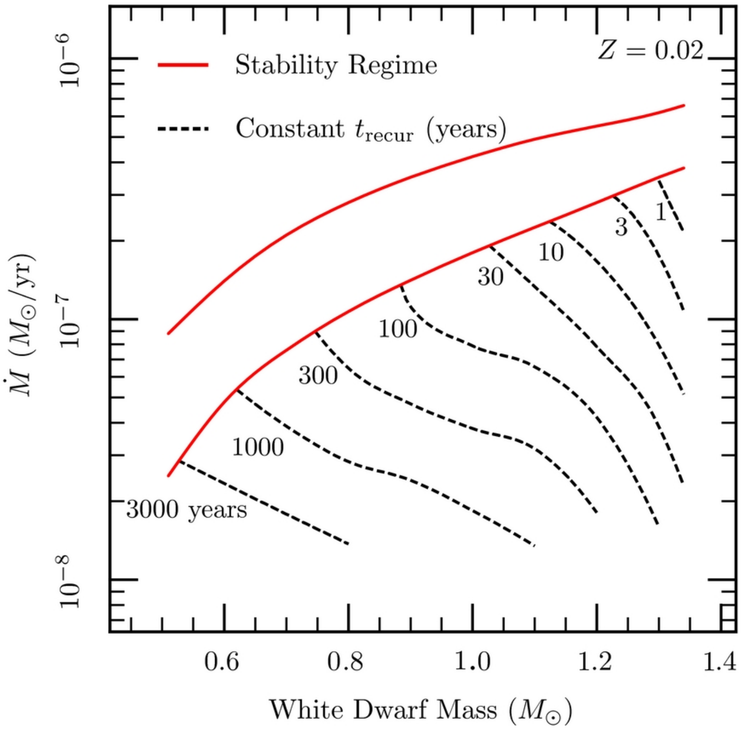

Figure 1.17: Accretion rate versus the mass of the white dwarf. The chemical composition of accreting material is X=0.7, Y=0.28, and Z=0.02. The red lines indicate the narrow region where white dwarfs can support steady hydrogen nuclear burning, which corresponds to the location of the supersoft X-ray sources. Below this band the material builds up on the white dwarf and eventually most of it is ejected in explosive flashes (nova eruptions). The recurrence period of these flashes is shorter for larger masses and higher accretion rates, and vice versa. Above the steady burning band, the matter piles up on the white dwarf forming a red-giant-like structure. Figure taken from Wolf et al. (2013).

Population synthesis models show that a sufficiently high accretion rate can allow efficient mass retention on the white dwarf through quasi-steady or episodic nuclear shell burning. Figure 1.17 shows that, depending on the accretion rate, there are three distinctive groups of nuclear burning white dwarfs (Nomoto et al., 2007):

- Classical and recurrent novae, i.e. systems accreting below the stable nuclear H burning limit ($\dot{M} < \dot{M}_{\rm stable}$), which will undergo sporadic and explosive nuclear burning. The recurrence times for nova eruptions are indicated by the dashed lines in Figure 1.17.
- Steady shell burning on white dwarfs. If the accretion rate falls within a narrow band ($\dot{M}_{\rm stable} \leqslant \dot{M} \leqslant \dot{M}_{\rm cr}$) the material forms a thick, non-degenerate shell on the white

dwarf surface and therefore H burns into He at the rate it is supplied by the donor. The peak of emission of these systems is in the soft X-rays, therefore they are referred to as Supersoft X-rays sources (SSSs).

- In systems where the accretion rate is above the steady nuclear burning limit ($\dot{M} > \dot{M}_{\rm cr}$, dotted line), the large amount of accreted material piles up forming a red-giant-like structure. The photosphere turns optically thick producing winds that remove some of the accreted material.

In this thesis, the emphasis is on the evolution of systems that undergo the steady nuclear burning phase.

Supersoft X-rays Sources as progenitors of Supernova type Ia

The first SSSs were discovered in the Large Magellanic Cloud by Long et al. (1981) with the *EINSTEIN* satellite and the absence of photons detected above ~0.5 KeV with *ROSAT* confirms them as a new class of supersoft source emitters (Trümper et al., 1991; Greiner et al., 1991). However, their binary nature was only revealed with optical observations that established the orbital periods of 1.04 d and 0.44 d for CAL 83 and CAL 87, respectively (Smale et al., 1988; Cowley et al., 1990). van den Heuvel et al. (1992) proposed the so-called close-binary supersoft source (CBSS) model that states that SSSs are the result of steady nuclear burning of H accreted onto massive white dwarfs, supplied by a more massive MS star or subgiant[2]. Indeed, the high effective temperatures (10^5–10^6 K) and luminosities (10^{36}–10^{38}erg s^{-1}) derived from the X-ray data suggest that these sources have effective radii comparable to those of white dwarfs.

The fact that these accreting white dwarf can grow in mass makes the close binary SSSs potential candidates of SNIa progenitors (Whelan & Iben, 1973). Simulations show that on a CO white dwarf the accreted H fuses into He, the He layer grows in mass and will eventually fuse steadily to C and O (Starrfield et al., 2004). Therefore, the increasing mass of the CO white dwarf can eventually reach the Chandrasekhar mass limit and lead to the SNIa explosion. However, the accretion rate decreases drastically once that the ratio of the masses of the two stars come close to unity, and therefore the H burning on the surface stops. If the white dwarf has not exploded by then, the binary system will continue its evolution as a CV towards shorter orbital periods.

---

[2] The existence of stable shell burning white dwarfs, and their appearance as luminous soft X-rays emitters was predicted by Shara et al. (1977) and (Iben, 1982), but those works were not connected to the sources discovered by Long et al. (1981)

Failing the Supernova type Ia explosion

As mentioned above, systems undergoing a thermal time scale mass transfer phase contain a companion star typically more massive than the Sun. Hence, these donor stars have undergone a considerable nuclear evolution before the onset of the mass transfer. Binary population syntheses show that CVs that start mass transfer with a slightly evolved secondary (with the mass fraction of the central H content less than 0.3) will not experience the period gap, or if they do, it will be at periods shorter than ~2 h (Pylyser & Savonije, 1989). Moreover, these CVs with nuclear evolved secondaries can evolve towards ultrashort orbital periods (~7 min) contributing to the population of AM CVn stars (Podsiadlowski et al., 2003).

The high initial masses of the companions in these failed SNIa imply that they were powered by the CNO burning during their lifetime as pre-CVs.

Products from CNO nuclear process

As introduced in Section 1.1.1 the CNO cycle is one of the two main nuclear fusion reactions through which the star converts H into He. When the temperature in the core reaches approximately 15×10^6 K, the CNO burning becomes the dominant energy source, which corresponds to stars with masses larger than $\simeq 1.3\,M_\odot$. CNO burning is a catalytic process which fuses four protons (p), using C, Nitrogen (N), and O isotopes as catalysts, to produce one α particle (He nucleus), two positrons (e^+), and two electron neutrinos (ν_e)

$$^{12}\mathrm{C} + \mathrm{p} \rightarrow {}^{13}\mathrm{N} + \gamma + 1.95\,\mathrm{MeV} \tag{1.17}$$

$$^{13}\mathrm{N} \rightarrow {}^{13}\mathrm{C} + \mathrm{e}^+ + \nu_e + 1.20\,\mathrm{MeV} \tag{1.18}$$

$$^{13}\mathrm{C} + \mathrm{p} \rightarrow {}^{14}\mathrm{N} + \gamma + 7.54\,\mathrm{MeV} \tag{1.19}$$

$$^{14}\mathrm{N} + \mathrm{p} \rightarrow {}^{15}\mathrm{O} + \gamma + 7.35\,\mathrm{MeV} \tag{1.20}$$

$$^{15}\mathrm{O} \rightarrow {}^{15}\mathrm{N} + \mathrm{e}^+ + \nu_e + 1.73\,\mathrm{MeV} \tag{1.21}$$

$$^{15}\mathrm{N} + \mathrm{p} \rightarrow {}^{12}\mathrm{C} + {}^{4}\mathrm{He} + 4.96\,\mathrm{MeV} \tag{1.22}$$

Reactions involving ν_e are weaker interactions and the slowest step is the proton capture on ^{14}N. During the evolution of the star, ^{14}N and ^{4}He become enriched, while ^{12}C and ^{15}O are depleted.

The Roche lobe overflow of the donor results that its outer layers are removed, and if the CV undergoes the thermal time scale mass transfer, the donor is rapidly stripped off a large fraction of its mass. In addition, due to the decreasing mass of the donor during the evolution it will start to experience convective mixing episodes with deeper extents, which will move material from the layers where CNO burning has operated, altering the surface composition which is what can be observed of the star.

In CVs, material from the outer layers of the secondary is accreted onto the white dwarf, and therefore enhancing the N and He abundances in the white dwarf atmosphere. A example is AE Aquarii which is considered to be a descendent of super-soft X-rays sources, since its ultraviolet spectrum shows strong N emission lines, and weak to absent C emission lines (Schenker et al., 2002).

Thesis structure

The structure of this thesis is organised as follows. Most of the data analysed corresponds to ultraviolet spectroscopy taken with *HST*, and therefore both *HST* spectrographs will be described in Chapter 2. The codes used to generate synthetic white dwarf spectra together with the fitting technique that models the ultraviolet spectroscopy is explained in Chapter 3. At the end of both of these chapters I briefly explain the analysis of *HST* data, which led to a number of side projects in which I was involved. In Chapter 4, I describe the work on G29-38, a pulsating white dwarf which shows metal abundances in its atmosphere due to the accretion of a disrupted planetary. In Chapter 5, I explain my work on GW Librae, a CV containing a pulsating white dwarf which the pulsations were damped out due to a dwarf nova outburst. In Chapter 6, I explain my work on two descendants of super-soft X-rays sources and the evolutionary models for N and C abundances that can be seen in CVs that are post super-soft X-rays sources. Finally, in Chapter 7 I summarise the most important conclusion of the three topics presented in this thesis.

Chapter 2

Hubble Space Telescope

The Hubble Space Telescope (*HST*) offers better high-resolution images than ground-based telescopes since it avoids the Earth's turbulent atmosphere, and it opens a window into the ultraviolet that is blocked by absorption in the atmosphere. Since its launch in 1990, *HST* has had a long story of discoveries and achievements: dark matter, protoplanetary discs around young stars, super massive black holes, gamma ray bursts, the collision of the comet Shoemaker-Levy with Jupiter, refined estimates of the Universe's age, and many others. Thanks to the in-orbit maintenance it has been possible to repair failed equipment and to incorporate new technologies in the telescope. Currently, a number of spectrographs and cameras which operate from the ultraviolet to the infrared are mounted. Because white dwarf science is the focus of this project, and as white dwarfs typically emit most of their flux in the ultraviolet, we mainly obtained ultraviolet spectroscopy using the Cosmic Origins Spectrograph (COS). Additional archival spectroscopy obtained with the Space Telescope Imaging Spectrograph (STIS) was used to complement the dataset in this project. Furthermore, these spectrographs offer the time-tag capability that records the incoming photons individually as function of time, therefore providing a powerful tool for the analysis of the variability in the systems studied in this thesis. I am going to describe below the key features of COS (Massa & et al., 2013) and, in less detail, those of STIS (Riley & et al., 2018).

2.1 The Cosmic Origins Spectrograph

COS enhanced significantly the performance of *HST* in the ultraviolet compared to STIS. The main science goals were the study of large scale structure in the Universe, the formation and evolution of galaxies, the origin of stellar and planetary systems, and the cold interstellar medium. Originally, it was designed to be a spectrograph but it also offers imaging

Table 2.1: COS grating specifications.

Channel	grating	wavelength range (Å)	resolving power R=λ / FWHM	dispersion (mÅ pixel^{-1})
FUV	G130M	900–1236	~11 500	9.97
		1065–1365	10 000–15 000	9.97
		1150–1450	16 000–20 000	9.97
	G160M	1405–1775	16 000–21 000	12.23
	G140L	900–2150	1500–4000	80.30
NUV	G185M	1700–2100	16 000–20 000	37
	G225M	2100–2500	20 000–24 000	33
	G285M	2500–3200	20 000–24 000	40
	G230L	1650–3200	2100–3900	390

capabilities with the Near-ultraviolet (NUV) detector.

COS is a slitless spectrograph with two science apertures, both having a field of view of 2.5 arcsec in diameter: the Primary Science Aperture (PSA) and the Bright Object Aperture (BOA) that attenuates brighter objects. COS also has two calibration apertures that are illuminated by internal calibration lamps: the Wavelength Calibration Aperture (WCA) and the Flat-Field Calibration Aperture (FCA). Two detectors are available: the photon-counting micro-channel plate Far-ultraviolet (FUV) Large format Cross Delay Line (XDL) detector that covers from 900 to 2150 Å and the NUV Multi-Anode Micro-channel Array (MAMA) covering from 1650 to 3200 Å. The former has a cesium iodide photocathode on the front micro-channel plate, when photons strike this photocathode, they produce photoelectrons that are amplified by a stack of micro-channel plates (each for segment, see below for details). The charge cloud that comes out of the micro-channel stack, lands on the delay line anode. The latter, has a semi-transparent cesium telluride (Cs_2Te) photocathode on a magnesium fluoride window and the photoelectron generated by this photocathode then falls onto the curved-channel micro-channel plate, which generates a cloud of electrons. Both channels are equipped with medium-resolution and low-resolution gratings (Table 2.1). In addition, the NUV channel has a mirror for imaging purposes. The left panel in Figure 2.1 shows the trajectory of the light inside COS, which depends on the set-up required for the observations. The light passes through one of the COS apertures and finds the Optics Select Mechanism 1 (OSM1), which is a rotating mechanism containing a mirror and the three FUV gratings (G130M, G160M, G140L). If the observations are performed in the NUV, the mirror will be set and the light will be redirected towards the collimating mirror, which will reflect the beam to the NUV detector (by using a second OSM and mirrors). In contrast, if the observations require the FUV channel, one of the three FUV gratings is set and the light

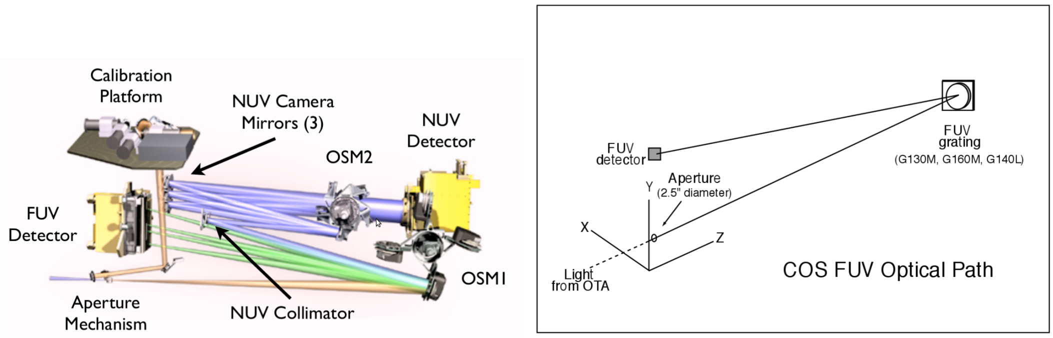

Figure 2.1: *left:* Design of COS. *Right:* trajectory that the light follows before hitting the FUV detector. Figures taken from the COS handbook (Massa & et al., 2013).

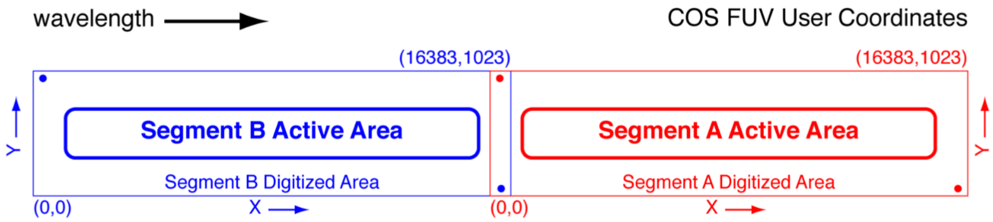

Figure 2.2: Configuration of the FUV XDL detector, consisting of two segments: FUVA and FUVB. This figure has been drawn to scale. Figure taken from the COS handbook (Massa & et al., 2013).

will be directed towards the FUV detector (Figure 2.1, right). The gratings are allowed to move to four different positions (FP-POS=1–4) such that the spectrum is slightly shifted in the dispersion direction to minimize the effects of fixed pattern noise. For the purposes of the science in this thesis, the data was taken with FUV channel, which I will describe in more details.

The FUV XDL consists of two segments (Figure 2.2) with 16 384×1024 pixel for each segment, however the active area is smaller for both segments, 14 200×540 for segment A (FUVA) and 14 150×400 for segment B (FUVB). They are separated by a physical gap of 9 mm making impossible the acquisition of a continuous spectrum across the two segments. Therefore, there is a choice of central wavelength positions to enable full coverage of the gap. When a photon hits any of these XDL pixels, a cascade of electrons is produced at the back side of the detector with a time resolution of 32 ms, which can be characterized by the pulse height amplitude (PHA). Therefore the detector can discriminate real events from electronic noise or cosmic events by the value of the PHA which ranges between 0–31 (higher values are associated with stronger events e.g. cosmic rays). The lower and upper

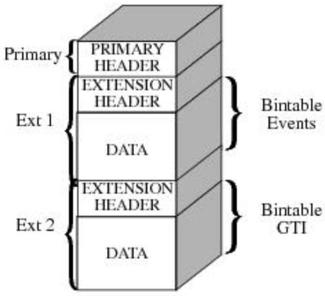

Figure 2.3: FITS file format for time-tag data stored in RAWTAG files.

PHA thresholds associated with real events are defined in `PHATAB` reference file [1]. In TIME-TAG mode, these events are stored in `rawtag_[a,b].fits` files. The suffix `a` or `b` denotes the detector segment, but for general purposes, henceforth I will refer to these files as `rawtag`.

The structure of `rawtag` files is shown in Figure 2.3. `Rawtag` are uncalibrated files that contain the primary header plus two extensions, each extension has its own separate header. The primary header stores keyword information (e.g. name and coordinates of the target, exposure time, detector, grating, central wavelength, etc). Extension 1 is the event list of the time-tag events, which contains the position (`RAWX`, `RAWY`) of each detected photon, its arrival time (`TIME`), and its `PHA`. Extension 2 contains the Good Time Intervals (GTI) table which stored the start and end times of an uninterrupted exposure, in case one visit requires more then one exposures (Table 2.2).

The observation of a target by *HST* is called "visit", and the set-up can change during the visit e.g. COS/FUV $\longrightarrow$ COS/NUV. However, as mentioned above the COS/FUV configuration was used for obtaining the data analysed in this thesis, therefore I will focus on this configuration. The visit consists of one or more orbits that are not necessarily taken subsequently. The visit is split into several exposures, the first three of which have very short exposures (~5 s) to perform a search of the target (ACQ/SEARCH), to determine the centroid of the spectrum in the cross dispersion direction (ACQ/PEAKXD) and to center the target (ACQ/PEAKD) in the aperture. The subsequent exposures need to be planned carefully considering the occultation of *HST* by the Earth. If the target has declination ± 61.5, it lies in the *continuous viewing zone* (star 2 in Figure 2.4), and could eventually be observed continuously, however if the target is occulted by the Earth the exposure time

---

[1] The reference files are the files that store the parameters and information used during the reduction and calibration of the COS data. They can be retrieved from the STScI archive or downloaded from ftp://ftp.stsci.edu/cdbs/lref/

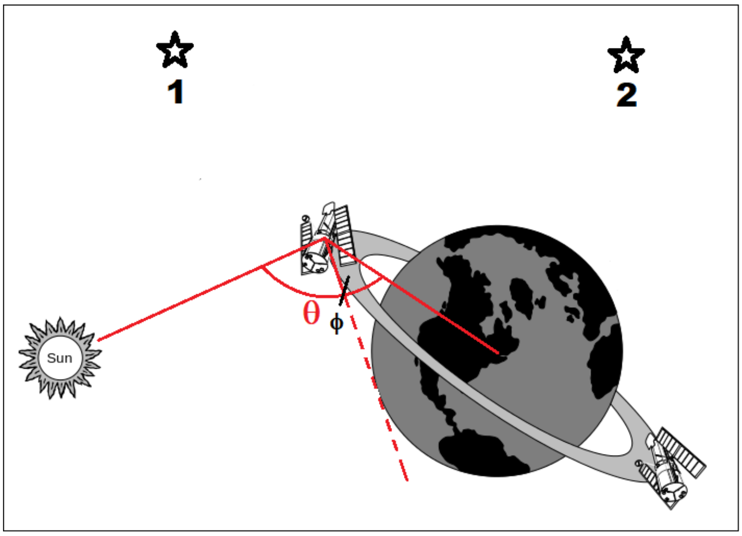

Figure 2.4: Illustration of *HST*'s orbital position. Star 1 is occulted for a significant amount of *HST*'s orbital period when the spacecraft passes behind the Earth. Star 2 is in the continuous viewing zone, and can be observed without interruptions.

Table 2.2: Details of the extensions in the `rawtag` files.

Column name	Description
Extension 1: EVENTS	
TIME (sec)	Elapsed time in seconds since the exposure start time
RAWX (pixel)	Pixel coordinate along the dispersion axis
RAWY (pixel)	Pixel coordinate along the cross-dispersion axis
PHA (pixel)	Pulse height amplitude (0–31)
Extension 2: GTI	
START (sec)	Start of good time interval since exposure time start
END (sec)	End of good time interval

reduces to less than *HST*'s orbital period (96.6 mins), e.g. targets lying in the orbital plane of *HST* are occulted for about 44 mins (star 1 in Figure 2.4). The time-tag data of each exposure is stored in one `rawtag` file, therefore according the specifications of the observations requested by the astronomer, a visit can result in one or more `rawtag` files, which preferably are taken at different FP-POS settings.

As mentioned above, COS was chosen because of the need of ultraviolet spectroscopy for this project, and because of its time-tag capability. However before starting the analysis, the time-tagged data need to be corrected, reduced and calibrated.

These files are processed by the COS calibration pipeline, called CALCOS, which is written in python and performs the reduction and calibration (Massa & et al., 2013). During this process CALCOS reads necessary information from the calibration reference files (e.g. flat fields, bad pixel tables, etc) generating several intermediate files. The output files are indicated with a solid arrow under the "Output" column in Figure 2.5. As can be seen in the flowchart, the pipeline performs several corrections, before the calibrations, and I will briefly explain the general procedure of the pipeline.

Basically the pipeline performs three main steps:

- Correction of instrumental effects: here the data stored in extension 1 in the `rawtag` file is corrected for noise, bad time intervals, thermal drifts, pixel-to-pixel variations in sensitivity, geometric distortion produced by different sizes of the pixels, Doppler shifts related to the orbit of *HST*, and pulse height filtering. The resulting corrections of `TIME` and positions (`XFULL`, `YFULL`) of the data are stored in a new file called `corrtag_[a,b].fits` (henceforth `corrtag`). The structure of the `corrtag` files is similar to `rawtag` files, they are composed of the primary header plus 3 extensions. Details of the contents of each extension are listed in Table 2.3.
- In the second step the wavelength calibration is performed, which uses onboard spectral line lamps. The wavelength is an entry in the extension 1 in the `corrtag` file.
- In the final step, the spectrum is extracted from every `corrtag` file. The background is subtracted and the response function is applied to create the (one-dimensional) flux-calibrated spectrum, which is stored in the `x1d` file (one per exposure). `x1d` files are averaged to create the final flux-calibrated (summed) spectrum for the entire observation (`x1dsum`).

The time-tag capability allows to build light curves (explained in more details in Section 2.3.1) to study systems that are variable on short time scales such as pulsating white dwarfs and cataclysmic variables, which are the scientific focus of this thesis. COS is very well complemented with STIS and for the work in this thesis I retrieved archival STIS observations of some systems of interest. Hence, I will also briefly explain some key characteristics of STIS.

2.2 Space Telescope Imaging Spectrograph

STIS provides solar blind imaging in the FUV, coronagraphic imaging in the optical and near IR, spatially resolved spectroscopy from 1150 to 10 300 Å at low to medium spectral resolution (R$\sim$500–17 000) and medium to high spectral resolution (R$\sim$30 000–110 000)

Table 2.3: COS `corrtag` details.

Column Name (Units)	Description
Extension 1: EVENTS	
TIME (sec)	Elapsed time since the start of the exposure time
RAWX (pixel)	Pixel coordinate along the dispersion axis
RAWY (pixel)	Pixel coordinate along the cross-dispersion axis
XCORR (pixel)	RAWX corrected from distortion
XDOPP (pixel)	XCORR corrected for Doppler shift due to *HST* orbital motion
YCORR (pixel)	RAWY corrected from distortion
XFULL (pixel)	XDOPP corrected for offset in the dispersion direction, based on the wavecal spectrum
YFULL (pixel)	YCORR corrected for offset in the cross-dispersion direction, based on the wavecal spectrum
WAVELENGTH (Å)	Only events in the active area are assigned wavelengths
EPSILON	Event weight based on flat field and deadtime
DQ	Data quality flag
PHA	Pulse height amplitude
Extension 2: GTI	
START (sec)	Start good time interval since exposure start
STOP (sec)	End good time interval
Extension 3: TIMELINE	
TIME (sec)	Time in 1 sec intervals from first entry
LONGITUDE (degrees)	Earth based longitude
LATITUDE (degrees)	Earth based latitude
SUN_ALT (degrees)	Altitude of the Sun above the geometric horizon
SUN_ZD (degrees)	Angle between *HST* and the Sun, seen from the center of Earth
TARGET_ALT (degrees)	Altitude of the target above the geometric horizon
RADIAL_VEL (km/s)	Instantaneous *HST* radial velocity toward the target
SHIFT1 (pixels)	Instantaneous dispersion direction shift
LY_ALPHA (counts/s)	Total count/sec in a box across the aperture at Ly α
OI_1304 (counts/s)	Total count/sec in a box across the aperture at O I 1304
OI_1356 (counts/s)	Total count/sec in a box across the aperture at O I 1356
DARKRATE (counts/s)	Counts/sec/pixel averaged over both dark regions

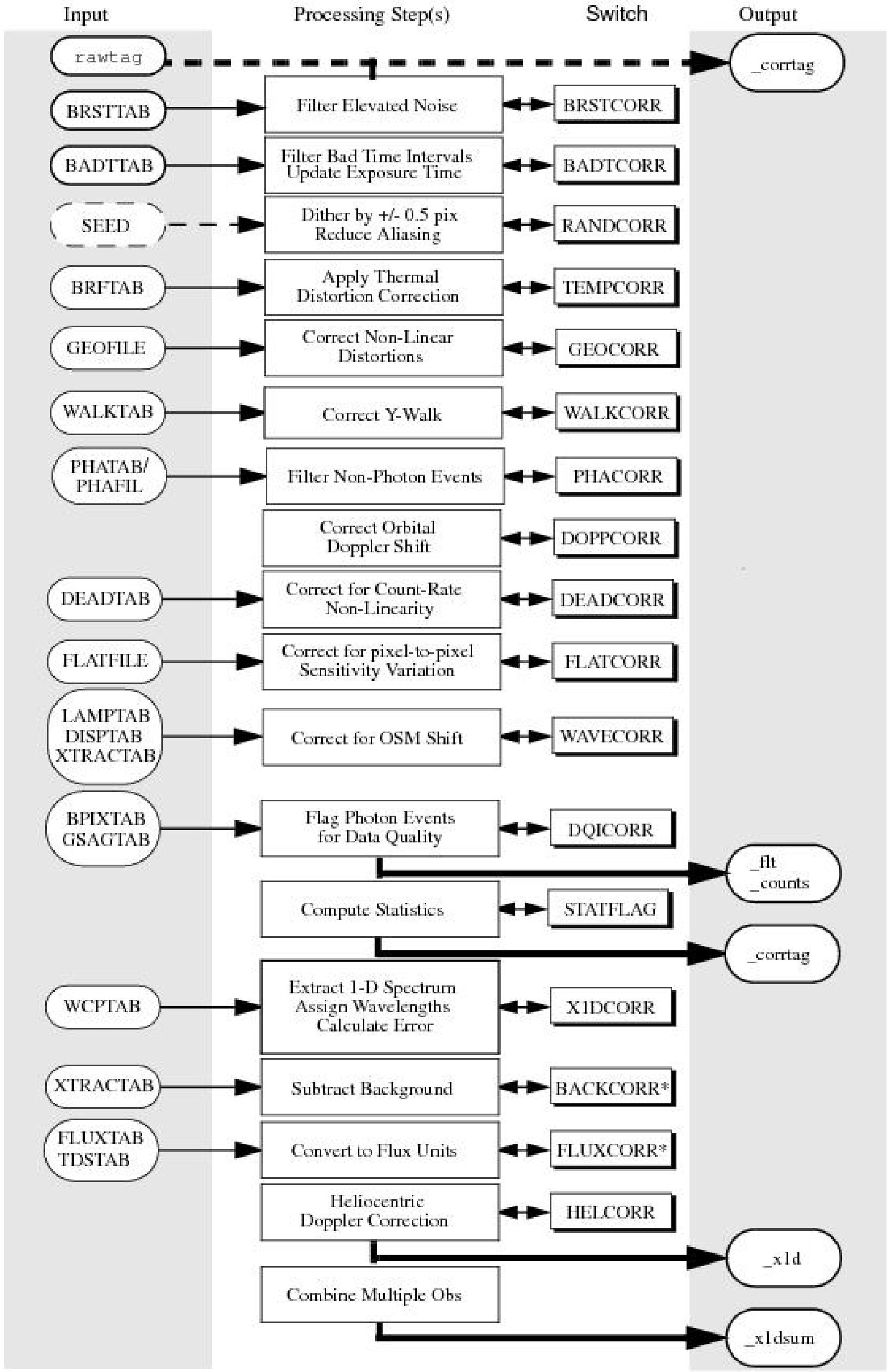

Figure 2.5: Flow chart of the processing steps of the CALCOS pipeline. BACKCORR and FLUXCORR tasks will be performed only if the extraction of the spectrum has been requested.

echelle spectroscopy in the ultraviolet (1150–3100 Å), and similarly to COS also provides time-tagging of photons in the ultraviolet for high time resolution studies. As mentioned above, this mode is very powerful for the science in this project.

The light is directed by a series of mirrors to the grating wheel which contains: a prism, and the first order and echelle gratings that are used for the all detectors. STIS has three detectors: an optical CCD, and two photon counting MAMA detectors: a FUV-MAMA and a NUV-MAMA. The data in this thesis were taken with FUV-MAMA using the G140L grating in time-tag mode. Therefore I will focus on the specifications of this set-up only.

The STIS/FUV-MAMA is a 1024×1024 pixel format detector and provides coverage from 1150 to 1700 Å. The data can be taken either in an accumulate (ACCUM) mode in which a time-integrated image is produced or in a time series (TIME-TAG) mode in which the location of the photons on the detector and time of arrival are recorded as an event stream. The FUV-MAMA can be set up together with four gratings, among them G140L, which was used for the observations analysed here. The G140L grating has a resolving power R≃1000, and covers a wavelength range from 1150 to 1700 Å. It has only one central wavelength configuration at 1425 Å.

In TIME-TAG mode, the MAMA produces an event stream of data points (`AXIS1`, `AXIS2`, and `TIME`) with a time resolution of 125 ms. The Doppler correction is applied during the post-processing of the data. The data is stored in `tag.fits` (henceforth `tag`) files that consist of a primary header plus extensions with their own header as shown in Figure 2.3. Details of the contents of the extensions are given in Table 2.4. The STIS data is reduced and calibrated with the CALSTIS pipeline to extract the one dimensional flux calibrated spectrum that is stored in `x1d` files.

The capability of time series spectroscopy allows flexible manipulation of the data with respect to time, e.g. unwanted data points in the spectroscopy can be discarded. In Section 2.3, I will present some applications of time-tag spectroscopy that have been important for this thesis and several side projects.

2.3 Time-tagged data manipulation

COS and STIS time-tag data can be manipulated in different ways according to the goals of the science. I will explain a handful of examples to illustrate the procedures I developed that

Table 2.4: Columns in the STIS time-tag data table.

Column name	Description
Extension 1: EVENTS	
TIME	Elapsed time in seconds since the exposure start
AXIS1	Pixel coordinate along the spectral axis with Doppler correction
AXIS2	Pixel coordinate along the spatial axis, no Doppler correction
DETAXIS1	Pixel coordinate along the spectral axis prior to Doppler correction
Extension 2: GTI	
START	Start good time interval
END	End good time interval

will be used throughout this thesis. Then I will make use of the time-tag data of the eclipsing pre-CV (see Section 1.2.2) binary QS Vir to illustrate the different usage of *HST*/COS data.

QS Vir (EC 13471–1258) is a detached binary composed of a white dwarf and a M-type main sequence star (O'Donoghue et al., 2003; Ribeiro et al., 2010). QS Vir has captured the attention since Doppler maps and X-rays observations showed signs of material that accretes onto the white dwarf at rates higher than expected for detached systems (Parsons et al., 2011; Matranga et al., 2012). Furthermore, the eclipses showed substantial timing variations (Parsons et al., 2010b), which was interpreted as the gravitational influence of circumbinary planets (Almeida & Jablonski, 2011). However, their configuration turns rapidly unstable (Horner et al., 2013) and hence the origin of these time variations remains unexplained. Additionally, the spectroscopy revealed large structures passing in front of both stars, which originate from the low-mass star (Parsons et al., 2016).

The white dwarf in QS Vir was observed for four *HST* orbits with COS in January 2015, using the G130M grating centred at 1291 Å. Four exposures were taken in each orbit, each exposure used a different FP-POS setting. There is a total of 2.35 h of ultraviolet time-tagged data stored in 16 `corrtag` files. The log of the observations is given in Table 2.3

2.3.1 Ultraviolet light curves

Light curves can be obtained from the COS `corrtag` and STIS `tag` files. Here I will explain in detail the procedure I developed to construct the light curves.

The FITS header has entries that specify the positions of the spectrum and the background regions along the spatial direction (`yfull`) together with the height of the box that

Table 2.5: Log of the COS observations of QS Vir.

filename	Date	UT (hh:mm:ss)	exp. time (s)	orbit
lcm001pdq	2015-01-04	16:08:33	530	1
lcm001pfq	2015-01-04	17:03:31	530	1
lcm001phq	2015-01-04	17:14:25	530	1
lcm001pjq	2015-01-04	17:25:19	529	1
lcm002urq	2015-01-18	09:43:09	522	2
lcm002v4q	2015-01-18	10:38:54	521	2
lcm002v6q	2015-01-18	10:49:30	521	2
lcm002v8q	2015-01-18	11:00:06	521	2
lcm003jwq	2015-01-11	12:09:00	530	3
lcm003jyq	2015-01-11	13:03:44	530	3
lcm003k0q	2015-01-11	13:14:38	530	3
lcm003k2q	2015-01-11	13:25:32	529	3
lcm004avq	2015-07-10	02:18:35	530	4
lcm004axq	2015-07-10	02:29:29	530	4
lcm004brq	2015-07-10	03:43:33	530	4
lcm004btq	2015-07-10	03:54:27	529	4

defines the regions of the extraction. Figure 2.6 shows the example of the extraction from the third exposure of 530 s taken during the first orbit (lcm001phq) of the COS observations of the post-common envelope binary QS Vir. The G130M/1291 Å set-up of the observations covers both segments. The spectrum (blue) is located at `yfull=526` and `yfull=586` in segments A and B, respectively and has a height of $H_\mathrm{S} = 35$ pixels. The two background regions (red) are taken above the spectrum (`yfull=561` and `yfull=621` for segments A and B, respectively) and below the spectrum (`yfull=491` and `yfull=551` for segments A and B, respectively) and the height of the two background boxes is the same as that of the spectrum, i.e. $H_\mathrm{B} = 35$ pixels. The total background region is scaled to the height of the region used to extract target photons, i.e. $H_\mathrm{S}/(2\times H_\mathrm{B})$.

Observations performed in the ultraviolet by spacecrafts in low Earth orbits have the problem that airglow emission contaminates the spectroscopy. These airglow emission lines are stronger during the daylight side, and hence depend strongly on the spacecraft orbital position. The dominant airglow corresponds to Lyman α at 1216 Å, and it is generally always present in the observations. The next strongest line is O i at 1302 Å. N i at 1200 Å, and O i at 1356 Å and 2471 Å may also appear while the spacecraft is on the daylight side. As a consequence, during the extraction of the light curve, the airglow emission lines are masked out as illustrated in Figure 2.6. However, this airglow contamination can be reduced by filtering the data using just the night side observations (Section 2.3.4).

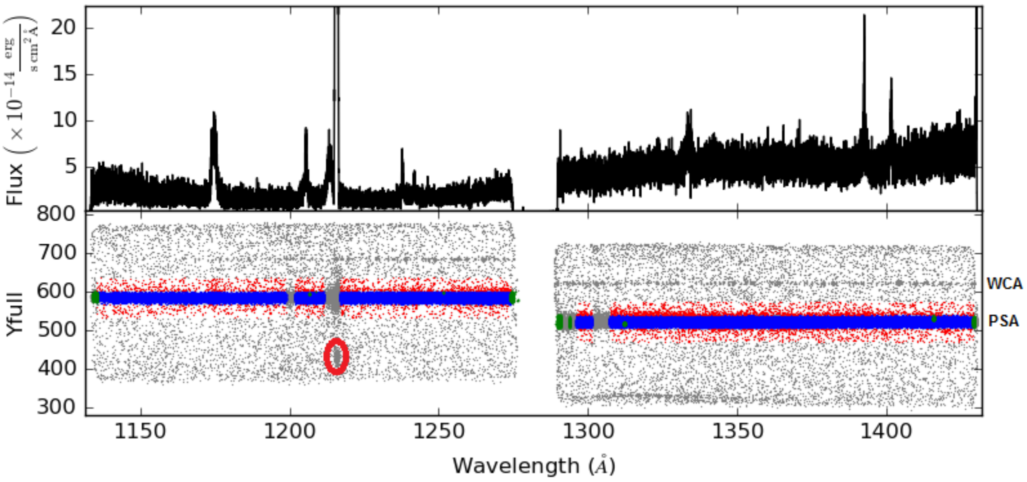

Figure 2.6: Extraction of the background (red) subtracted spectrum (blue) to build the light curve (Figure 2.7) for QS Vir, observed with COS/G130M centred at 1291 Å on 2015-01-04, with an exposure time of 530 s. This COS set-up collects data using both detector segments. Green data points have been flagged as bad quality data which are discarded. The red circle encloses the Lyman α airglow in the Bright Object Aperture (BOA). The Wavelength Calibration Aperture (WCA) and Primary Science Aperture (PSA) positions in segment A are indicated. The gaps in the extraction correspond to airglow emission lines (from left to right) of N I, Lyman α, and O I at 1200 Å, 1216 Å, and 1302 Å, respectively. These features originate in the Earth exosphere, and are therefore masked out. The top panel shows the extracted spectrum.

I corrected the spectrum and the background data from flat-field and dead time effects. The `epsilon` array carries the model of the photon counting efficiency of the detector (dead time) as well as the flat-field value at the location of the event. This array is contained in extension 1 of the `corrtag` file. The corrected object and background counts are weighted by the inverse of a time-and-wavelength-dependent factor. This factor corresponds to the sensitivity function multiplied by time-dependent-sensitivity correction function. The sensitivity curve is read from the `FLUXTAB` reference file and converts the binned data into flux units. The time-dependent-sensitivity function corrects from temporal changes in the instrumental sensitivity, and it is read from the `TDSTAB` reference file. I proceed to subtract the object counts (blue) by the scaled background counts (red) at each wavelength. Finally, I construct the light curve by binning in time and counting the number of counts in each bin. The light curve of QS Vir extracted from the COS exposure in Figure 2.6 is shown in Figure 2.7.

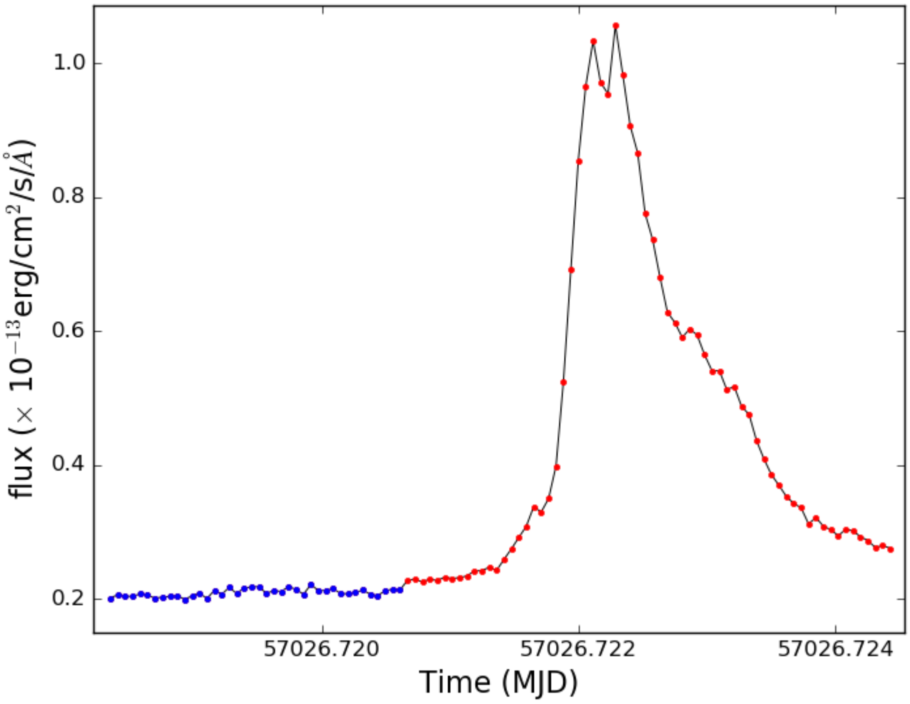

Figure 2.7: Light curve extracted from the third exposure (LCM001PHQ) obtained during the first orbit of the COS observations of QS Vir (Table 2.3) shown in Figure 2.6 using a bin width of 5 seconds. The increase of the flux is due to a flare of the M-star. Blue and Red points indicate the time intervals that were used to extract two spectra, before and during the flare.

2.3.2 Spectra from selected time intervals: Peaks & troughs

The light curve of QS Vir shows an increase of flux during the second half of the exposure (Figure 2.7). This brightening is due to activity of the M-dwarf, producing substantial flares (Ribeiro et al., 2010). In principle, the shape of the spectrum should be different during this brightening[2]. Therefore, to investigate the changes in the spectral appearance due to variability of any kind, it is very useful to extract spectra corresponding to specific regions of the light curve. Henceforth, I will explain the procedure to construct a spectrum using selected chunks from time-tag data, using, QS Vir as example. I extracted two spectra using the light curve to define a flux level of $\sim 2.3 \times 10^{-13}$erg/cm^2/s/Å and to extract one spectrum above this threshold (red dots in Figure 2.7) and one below (blue dots in Figure 2.7). I created new `corrtag` files, where I cloned extensions 1 and 3 from their original

---

[2] It is worth mentioning that the systems that will be analysed in this thesis show changes in their ultraviolet flux as well, however the source of these variations is due to pulsations driven in the white dwarf envelope.

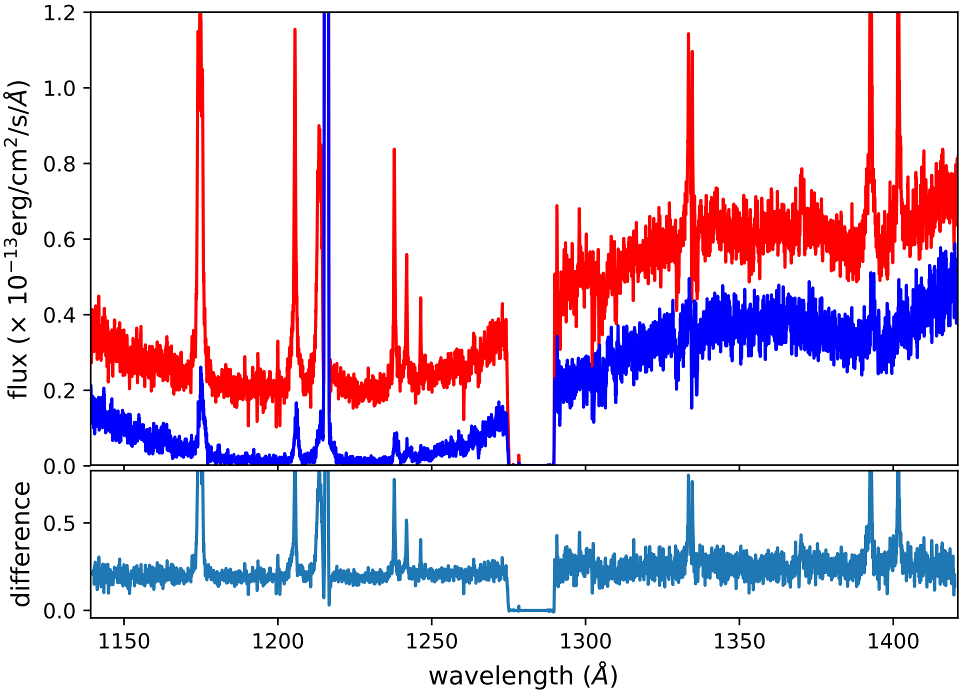

Figure 2.8: Extraction of two spectra of QS Vir. The red and blue spectra are build from the time intervals indicated by red and blue dots in Figure 2.7, respectively. No offset has been applied. The red spectrum was obtained during the M-star flare. The bottom panel shows the difference between these two spectra.

`corrtag` files. The extension 2 contains the interval of time(s) from which the spectra will be built. In this example I built the (red) peak spectrum of QS Vir from the interval 195–525,s, while the (blue) quiescent spectrum was assembled from the interval 0–195 s. The next step is to perform the extraction of these new `corrtag` files using the `X1DCORR` task from the CALCOS pipeline. This task corrects the Doppler motions of *HST* in the heliocentric reference frame and also performs the flux calibration, writing the spectrum into the `x1d` files. Finally, these `x1d` files are averaged using the `fpavg` function from the CALCOS processing pipeline. The two spectra are shown in Figure 2.8. While there is an increase in the total flux, the overall shape remains broadly the same, indicating that the flare spectrum is approximately flat in F_λ, superimposed by emission lines of C, N, O, and Silicon (Si).

2.3.3 Radial velocity corrections for the eclipsing binary QS Vir

In long observations of white dwarfs in binary systems, the spectral lines are broadened by the orbital motion. However, the lines can be corrected for this broadening if the orbital parameters are known. QS Vir data will be used again to demonstrate this step. As mentioned before, the M-dwarf presents flares, one of which was observed during the first *HST* orbit. Consequently, to perform the radial velocity correction, the data from the first orbit will be excluded from the spectroscopy, leaving 1.76 h of ultraviolet time-tagged data in 12 spectra stored in `x1d` files.

The wavelength of each of these spectra can be corrected for the orbital motion of the white dwarf. Using Gaussian fits to the C ii absorption line at 1335 Å, I determined an orbital period of $P_{\text{orb}} = 0.15075(6)$ days, a systemic velocity of $\gamma_{\text{sys}} = 39 \pm 11\,\text{km}\,\text{s}^{-1}$, and white dwarf radial velocity amplitude of $K_{\text{WD}} = 147 \pm 16\,\text{km}\,\text{s}^{-1}$, which agree with previous estimates (Parsons et al., 2016). Using the orbital parameters and the orbital position of the spacecraft stored in extension 3 in the `corrtag` files, I was able to correct the wavelengths of the 12 `x1d` files, which I re-reduced and re-calibrated to built the average spectrum in the rest frame of the white dwarf. Figure 2.9 shows the C ii absorption lines in the resulting wavelength-corrected spectrum (blue), in contrast, the uncorrected spectrum retrieved from the STScI archive (red) has the C ii spectral lines fully smeared out. The grey band shows interstellar absorption line of C ii at 1334.5 Å, which as it does not originate on the white dwarf has a constant wavelength in all exposures. Therefore, the correction of radial velocity to the white dwarf rest frame wavelength will cause the interstellar line to move around, adding some broadening of nearby spectral lines. Therefore the interstellar lines were masked out.

2.3.4 Reducing the effects of airglow

As mentioned above, the spectroscopic observations are contaminated by airglow emission originating in the Earth's exosphere due to different processes: recombination of photoionised atoms, chemical reactions between oxygen or nitrogen with hydroxyl (OH) ions, and luminescence caused by cosmic rays striking the upper atmosphere. The common strategy to reduce these effects is masking them out. Considering the fact that the intensity of the airglow decreases on the night side, then time-tag data can be filtered setting a condition regarding the position of *HST*, i.e excluding all data taken when *HST* is above the horizon. The parameter to track the position of *HST* with respect to the Sun is `sun_alt`, which is the subtraction between two angles, the angle from the *HST* that connects the centres of mass of the Sun and the Earth (θ in Figure 2.4, $\theta = 0$ the Sun is right behind the Earth from *HST*'s point of view), and the angle between the direction of the centre of the Earth from *HST* and the tangent to the limb of the Earth (ϕ in Figure 2.4). This parameter is stored in Extension 3 in the `corrtag` files.

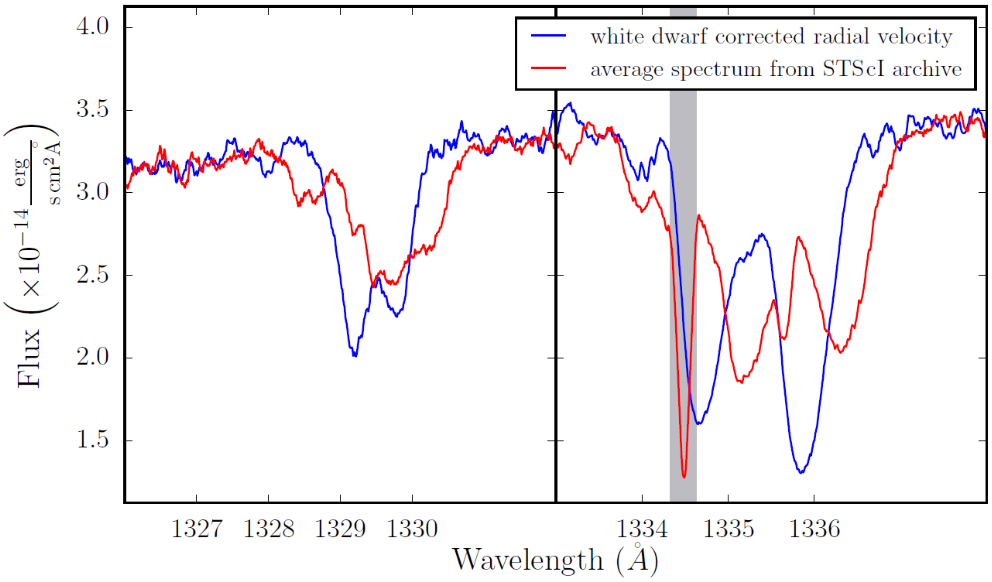

Figure 2.9: Photospheric C II absorption line corrected (blue) and uncorrected (red) for the radial velocity of the white dwarf. The grey band indicates the location of interstellar C II absoption, which has been masked.

Using the TIMEFILTER module from the STSCI_PYTHON library will create a new `corrtag` file containing the filtered data (e.g. `sun_alt` > 0). Finally, the `X1DCORR` and `fpavg` tasks are used to extract the flux-calibrated spectra and average them, respectively. In the example of QS Vir, the average of the 16 spectra taken during the four orbits shows strong emission of O I at 1302 Å (black in Figure 2.10). Excluding all dayside data of the observations (red), a sharp absorption feature at 1302 Å, can be identified, which corresponds to an interstellar line of O I. Additional features can also be identified as photospheric O I at 1304 Å and Si II at 1311 Å, substantially broadened by the orbital motion of the white dwarf.

2.4 Side Projects: Analysis of light curves

Here I will briefly explain my contribution in side projects that led to publications.

2.4.1 Spectroscopy from *HST*/COS of the southern nova-like BB Doradus in an intermediate state, Godon et al. 2016, APJ, 833, 146)

As introduced in Section 1.2.4, nova-likes are non-magnetic or weakly magnetic CVs characterised by their high mass accretion rate, as a consequence the ultraviolet and the optical flux are dominated by the disc. There is a subclass of nova-likes known as VY Scl stars, which occasionally drop into a low-brightness state, and the hot white dwarf becomes vis-

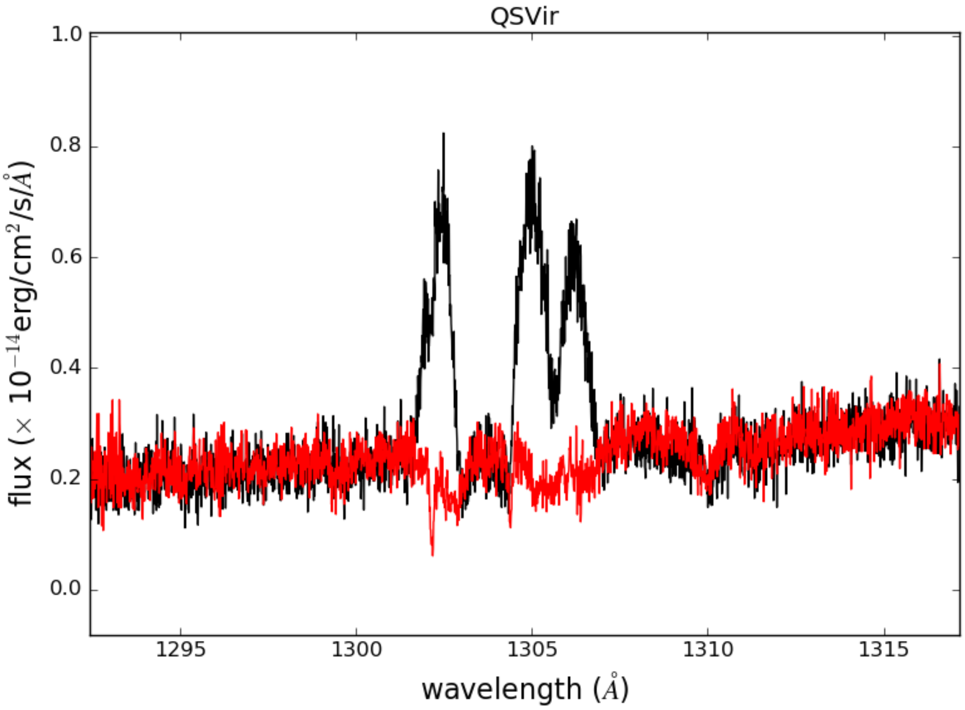

Figure 2.10: The average spectrum of the COS observations of QS Vir obtained over four *HST* orbits (black) shows clear emission lines from O I airglow at 1302 Å. Averaging only the data taken on the nightside (red), reduces significantly the emission.

ible. In these systems the effects of heating the white dwarf as a consequence of accretion can be studied. BB Doradus belongs to this subclass, and has been observed occasionally in low states (Rodríguez-Gil et al., 2012; Schmidtobreick et al., 2012). BB Doradus was observed with *HST*/COS on February 2013. At the time of the */HST* observations, BB Dor was already on the rise from a low state, and the accretion activity was at an intermediate level. The COS data consist of a total of 7272 s of good exposure in time-tag mode. The average spectrum is shown in Figure 2.11. Fitting this spectrum using two-component model, we aim to determine the accretion rate and the effective temperature of the white dwarf in BB Doradus. The two components account for the white dwarf, modelled with synthetic spectra generated using TLUSTY, SYNSPEC, and ROTIN, and the accretion disc, modelled as a combination of several annuli generated with TLUSTY, SYNSPEC, and DISKSYN (Hubeny & Lanz, 1995).

My contribution to this project was to estimate the contribution of the white dwarf to the total flux. I used the time-tag data to generate three light curves. A first light curve

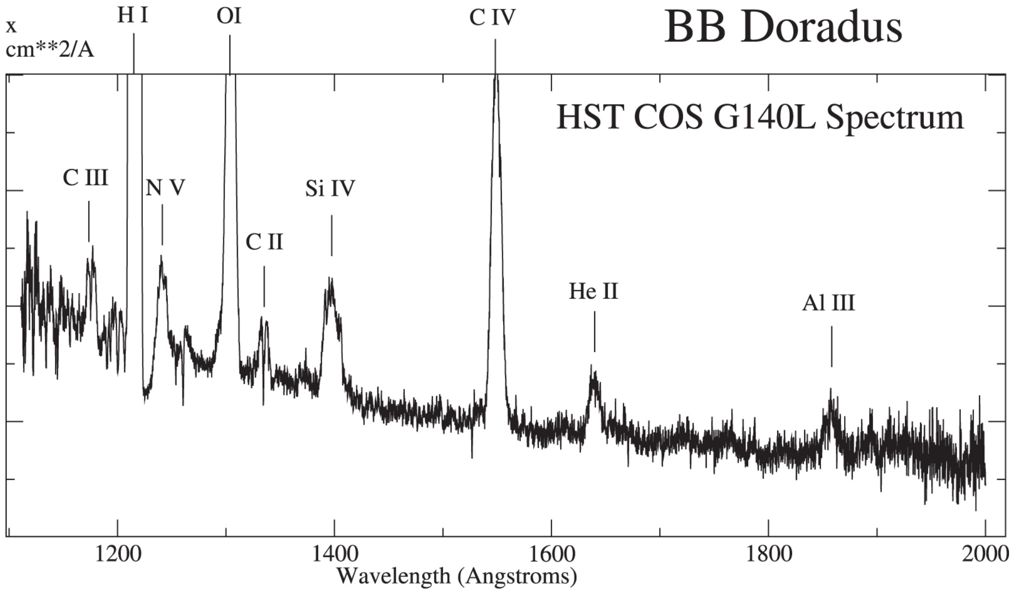

Figure 2.11: *HST*/COS average spectrum of BB Doradus. The spectrum shows some broad and strong emission lines of high ionisation species such as C iii at 1175 Å, N v at 1240 Å, Si iv at 1400 Å, and C iv at 1550 Å. Also shows lower ionisation species such as C ii at 1335 Å and He ii at 1640 Å. The Lyman α at 1216 Å and O i at 1302 Å are geocoronal airglow emission lines. Figure taken from Godon et al. (2016).

is generated by integrating all the data over the wavelength range 1100–1950 Å excluding the airglow emission lines of Lyman α, O i, and N i; a second light curve was made with the C iv line (1535–1564 Å); and a third light curve was made using the continuum in the range 1424–1523 Å. The three light curves are shown in Figure 2.12, each was normalized to one. The continuum varies in the same way as the C iv emission, which does not come from the white dwarf. Therefore, if the continuum is the sum of the disc and white dwarf, the fact that the variability (20% of the total flux) is produced by the disc indicates that the white dwarf cannot contribute more than 80% of the flux.

We concluded that BB Doradus, during the COS observations, is likely to have a mass accretion rate $\dot{M} \sim 10^{-10}\,M_{\odot}\,\mathrm{yr}^{-1}$ and the white dwarf has an effective temperature of ~35 000 K to ~50 000 K.

2.4.2 The composition of a disrupted extrasolar planetesimal at SDSS J0845+2257, Wilson et al. 2015, MNRAS, 451, 3237

As mentioned in Section 1.1.2, the origin of the metals seen in cool white dwarfs are planetary bodies that are tidally disrupted and accreted onto the white dwarf. Consequently,

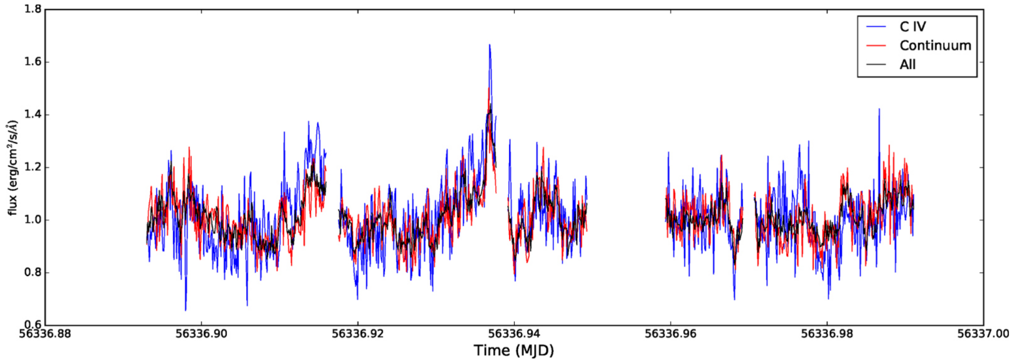

Figure 2.12: Light curves of BB Dor are shown for (i) the entire spectral range of COS (in black), (ii) the carbon C IV line only in the region 1535–1564 Å(blue), and (iii) the continuum in the range 1424–1523 Å(red). The five segments correspond to the five COS exposures. The flux has been normalized to one. Figure taken from Godon et al. (2016).

these systems provide a unique opportunity to study the bulk chemical composition of extrasolar planetary systems. In this work we presented ultraviolet and time series optical spectra of the metal-polluted DB white dwarf SDSS J084539.17+225728.0 (hereafter SDSS J0845+2257). Eight orbits of time-tag data were obtained for SDSS J0845+2257 with *HST* on 2010 March 31 and 2010 April 01. The total exposure time corresponds to 2735, 4994 and 14397 s with the G130M, G160M and G230L gratings, respectively. The spectrum is shown in Figure 2.13.

My contribution was to probe for any short term variability in the light curve due to ongoing accretion. I used the time-tag COS photon event files to construct a light curve, following the same procedure explained in Section 2.3.1. The N I at 1200 Å, Lyman α at 1216 Å, and O I at 1302 Å airglow emission lines were masked and the edges of the detector segments excluded to reduce the instrumental noise. Figure 2.14 shows a background-subtracted, normalized light curve binned to 5 s.

To test the variability in the flux from SDSS J0845+2257 I used a χ^2 test, on a light curve using a bin size of 32 ms, i.e. the intrinsic time resolution of COS in time-tag mode. The box for the extraction of the spectrum was defined so that all counts of the target were included, while minimising the amount of background contribution. We set our null hypothesis that each light curve chunk is constant at the mean rate. We find that a constant light curve has a probability of 8–90 per cent of having the observed distribution, meaning that we cannot reject the hypothesis that the light curve is constant. The large range in probability is caused by the different total exposure times of the individual light curve chunks. To confirm this result and investigate any contribution to the variability from the

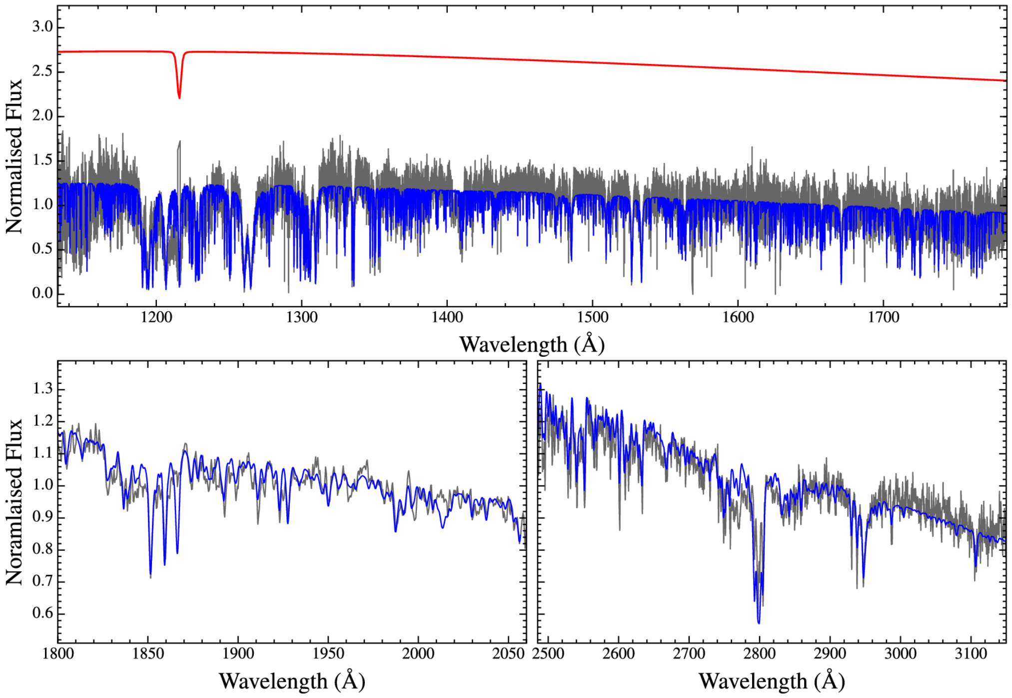

Figure 2.13: *HST*/COS FUV (top) and NUV (bottom) spectrum of SDSS J0845+2257 , the best model fit that includes photospheric metals is overplotted in blue. Plotted in red is a model spectrum for a white dwarf with the same T_{eff}=19780 K and log g=8,18 dex, but with no metals. The comparison of these two model shows the large amount of metals polluting the white dwarf atmosphere: carbon, oxygen, silicon, calcium, aluminum, magnesium, titanium, chromium, nickel, iron, and manganese. Figure taken from Wilson et al. (2015).

background we repeated the process, this time with a wider box for extracting the spectrum to incorporate more background counts, as well as an identical test across the whole light curve. The difference in the results is not significant, so we conclude that the *HST*/COS data do not show significant variability on time-scales of 32 ms to ≃30 min.

We conclude that the star is accreting at a rate of $1.6{\times}10^{10}\,\mathrm{g\,s^{-1}}$ and the mass of metals in the convection zone implies a parent body larger than 100 km in diameter. Measurements of 10 metals have shown that the disrupted planetesimal was similar to the Earth in composition.

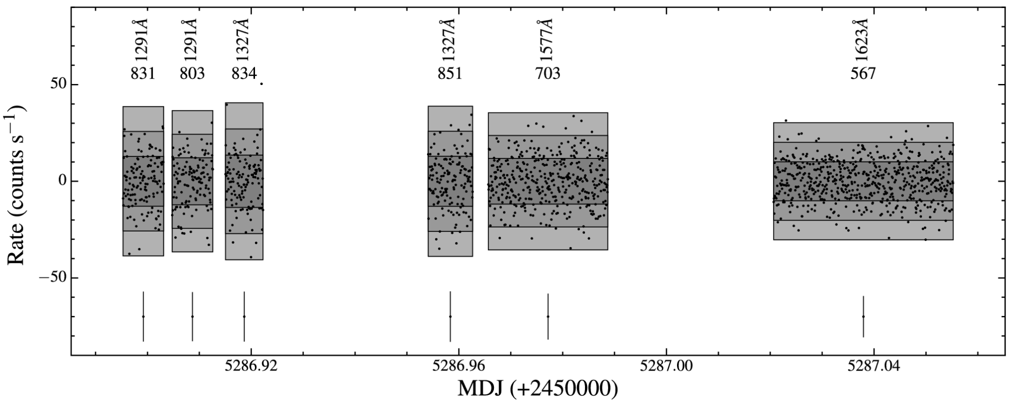

Figure 2.14: Light curve of SDSS J0845+2257. Dark grey, grey and light grey areas represent 1σ, 2σ and 3σ standard deviations, respectively, assuming a normal distribution for the count rate in each observation. The vertical and horizontal numbers above each spectrum are the central wavelength and mean count rate, respectively. An error bar illustrating the typical photon noise is shown underneath of each spectrum. Figure taken from Wilson et al. (2015).

Chapter 3

Fitting HST spectroscopy of white dwarfs

The spectral energy distribution of white dwarfs peaks at ultraviolet wavelengths. Indeed in low-accretion rate CVs, the white dwarf contributes 70–90% of the ultraviolet light (Szkody et al., 2010a). Using white dwarf atmospheric modelling that reproduces the ultraviolet observations can provide measurements of the white dwarf atmospheric parameters: $T_{\rm eff}$, $\log g$, and abundances.

3.1 White dwarf model atmospheres

There are many codes available that model stellar atmospheres, however only a few are set up to deal with the extreme conditions encountered in white dwarfs, i.e. extreme densities, and a very large range of effective temperatures. In this thesis TLUSTY/SYNSPEC (Hubeny & Lanz, 1995) and ATM/SYN (Koester, 2010) were used to calculate white dwarf models. These codes have the common following assumptions:

- homogeneous, plane parallel layers: the depth of the atmosphere is considerably smaller than the white dwarf radius. Therefore, the density, pressure and temperature depends only upon the height, z. Hence, these codes are refers as 1D-atmosphere codes.
- hydrostatic equilibrium: the gradient of the gas pressure in the photosphere is in equilibrium with gravity.
- radiative and convective equilibrium: The energy is conserved in the photosphere. In addition to radiation, energy is transported from the interior to the surface due to conduction or convection.

- Local Thermodynamic Equilibrium: the mean free path of photons is small compared to the gradients in temperature and pressure, and the densities are sufficiently high that collisions dominate over photoionisation/excitation. Therefore, the ionisation states, excitation states, and formation/dissociation of molecules are determined by the classical equations of thermodynamics. This assumption considerably lightens the computational effort.

The codes comprises two main parts: the first computes the atmospheric structure and the second computes the emerging spectrum.

3.1.1 White dwarf atmospheric structure: ATM and TLUSTY

The ATM (Koester, 2010) and TLUSTY (Hubeny & Lanz, 1995) codes calculate the atmospheric structure. In general, these codes solve the radiative transfer equation, which describes the balance between the emission and absorption of photons. Additional constraints come from the hydrostatic equation that describes the balance between the gradient of the gas pressure, and gravitational and radiative forces, therefore it provides the relation between pressure scale, geometrical, and optical depth. Another constraint is that the energy flux transported throughout the atmosphere is constant. The energy transport by convection is described by the mixing-length approximation, which depends on a unique parameter: the ratio of the mixing length to the pressure scale height $\alpha = l/H_P$.

Additional calculations are required for the computation of the structure: the Equation of State, which provides the thermodynamical quantities of the atmospheric structure (density, electron pressure, entropy); the Saha equation which describes the ionisation states; the Boltzmann equation which provides the excitation balance; and the absorption coefficients which describe the probability of absorbing or scattering the photons. TLUSTY perfoms all these calculations at once, however ATM uses an auxiliary program called KAPPA, which solves the Equation of State and computes the absorption coefficients.

3.1.2 Synthetic emergent spectrum: SYN and SYNSPEC

The calculation of the atmospheric structure in each layer of the atmosphere is done using a wavelength grid with a limited number of points (~1000) that covers from X-rays to the far infrared to ensure that the entire spectral energy distribution is accounted for. Once the structure has been calculated, the radiative transfer equation can be solved wavelength by wavelength. Therefore, the codes SYN and SYNSPEC calculate the radiation field in a specified wavelength range at much higher resolution. During this step, more details of the spectral lines can be included. e.g. more sophisticate broadening theories and additional weaker spectral lines.

Using these codes, the computation of a white dwarf model depends only on $T_{\rm eff}$, $\log g$ and metallicity. Therefore, large grids of white dwarf models can be computed varying these parameters. Given spectroscopic data, the best parameter model that describes the observations can be found from this grid using some type of fitting technique.

3.2 Markov Chain Monte Carlo ensemble sampler

In astrophysics the modelling of observational data usually needs free parameters and the more complex the model, the more expensive is the computation of the best fit. The probabilistic data analysis in the Markov Chain Monte Carlo (MCMC) framework has become one of the preferred methods for the data analysis in astrophysics. The Bayesian inference has the advantage over frequentist methods because it allows to take into account prior information on the parameters of the model along with the data to fit. Furthermore, it provides practical information of the parameters in the model, e.g. how they are are correlated (e.g. no correlated, non-linear correlation, etc), the distribution from which formal errors can be calculated (e.g. one sigma error from a Normal distribution). Here, I will explain the MCMC method which involves the Bayesian inference, i.e. describes the probability of an event, based on prior knowledge of the conditions that are related to the event.

If there is a set of observed data, D, that can be described by a model, Θ, then the distribution of the parameters of the model that is consistent with the dataset is given by the *posterior probability function*. Using Bayes theorem, the MCMC method aims to draw samples Θ_j from the posterior probability density,

$$P(\Theta|D) = \frac{P(\Theta)P(D|\Theta)}{P(D)}. \tag{3.1}$$

$P(\Theta)$ is known as the prior distribution which encodes every piece of information about the parameters such as results from previous experiments or physically acceptable values (e.g. the mass can never take negative values). $P(D)$ is the normalization constant known as evidence which is usually very expensive to compute since the integration is carried out over all possible parameter values, $\int_\theta P(D|\theta)P(\theta)d\theta$. However, I will explain later the reason why it is usually not necessary to calculate the evidence, meaning that the posterior, $P(\Theta|D)$, can be sampled without computing $P(D)$. Finally $P(D|\Theta)$ is the likelihood function, which is the probability distribution over the dataset, i.e. how it is anticipate that the data are distributed.

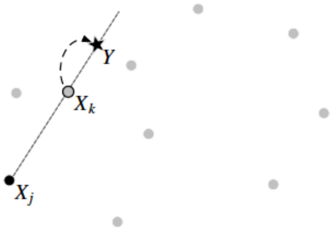

Figure 3.1: Y is a proposed position for walker X_k using a stretch move along the line connecting the walker with a complementary helper X_j from the ensemble. The light grey dots represent the position of other walkers in the ensemble which do not participate in the move.

The technique of MCMC consists in sampling the parameter space aiming to find the region that maximizes the posterior. The samplers, called *walkers*, generate random walks in this parameter space. The method used in this thesis to move the walkers is the *stretch move* ensemble sampler method (Goodman & Weare, 2010). This technique proposes new positions for the walkers using the current walker positions and performs an accept/reject analysis.

In an ensemble of M walkers, $\vec{X}(t)$=[$X_1(t)$, $X_2(t)$...,$X_{\mathrm{M}}(t)$] varies in time, t. The suggested positions of the walkers in the ensemble are invariant under an affine transformation. The property of affinity lies in connecting two affine spaces for which the transformation preserves the ratios of distances between points lying on a straight line. An example of an affine transformation is a rotation of a image. The affine invariant of the walker $X_k(t)$ in the ensemble is a stretch move, along the line connecting an auxiliary walker $X_j(t)$, as shown in Figure 3.1. The move is given by:

$$X_k(t) \longrightarrow Y = X_j + Z(X_k(t) - X_j) \tag{3.2}$$

where Z is the stretching variable ($Z = 1$ means no change) which is drawn from a distribution $g(Z)$ which satisfies the symmetric condition: $g\,(1/Z) = Z\,g(Z)$. Consequently the move is symmetric, meaning that the probability of $X_j \longrightarrow X_k$ is the same as the probability of $X_k \longrightarrow X_j$. The particular distribution defined by Goodman & Weare (2010) is based on an adjustable scale parameter a (set to 2 according to Goodman & Weare 2010) and it has the form:

$$g(Z) \propto \begin{cases} \frac{1}{\sqrt{Z}} & \text{if } Z \in \left[\frac{1}{a}, a\right] \\ 0 & \text{otherwise} \end{cases} \tag{3.3}$$

Finally the proposed position in the parameter space is analysed according to the acceptance probability. The acceptance probability is based on the ratio between the posterior probabilities of the proposed and the current positions, and will accept the lower value in

$$\min\left(1, Z^{n-1}\frac{P(Y)}{P(X_k(t))}\right) \tag{3.4}$$

The factor Z^{n-1} corresponds to the fact that the proposed position is chosen from a one-dimensional subset of the n-dimensional space. Above I mentioned that the evidence, $P(D)$, does not need to be computed. The reason can easily be understood from equation 3.4. The evidence is based only on the data and will therefore be the same in both posterior probabilities, cancelling out from the acceptance ratio.

The procedure is repeated, and if the choice of the model appropriately describes the data, the chain of walkers will converge to a stationary state, which represents the largest posterior in that parameter space. However, it is worth note few points that are unclear how to deal with: it is unclear how long the chain should run to achieve a convergence, and the posterior distributions can be strongly dependent on the assumed priors, in which case an inadequate prior can mislead result of the parameters.

3.2.1 Example: white dwarf radial velocity of QS Vir

To illustrate the effectiveness of the MCMC fitting technique, I will make use of radial velocity of the white dwarf in QS Vir as an example. The model for the radial velocity of the white dwarf can be described by

$$V_{\tan} = \gamma_{\rm sys} + K_{\rm WD} \times \sin(2\pi\,\phi) \tag{3.5}$$

where $\gamma_{\rm sys}$, $K_{\rm WD}$, and ϕ are the systemic velocity, the amplitude of the radial velocity and the orbital phase, respectively. In section 2.3.3 I measured a systemic velocity of $\gamma_{\rm sys} = 39 \pm 11\,{\rm km\,s^{-1}}$ and a velocity amplitude of $K_{\rm WD} = 147 \pm 16\,{\rm km\,s^{-1}}$ from the COS spectroscopy. I am going to assume that the mean of these values are the *true* parameters and generate artificial data which I will fit using MCMC. If the probabilistic concept behind MCMC method is correct, then the values of the parameters obtained from the MCMC should be very similar to those measured from the *HST* data.

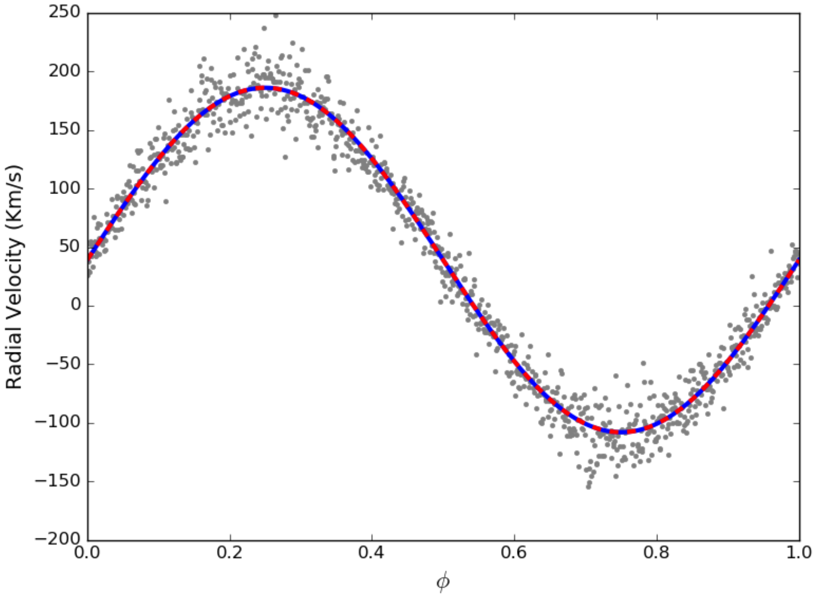

Figure 3.2: Synthetic data for the radial velocity of the white dwarf in QS Vir including artificial noise (dots). The blue line corresponds to the *true* values (see text for details) of the radial velocity $\gamma_{\rm sys} = 39\,{\rm km\,s^{-1}}$ and $K_{\rm WD} = 147\,{\rm km\,s^{-1}}$. The red line represents the best MCMC fit to the synthetic data, $K_{\rm sys} = 39.01 \pm 0.02\,{\rm km\,s^{-1}}$ and $K_{\rm WD} = 147.01 \pm 0.03\,{\rm km\,s^{-1}}$.

To generate the data, D_i, I selected $N = 1000$ random values from the Gaussian distributions of the $\gamma_{\rm sys}$ and the $K_{\rm WD}$ in equation 3.5 (black dots in Figure 3.2). This example, and in general the spectroscopic data in this thesis, consists of N data points that have uncertainties, σ_i, which follow a Gaussian distribution. Therefore it is common to work in logarithmic space. The Gaussian likelihood distribution will be given by

$$\ln P(D|\Theta) = \sum_i^N -\frac{1}{2}\ln{(2\pi\sigma_i^2)} - \frac{1}{2}\frac{(D_i - \Theta_i)}{\sigma_i^2}. \tag{3.6}$$

Therefore, the posterior distribution to be maximized is,

$$\ln P(\Theta|D) \propto \ln P(\Theta) - \frac{1}{2}\sum_i^N \frac{(D_i - \Theta_i)^2}{\sigma_i^2}. \tag{3.7}$$

For the case of QS Vir, I set a flat logarithmic prior that constrains the parameters to be always positive, i.e.

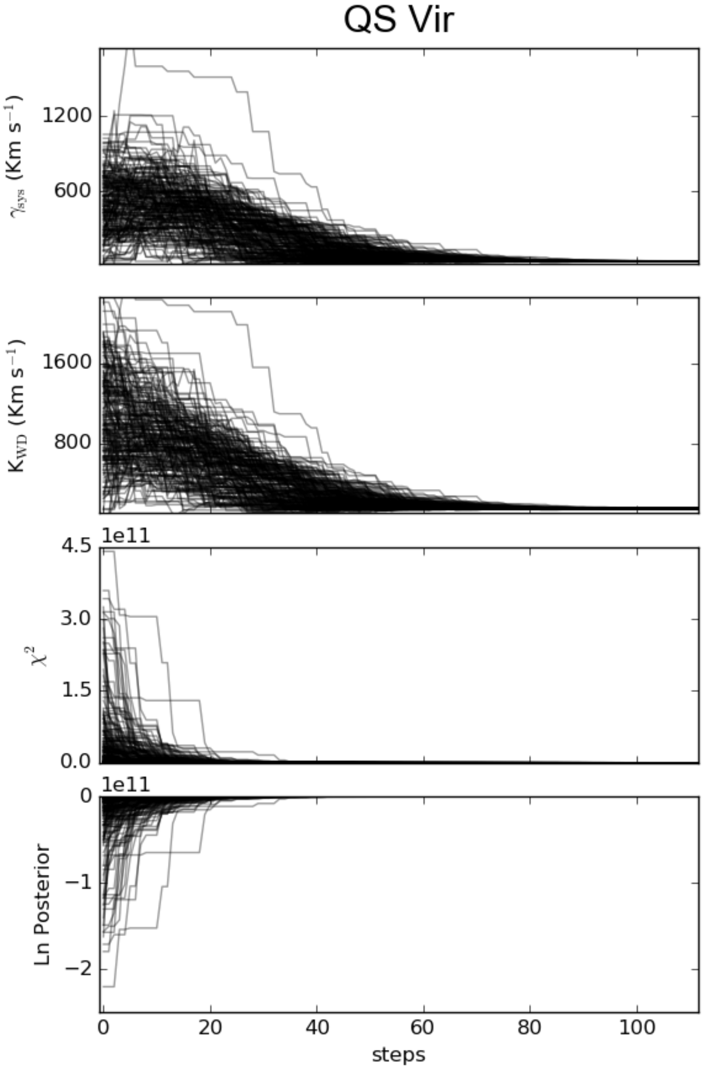

Figure 3.3: This plot is commonly called "Burn in" diagram and illustrates the convergence of the parameters $\gamma_{\rm sys}$ and $K_{\rm WD}$ for the radial velocity of QS Vir. Also shown is the χ^2 in comparison with the posterior probability.

$$\ln P(\Theta) = \begin{cases} 0 & \text{if parameter} > 0 \\ \text{-}10^{30} & \text{otherwise.} \end{cases} \tag{3.8}$$

The model Θ, is given by equation 3.5. The errors, σ, will be the difference between the synthetic data and the true values (blue line in Figure 3.2). Therefore, data points that are farther from the blue line will have less priority to be fitted than those that are closer, increasing the likeliness to find the true values.

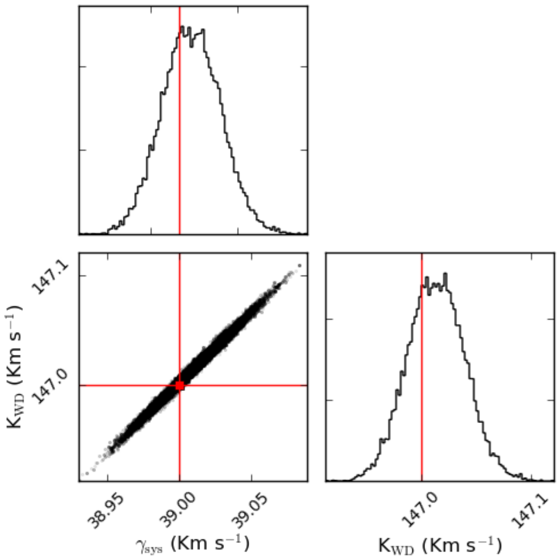

Figure 3.4: Corner plot displaying the Gaussian distribution of the best-fit parameters with values of $K_{\mathrm{sys}} = 39.01 \pm 0.02\,\mathrm{km\,s^{-1}}$ and $K_{\mathrm{WD}} = 147.01 \pm 0.03\,\mathrm{km\,s^{-1}}$. The lines represent the *true* values (see text for details) $K_{\mathrm{sys}} = 39\,\mathrm{km\,s^{-1}}$ and $K_{\mathrm{WD}} = 147\,\mathrm{km\,s^{-1}}$. The two parameters are strongly correlated.

I set 200 walkers to sample the parameter space composed by two parameters, K_{sys} and K_{WD}, iterating 500 times. The walkers sample a wide range of initial values but converge quickly within less than 100 iterations (Figure 3.3). To obtain the best-fit parameters, the sequence is cut-off in the region where the walkers have not converged, and the remaining burnt-in sequence is projected into histograms. The mean and standard deviation in these histograms correspond to the best-fit values. Figure 3.4 shows the distribution of the parameters from the fit to the synthetic radial velocity data for QS Vir. They can be described by Gaussians: $K_{\mathrm{sys}} = 39.01 \pm 0.02\,\mathrm{km\,s^{-1}}$ and $K_{\mathrm{WD}} = 147.01 \pm 0.03\,\mathrm{km\,s^{-1}}$, which are extremely close to the true values.

3.3 White dwarf T_{eff} and $\log g$ from fits to ultraviolet spectroscopy: the need for constraints

The detailed shape of the ultraviolet spectrum of DA white dwarfs is very sensitive to small changes of T_{eff} and $\log g$, specially for the range of temperatures of ZZ Cetis. The strength of the Lyman α absorption line depends mainly on the degree of ionization of hydrogen, and hence through the Saha equation, to the atmospheric pressure and the effective temperature. Since to sustain ionisation high temperatures are needed, in contrast higher surface gravities, which lead to higher atmospheric pressure, decrease the degree of ionisation. Therefore, balancing adequately T_{eff} and $\log g$ causes a strongly correlated degeneracy (Figure 3.5). As a consequence, fitting synthetic white dwarf models will provide very little constraints on these parameters. Therefore, additional constraints are required to break this degeneracy and to provide a better constrained solution. Adding magnitudes in the optical can constrain the slope of the spectral energy distribution. Moreover, the distance from an independent measurement (e.g. parallax) can constrain the relation between the radius (or $\log g$) and T_{eff} (through the use of a mass–radius relation). To illustrate this approach, I will estimate the T_{eff} and $\log g$ for the nearby DA white dwarf, WD1919+145.

WD1919+145 was observed with COS on March 2016, using the G130M/1291 Å set up. Two exposures resulted in ~1000 s of time tagged spectroscopy.

The grid of DA white dwarf models used in the fits was computed using the KAPPA, ATM, and SYN codes (see Section 3.1). The grid covers T_{eff}=12 000–20 000 K in steps of 100 K and $\log g$=7.5–8.5 in steps of 0.1 dex. Each model (F_{WD}) in the grid can be scaled to the COS spectroscopy (F_{obs}) by a factor s, which can be derived by using the conventional minimization of least squares,

$$s = \frac{\sum F_{\text{WD,i}} \times F_{\text{obs,i}}/e_i^2}{\sum F_{\text{WD,i}} \times F_{\text{WD,i}}/e_i^2}, \tag{3.9}$$

and e are the uncertainties of the observations. A χ^2 contour plot of a straight comparison of the COS spectrum against every (scaled) model is shown in Figure 3.5. It results that a large valley in the T_{eff}–$\log g$ space provides fits that are nearly equally good as a consequence of the degeneracy described above. Therefore, it is clear that additional information is needed for a reliable measurement of T_{eff} and $\log g$, which can be provided as priors.

3.3.1 Distance as a prior

As explained in Section 3.2, MCMC maximizes the posterior probability given by equation 3.7, and I define below the components that enter in this equation, which are the likelihood and the distance prior.

In this example for WD1919+145, the likelihood comprises the spectroscopic data ($D = F_{\text{obs}}$), the uncertainties of the spectroscopy ($\sigma = e$), and the model is given by

$$\Theta = 4\,\pi \left(\frac{R_{\mathrm{WD}}}{d}\right)^2 \times F_{\mathrm{WD}}(T_{\mathrm{eff}}, \log g) \tag{3.10}$$

where R_{WD} is the white dwarf radius and d is the distance. Note that the distance, d, is a parameter to be fitted, however it is constrained by the distance prior that carries knowledge of the parallax measurement. The parallax distance of WD1919+145 is $D = 19.80 \pm 2.2$ pc[1] (Bédard et al., 2017). Hence, the Gaussian distance prior is

$$\ln P(D) = -0.5 \times (19.80 - D)^2/2.2^2 \tag{3.11}$$

The MCMC will provide a best-fit distance that is closest to the distance mean. However, the knowledge of the parallax distance in equation 3.11 does not provide any constraint on the white dwarf model as it is. Since the white dwarf radius can vary freely, it will scale the model as best as it can, which could even result in physically unrealistic values. Therefore, the radius also requires some constraints, which can ideally be linked to $\log g$. This translates into the inclusion of a mass–radius relation.

White dwarf masses and radii can be obtained from detailed evolutionary cooling models, and define together the surface gravity, $\log g$. Therefore, interpolating these cooling sequences, a mass–radius relation can be computed. The cooling models used in this thesis are for pure hydrogen white dwarfs, with temperatures below 30 000 K, taken from Fontaine et al. (2001).

Therefore, the situation MCMC is dealing with is that each walker draws T_{eff}, $\log g$, R_{WD}, and d from the posterior. Using T_{eff}, $\log g$, and the mass–radius relation, the white dwarf mass and radius can be computed. The latter is then compared with R_{WD} drawn by the walker to evaluate consistency. In principle, also the relation $g = GM/R^2$, can be used to link the surface gravity, the white dwarf radius and the mass, however the mass is obtained from the mass–radius relation, so the mass–radius relation is required.

The best-fit is shown in red in the top panel in Figure 3.6, which corresponds to the parameters $R_{\mathrm{WD}} = 0.0125 \pm 0.0001\,\mathrm{R}_\odot$, $d = 19.98 \pm 0.07$ pc, $T_{\mathrm{eff}} = 14\,790 \pm 23$ K and $\log g = 8.06 \pm 0.01$. Inserting the latter two into the mass–radius relation gives a mass of $\simeq 0.65\,M_\odot$ and a radius of $\simeq 0.0125\,\mathrm{R}_\odot$, and as expected, this radius is consistent with the best-fit radius, R_{WD}. The uncertainties are purely statistical of the MCMC method. The distance, d, also agrees within the uncertainties of the measured value (Bédard et al., 2017). Furthermore, comparison with previous works of Koester et al. (2009) and Sion

---

[1] At such a small distance, reddening is negligible

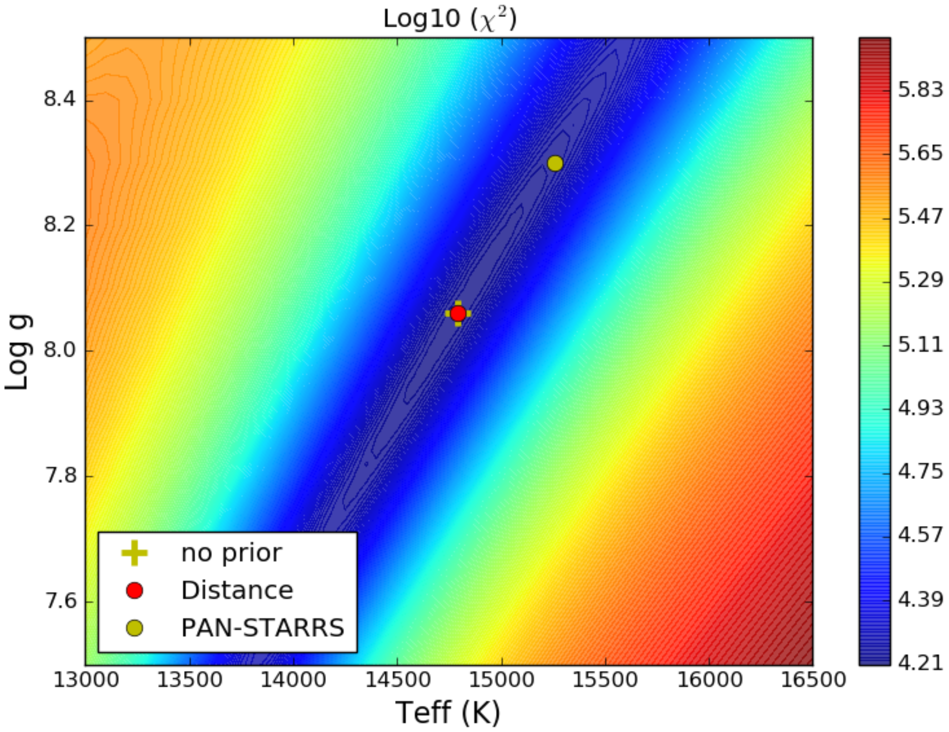

Figure 3.5: χ^2 contour in $T_{\rm eff}$–$\log g$ space for spectral model fits to COS spectroscopy of WD1919+145 with the minimum indicated with a green cross. Two independent MCMC fits were performed using prior on the distance (red dot) and adding a second likelihood from optical Pan-STARRS magnitudes (green dot).

et al. (2009), the surface gravity agrees with their estimates but the effective temperature is lower by ~300 K than those in their analyses. However, an additional measurement from fits to the Balmer lines performed by Gianninas et al. (2011) found $\log g = 8.20 \pm 0.04$ and $T_{\rm eff} = 15\,280 \pm 247$ K, which suggests larger surface gravity and higher effective temperature. Figure 3.5 shows the position of the best-fit with a red dot, which coincides with the minimum along the valley indicated with a green cross. It is worth to note that the distance error is large, $\simeq$10%, and the weight the distance prior has on the posterior is diluted by the likelihood, in other words it mimics the behaviour as if only the ultraviolet spectroscopy is being fitted. Therefore, in this case the $T_{\rm eff}$–$\log g$ degeneracy, introduced above, needs to be considered and the larger surface gravity and higher effective temperature as found by Gianninas et al. (2011) also provides a good solution in the valley in Figure 3.5. Another motivation to re-evaluate these results is the use of the mass–radius relation. As introduced in Section 1.1.2, there is not a universal mass–radius relation and it is still under intensive studies (e.g. Bédard et al., 2017). Therefore, a slightly different approach that does not require the use of mass–radius relation would be ideal to compare results. In the next Section 3.3.2, the knowledge from optical magnitudes is used.

3.3.2 Constraints from optical photometry

The model in the likelihood changes to

$$\Theta = S \times F_{\rm WD}(T_{\rm eff}, \log g) \tag{3.12}$$

Note that S is an additional parameter to be fitted besides $T_{\rm eff}$ and $\log g$ and is different from equation 3.9). The Panoramic Survey Telescope and Rapid Response System (Pan-STARRS) measured very accurate magnitudes of $g = 12.942 \pm 0.008$, $r = 13.172 \pm 0.001$, $i = 13.477 \pm 0.001$, $z = 13.698 \pm 0.003$, and $y = 13.843 \pm 0.003$. Therefore, the likelihood for the magnitudes can be defined as

$$\ln P(\theta) = -0.5 \sum \frac{(m_{\rm j} - m_{\rm syn,j})^2}{\sigma_{\rm j}^2}, \tag{3.13}$$

where $m_{\rm j}$ and $\sigma_{\rm j}$ are the magnitudes and their uncertainties, respectively, with j denoting the g, r, i, z, and y bands, and $m_{\rm syn,j}$ are the synthetic magnitudes. The latter are computed from the integration of the white dwarf model spectra convolved with the transmission function $T_{\rm j}$ of the filter j, which in the AB system results in

$$m_{\rm syn,j} = -2.5\,{\rm Log}_{10}\left(\frac{\int T_{\rm j} \times F_{\rm WD}(T_{\rm eff}, \log g)\, d\lambda/\lambda}{\int T_{\rm j} \times 3631 \times 10^5\, d\lambda/\lambda}\right). \tag{3.14}$$

The best-fit results are $T_{\rm eff}$= 15 260 ± 3 K and $\log g$= 8.300 ± 0.002 (represented with a green point in Figure 3.5), which is offset from the centre of the valley, but still acceptable. Using the mass–radius relation a mass of $\simeq 0.80\, M_{\odot}$ and a radius of $0.0105\,{\rm R}_{\odot}$ are derived. Using the scaling factor, S, and the radius, a distance of 18.33 pc is calculated which is within the error of the measured parallax distance (Bédard et al., 2017).

Figure 3.6 shows a comparison of the fits including optical magnitudes (green) and distance (red). Both of them have a similar quality in the ultraviolet, however clearly disagree at optical wavelengths.

In conclusion, spectral fits to ultraviolet spectroscopy do not necessarily provide results that agree with additional information from independent measurements such as optical magnitudes and distances. Therefore, better results can be obtained if additional

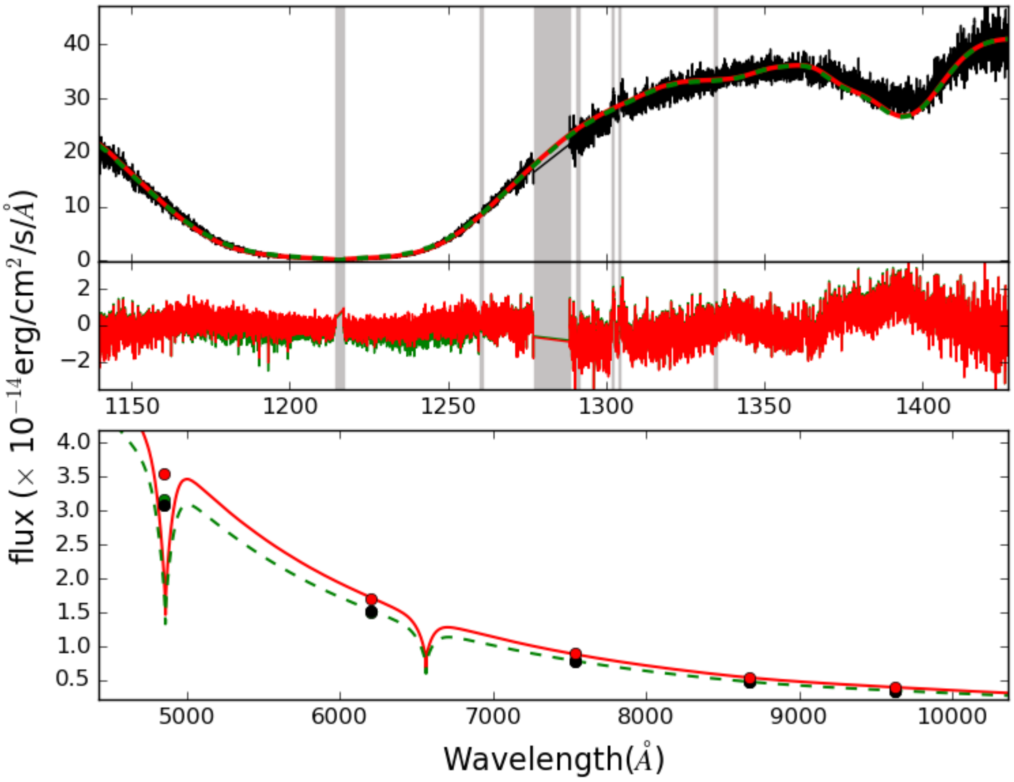

Figure 3.6: Best-fit parameters for the COS spectroscopy of WD1919+145 (black) using MCMC adding constraints from the parallax distance (Bédard et al., 2017) or Pan-STARRS photometry (black dots in the bottom panel). Red line uses the distance as a prior in addition to a mass–radius relation from cooling models (Fontaine et al., 2001), and green line uses Pan-STARRS optical magnitudes as a second likelihood. Synthetic magnitudes are calculated for both approaches, distance (red dots) or optical photometry (green dots), which are shown in the bottom panel. The residuals (middle panel) show that both approaches provide similar quality in the ultraviolet, however the g, r, i, z, and y magnitudes (from left to right in bottom panel) disagree considerably.

information is considered in the fit.

3.4 Side projects

Here I will briefly describe my contribution in side projects involving the analysis of COS spectroscopy that led to the publication of two papers.

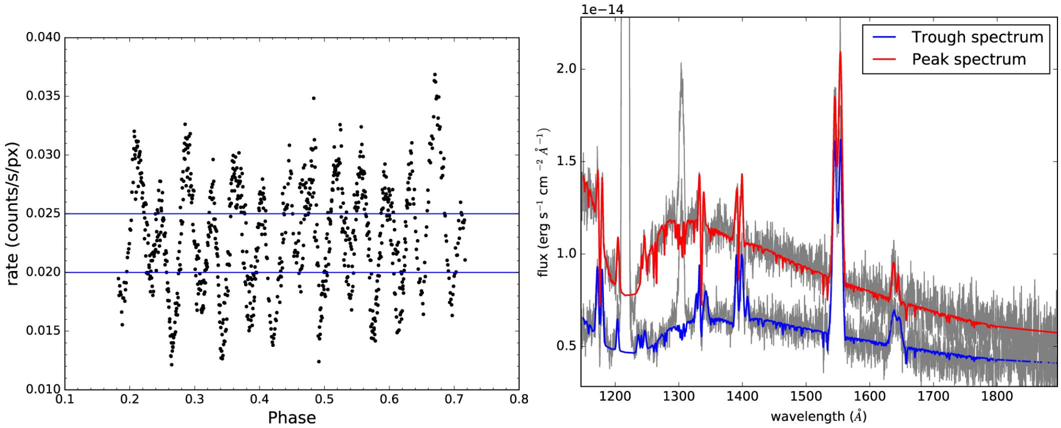

Figure 3.7: *Left: HST* count rate light curve of CC Scl showing the regions used to create the peak spectrum (above the top line) and the trough spectrum (below the bottom line). *Right:* The spectra created from the peaks (top gray), and troughs (bottom gray) are fitted with one and two white dwarf models, respectively where both approches include a power law to account for the seocnd component (see text for details). The trough spectral fit (blue) is for a $T_{\rm eff}$=15 612 K white dwarf along with a power law contributing 65% of the far ultraviolet flux, while the peak fit uses a two-temperature white dwarf with $T_{\rm eff}$=15 612 K and $T_{\rm eff}$=24 170 K (red) along with a power law contributing 42% to the total flux (see text for details).

3.4.1 The intermediate polar CC Sculptoris, Szkody et al. 2017, AJ, 153, 123

CC Sculptoris (CC Scl) was identified as an Intermediate polar (IP) which presents short duration (≃9 day) outbursts during which it exhibits superhumps with a period of 1.443 hr (Woudt et al., 2012). Its spin period (389.5 s, visible during the 2011 outburst Woudt et al. 2012) is not synchronised to its orbital period (≃1.40 hr Chen et al. 2001; Woudt et al. 2012; Ishioka et al. 2001; Kato et al. 2015). CC Scl is suggested to have a very low mass ratio, q =0.072±0.003, such that it could be a post-period bounce system (Longa-Peña et al., 2015).

About 1.3 h of time-tag ultraviolet data of CC Scl was obtained in June 2013 in two *HST* orbits. The COS/G140L set up covered the wavelength range 1121–1960 Å. The light curve extracted from the observations (left in Figure 3.7) shows the harmonic of the spin at 194.6 s with a much higher amplitude (220 mma) than the spin period of 389 s (90 mma). For the first time, the spin period, previously only identified during an outburst, is visible in quiescence.

IPs have additional contributions to the ultraviolet light from the accretion curtains, and the heated areas on the white dwarf near the magnetic poles. Observations in the ultraviolet of many polars show large variations of the white dwarf temperature throughout the orbital cycle as the areas near the magnetic poles, which are heated by irradiation from the accretion columns, come into view (Gänsicke et al., 1995, 1998, 2006; König et al., 2006). A realistic model of this heated spot area needs to encompass a temperature change from the center of the spot to the unheated regions of the white dwarf (Gänsicke et al., 2006) as well as non-circular spots (Linnell et al., 2010). However, the wavelength and orbital coverage of the COS data is limited, and therefore a more simplistic model is chosen in order to estimate the temperature of the heated accretion areas. A procedure similar to the one used to study the temperature variations in the dwarf nova GW Lib (Section 5) was used, which involves spectral fits using the MCMC. Two spectra, one obtained from the peaks of the light curve and a second obtained from the troughs were modelled. The range of count rates used to create these peak and trough spectra are shown in the left panel in Figure 3.7, and the resulting two spectra are shown on the right. The spectra clearly show flux differences, and the broader Lyman α absorption line indicates a decrease of temperature for the trough spectrum. The peak spectrum corresponds to the spin phases when both heated and unheated regions are visible, while it is assumed that the trough corresponds entirely to the unheated areas of the white dwarf.

A grid of white dwarf models was created using TLUSTY & SYNSPEC (Hubeny & Lanz, 1995). It covers a temperature range of 9000–30 000 K in steps of 100 K. The metallicity was set to 0.2 times the solar abundances which reproduce the absorption of the metal lines. Finally, $\log g$ was fixed to 8.35 which corresponds to the average of the mass distribution for white dwarfs in CVs (Zorotovic et al., 2011). The airglow emission lines of Lyman α and O I were masked out in the range of 1207.20–1225.26 Å and 1295.30–1312.44 Å, respectively. The emission lines of C III at 1176 Å, C II at 1335 Å, Si IV at 1400 Å, and C IV at 1550 Å were fitted with Gaussians.

The temperature of the unheated region is obtained from fitting the trough spectrum using a single white dwarf model. The peak spectrum is approximated by two white dwarf models with different temperatures accounting for the heated and unheated regions, in which one of these temperature is fixed to the one determined from the trough spectrum. However, In both cases, the core of the Lyman α absorption reveals evidence for a second component that contributes additional flux to the trough and peak spectra (see Section 5.4.2 for a discussion of this second component), which is modelled with a power law.

The sinusoidal-like shape of the light curve of CC Scl suggests that the hot areas are not fully self-eclipsed, hence the estimate of the temperature of the underlying unheated white dwarf temperature should be considered as an upper limit. A temperature $15\,612^{+139}_{-129}$ K is obtained from fitting the trough spectrum of CC Scl, which is likely an average of a lower-temperature white dwarf and some warmer area. This fit is shown in in blue in the right panel in Figure 3.7 and it includes a power law that contributes 65% to the total observed flux. The fit to the peak spectrum results in the temperature of the heated spot to be $24\,170^{+848}_{-586}$ K which covers an area of less than 9.5% of the visible surface of the white dwarf. The power-law component contributes 42% to the total flux. As mentioned above, the simplicity of the model does not allow good constraints to the temperatures, but it can be concluded that the temperature of the area viewed during ultraviolet peak phases is several thousand degrees hotter than that at the trough phases.

3.4.2 The ultraviolet spectrum of the radio pulsar AR Sco Marsh et al. 2016, Nature, 537, 374

The discovery of AR Scorpii (AR Sco), a white dwarf radio pulsar plus a cool M-type star binary, was recently reported. The muti-wavelength observations analysed comprised photometry and spectroscopy, covering radio, near infrared, optical, ultraviolet, and X-rays (see Figure 3.8), and showed that AR Sco pulses with a period of 1.97 min. During these intense pulses the optical flux can increase up to four times within 30 s, and they are detectable from ultraviolet to radio frequencies.

They reflect the spin period of a strongly magnetic white dwarf which we found to be slowing down on a $\simeq 10^7$ yr timescale. The spin-down power is an order of magnitude larger than that emitted in electromagnetic radiation, which, together with an absence of obvious signs of accretion, suggests that AR Sco is primarily spin-powered. Although the pulsations are driven by the white dwarf's spin, they originate in large part from the cool star. AR Sco's broad-band spectrum is characteristic of synchrotron radiation, requiring relativistic electrons. These must either originate from near the white dwarf or be generated in situ at the M dwarf through direct interaction with the white dwarf's magnetosphere.

My contribution in this study was the analysis of the *HST* spectroscopy. In January 2016, AR Sco was observed with *HST*/COS using the G140L grating centred at 1105 Å. Five orbits provide $\simeq 3.37$ hr of time tag data. The average spectrum of the observations is shown in black in right panel of Figure 3.9.

To constrain the contribution of the white dwarf to the SED, a spectrum was built using the lowest count rate of the light curve indicated in blue in Figure 3.9. The corresponding spectrum is shown in blue in the right panel of Figure 3.9, the emission lines mainly come from the irradiated face of the M star. Assuming a surface gravity of 8.0 and a distance of

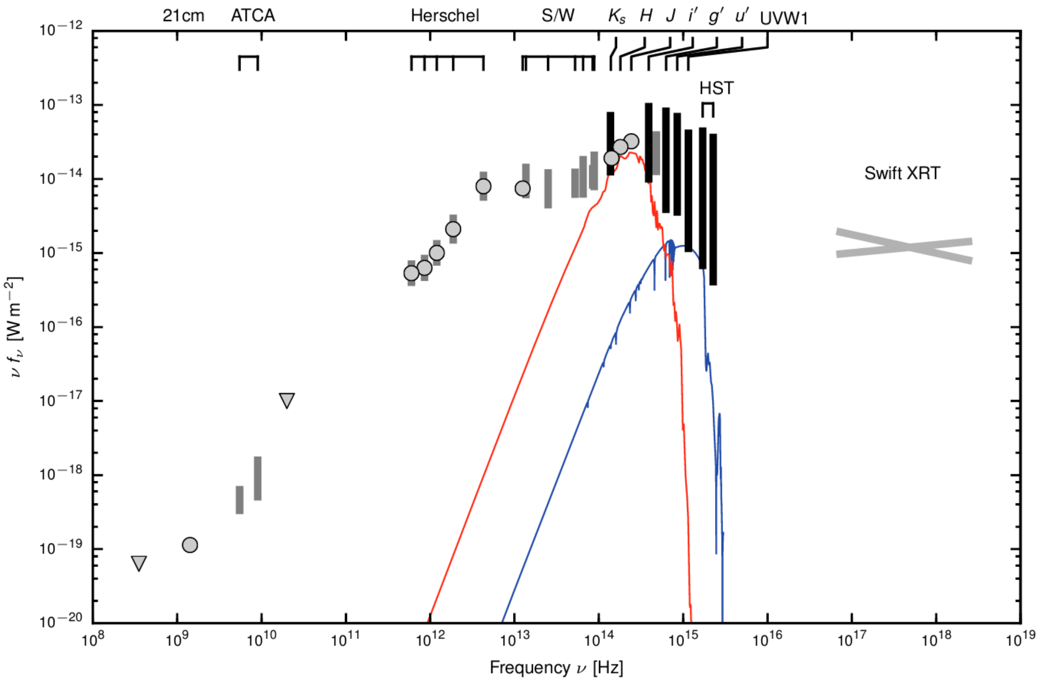

Figure 3.8: Spectral Energy Distribution of AR Sco. Black bars are intensive photometry and time-resolved spectroscopy; grey bars represent more limited datasets that cover less than the full flux variation. Grey points with error bars (1σ) are single exposures, where triangles are upper limits. The grey lines represent the $\pm 1\sigma$ range of X-ray spectral slopes. "S/W" stands for Spitzer and WISE data. The red and blue lines show model atmospheres, extended at long wavelengths with black-body spectra, for the M star (R=0.36 R$_\odot$, $T_{\rm eff}$=3100 K) and white dwarf (R=0.01 R$_\odot$, $T_{\rm eff}$=9750 K upper limit) at a distance d=116 pc. For details of observations see extended data in Marsh et al. (2016).

116 pc, estimated from the M-dwarf secondary, the upper limit for the effective temperature is $T_{\rm eff}$=9750 K, a white dwarf model with these atmospheric parameters is shown in Figure 3.8.

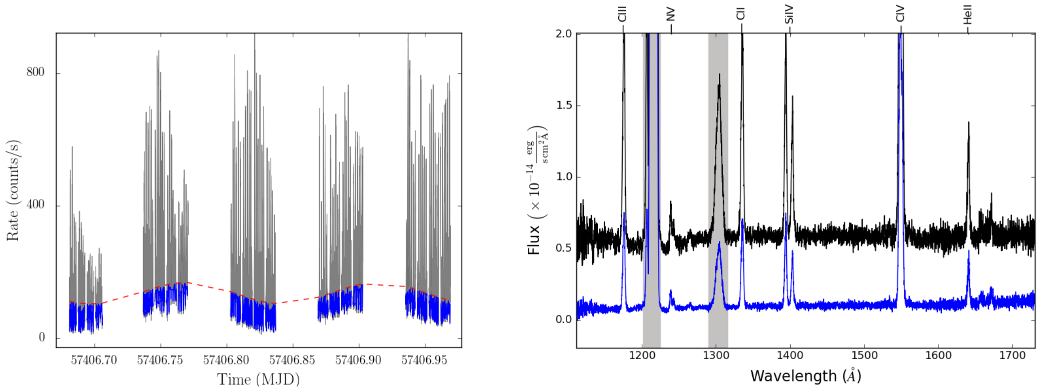

Figure 3.9: *Left: HST* ultraviolet light curve of AR Sco, the bottom of the light curve (blue) was used to built the minimum spectrum. *Right:* the average *HST* and the minimum (blue) spectra with geocoronal airglow emission indicated by grey bands. The strongest emission lines are labelled. Note that no offset in flux has been applied.

Chapter 4

G29-38: a pulsating white dwarf with metal pollution

4.1 Introduction

G29-38 is one of the brightest (V≃13.05) and closest (d ≃17 pc) white dwarfs, which was discovered to present large amplitude variability due to non-radial pulsations (McGraw & Robinson, 1975). Several modes have been identified since its discovery, which are not all excited at the same time, and therefore G29-38 shows a very unstable pulsational behaviour (Kleinman et al., 1998). However, the DAV G29-38 quickly captured attention, because it was the first white dwarf found to have an infrared excess (Zuckerman & Becklin, 1987; Graham et al., 1990) interpreted this as a dusty debris disc that formed from the tidal disruption of a planetesimal (Jura, 2003). The ongoing accretion from this debris disc explains the metals seen in the white dwarf atmosphere of G29-38 (Koester et al., 1997). However, the geometry and the process of the accretion are not yet clearly understood, in particular the distribution of the metals across the white dwarf surface. All published studies of the photospheric abundances of debris-polluted white dwarfs assume a homogeneous distribution of the metals across the white dwarf surface (Zuckerman et al., 2007; Gänsicke et al., 2012), any inhomogeneity would affect the conclusions of these analyses.

Some insight can be brought into this context from the theory of accretion developed for low-accretion rate cataclysmic variables (e.g. dwarf novae), though this theory itself fails to explain the low X-ray luminosity observed during quiescence, which falls below the predictions by more than a order of magnitude. This model suggests that the flow of the particles originates in a corona above the disc formed by evaporation of the disc (Meyer & Meyer-Hofmeister, 1994). In this scenario the accretion of the metals would result in a homogeneous distribution all over the white dwarf surface. In contrast, accretion via a boundary layer or an accretion belt (Piro & Bildsten, 2004) would result in the deposition of metals in an equatorial belt, and it is not clear if, and how fast this material could spread towards the poles. The non-radial pulsations driven in G29-38 offer a unique opportunity to diagnose any inhomogeneity of the metals across the white dwarf surface. Mapping the equivalent width of the calcium absorption lines as function of pulsation phase suggests that metals are likely deposited at the equator (Montgomery et al., 2008b; Thompson et al., 2010). However, Montgomery et al. (2008b) concluded that among the many pulsating modes excited in G29-38, only two provide clear evidence of non-uniform metal distribution. The goal of the study presented here is to investigate any inhomogeneity of the metal distribution using time-tagged COS observations of G29-38, which can provide information about the geometry of the accretion process.

4.1.1 Previous studies

Considerable amounts of effort have been carried out to measure the atmospheric parameters and abundances of G29-38, which I will summarise below.

Distance

Different distance measurements have been reported in the literature. The first, included in the Yale General Catalog of Trigonometric Stellar Parallaxes (van Altena et al., 1994) places G29-38 at 13.62±0.74 pc. Distances from parallaxes are a more reliable method for closer objects, and the Yale parallax puts G29-38 among the $\simeq$50 closest white dwarfs. However, Holberg et al. (2008) determined spectrophotometric distances to white dwarfs corresponding to the $UBVRI$ photometry, based on their $T_{\rm eff}$ and $\log g$ measurements, and estimated a value of 16.33±0.18 pc for G29-38, larger than the parallax distance. Additional spectrophotometric distances also suggest larger values (19 pc; Pauli et al. 2006 and 17 pc; Gianninas et al. 2011). The Yale parallax measurement was determined using earlier USNO photographic plates that were unguided and with a bad centre of field (Subasavage private communication) resulting in an erroneous measurement. An updated parallax value, using new CCD imaging, corresponds to 17.5±1.2 pc (Subasavage et al., 2017), which agrees better with the indirect methods. An advantageous fact of the nearby location of G29-38 is that the effects of reddening are negligible [1].

---

[1] On 25 April, 2018 the second *Gaia* data release occurred after thesis submission. The *Gaia* parallax gives a distance of 17.54±0.02 pc, which agrees very well with the distance from Subasavage et al. (2017) which was used throughout this thesis, and hence results presented here are not affected

Table 4.1: Atmospheric abundances of G29-38 determined by Xu et al. (2014). The values listed on the right correspond to upper limits.

Z	[Z/H]	Z	[Z/H]
C	-6.90±0.12	N	<-5.70
O	-5.00±0.12	Na	<-6.70
Mg	-5.77±0.13	Al	<-6.10
Si	-5.60±0.17	S	<-7.00
Ca	-6.58±0.12	Mn	<-7.20
Ti	-7.90±0.16	Ni	<-7.30
Cr	-7.51±0.12		
Fe	-5.90±0.10		

Abundances

As mentioned above, G29-38 is metal-polluted by its debris disc, therefore presents strong metal lines in its ultraviolet and optical spectroscopy. Here I will summarise the published studies of the abundances of G29-38, where the method used to measure the abundances is the same in all the works, and relies on a detailed comparison of the equivalent widths of the spectral lines with those from synthetic spectra.

- Koester et al. (1997) identified Mg II resonance lines and several Fe II features in their 6 Å-resolution FOS/*HST* spectrum. They also identified in their 3.8 Å-resolution optical spectra the feature in the blue wing of Hϵ as the H component of the Ca II resonance doublet. They estimated $\log[\mathrm{Mg/H}] = -6.28 \pm 0.12$, $\log[\mathrm{Ca/H}] = -7.2 \pm 0.2$, and $\log[\mathrm{Fe/H}] = -6.28 \pm 0.24$.
- As part of a large search for calcium absorption in the sample of white dwarfs of the ESO Supernova Ia Progenitor Survey Koester et al. (2005), determined from R≃18500-resolution UV-Visual Echelle Spectroscopy (UVES) $\log[\mathrm{Ca/H}] = -6.8$.
- von Hippel & Thompson (2007) determined $\log[\mathrm{Ca/H}] = -6.8$ from optical time series spectroscopy with a resolution of ≃7 Å, and found that the Ca II K line strength varies significantly in G29-38.
- The most detailed work on the photospheric abundances of G29-38 was performed by Xu et al. (2014). Their measurements were mostly obtained from optical spectroscopy with the High Resolution Echelle Spectrometer (HIRES)/Keck that provides a spectral resolution of R≃40000. They detected eight elements and provided upper limits for further six (Table 4.1).

In general these studies assumed that the distribution of the metals across the white dwarf surface is homogeneous and that the effect of pulsations is to cause variations on the (Ca) line strength. Here I propose to measure the abundances in a localised region on the white dwarf surface using the pulsations as a searchlight illuminating that region.

Pulsation periods

The pulsational behaviour of G29-38 is very unstable, and I will review the work carried out on pulsation mode identification.

G29-38 exhibits *very large-amplitude* and complex pulsations that have motivated extensive follow-up studies. It has been a real challenge to disentangle the pulsation modes in G29-38 because the power spectrum is dramatically unstable. Kleinman et al. (1998) found a total of 19 normal modes from 10 years of time-series photometry, however these modes are not all excited simultaneously (see Table 4.2). Later, Clemens et al. (2000a), based on modelling the fractional amplitude for six of the largest modes (chromatic technique; Robinson et al. 1995), concluded that five of these modes (283 s, 430 s, 614 s, 653 s, and 815,s) are l=1 while the 776 s-mode corresponds to l=2, also four result from combinations of the independent modes (317 s, 409 s, 2469 s, and 351 s). Thompson et al. (2008), using same technique of chromatic amplitudes, confirmed two modes identified by Clemens et al. (2000a) and found three additional modes: l=1 (835 s and 937 s), l=2 (681 s), and l=3 or 4 (353 s). These studies demonstrate the complexity of the pulsational behaviour in G29-38. The large amplitude pulsations reflect strong variations in the temperature across the white dwarf surface (Robinson et al., 1982) and complicate any attempt to determine the atmospheric parameters of G29-38, which likely explains the significant disagreement between previous studies that will be summarised in the next Section.

Effective temperature and surface gravity measurements

Many studies have been carried out attempting to measure the atmospheric parameters, T_{eff} and $\log g$, of G29-38. Here I will briefly describe these measurements and the method they are based upon:

- Bergeron et al. (1995) found that using a mixing length of ML2/α=0.6, the effective temperatures determined from *IUE* ultraviolet spectroscopy and Hβ-H$_{10}$ Balmer lines fits are consistent. This work was revisited by Bergeron et al. (2004) estimating T_{eff}=11829±200 K and $\log g$=8.00±0.05 (the uncertainties are based on the spectroscopic method in the ZZ Ceti region as estimated by Fontaine et al. 2003).
- Koester et al. (1997) obtained T_{eff}=11600 K and $\log g$=8.05 by fitting the Hβ-H$_8$ Balmer lines which provides consistency with the overall shape of their ultraviolet

Table 4.2: Detected pulsation modes in G29-38 from the literature.

Mode (s)[a]	Mode (s)[b]	Mode (s) – Amp (mma)[c]	Mode (s) – Amp (mma)[d]
110	614	615 – 27.7 ± 1.0	614.4 – 32.8
177	818	811 – 22.9 ± 1.0	809.4 – 30.1
237	653	835 – 13.4 ± 1.0	859.6 – 24.6
284	776	353 – 10.7 ± 1.0	894.0 – 14.0
355	283	937 – 10.5 ± 1.0	400.5 – 9.1
400	430	681 – 8.3 ± 1.0	496.2 – 7.9
500	351		655.1 – 6.1
552	2469		770.8 – 5.1
610	409		283.9 – 4.8
649	317		363.5 – 4.7
678			1150.5 – 3.6
730			1185.6 – 3.4
771			1239.9 – 1.9
809			218.7 – 1.5
860			
894			
915			
1147			
1240			

[a] Table 3 from Kleinman et al. (1998)

[b] Values taken from Figure 4 of Clemens et al. (2000a)

[c] Table 2 from Thompson et al. (2008)

[d] Table 21 from (Castanheira & Kepler, 2009), which lists the mean of the modes from Kleinman et al. (1998)

HST/FOS spectrum.

- Clemens et al. (2000b) found $T_{\rm eff}$=11850 K and log g=8.05 fitting the Balmer lines, however they showed that fitting each Balmer line individually results in large differences, $T_{\rm eff}$=11620–12885 K and log $g\simeq$8.0–8.5, and that the gravity and temperature are dominated by the lines of higher excitation (e.g. Hϵ) and lower excitation (e.g. Hβ), respectively.

- Koester & Allard (2000) estimated $T_{\rm eff}$=11510±120 K and log g=8.00±0.15 from fits to ultraviolet *IUE* spectroscopy and the visual magnitude.

- Koester et al. (2001) obtained $T_{\rm eff}$=11515±22 K and log g=7.97±0.01 from fitting Hα-H$_8$ in high resolution echelle spectroscopy, the same data was revisited with the aim to measure the calcium abundance from the Ca II K line ($T_{\rm eff}$=12100 K and log g=7.9, Koester et al. 2005), and again in 2009 ($T_{\rm eff}$=11485±8 K and log g=8.071±0.002, Koester et al. 2009).

- Liebert et al. (2005) estimated $T_{\rm eff}$=11 820 K and log g=8.15 from Hβ-H$_8$ Balmer lines fits.
- Lajoie & Bergeron (2007) fitted the Balmer lines obtaining $T_{\rm eff}$=11 817 K and log g=8.15 where the uncertainties are given using the method of Liebert et al. (2005) (1.2% in $T_{\rm eff}$ and 0.038 dex in log g). Additionally they fitted *IUE* spectroscopy fixing the surface gravity to the optical value and found an effective temperature of $T_{\rm eff}$=11 632±400 K, which agrees with their optical measurement. Therefore, defining $T_{\rm eff}$=11 596±364 K accounts for their two measurements.
- The parameters presented in Koester (2009) ($T_{\rm eff}$=11690 K and log g=8.11) are calculated from three independent measurements (Liebert et al., 2005; Koester et al., 1997; Voss, 2006).
- Holberg et al. (2008) obtained spectroscopic determinations of $T_{\rm eff}$=11817±53 K and log g=8.146±0.021.
- Gianninas et al. (2009) determined $T_{\rm eff}$=12200±187 K and log g=8.22±0.05 using the spectroscopic technique.
- Assuming l=1 in the asteroseismology technique, Castanheira & Kepler (2009) found $T_{\rm eff}$=11700 K.
- Based on the spectroscopic technique, and correcting the surface gravity of the "high log g problem" with an empirical relation, Giammichele et al. (2012b) estimated $T_{\rm eff}$=12206±187 K and log g=8.04±0.05.
- Using asteroseismology Romero et al. (2012), and assuming l=1,2, calculated $T_{\rm eff}$=11471±60 K and log g=8.01±0.03.
- Chen & Li (2013) added an additional l=3 mode to model the ~353 s period. They found the best fit for $T_{\rm eff}$=11900 K and log g=8.30.
- Xu et al. (2014) constrained the surface gravity, using the parallax distance (13.62±0.74 pc) and the *BV* magnitudes, to log g=8.40±0.10, and determined $T_{\rm eff}$=11820±100 K from the Balmer lines. Their estimates agree very well with the COS/G130M spectroscopy, however their surface gravity is the largest value reported.

In summary, using different techniques, the estimates of the effective temperature and surface gravity span a large range, $T_{\rm eff}\simeq$11400–12400 K and log $g\simeq$7.9–8.4 dex, respectively.

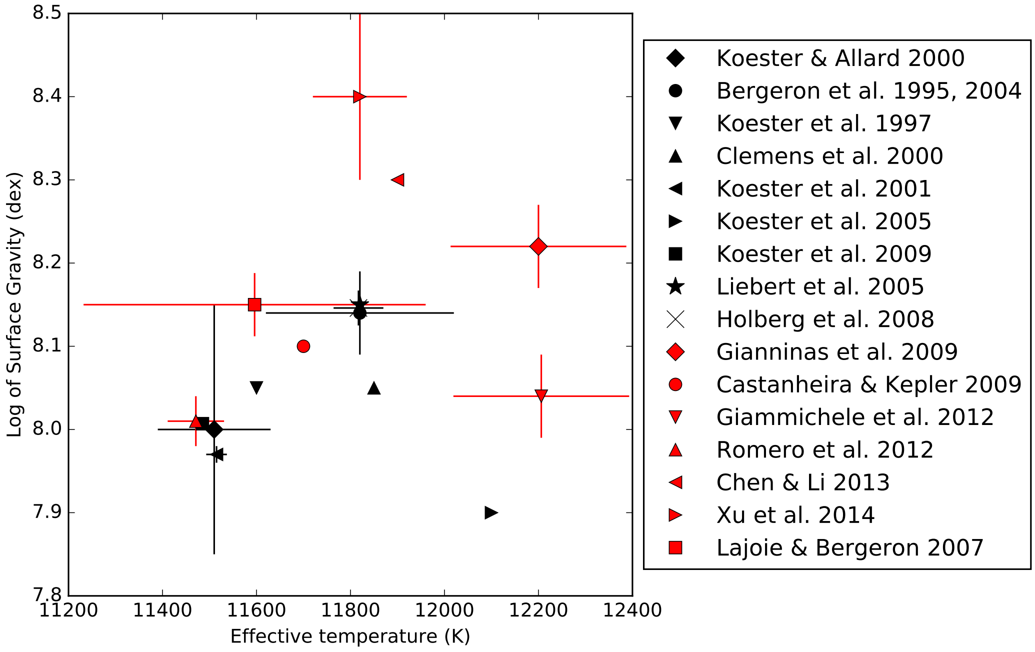

Figure 4.1: Measurements of the effective temperature and the surface gravity of G29-38 from the literature (see text for details).

The large disagreements of the temperature estimates could be understood as being related to the pulsations. However, the geometric distortions caused by the pulsations are negligibly small. As a consequence, the surface gravity should not vary as much as the published studies imply, and therefore the surface gravity appears poorly constrained.

4.2 Flux variations due to the non-radial pulsations

One potential problem in analysing spectroscopy and photometry of G29-38 is that the pulsations result in changes in the temperature across the visible stellar hemisphere on time scales of ~2-20 min (Table 4.2). Therefore, if the exposure time of the spectroscopy is long enough, the spectrum averages the flux variations for several pulsation cycles, leading to the determination of an average temperature throughout the observations. In contrast, short exposure times (shorter than the pulsation periods), which are possible due to the brightness ($V \simeq 13.05$) of G29-38, can result in a snapshot of a steep gradient in the temperature across the white dwarf surface, as shown in (c) in Figure 4.2.

The optical light curve of G29-38 was modelled by Montgomery (2005) under the

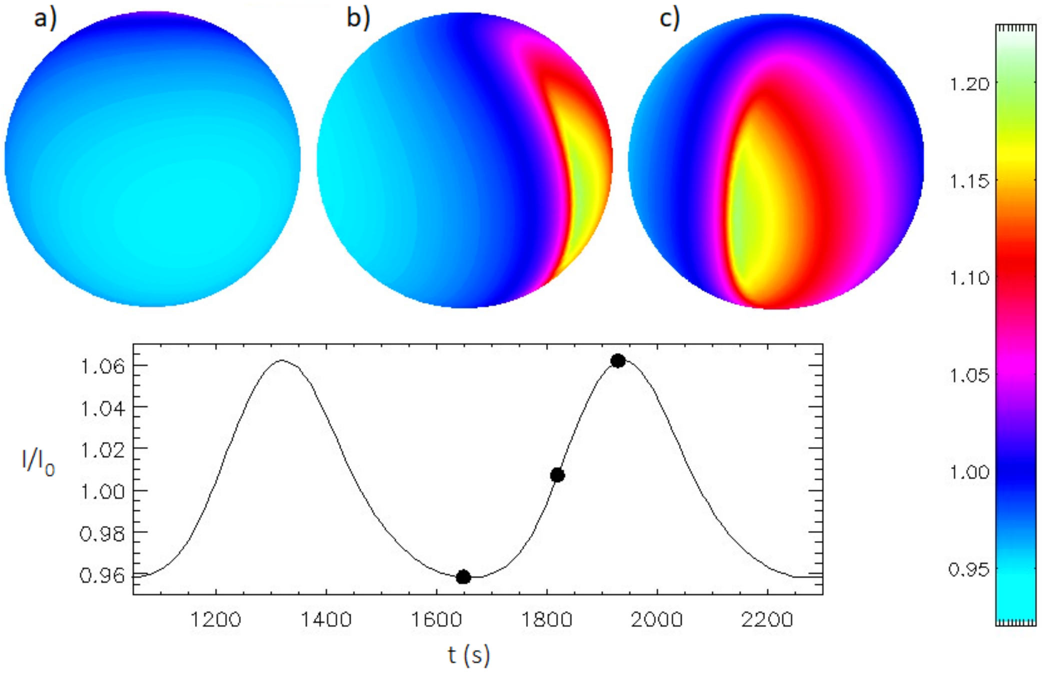

Figure 4.2: Model of the optical light curve of G29-38 assuming $l = 1$. Figure taken from http://www.as.utexas.edu/ mikemon/pulse.html.

assumption of energy conservation, i.e. that the flux emitted from the photosphere excludes the energy absorbed by the convection zone, therefore the energy absorption depends only on the photospheric flux which is temperature dependant. Assuming that the flux emitted the base of the convection zone is described by the spherical harmonics, they found the best solution for $l = 1$ and $m = 1$. Therefore, their (optical) light curve model shows that a bright, hot region travels across the white dwarf surface (Figure 4.2). The flux emitted from this region dominates the spectrum resulting in an increase in flux, and in a change of the shape of the spectrum.

4.3 COS time-tagged spectroscopy

G29-38 was intended to be observed for four orbits during Cycle 23 as part of programme 12290 (PI Jura). However, the visit partly failed due to a malfunction of a gyroscope and only the first orbit provided useful data. Therefore G29-38 was revisited with three additional orbits to complete the programme. The G130M grating was used, centred at 1300 Å. Table 6.1 gives the log of the observations. The average spectrum of the entire observation is shown in black in the top panel of Figure 4.7.

Table 4.3: Log of the COS observations of G29-38.

filename	Date	UT (hh:mm:ss)	exp. time (s)	status
lbhk05isq	2010-10-17	11:42:27	1999	good
lbhk05iwq	2010-10-17	13:01:16	2956	failed
lbhk05j8q	2010-10-17	14:37:07	2956	failed
lbhk05jgq	2010-10-17	16:12:57	2956	failed
lbhk55oiq	2011-01-19	01:57:45	1999	good
lbhk55omq	2011-01-19	03:16:11	2438	good
lbhk55ouq	2011-01-19	04:52:02	2598	good

4.4 Ultraviolet pulsation periods

The extraction of the COS light curve followed the procedure explained in Section 2.3.1. The light curve is shown in Figure 4.3, the extraction was performed in the wavelength range 1145–1443 Å, using a bin size of five seconds. Airglow emission lines are present during the COS observations. The strong Lyman α airglow was masked in the range of 1213.02–1218.14 Å while a second mask in the range between 1288.1–1308.69 Å covers the gap between the detector segments and the O I airglow emission line.

The top panel of Figure 4.4 shows the Discrete Fourier Transform spectrum of the single successful observation taken during the first *HST* orbit in October 2010, while the bottom panel shows the power spectrum of the entire COS observations taken in January 2011, corresponding to three *HST* orbits. The window function for the latter looks peculiar due to the gaps in the observations introducing aliases. The power spectrum of G29-38 is known to be very unstable showing different periods over the time (Clemens et al., 2000b; von Hippel & Thompson, 2007; Castanheira & Kepler, 2009; Romero et al., 2012). Indeed, the COS observations show a change of the power spectrum in the three months between the observations. I calculate the false alarm probability (FAP) for the five peaks above the significance level defined as four times the mean (Aerts et al., 2010). I use the bootstrap method in the LombScargle algorithm from the ASTROPY.STATS package which, under the assumption that there is no periodic signal in the data, provides the probability of detecting a peak with a given amplitude or higher. It results that the three strongest peaks (884 s, 415 s, and 302 s) are real with a FPA of 0.0 per cent, the fourth (203 s) and fifth (155 s) strongest peaks have a probability of 70 per cent and 100 per cent, respectively of being noise. These three real periods plus the less reliable are shown in Figure 4.4, where the strongest period in both power spectra is at ~884 s, while the shortest detection is considered at ~203 s.

Consequently, a snapshot of a particular state of the white dwarf can be obtained

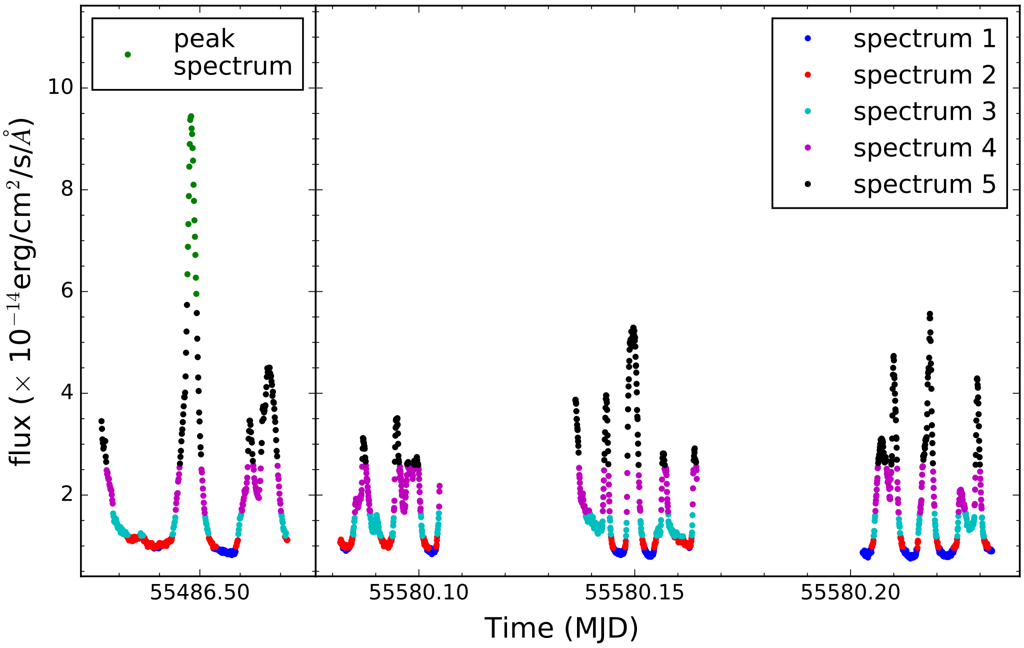

Figure 4.3: Light curve of the successful *HST*/COS observations of G29-38. The left panel shows the single orbit obtained in October 2010, while the right panel shows the observations from January 2011. The coloured bands represents the data points used to construct a series of five spectra plus a peak spectrum that are shown in Figure 4.5. The data in the green region is included in the extraction of the spectrum 5 (black).

from integrating during a time < 200 s. For example extracting an spectrum that accounts for one of the peaks in the light curve (e.g. building a spectrum from the green dots in Figure 4.3, which spans $\simeq$100 s) will correspond mainly to the emission of a very hot area on the white dwarf, and differs radically from the average spectrum. However, assuming $l = 1$, the COS light curve shows four prominent periodicities, which could mean that the heating of different regions on the white dwarf surface can coincide simultaneously, producing hot patches that are more complicated than the single bright region illustrated in Figure 4.2. Nevertheless, the effect of the increasing flux in the spectrum due to these patches can still be observed. Indeed, to illustrate the change of the shape of the spectrum I performed the extraction of a series of five spectra that are extracted at different flux levels from the light curve. The extraction of these spectra followed the procedure explained in Section 2.3.2, where the different colour shown in Figure 4.3 indicate the regions taken to build the spectra. The number of data points used to construct the spectra is the same for all of them, so that the signal of all the spectra is similar. The spectra are shown in Figures 4.5. The absorption of Lyman α is very sensitive to the effective temperature, therefore assuming a

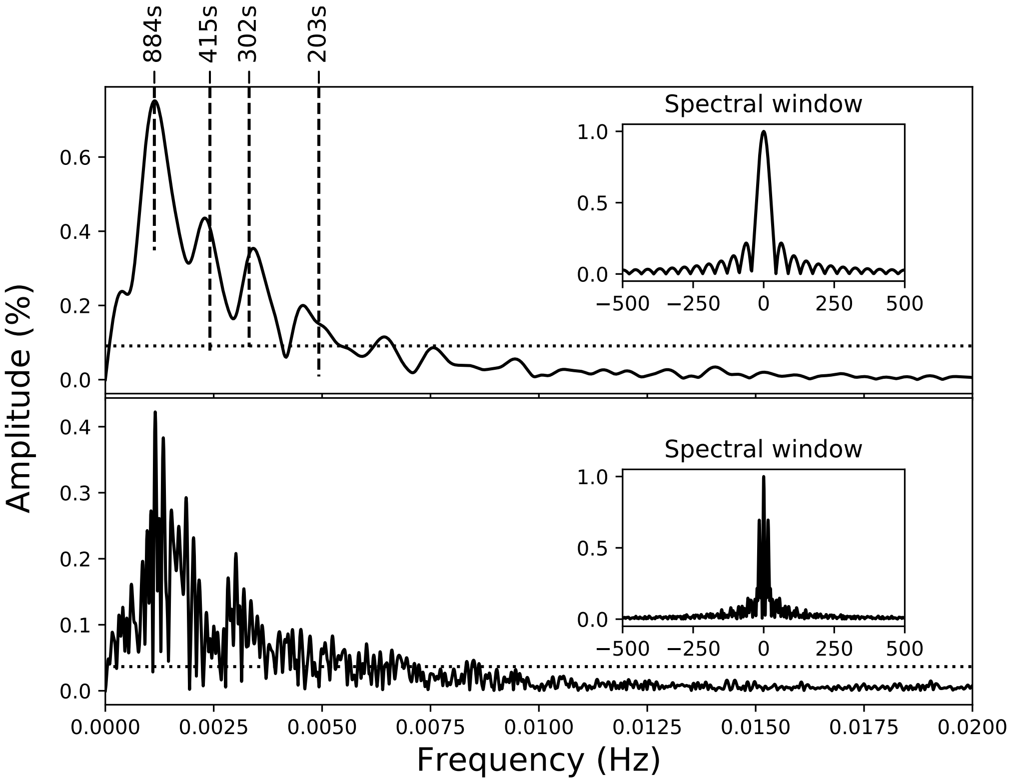

Figure 4.4: Power spectra from the COS light curves shown in Figure 4.3. The top panel corresponds to the first orbit taken in October 2010, while the bottom panel comprises the three orbits taken in January 2011. The vertical lines denote the significant periods.

single temperature for each spectrum, the peak spectrum is the hottest, and the temperature decreases towards the spectrum at the bottom labelled as spectrum 1. This statement will be demonstrated later in Section 4.5.3.

The average of the entire observations into one spectrum is accounting for the heated areas caused by the pulsations during the observations. As mentioned above if the integration time is very long this effect can be diluted, and hence one might assume that the spectrum could be fitted using a single temperature, and obtain the effective temperature of the white dwarf. While, the total time of the observations corresponds to ≃9000 s, which covers several cycles of the longest pulsation period, ≃885 s, but not be sufficiently long, hence the average spectrum can not be fitted with a single effective temperature.

As mentioned in Section 3.3, there is a degeneracy between the effective temperature and the surface gravity, and to break this degeneracy, additional information needs to be considered during the fits. It is worth noting that G29-38 is a pulsating white dwarf

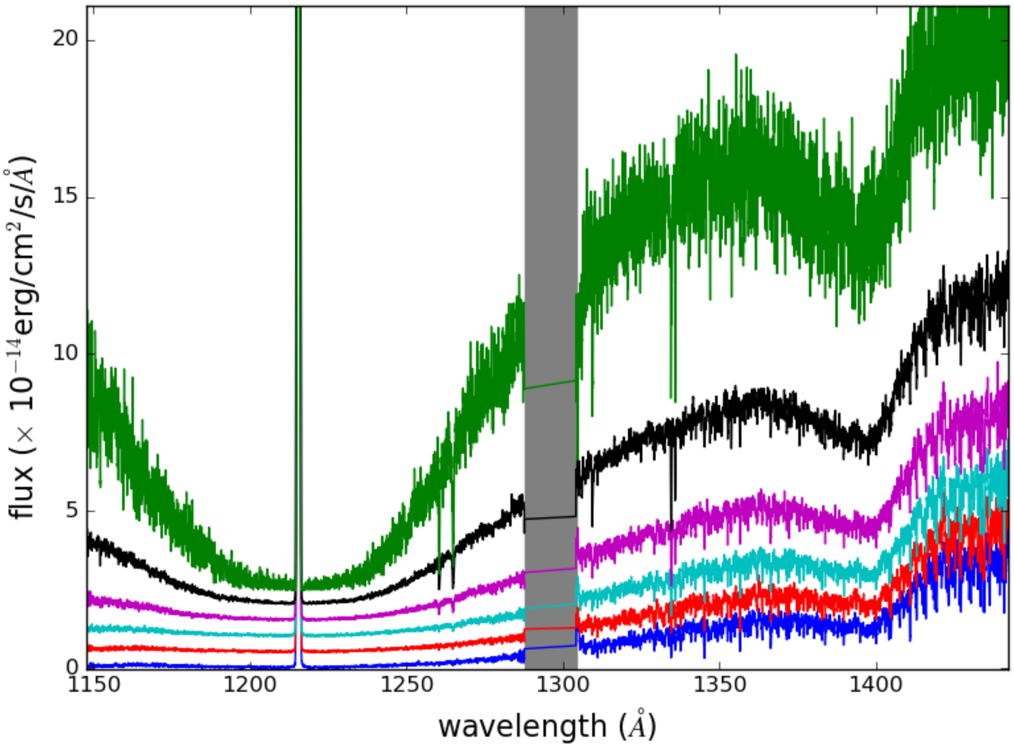

Figure 4.5: Series of spectra extracted from the light curve shown in Figure 4.3. The color represent the spectrum taken from the data points with the same color. The absorption Lyman α clearly broadens from top to bottom, indicating that the spectrum taken with the highest flux level is the hottest. The gray band corresponds to the gap between the detector segments.

and the spectroscopy and photometry average the effects of flux variations produced by the pulsations, therefore using optical photometry as priors, as in the example given for the DA white dwarf WD1919+145 (Section 3.3), needs to be considered carefully. For example, G29-38 was observed as part of the AAVSO Photometric All-Sky Survey (APASS). This survey has been conducted in five filters: Johnson *B* and *V* in addition to Sloan *g*', *r*', and *i*', however the exposure times are either 90 s or 180 s which are shorter than the pulsation periods and therefore they will sample random phases of the pulsations. Therefore, optical magnitudes from single observations can not be used as priors. Regarding the use of the distance as a prior, it can only be considered if the radius is also constrained. However, if the average spectrum is dominated by the flux emitted from the heated areas, indeed these areas can be modelled with hotter white dwarf of a smaller area, and therefore the implied radius will be smaller than the actual radius of the white dwarf (this temperature–radius correlation will be analysed in more detail in Section 4.5.3).

Nevertheless, my first attempt will be to fit the average spectrum and inspect whether the atmospheric parameters from these fits are physically meaningful.

4.5 Spectral fits

For the purpose of measuring the atmospheric parameters of G29-38, our method relies on comparing synthetic spectra with the COS observations. However, as explained in Section 3.1, the computation of synthetic spectra requires as input parameters the effective temperature and the surface gravity in addition to the abundances.

4.5.1 Grid of white dwarf models

A grid of white dwarf models was computed using the KAPPA, ATM and SYN codes (Koester, 2010). I adopted a mixing length of ML2/α=0.8 for the convective atmosphere of G29-38. The grid covers $T_{\rm eff}$=10 000–16 000 K in steps of 100 K and log g=7.5–9.0 in steps of 0.1 dex.

When the temperature of the white dwarf drops to below 16 000 K, the appearance of strong broad absorption features at 1400 Å and 1600 Å are evident in the ultraviolet spectrum. These features are quasimolecular H_2 and H_2^+ absorption lines formed in the stellar atmosphere from radiative collisions of excited atomic hydrogen with unexcited neutral hydrogen atoms. This process causes several absorption lines in the vicinity of Lyman α and β in the ultraviolet. Indeed, the features at 1400 Å and 1600 Å are the satellites of Lyman α (Allard et al., 1994), while the satellites in the red wing of Lyman β are in the 1015–1075 Å region (Allard et al., 1998). The strength of these features depends very strongly on the ionisation of the atmosphere, and thus on $T_{\rm eff}$ and log g (Allard et al., 2004a). Therefore, these lines are included in the models.

Furthermore molecular hydrogen was detected for the first time in the ultraviolet spectroscopy of G29-38 (Xu et al., 2013), which was an unexpected discovery since molecular hydrogen is expected to form in much cooler environments. The absorption features were identified as Lyman band transitions from v''=2,3,4,5 to v'=0 and Werner band transitions v''=2,3 to v'=0 (Abgrall et al., 1993b,a), which were also included in our models. It is worth to note from Figure 4.5 that H_2 are very sharp in the peak spectrum, and the strength of the lines decreases accordingly the flux (temperature) decreases.

Additionally, as explained above, the detailed work on the abundances of G29-38 by Xu et al. (2014) identified the presence of C, N, O, Na, Mg, Al, Si, S, Ca, Ti, Cr, Mn, Fe, and Ni in the optical and the ultraviolet spectroscopy. Therefore the models include these chemical abundances fixed to the values shown in Table 4.1. However, only Si, C, and O are clearly seen in the COS observations.

Finally, the white dwarf models in the grid are convolved with the instrumental resolution of COS/G130M (R=λ/FWHM$\simeq$18000).

4.5.2 Average spectrum

The analysis is performed on a slightly manipulated COS spectrum. The corrections involve the white dwarf radial velocity and eliminate the airglow emission lines. Xu et al. (2013) measured a radial velocity for the white dwarf of 40±4 Km/s using photospheric lines of C I, O I, and Si II identified in the same COS data analysed here, therefore the spectrum is corrected to the rest wavelength using their estimate of the radial velocity. The airglow lines are masked out using the same wavelength ranges as for the light curves represented with grey bands in the top panel in Figure 4.7. The wavelength range considered in the fit is 1132.46–1437 Å.

The model is defined as,

$$F_{\rm obs} = 4\pi\, S \times F_{\rm syn}(T_{\rm eff}, \log g), \tag{4.1}$$

where S is a scaling factor, and $T_{\rm eff}$ and $\log g$ define the white dwarf model from our bilinearly interpolated grid. The MCMC fitting technique (Chapter 3) is used where 100 walkers draw from the posterior distribution defined by equation 3.7. The walkers quickly converge to the best solution before 300 steps. The projection of the samples (Figure 4.6) determines the best values of the parameters, that I will explain one by one.

On one hand, the samples of the effective temperature follow a Gaussian distribution with $T_{\rm eff}$=12359±6 K. The standard deviation is very small, and comprises only the statistical errors derived by the MCMC fitting.

On the other hand, the samples of the surface gravity are not perfectly symmetric, $\log g$=$8.501^{+0.003}_{-0.002}$. However, comparing the median of this distribution against the results of previous studies of G29-38 (Section 4.1.1) makes it the largest measurement, which seems

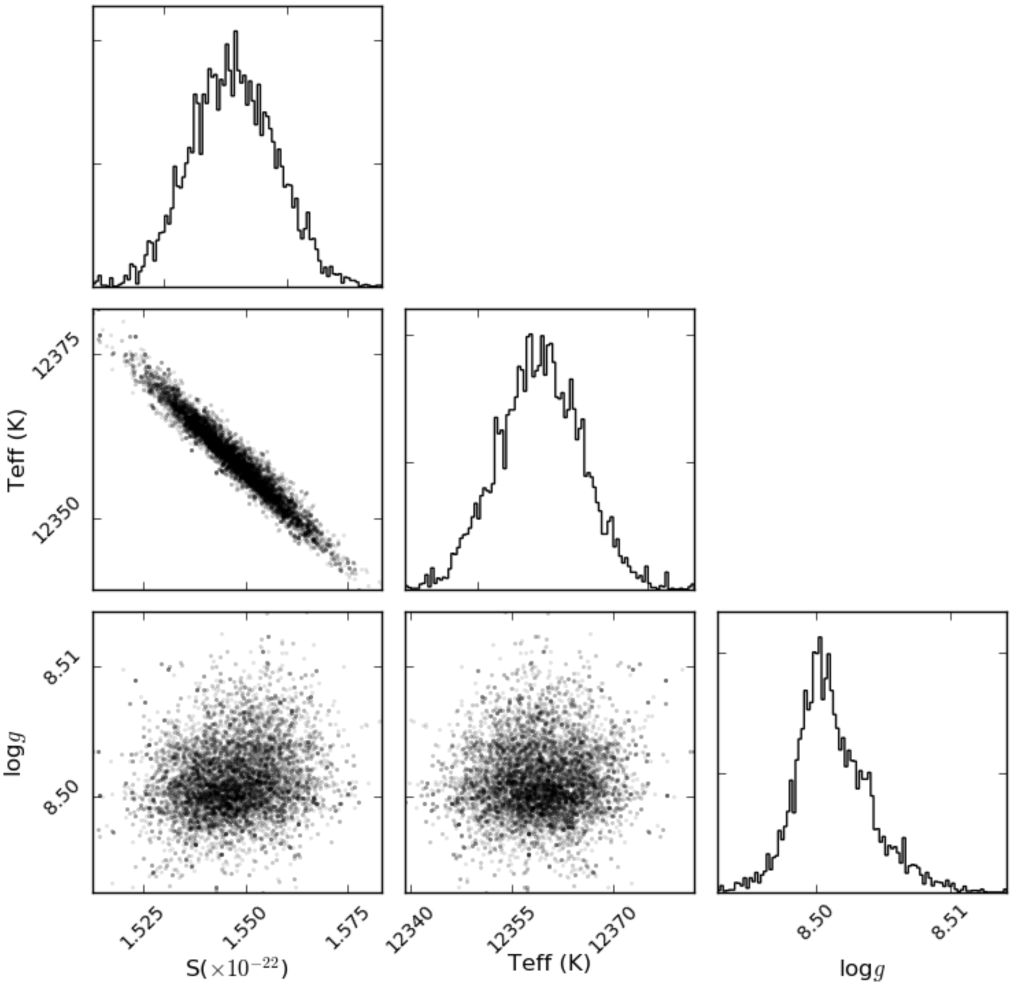

Figure 4.6: Corner plot from the samples of the fit to the average COS spectrum of G29-38.

unlikely.

Finally, the scaling factor is described by a Gaussian $S = 1.55^{+0.02}_{-0.02} \times 10^{-22}$, and shows a correlation with the effective temperature. For completeness, the distance can be inferred from the scaling factor according to the expression:

$$S = \left(\frac{R_{\mathrm{WD}}}{D}\right)^2, \tag{4.2}$$

which can be compared with the parallax distance measurements. Therefore, I make use of the mass–radius relation using T_{eff}=12341 K and log g=8.501 from the fits to derive a white

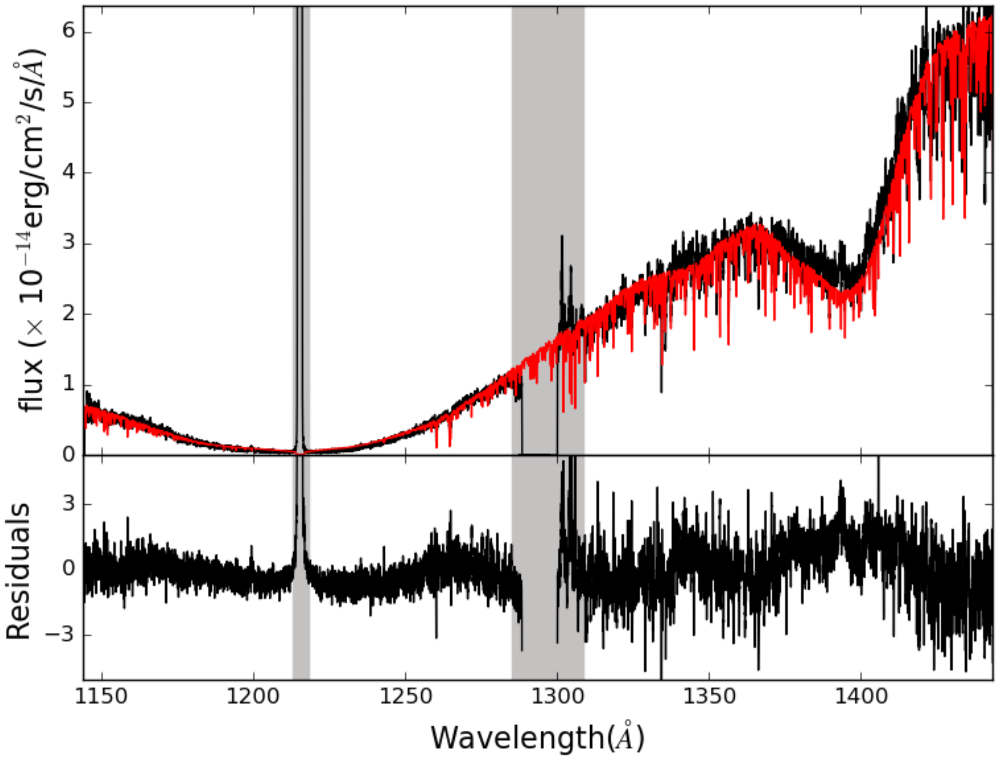

Figure 4.7: Best fit to spectroscopy. The top panel shows G130M/1300 COS spectroscopy (black), where the prominent absorption lines are labelled. The best fit single temperature model ($T_{\rm eff}$=12359±6 K and log g=8.501$^{+0.003}_{-0.002}$). The data within grey bands correspond to Lyman α at 1216 Å O I at 1302 Å airglow lines and the gap between the detectors. The bottom panel shows the residuals of the fit.

dwarf mass of 0.92 $M_\odot$ and a white dwarf radius of 0.0090 $R_\odot$. Finally, this radius and scaling factors in equation 4.2 gives a distance of 16.23 pc, which agrees with the measurements reported in the literature (Subasavage et al., 2017; Gianninas et al., 2011; Holberg et al., 2008). While this suggests that the atmospheric parameters determined from fitting the COS average spectrum provides reliable estimate, the large a surface gravity of 8.5 seems unlikely when compared to previous estimates. Indeed, the effective temperature is also the highest measurement obtained so far, and therefore the solutions lies in the $T_{\rm eff}$–log g valley problem of fitting ultraviolet spectroscopy introduced in Section 3.3.

The best fit is shown in red in the top panel in Figure 4.7, and the residuals of the fit are shown in the bottom panel which illustrates that the quality of the fit is poor. Therefore, I anticipate that the estimate of the atmospheric parameters is not reliable and further analysis is required.

4.5.3 Five spectra

As mentioned above, in a snapshot of the white dwarf while displaying a heated area as shown in (c) in Figure 4.2, the ultraviolet spectroscopy will be largely dominated by the flux emitted from this heated area. Consequently, its spectrum can also be modelled with a hotter white dwarf that appears smaller than the true size. Therefore, there is a inverse relation between the temperature (or flux) and the *apparent* radius. Here, using the five spectra extracted from the light curve (Figure 4.5), I am going to test this hypothesis.

A close inspection to the spectra reveals a drop of flux at wavelength, $\lesssim$1170 Å that is clearly present in the spectra 1, 2, and 3 which are those with the lowest flux (Figure 4.9), while it is not present in the spectra 4 and 5 (Figure 4.10), suggesting that this feature is real and not an artefact from the calibration. The nature of this feature could be a H_2 quasimolecular satellite of Lyman β that has been claimed to be detected in the far ultraviolet spectroscopy of another pulsating white dwarf, G226-29 (Allard et al., 2004b). However, the COS data with G130M/1300 Å set up covers only $\lambda \geq 1150$ Å (Table 2.1), and hence the absence of data towards shorter wavelengths does not allow to draw a robust conclusion about the nature of this drop in flux. Consequently, the region $\lesssim$1170 Å is masked out, together with airglow emission lines and the gap between the detector segments as detailed for the average spectrum in the previous (Section 4.5.2).

The model fit to these five spectra were done in the same way as for the average spectrum, given by equation 4.2. As the ultraviolet data alone is not sensitive to the surface gravity, I fix $\log g$. While the pulsations cause changes in the effective temperature, the geometric distortions are very small that can be neglected, and therefore the surface gravity can be considered constant throughout the full pulsation cycle. In a detailed study of the white dwarf mass distribution, Tremblay et al. (2016) found that the observed mean mass for DA white dwarfs in the range of temperatures within 12 000–16 000 K, which contains the effective temperatures of ZZ Ceti stars, is $0.643 \pm 0.100\,M_{\odot}$ ($\log g \sim 8.05$). Moreover, 6 out of 16 of the measurements of the surface gravity of G29-38 from previous studies are in the range 8.00–8.10 dex (see Figure 4.1). Hence for the purpose of this analysis here the surface gravity will be fixed to 8.05. Therefore, the parameters to be fitted are the effective temperature (T_{eff}) and the scaling factor (S).

The results are shown in Figure 4.8. It is important to note that the y-axis is labelled as *apparent* white dwarf radius, R_{app}. The white dwarf apparent radius is computed from

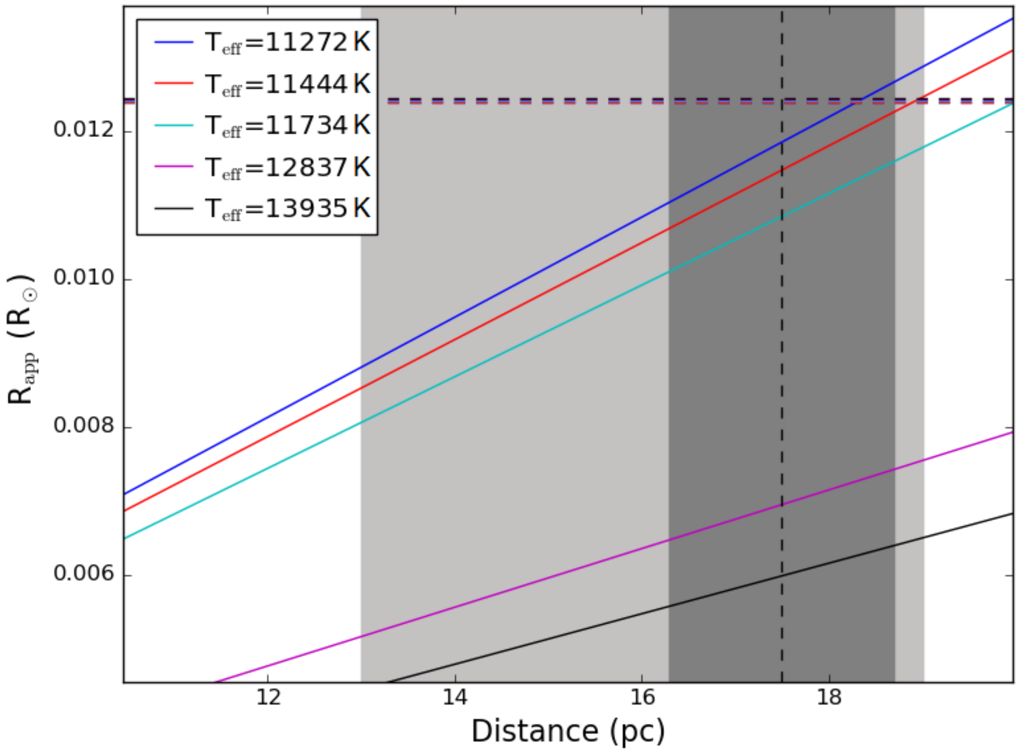

Figure 4.8: Results of the MCMC fits to the five spectra constructed using the data in the coloured bands from in the COS light curve (4.3). From top to bottom: spectrum 1 to spectrum 5. The light grey band encloses all the distances reported in the literature, and the dark grey band is the parallax distance reported by Subasavage et al. (2017). Dashed lines represent the radius estimated from the mass–radius relation for $\log g$=8.05 and $T_{\rm eff}$ listed in the legend.

the scaling factor as function of the distance within the range of the distance measurements reported in the literature (van Altena et al., 1994; Pauli et al., 2006; Holberg et al., 2008; Gianninas et al., 2011; Subasavage et al., 2017). In general, while the temperature increases the radius reduces. Assuming that the latest distance measurement (17.5±1.2 pc, vertical back dashed line) to be the correct, the radius calculated from the coolest (blue) and the hottest (black) spectra are $\simeq$0.012 $R_{\odot}$ and $\simeq$0.006 $R_{\odot}$, respectively, and it is clearly unphysical that the radius reduces half of its size. In fact, I demonstrated the correlation between the dominant surface temperature and the apparent radius, the hotter are the heated areas on the white dwarf surface, the smaller is their area on the white dwarf, resulting in a smaller apparent radius. It can hence be deduced, that due to different temperatures across the white dwarf surface, these spectra can not be modelled using only one white dwarf model of a given temperature, and consequently the quality of the fit decreases for

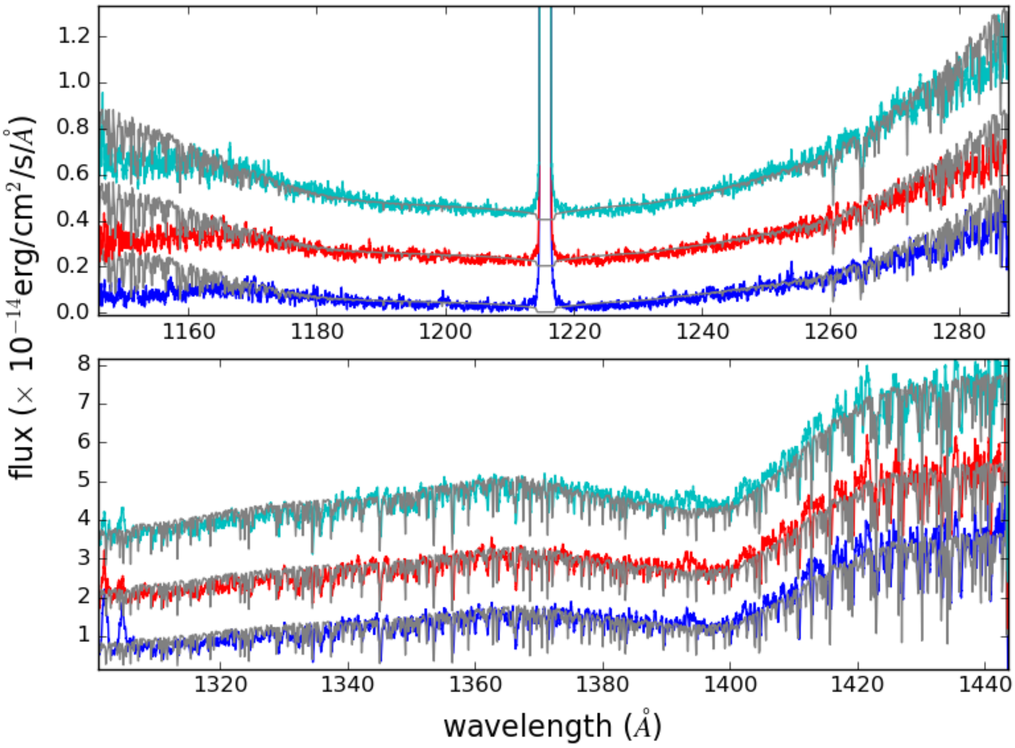

Figure 4.9: Best fits to the spectra 1 (blue), 2 (red) and 3 (cyan) constructed from the data points of the same colour in the light curve (Figure 4.3). An offset has been applied for display purposes.

the spectra with the highest flux, as it can clearly be seen in Figure 4.10. These two spectra (4 and 5) are averaging larger flux variations ($\Delta f > 1 \times 10^{-14}$ erg/cm^2/s/Å) as seen in the height of the coloured band from which these spectra were extracted from the light curve (4.3). Furthermore, calculating the radius using the mass-radius relation for $T_{\rm eff}$ from the fits (horizontal dashed lines), present strong disagreements with the apparent radius, which is indeed as expected.

Qualitatively, the fits to spectra 1 to 3 are better (Figure 4.9). Spectrum 1 (blue) was built using COS data near the lowest flux level. The amplitude of the corresponding flux variations are very small, therefore the flux at which this spectrum was built is roughly constant at a minimum flux of $F_{\rm low} \sim 0.95{\times}10^{-14}$ erg/cm^2/s/Å (blue in Figure 4.3). Therefore this spectrum present the most homogeneous temperature distribution across the visible white dwarf surface as shown in (a) in Figure 4.2 and consequently, its fit can provide a more reliable estimate of the surface gravity. Indeed, this is the coolest spectrum and corresponds to a larger radiating area, which is the only one that matches the radius computed from

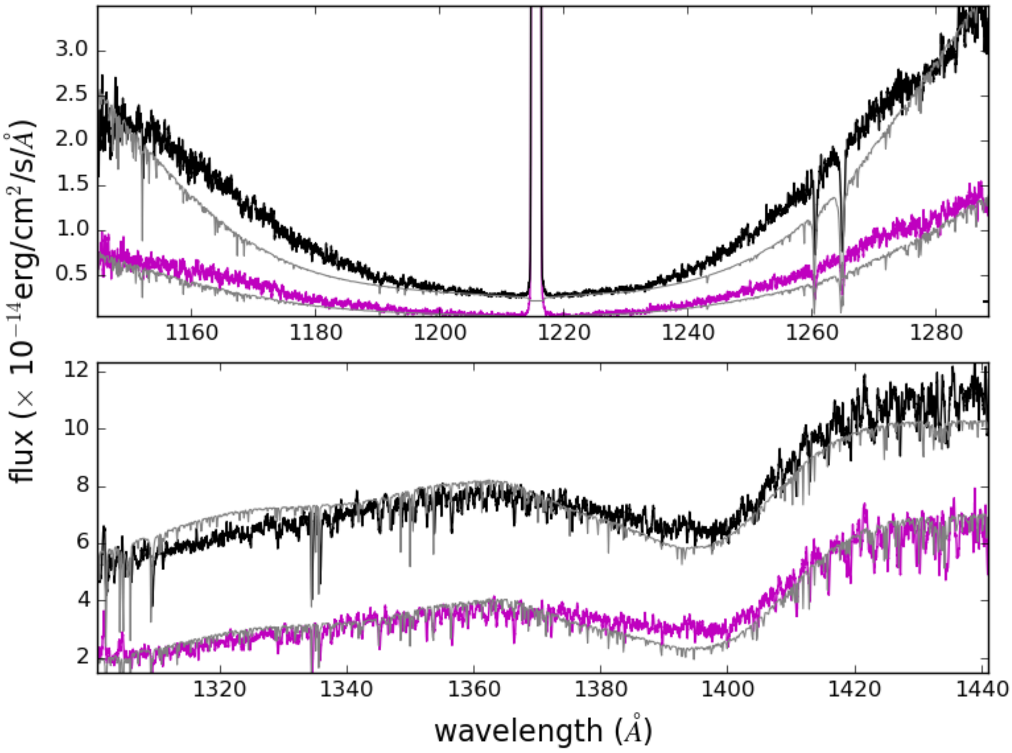

Figure 4.10: Best fits to the spectra 4 (black) and 5 (meagenta), the colour corresponds to the data points of the same colour in the light curve (Figure 4.3). The best fits are overplotted in grey. An offset has been applied for display purposes.

the mass radius-relation within the most reliable distance measurement (dark grey band in Figure 4.8), suggesting that the surface gravity that will be determined below is not too far from the value of 8.05 dex assumed here.

4.6 Surface gravity of G29-38 from the lowest flux spectrum 1

As discussed above, previous studies have failed to constrain the atmospheric parameters, and while the disagreements found in the effective temperature measurements could be caused by the pulsations, the surface gravity should be better constrained since the pulsations have a negligible effect on it. However, as shown in Section 4.5.3 and 4.5.2, fitting the average spectrum and short exposures affected by pulses results in unreliable values for the surface gravity. Therefore, the first step will be to constrain the surface gravity from spectral fits. As explained in Section 3.3, one complication of fitting only ultraviolet spectroscopy is the $T_{\rm eff}$-log g valley of solutions, and better constrained results can be obtained if additional constraints are included. Therefore, besides including the distance (17.5±1.2 pc, Subasavage et al. 2017) as a prior in the fits, optical magnitudes will also be included. However, the latter suffer same effects of variability due to the non-radial pulsations. As, for the reasons explained above, the lowest flux spectrum 1 will be fitted, therefore the optical magnitudes have to be measured at the lowest optical flux as well.

Hence, G29-38 was observed with the high-speed ULTRACAM (Dhillon et al., 2007) mounted on the 3.6m NTT at La Silla on November 19, 2017, UT 00:27:30 - 03:08:14, with the u', g', r' filters. The exposure time in u' was 0.45 seconds while in g' and r' bands was 0.225 seconds. A total of 42904 images were taken (Figure 4.11). The u', g', r' shows amplitudes up to ~ 0.1 mags. The u' band filter used in these observations was a non-standard one and presents complications in the calibration, therefore the u'-band data will not be used in the fit. The 2000 lowest data points are taken from the ULTRACAM photometry (black dots in Figure 4.11) to calculate the magnitudes of g'=13.0350±0.0056, and r'=13.1853±0.0056. The errors are the standard deviations of the mean, and do not include systematic errors in the calibration.

In summary, the lowest flux spectrum 1 is fitted using MCMC where the distance and the g' and r' magnitudes are included.

As I want to measure the surface gravity in addition to the effective temperature, the data is fitted with a new model defined as:

$$F_{\text{obs}} = 4\pi \left(\frac{R_{\text{WD}}}{D} \right)^2 \times F_{\text{mod}}(T_{\text{eff}}, \log g). \tag{4.3}$$

The spectrum is fitted in the range 1175–1437 Å to exclude the feature at ~1150 Å discussed previously. Additionally the airglow emission lines are masked out.

The resulting corner plot is shown in Figure 4.12. All the parameters follow a normal distributions: D=17.7 ±0.2 pc, R_{WD}=0.0130±0.0002 $R_{\odot}$, T_{eff}=11 150±10 K, and $\log g$=7.99±0.02 dex. Using the mass-radius relation, the mass and radius of the white dwarf are M_{WD}=0.60 $M_{\odot}$ and R_{WD}=0.0130 $R_{\odot}$, which agree very well with the parameters from the fit. Also the distance agrees very well with the parallax estimate (Subasavage et al., 2017). The best fit is shown in red in Figure 4.13. The quality of the fit has improved considerable in comparison to the average spectrum fit. The bottom panel shows that the ULTRACAM magnitudes and the synthetic magnitudes, g'=13.0507 and r'=13.1843, are consistent.

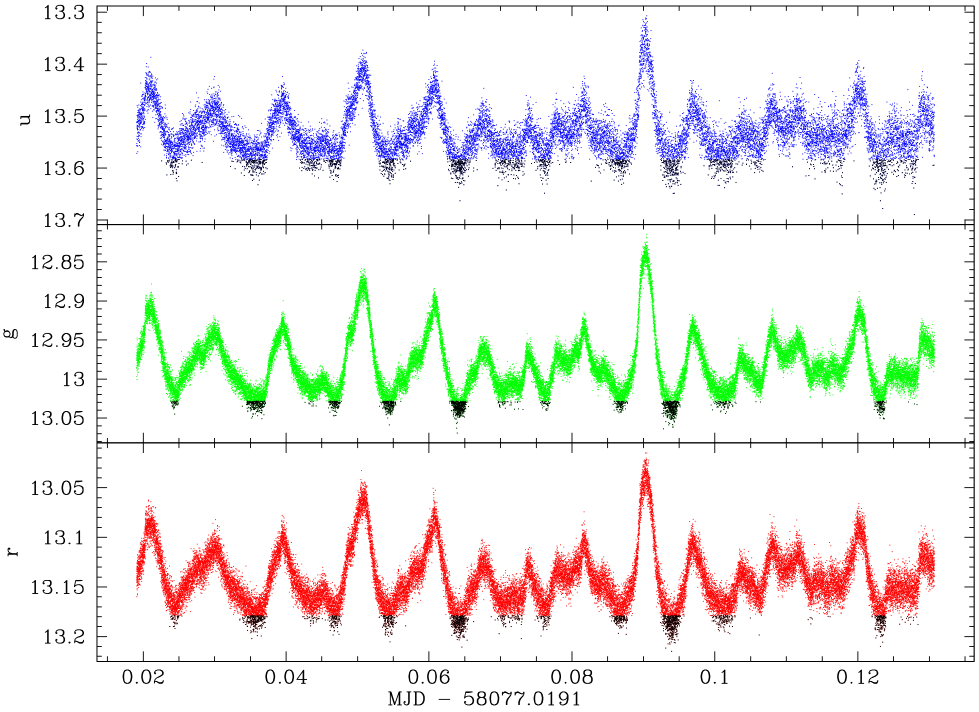

Figure 4.11: ULTRACAM photometry of G29-38 taken in November 2017.

In summary, the effective temperature and surface gravity are T_{eff}=11 150±10 K, and log g=7.99±0.02 dex, respectively. Regarding the effective temperature, this is the coolest measurement and therefore it might represent the closest measurement of the underlying white dwarf (assuming the white dwarf does not drive pulsations). But more importantly, the surface gravity of the white dwarf has robustly been constrained to 7.99±0.02 dex. Hence, the surface gravity will be fixed in the following fits which aim to measure the chemical abundances in G29-38.

4.7 Chemical abundances

Xu et al. (2014) determined photospheric abundances for eight elements, and upper limits for an additional six (Table 4.1) using the same COS spectroscopy analysed here as well as additional optical spectroscopy. The abundances for magnesium, sodium, aluminium, calcium, titanium, chromium, and manganese were measured from their optical spectroscopy. Regarding iron, the major constraints comes from optical spectroscopy, because there are

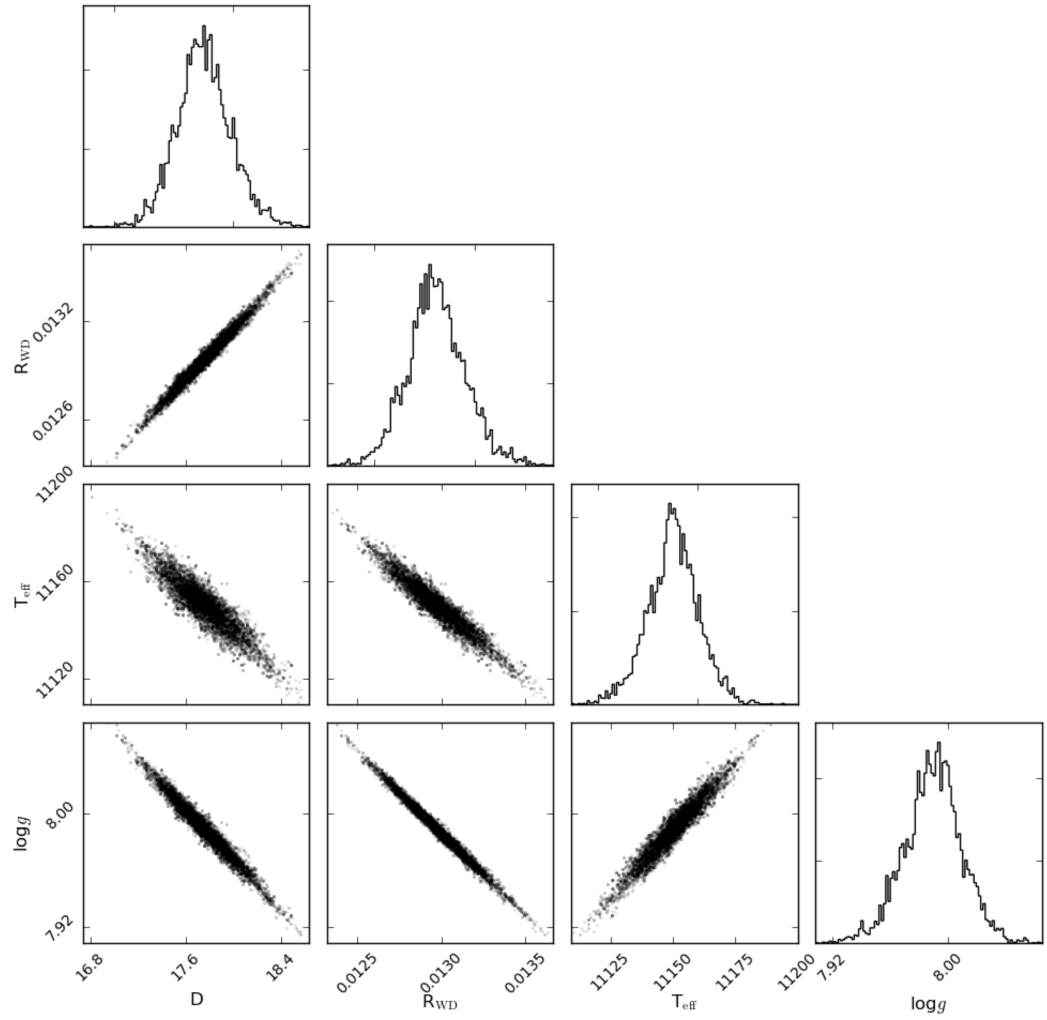

Figure 4.12: Corner plot from fitting the lowest flux COS spectrum (blue in Figure 4.3) of G29-38. .

no strong features in the ultraviolet. From the COS data, they obtained upper limits for nitrogen, sulphur, and nickel. These measurements were based on only one line of each element which were not strong enough to provide an accurate abundance determination: N I at 1411.9 Å, S I at 1425.03 Å, and Ni II at 1335.2 Å (Figure 4.14). Therefore, the only elements for which the ultraviolet spectroscopy can provide reliable estimates are carbon, oxygen, and silicon. The COS average spectrum shows clear features of C I at 1329.6 Å, and 1277.6 Å, C II at 1335.7 Å, O I at 1152.2 Å, and Si II at 1260,1265 Åand 1309.3 Å.

The goal of the analysis carried out here is to test if the accreted metals are homo-

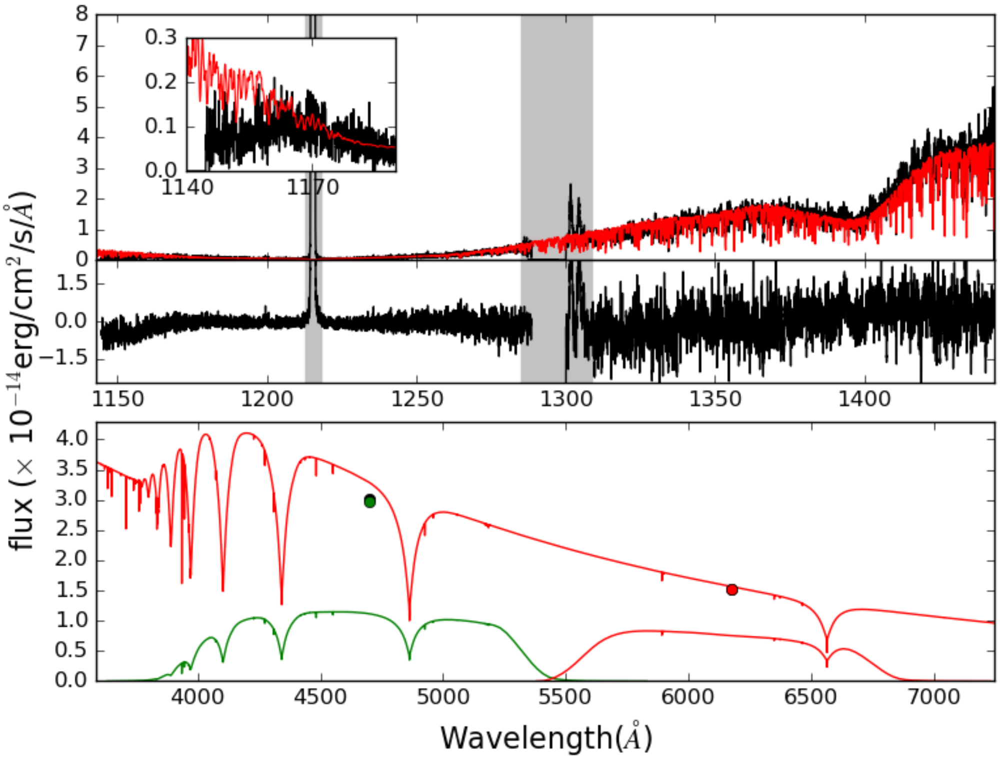

Figure 4.13: Same as Figure 4.7 but the spectrum 1 was constructed using the time segments indicated by the blue data points in the light curve shown in Figure 4.3. The red curves show the best model to spectrum 1, including the g' and r' photometry corresponding to flux minimum and the parallax distance of 17.5±1.2 pc from Subasavage et al. (2017) . The residuals shows that the fit is good, with the exception the blue end of the spectrum, which is zoomed in the box inserted in the plot. This feature might be a quasimolecular H_2 the satellite of Lyman β. The bottom panel shows the ULTRACAM photometric measurements corresponding to the minimum flux level in the optical light curve (black dots, Figure 4.11) which are very well reproduced by the g' and r' sythetic magnitudes computed for the g' (red) and r' (green) bands.

geneously distributed across the white dwarf surface. The heating caused by the pulsations provides the opportunity to measure the abundances in a localised region on the white dwarf surface, since the flux emitted from this hot spot dominates the COS spectrum. The times at which the hot spots come into view correspond to the peaks of the light curve (Figure 4.3). As the power spectrum of the light curve shows the shortest significant period at ~203 s (Section 4.4), averaging the spectroscopy during one of these peaks (with an integration time less than 200 s), results in a spectroscopic snapshot of the white dwarf while having heated region(s) on the visible hemisphere as shown in (c) in Figure 4.2. The first *HST* orbit shows a very large amplitude pulse, from which I built the highest count rate peak spectrum (green

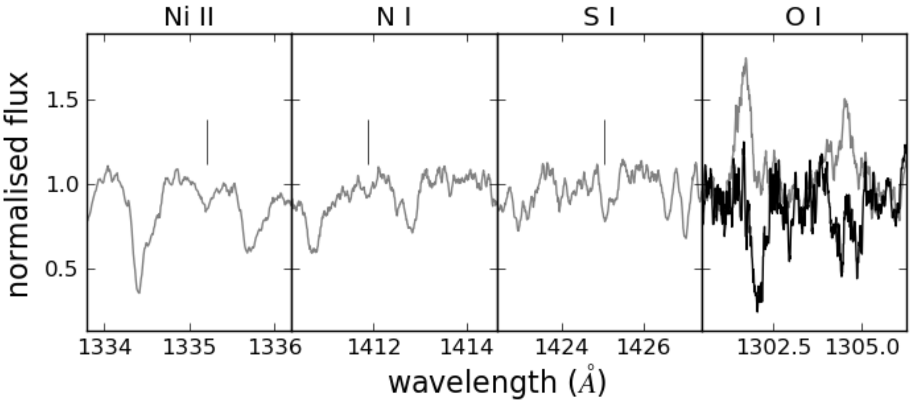

Figure 4.14: Ultraviolet abundance of nitrogen, nickel, and sulphur for G29-38, which present only one spectral line in the COS wavelength coverage of the observarions. These features are too weak to provide reliable abundance measurements. The rightmost panel shows the region of O I, which is contaminated with geocoronal airglow emission (grey), though after extracting the night side data the features becomes clear.

dots in Figure 4.3), which spans ≃100 s. The large amplitude (> $9{\times}10^{-14}$ erg/cm^2/s/Å) and short duration of this pulse in comparison with the other peaks observed in the later *HST* orbits suggests that it corresponds to the superposition of two (or more) pulses of different modes and I will use this spectrum to estimate the abundances in a localised region on the white dwarf region.

In contrast, the lowest count rate spectrum (spectrum 1) from the COS spectroscopy offers the best situation in which the temperature distribution across the white dwarf surface can be assumed to be nearly homogeneous, such as illustrated in (a) in Figure 4.2. Thus, the radius G29-38 estimate from this spectrum represents the closest estimate of the true value. Fitting this spectrum provides, therefore a realistic estimate of the average abundance values across the white dwarf surface.

In the case that the abundances are uniformly distributed, the measurements from both spectra, peak and minimum, should match. The next steps will therefore be to measure the abundances of carbon, silicon, and oxygen in these two spectra. Indeed, the spectral line Si II at 1260 Å, is very suitable for this approach, since the strength of the line increase with increasing the effective temperature.

4.7.1 Average abundances on the white dwarf

As explained in Section 3.1, the computation of synthetic spectra which model the atmosphere of G29-38 to measure the average chemical abundances requires knowledge of the surface gravity and the effective temperature. The main element in the atmosphere of G29-38 is H, and the small contribution of metals will not affect the general structure of the model atmosphere. Therefore, the main parameters to compute the structure of the white dwarf atmosphere are the surface gravity, and the effective temperature, adopting pure H composition (using KAPPA and ATM). Using this same structure, the metals abundances can be added to compute the emergent synthetic spectrum (using SYN) and the value of the individual abundances for each element can be varied until the model matches the spectroscopy.

The lowest flux spectrum used to determine the surface gravity (spectrum 1) accomplished the purpose to determine the surface gravity (and effective temperature), since both parameters are defined by the shape of the Lyman α absorption at 1216 Å. However, to measure the abundances it is crucial to fit a spectrum with a reasonable signal-to-noise ratio, where the spectral lines are clearly detected. Thus, the two lowest count rate spectra (spectra 1 and 2) are combined into one spectrum, henceforth *minimum* spectrum. Because of the addition of a bit more flux it is likely that the temperature of the minimum spectrum increases with respect to $T_{\rm eff}$=11150±10 K obtained from spectrum 1. The strength of the spectral lines is a strong function of the effective temperature, therefore it is important to obtain the effective temperature that best describe the minimum spectrum.

As the surface gravity was measured to be $\log g$=7.99±0.02 dex (Section 4.6), therefore there is no need to have the radius as a free parameter, and the simpler model in equation 4.2 can be used. To find the effective temperature, the minimum spectrum is fitted following same procedure as used for the average spectrum (Section 4.5.2). It is found that the best parameters follow Gaussian distributions described by $T_{\rm eff}$=11311±7 K and S=2.91±0.03, for the effective temperature and the scaling factor, respectively. As expected, the effective temperature is slightly hotter (+150 K) than the one measured from the lowest flux spectrum (1) used to determine the surface gravity.

As mentioned above, once the structure of the atmosphere model that best describes the minimum spectrum is known, the metal abundances are allowed to vary. Strong features of oxygen, silicon and carbon are clearly visible in the minimum spectrum, however some of their spectral lines are contaminated with interstellar absorption and airglow emission lines.

Interstellar absorption contaminates some absorption features of carbon and silicon.

In case of carbon, the C II 1335.7 transition has larger statistical weight than C II 1334.5, and hence the former should be stronger in the photosphere of G29-38[2]. However, the COS data show the contrary, indicating the additional contribution of of interstellar absorption. In addition, C II 1334.5 Å is contaminated by H_2. Another spectral feature that suffers from interstellar contamination is Si II 1260.4 Å. Therefore these lines will be excluded from the fits, but they will be used for visual inspection, once the abundances have been measured.

The geocoronal airglow emission line of O I at 1302.2,1304.9 Å contaminates several lines of oxygen in this wavelength region. Extracting the night side of the entire COS observations, as explained in Section 2.3.4, and averaging into one spectrum, features of oxygen and silicon are clearly present (rightmost panel in Figure 4.14). The bluest absorption line corresponds to O I 1302.2 Å which can have some additional contribution from interstellar absorption. The next two strongest and very close features are Si II 1304.4 Å and O I 1304.9 Å, however performing further cuts on the data to obtain the minimum spectrum free of O I airglow contamination, results in a very low signal-to-noise ratio and therefore these oxygen features are discarded from the fit. In addition, O I at 1152.2 Å falls in the region where the flux declines in the minimum spectrum. This drop in flux is probably related to a quasimolecular H_2 satellite (Section 4.5.3) that is not well reporduced by the model, which combined with the low flux in this region prevents the opportunity to fit the O I 1152.2 Å line. Hence, the oxygen abundance can not be accurately measured from the minimum spectrum.

In summary, it results that the only spectral features that can be fitted are carbon and silicon. For this purpose, two subgrids of white dwarf models are computed, where $T_{\rm eff}$ and $\log g$ are fixed to 7.99 dex and 11 311 K, respectively. The first grid is computed accounting just for carbon as an additional constituent, and the second grid considers only silicon. The grids span $\log[\mathrm{Z/H}] = -4.5$ to -8.5 with steps of 0.1, where Z stands for carbon or silicon.

The minimum spectrum is fitted independently for each element. First, the regions were the spectral lines of C I 1277.6 Å, C I 1329.6 are located are fitted and then the region of the Si II 1265.0 doublet is fitted. The results are listed in Table 4.4 and shown as red lines in the top panels of Figure 4.15. The vertical lines at the top indicate the positions of the features that are included (red) or not included (black) in the fit to account for contamination by interstellar absorption. A model that includes the contribution of molecular hydrogen is overplotted in blue, which fails to fully reproduce the minimum spectrum,

---

[2] C II 1334.5 is a ground state transition, therefore it is very strong in the interstellar medium. C II 1335.7 Å arises from a state 0.008 eV above the ground state, which is less populated in the interstellar medium.

Table 4.4: Atmospheric abundances of silicon and carbon for G29-38.

	Xu et al. (2014)	minimum spectrum	peak spectrum
C	-6.90 ±0.12	-7.07±0.08	-7.05±0.2
Si	-5.60 ±0.17	-6.40 ±0.3	-5.98±0.1

showing additional H_2 features that are not present in the data. The most likely explanation for this discrepancy is the insufficient molecular data for H_2, appropriate for the conditions encountered in the atmosphere of G29-38. However, with the exception of C I 1277.25 Å and C II 1334.5 Å, molecular hydrogen does not contaminate any other carbon and silicon lines.

As seen in the top panel in Figure 4.15 the two spectral lines of carbon considered in the fit may seem not sufficiently strong in the red lines. but the estimate of $\log[\mathrm{C/H}] = 7.07 \pm 0.08$ does not overestimate the strength of the C II lines contaminated with interstellar absorption and $\mathrm{H_2}$lines (blue lines). Therefore this estimate can be considered as an upper limit of the carbon abundance. Regarding to silicon, the features are stronger than those of carbon. Si II 1260 is blended with the interstellar absorption line, which can be seen as second component in the blue wing of the line, however the abundance of $\log[\mathrm{Si/H}] = -6.40 \pm 0.3$ fits very well the red component of the doublet, confirming the robustness of the fit.

4.7.2 Abundances in a heated spot

To determine the abundances in a heated spot on the white dwarf, the peak spectrum (green in Figure 4.5) is fitted, following the same procedure as for the minimum spectrum, i.e. fixing $\log g$=7.99. The best parameters of the MCMC chain correspond to T_{eff}=14 676±18 K, and $S = 1.01 \pm 0.01$. Using the scaling factors obtained from the minimum and peak spectra, it is found that this hot spot covers less than ~34 per cent of the visible white dwarf surface.

The carbon lines at 1277.60 Å and 1329.60 Å, which were used to fit the minimum spectrum, are very weak, almost absent (bottom panel Figure 4.15). Instead, the lines of C II 1334.5,1335.7 Å are used, since it can be seen that C II 1335.7 Å is stronger than C II 1334.5 Å, which is expected if interstellar absorption is weak. However, these carbon lines show clearly contribution of interstellar absorption lines in the minimum spectrum, therefore the contribution to the total absorption in the peak spectrum seems to be smaller. In contrast, the silicon lines at 1264.7,1265.0 Å are even stronger than for the minimum spectrum, and can provide a reliable measurement in the fits.

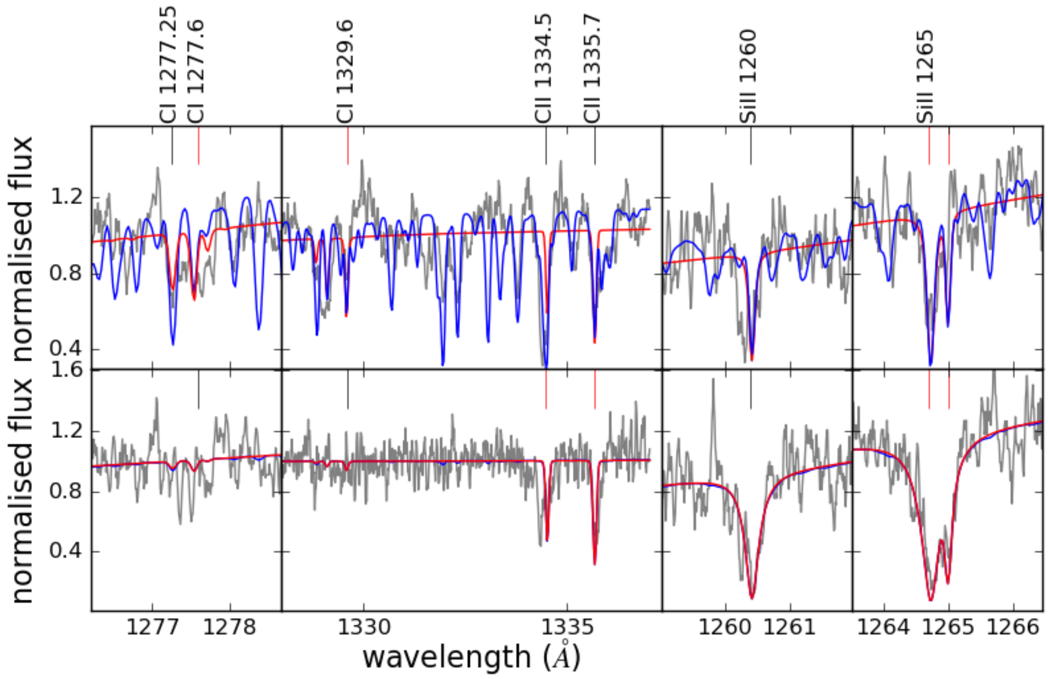

Figure 4.15: Best fit for carbon and silicon to the minimum spectrum (top) and peak spectrum (bottom). The blue and red lines represent the fit with and without contribution of molecular hydrogen, respectively. The vertical lines on the top show the features that were considered (red) or not considered (black) due to contamination of interstellar absorption lines.

Therefore, two new subgrids were computed, one for silicon, and one for carbon, where the surface gravity and effective temperature were fixed to T_{eff}=14676 K and log g=7.99, respectively. I then proceeded to fit the peak spectrum independently using the regions where the carbon and silicon lines lie as described above. The results are listed in Table 4.4 and shown in red in the bottom panel in Figure 4.15. In addition, the model including molecular hydrogen in overplotted in blue, which shows an almost negligible contribution of H_2 features. The carbon abundance of $\log[\mathrm{C/H}] = -7.05 \pm 0.2$ reproduces well the fitted features, moreover from inspection of C I at 1277.25 Å, 1277.60 Å, and 1329.6 Å it can be deduced that the abundance can not be larger than this value. This measurement is in good agreement with the abundance estimated from the minimum spectrum. The silicon abundance is found to be $\log[\mathrm{C/H}] = -5.98 \pm 0.1$, which reproduces very well the fitted lines, as well as the Si II 1260 Å feature. Although this measurement hints to a higher abundance, it is still in agreement, within the uncertainties, with the abundance determined from the minimum spectrum.

These results favour a homogeneous distribution of the metals across the white dwarf surface. However, this study is based on only two elements, one of which (carbon) does not provide reliable estimates, due to the low signal-to-noise ratio of its spectral lines. While the fits to the silicon features tentatively suggest some variation in the silicon abundances it is too early to draw a definite conclusion on the distribution of the metals across the surface of G29-38.

4.8 Conclusions

Here I have presented the analysis of archival COS time-tagged data of G29-38. A long record of studies have been performed to estimate the atmospheric parameters of G29-38, but present strong disagreements among them. Using a new method which fits the COS spectroscopy simultaneously with g' r' optical photometry and the most recent distance, I found that the surface gravity can finally be constrained to $\log g$=7.99±0.02.

A previous analysis of this ultraviolet spectroscopy found the presence of molecular hydrogen, which is not expected to be found in the atmospheric conditions of G29-38 (Xu et al., 2013). Here, I found that the presence of molecular hydrogen is strongly dependent of the effective temperature, and at temperatures at high as ∼ 14 500 K the molecules dissociate.

The study performed by (Xu et al., 2014) on this same COS data provided the first detailed measurements of the metals on the white dwarf G29-38, but this study made used of the average spectrum. Here, the analysis of this archival COS data of G29-38 shows the potential of time tagged ultraviolet spectroscopy to test the distribution of the chemical abundances across the white dwarf surface. The ZZ Ceti G29-38 presents large variations of flux (up to a factor of ten) due to non-radial pulsations. During the first orbit, the white dwarf presented a dramatic brightening, which can be explained by the superposition of two or more pulses overlapping on the same area on the white dwarf surface. This region covers a fraction of less than ∼35% of the white dwarf surface and heats up increasing the observed flux in the ultraviolet. Therefore, there is a steep temperature gradient between this hot spot ($T_{\rm eff}$∼14 676 K) and the overall unheated areas ($T_{\rm eff}$∼11 311 K). The carbon and silicon abundances in this region are -7.05±0.2 and -5.98±0.1, respectively, while and average of these abundances across the white dwarf surface corresponds to -7.07±0.08 and -6.40±0.3 for carbon and silicon, respectively. It suggests that the distribution of the abundances is uniform, however, in contrary to silicon, the carbon lines can not provide strong constraints, and this study can not be conclusive based in only one silicon line. While I demonstrated the potential of this method, this study should be repeated with higher signal-to-noise ratio data, and spanning a wider wavelength range that includes transitions of additional elements.

Chapter 5

GW Librae: a cataclysmic variable with a pulsating white dwarf

5.1 Introduction

A handful of quiescent dwarf novae show photometric variability at periods in the range 100−1900 s, consistent with non-radial g-mode pulsations on the white dwarf (Mukadam et al., 2006). These accreting pulsating white dwarfs have H-dominated atmospheres, but are generally too hot to fall within the instability strip of isolated white dwarfs (Szkody et al., 2010a), which empirically extends from ≃11 100−12 600 K for ZZ Ceti stars (Gianninas et al., 2011). However, ongoing accretion from a low-mass companion may result in an enhanced helium abundance, which can drive oscillations at higher temperatures, 15 000−20 000 K, as a result of a subsurface He II partial ionization zone (Arras et al., 2006; Van Grootel et al., 2015). Isolated white dwarfs cool white radiate away the flux generated by the hot carbon-oxygen core. In case of an accreting white dwarf, it inherits the composition of the companion. The accretion generates a compressional heating luminosity (i.e. internal gravitational energy release, Townsley & Bildsten 2002) at the base of the envelope which defines the equilibrium temperature of the carbon-oxygen core over time scales of Gigayears. Therefore, the temperature profile differs from isolated white dwarfs, because the flux is generated at the base of the envelope and not in the core.

Non-radial pulsations in accreting white dwarfs are potentially useful to learn about their internal structure using asteroseismic techniques. In particular, CV white dwarfs are heated during outbursts (e.g. Godon & Sion, 2003; Piro et al., 2005), and subsequently cool back to their quiescent temperature. As a result, accreting white dwarf pulsators can evolve through the instability strip in a few years, *much* faster than their isolated counterparts, which cool through the strip on evolutionary time scales of $5-10\times10^{8}$ yr. Just as with isolated white dwarfs, it is expected that as an accreting white dwarf cools, its convection zone deepens, driving longer-period pulsations (Brickhill, 1991; Mukadam et al., 2006).

GW Librae (GW Lib) is the prototypical dwarf nova that exhibits non-radial pulsations in quiescence (van Zyl et al., 2000). These authors reported optical pulsation periods near 650, 370, and 230 s that, with the exception of the 230 s mode, remained fairly constant for years after discovery (van Zyl et al., 2004). Follow-up *HST* ultraviolet observations confirmed the pulsation origin of this optical variability: the Fourier transform of the ultraviolet light curve shows periodic signals at 646, 376, and 237 s, but with amplitudes roughly 10 times higher than in the optical (Szkody et al., 2002). Such a wavelength-dependent amplitude is expected because the ultraviolet lies in the exponential Wien tail of the spectral energy distribution, where the flux is more sensitive to changes in the temperature than at optical wavelengths (Robinson et al., 1995). Additionally the amplitude depends also on the wavelength-dependent limb darkening. Towards optical wavelengths the limb darkening decreases, increasing the geometric cancellation effects, therefore the amplitudes are highly reduced (Robinson et al., 1995).

GW Lib underwent a large-amplitude outburst in 2007 April which took its magnitude from $V \simeq 17$ mag (Thorstensen et al., 2002a) to $V \simeq 8$ mag (Templeton et al., 2007). The stable pulsation signals reported by van Zyl et al. (2000) were immediately swamped by the light from the accretion disk and an orbital superhump near 80 min became the dominant variability in the optical light curve (Kato et al., 2008; Bullock et al., 2011). To date, several prominent signals have recurrently shown up (Copperwheat et al., 2009; Schwieterman et al., 2010; Bullock et al., 2011; Vican et al., 2011; Szkody et al., 2012). Except for a signal near 290−300 s, all other signals have relatively long periods (∼19 min, ∼ 2 h, and ∼4 h).

A 296 s periodicity was first detected on 21th Jun 2008 in optical photometry obtained with the high speed ULTRACAM photometer (Copperwheat et al., 2009). *HST* ultraviolet observations in 2010 revealed multiple closely spaced periodicities, but with the highest peak at 292 s. The signal was also detected in 2011 with *HST* near 293 s, with an amplitude more than twice as large as in 2010 (Szkody et al., 2012). If this signal is the return of the ∼237 s period after outburst, it demonstrates the unique opportunity that dwarf nova outbursts offer to study the evolution of the pulsation spectrum as a function of white dwarf cooling.

The ≃19 min signal was first detected from mid-March to July in 2008 in the optical

(Copperwheat et al., 2009; Schwieterman et al., 2010; Vican et al., 2011; Bullock et al., 2011), returning in May 2012 (Chote & Sullivan, 2016). Although its origin was associated with an instability in the accretion disc (Vican et al., 2011) another possibility is that it could be a different pulsation mode driven by the white dwarf (Chote & Sullivan, 2016).

The $\simeq$2 h signal has been detected prior- and post-outburst. It was first seen in May 2001 in the optical by Woudt & Warner (2002). In May 2005, it was identified in optical data by Copperwheat et al. (2009) and again in August by Hilton et al. (2007). Also it was reported in post outburst optical data in 2008 (Vican et al., 2011), confirming it to be a recurrent feature, though not always present in photometric observations.

The $\simeq$4 h variability has been observed at optical and ultraviolet wavelengths (Schwieterman et al., 2010; Bullock et al., 2011; Vican et al., 2011). Bullock et al. (2011) obtained ultraviolet (GALEX FUV and NUV) and ground-based optical photometry over a period of three years following the 2007 outburst. In their ultraviolet observations, a $\simeq$4 h variability made its first apparition in 2008, increasing in amplitude during the following two years. In the optical, the variability was intermittently detected in 2009. Vican et al. (2011) performed an intensive ground based campaign of time series photometry covering the 2007 outburst, as well as two different years after the outburst, 2008 and 2010. They showed that, in fact, the $\simeq$4 h variability was present in 2008, and became stronger in 2010. In addition, Schwieterman et al. (2010) also reported a $\simeq$4 h signal detected in their photometric data taken in 2008. The three groups agree that this is a recurrent signal that wanders in phase and amplitude on time scales of days and occasionally disappears. These detailed photometric studies presented in those papers suggest that the detected $\simeq$4 h periodicity is, in fact, the fundamental of the $\simeq$2 h signal, that was repeatedly detected earlier.

Here, observations of GW Lib are presented. They were performed with *HST*/COS on 2013 May 30. In Section 5.2, I describe the observations and the light curve analysis, revealing the presence of a large amplitude variability with period similar to the $\simeq$4 h signal detected previously, which I discussed above. In Section 5.3, I outline the spectral fitting procedure I performed to determine atmospheric parameters, emphasizing the use of the MCMC method. I discuss the results in Section 5.4, and summarise our conclusions in Section 5.5. Finally, in Section 7 I am appending the preliminary analysis of the *K2* observations.

Table 5.1: Log of all *HST* observations of GW Lib taken in time-tag mode and using the G140L gratings. The central wavelength was set to 1425 Å and 1105 Å for the STIS and COS observations, respectively.

instrument	orbit	date	UT Time	Exp. Time (s)
STIS	1	2002-01-17	01:52:00	2105
STIS	2	2002-01-17	03:14:04	2603
STIS	3	2002-01-17	04:50:15	2603
STIS	4	2002-01-17	06:26:25	2580
COS	5	2010-03-11	10:16:45	2906
COS	1	2011-04-09	14:07:50	2128
COS	2	2011-04-09	15:43:41	2971
COS	1	2013-05-30	11:41:59	2182
COS	2	2013-05-30	13:11:34	1746
COS	2	2013-05-30	13:42:25	876
COS	3	2013-05-30	14:47:15	864
COS	3	2013-05-30	15:03:34	1748

5.2 Observations

5.2.1 Ultraviolet spectroscopy

GW Lib was observed as part of a far-ultraviolet COS survey to determine the mass and temperature distribution of accreting white dwarfs (Cycle 20 programme 12870). A total of 123.6 min of time-tagged spectroscopy of GW Lib was obtained on 2013 May 30 over three consecutive orbits using the G140L gratings, which covers the wavelength range 1150 − 1800 Å with roughly 0.75 Å resolution (red line in Fig. 5.1).

Additionally, I retrieved from the *MAST* archive all STIS and COS ultraviolet data taken with the G140L grating, and using the time-tag mode: four STIS orbits taken prior to the 2007 outburst (for more details see Szkody et al. 2002), and a total of three COS orbits post-outburst data (see Szkody et al. 2012). Table 6.1 summarizes the observations and the time-averaged spectrum of each observation is shown in Fig. 5.1.

The time-averaged spectrum of each epoch is dominated by the white dwarf. However, it is clear that there is some flux contribution from an additional continuum component since the core of Lyman α does not reach zero. This second component seems to be flat and without significant features. Such a flux component has been identified in *HST* observations of many other dwarf novae (e.g. VW Hyi, Godon et al. 2004; Long et al. 2009; VY Aqr & WX Ceti, Sion et al. 2003; SW UMa & BC UMa, Gänsicke et al. 2005). In the case of

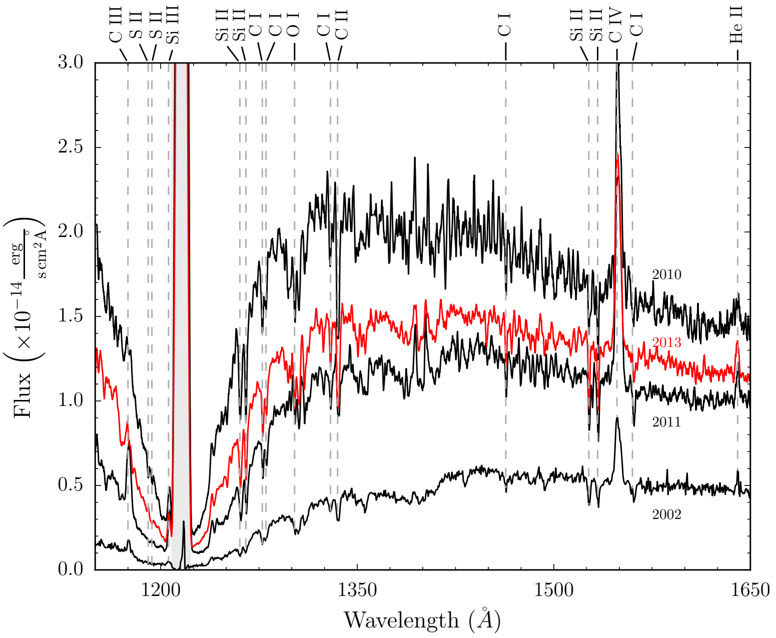

Figure 5.1: Average COS/G140L and STIS/G140L spectra of GW Lib (no flux offsets were applied). Black lines from top to bottom show the observations from 2010, 2011 (both COS), and 2002 (STIS). The red line corresponds to the new 2013 COS observations, which unexpectedly show a higher flux level than the 2011 observations. The most prominent lines are labelled and the airglow emission Lyman α at 1216 Å is shaded in light grey.

VW Hyi a flat and featureless continuum contributing at shorter wavelengths has also been detected with FUSE (< 970.8 Å; Godon et al. 2008; Long et al. 2009). In all cases the flux contribution of this second component is small ($\lesssim$ 20 per cent). The exact origin of that second component is not well understood; possible locations are the hot innermost region of the accretion disc, or a boundary/spreading layer on the white dwarf (Godon et al., 1995, 2008).

Following the 2007 outburst, the white dwarf in GW Lib is expected to gradually cool while it is relaxing to its quiescent state. However, the average flux observed in 2013 is higher than in 2011.

5.2.2 Variability

I was able to construct ultraviolet light curves of GW Lib following the procedure explained in Section 2.3.1. Lyman α at 1216 Å and O I at 1302 Å airglow emission lines were masked along the spatial direction. Finally I binned the data to 10 s resolution (Fig. 5.2).

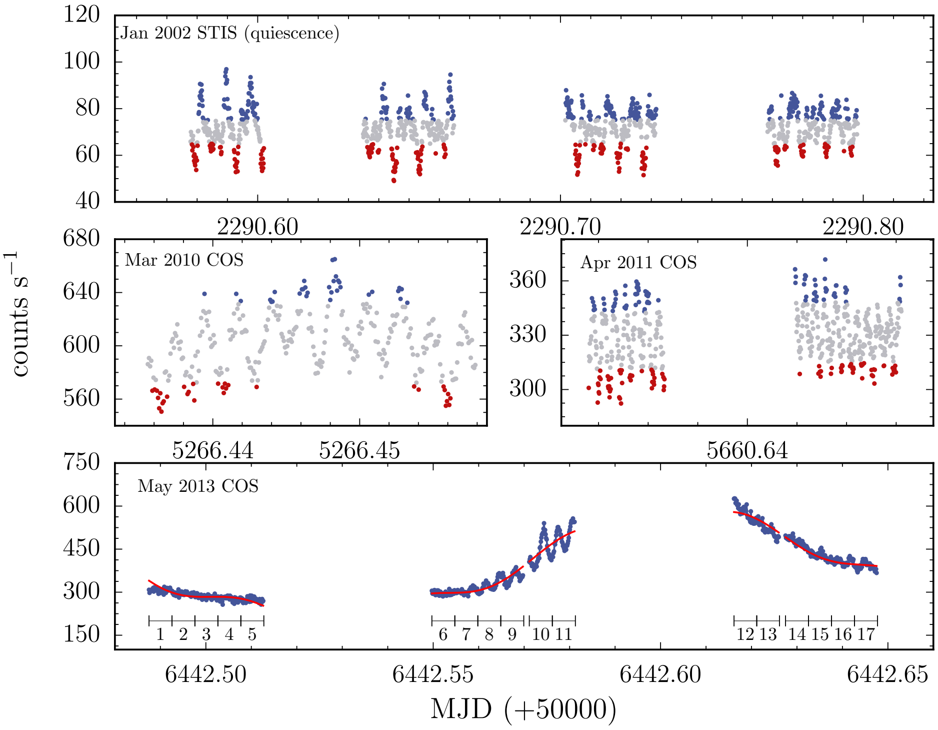

Figure 5.2: Light curves of GW Lib constructed from the time-tag data in 10 s bins. The upper panel shows the STIS/G140L pre-2007 outburst light curve while the other panels correspond to COS/G140L post-outburst observations. The count rate strongly fluctuates in the 2013 observations, increasing likely beyond 600 counts s^{-1} during the gap in the data (comparable to the mean level in 2010). In addition, short-term oscillations are clearly visible during the second orbit. From the observations obtained in 2002, 2010, and 2011, I extracted two spectra, one *peak spectrum* constructed from the intervals with the highest count rate (blue dots), and one *trough spectrum* from those with the lowest count rate (red dots). For the 2013 observation a set of 17 spectra was created, as labelled underneath the light curve. I performed spectral fits to these spectra to investigate variations in the effective temperature (see Section 5.3 for details). The fundamental plus the first and second harmonics are overplotted in red.

While in 2002, 2010, and 2011 the system showed periodic variations on timescales of ~230−650 s, interpreted as non-radial white dwarf pulsations (Szkody et al., 2002, 2012, top and middle panels in Fig. 5.2), the new observations in 2013 reveal an intriguing and puzzling feature: the light curve is dominated by a large-amplitude variability spanning the entire *HST* visit.

From the observations, it is not known if the large-amplitude variability is cyclical or not; nevertheless I fitted the entire light curve with a sinusoidal function plus the 2nd and 3rd harmonics, using the Levenberg-Marquardt method for non-linear least squares minimization of the PERIOD04 package (Lenz & Breger, 2005). Based on the F-test, adding the 4th harmonic does not provide any significant improvement. The best fit of the fundamental period corresponds to 4.39 ± 0.09 h and its amplitude is 175 ± 3 counts s^{-1}. This period is close to the ≃4 h period of the signal that has been repeatedly detected in ultraviolet and optical photometry (Schwieterman et al., 2010; Bullock et al., 2011; Vican et al., 2011) .

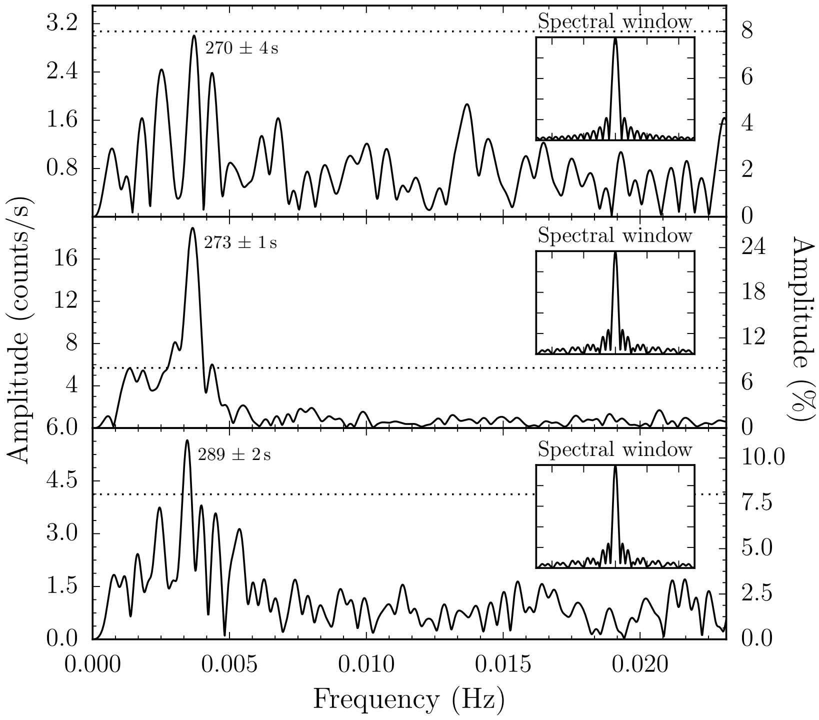

Figure 5.3: Power spectra for each orbit of the 2013 *HST* observations. The Discrete Fourier Transforms were computed after subtracting the long period variability with a polynomial fit. In each orbit the strongest signal is in the range 270 – 290 s, with a significant detection in the second and third orbit, and just falling short of the detection threshold in the first orbit. The significance level (dotted line) was defined as four times the mean of the amplitude calculated from 0 up to the Nyquist frequency.

In addition to the large-amplitude variability of the ultraviolet flux, the light curve shows periodic fluctuations with the highest amplitude during the second orbit (bottom panel of Fig. 5.2). I performed a Discrete Fourier Transform using the PERIOD04 package

(Lenz & Breger, 2005) on the light curve for each *HST* orbit after subtracting the long-term trend, larger amplitude variability, by fitting a second order polynomial independently to each orbit (Fig. 5.3). In each orbit the strongest peak is found in the range 270−290 s, with a statistically significant detection in the second and third orbits at 273 ± 1 s and 289 ± 2 s, respectively. I adopted the significance as four times the mean of the amplitude which provides 99.9% of confidence of a peak not to be noise (Aerts et al., 2010). For completeness, I computed the false-alarm probability for each orbit from the LombScargle periodogram using the ASTROPY package, which using the bootstrap method gives a probability of 0.0 of being false. Both periods are close to the 293 s period detected in 2010 and 2011, so I suggest these periodicities correspond to white dwarf pulsations.

5.3 Spectral fitting

5.3.1 2002, 2010, and 2011 observations

The excitation of gravity modes in a white dwarf is primarily a consequence of some heat flux being converted into mechanical motion in the H (He) ionisation zones, which could be either produced by an increase of the opacity compressing the overlying layers (κ-mechanism; Dziembowski & Koester 1981), or more likely, the increase of opacity leads to the generation of a convecting zone (Brickhill's ”convective driving” mechanism; Brickhill 1983, Wu & Goldreich 1999). The pulsations cause geometrical distortions in the white dwarf, leading to changes in the surface gravity, which are however, too small to be measured. The dominant effect of the pulsations is the appearance of hot and cool patterns on the white dwarf surface (Robinson et al., 1995; Clemens et al., 2000b). The three pulsations with well-defined periods identified during quiescence (2002 data), as well as the 293 s period found post-outburst (2010 and 2011 data), are generally believed to be due to non-radial white dwarf pulsations. Therefore, I investigated the difference in temperature produced by these pulsations. To that aim, I performed fits to two spectra, for each of the 2002, 2010, and 2011 observations, generated from the time-tag photon files. One spectrum was constructed using the photons corresponding to the sections of the light curve with the highest count rate (blue dots in Fig. 5.2) and a second spectrum from the sections with the lowest count rate (red dots in Fig. 5.2), hereafter referred to as *peak* and *trough* spectra. The thresholds of the high and low count rate are defined as a percentage above or below the mean for the full *HST* visit in 2002 and 2010, while for the 2011 data, the mean was calculated for each individual orbit (since the second orbit has a higher mean level, see right middle panel in Fig. 5.2). The percentages were chosen to use only as much of the peak and trough data as to achieve an acceptable signal-to-noise ratio in the resulting spectra (7, 5, and 6 per cent for the 2002, 2010, and 2011 data, respectively).

After defining the count rate thresholds, the peak and trough STIS and COS spectra were obtained by splitting, reducing, flux-calibrating and combining the time-tag files using a series of PyRAF routines from the STSDAS task package and modules of the STSCI_PYTHON2.15 library.

For the spectral fits, I used a grid of white dwarf models generated with the latest version of TLUSTY204N and SYNSPEC49T (Hubeny & Lanz, 1995). The grid covers $T_{\rm eff}$= 9 000−69 900 K in steps of 100 K, $\log g$=8.35 dex, and a metallicity of 0.1 times the solar metallicity, which reproduces well the metal absorption lines. The models cover the wavelength range 1000−1800 Å with a spectral resolution of 0.094 Å. I performed a bilinear interpolation of the grid in wavelength and effective temperature. I fixed $\log g$ at 8.35, which, using the white dwarf mass-radius relation derived from cooling models for white dwarfs (Holberg & Bergeron, 2006; Kowalski & Saumon, 2006; Bergeron et al., 2011; Tremblay et al., 2011), corresponds to previous estimates of the white dwarf mass in GW Lib based on the observed gravitational redshift ($M_{\rm WD}$=0.84±0.02 $M_\odot$; van Spaandonk et al. 2010, $M_{\rm WD}$=0.79±0.08 $M_\odot$; Szkody et al. 2012).

The core of the broad photospheric Lyman α absorption line shows evidence of an additional flat and featureless continuum component. Previous studies have modelled this additional continuum component by either a power-law, a blackbody spectrum or as flat in F_λ (Szkody et al., 2010a, 2012; Gänsicke et al., 2005) and found that the exact choice of the model for the second component does not significantly affect the white dwarf parameters derived from the fit. I adopted in our analysis a flux component constant in F_λ, as it reduces the total number of free parameters and fit the peak and trough spectra for the effective temperature ($T_{\rm eff}$), the scaling factor (S), and k, the flux of the constant F_λ component.

I used the EMCEE open-source code implemented in Python (Foreman-Mackey et al., 2013). I constrained $T_{\rm eff}$ with a flat prior function over the range 10 000−20 000 K, based on previous measurements (Szkody et al., 2002, 2012), as well as k and S to be positive. Finally, I defined the log-likelihood function to be $-\chi^2/2$. To estimate an initial guess for the parameters I used the Levenberg-Marquardt minimization method. I masked the Lyman α airglow line and the C IV emision line during the fit, using the ranges of 1208−1223 Å and 1543−1555 Å, respectively.

In general, the MCMC samples were well burnt-in before 100 iterations, and the one-

Table 5.2: Best-fit parameters obtained using the affine-invariant ensemble sampler for MCMC, with a fixed $\log g$=8.35. Uncertainties are the 1-σ confidence interval resulting from flat priors on $T_{\rm eff}$, S and k. White dwarf radii ($R_{\rm WD}$) are computed from the flux scaling factor adopting a distance of 104^{+30}_{-20} pc (Thorstensen, 2003).

Parameter	Peak spectrum	Average spectrum	Trough spectrum
$T_{\rm eff,2002}$ (K)	$14\,918^{+18}_{-20}$	$14\,695^{+13}_{-11}$	$14\,440^{+22}_{-22}$
$T_{\rm eff,2010}$ (K)	$18\,343^{+62}_{-69}$	$17\,980^{+14}_{-14}$	$17\,872^{+75}_{-72}$
$T_{\rm eff,2011}$ (K)	$16\,160^{+62}_{-61}$	$15\,915^{+9}_{-9}$	$15\,748^{+62}_{-61}$
$R_{\rm WD,2002}$ ($R_\odot$)	$0.015^{+0.009}_{-0.005}$	$0.014^{+0.009}_{-0.005}$	$0.015^{+0.009}_{-0.005}$
$R_{\rm WD,2010}$ ($R_\odot$)	$0.017^{+0.010}_{-0.006}$	$0.016^{+0.010}_{-0.006}$	$0.016^{+0.010}_{-0.006}$
$R_{\rm WD,2011}$ ($R_\odot$)	$0.018^{+0.010}_{-0.006}$	$0.018^{+0.010}_{-0.006}$	$0.018^{+0.011}_{-0.006}$
k_{2002} ($\times10^{-16}$ erg s^{-1} cm^{-2} Å^{-1})	$4.5^{+0.2}_{-0.2}$	$3.92^{+0.07}_{-0.07}$	$2.7^{+0.1}_{-0.1}$
k_{2010} ($\times10^{-15}$ erg s^{-1} cm^{-2} Å^{-1})	$2.8^{+0.2}_{-0.2}$	$3.22^{+0.05}_{-0.05}$	$2.4^{+0.2}_{-0.2}$
k_{2011} ($\times10^{-15}$ erg s^{-1} cm^{-2} Å^{-1})	$1.2^{+0.1}_{-0.1}$	$1.30^{+0.02}_{-0.02}$	$1.2^{+0.1}_{-0.1}$

dimensional projection of the posterior probability distributions of the parameters follow a Gaussian distribution. Therefore, I chose the median (50 percentile) of this distribution to be the best-fit value for the given parameter, and defined the internal uncertainty as calculated based on the 15.87 and 84.1 percentiles of the posterior probability distribution, since one standard deviation to either side of the median account for 84.1-15.87=68.23% of the samples.

The best fit effective temperatures for the peak and trough spectra of 2002, 2010, and 2011 are listed in Table 5.2. The results show that the pulsations led to a difference of nearly 500 K over the visible surface of the white dwarf. This temperature difference is clearly noticeable between the peak and trough spectra, as shown in Fig. 5.4 for the 2002 STIS data.

The white dwarf radius ($R_{\rm WD}$) can be derived using the scaling factor (S) and the distance (d) of 104^{+30}_{-20} pc (Thorstensen, 2003),

$$S = \pi \left(\frac{R_{\rm WD}}{d} \right)^2 . \tag{5.1}$$

The resulting radii are listed in Table 5.2, where the large uncertainties are primarily systematic in nature, resulting from the error on the distance measurement. Within the uncertainties, the derived radii agree with the expected radius of a white dwarf of mass $\simeq 0.84\,M_\odot$ located at the distance of GW Lib[1]

---

[1] The radius was derived from DA cooling models (Holberg & Bergeron, 2006; Kowalski & Saumon, 2006;

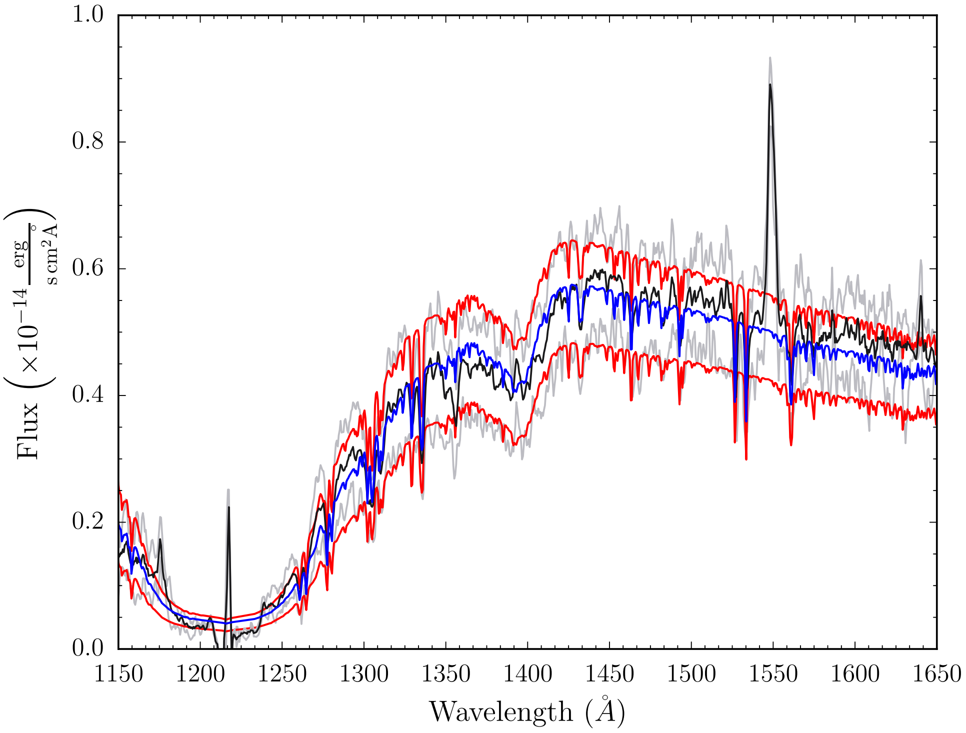

Figure 5.4: The black solid line represents the average spectrum for the 4 orbits of the STIS data taken in 2002. The blue line corresponds to the best MCMC-fit with T_{eff}=14 695$^{+13}_{-11}$ K. The upper and lower gray lines show the peak and trough spectra, respectively (see Section 5.3.1 and Fig. 5.2). The red lines are the best-fit models, T_{eff}=14 918$^{+18}_{-20}$ K (peak) and T_{eff}=14 440$^{+22}_{-22}$ K (trough).

The measured temperature variations of a few hundred Kelvin are consistent with non-radial pulsations producing an inhomogeneous photospheric temperature distribution across the visible white dwarf hemisphere, which is reflected in flux and colour variations (Fontaine et al., 1982).

5.3.2 2013 observation

While I expect that white dwarf pulsations cause the short-period oscillations seen in the light curve, particularly in the second orbit, the nature of the ≃4.4 h flux variation (bottom panel Fig. 5.2) is unclear, as is its physical location within the CV. Here, I explore a white

---

Bergeron et al., 2011; Tremblay et al., 2011) http://www.astro.umontreal.ca/~bergeron/CoolingModels dwarf photospheric origin. For that purpose, I process the 2013 COS data into a set of 17 spectra, as labelled underneath the light curve in the bottom panel of Fig. 5.2. The average exposure time for each spectrum is ≃435 s.

Two-component model

I then fitted this set of time-resolved spectra following the same procedure as described in Sect. 5.3.1. In each of the spectra the dominant ultraviolet flux component can be described by a white dwarf model. In addition, a small second continuum component, which I modelled with a constant F_λ k, is required, as easily identified near the core of the broad photospheric Lyman α absorption. The sequence of spectra clearly shows a smooth variation in both total flux and overall shape. The Lyman α line is broadest in spectrum #1 (grey line in Fig. 5.5), becomes narrower throughout the sequence up to spectrum #12 (black line in Fig. 5.5), and then broadens again. I found that the observed change in the width of the Lyman α absorption can be reproduced by an increase and subsequent decrease in the effective temperature of the white dwarf. The results are shown in blue dots in Fig. 5.6. The white dwarf temperature ($T_{\rm eff}$) changes from $15\,975^{+39}_{-37}$ K (spectrum #5) up to $18\,966^{+46}_{-47}$ K (spectrum #12) which correlates with the constant flux (k) and anticorrelates with the *apparent* white dwarf radius ($R_{\rm APP}$). I adopt the designation of apparent radius as a change in the actual white dwarf radius is unphysical. I interpret these results as heating of a localised region on the white dwarf. This region dominates the ultraviolet flux, resulting in a decrease of the apparent radius.

Three-component model

To confirm our assumption of a hotter region on the white dwarf surface, I repeated the fits, however in addition to the global white dwarf model and the second continuum component, k, I included a second, hotter, white dwarf model to model this region. The area covered by this hot region was a free parameter, and the temperature of the global white dwarf was fixed to 15 975 K, which corresponds approximately to the temperature of the coolest spectrum (labelled as #5 in Fig. 5.2). To avoid a temperature inversion between the hot region and the cool underneath white dwarf, I constrain the temperature of the hot spot to be higher than $T_{\rm eff}$=15 975 K. Based on the F-test, the addition of a second white dwarf to model the hot spot provides better fit. All the fits spectra have p-values under 0.005, except the fifth spectrum which gives p-value≃0.21.

The best-fit parameters are illustrated in red dots in Fig. 5.6. The temperature of the

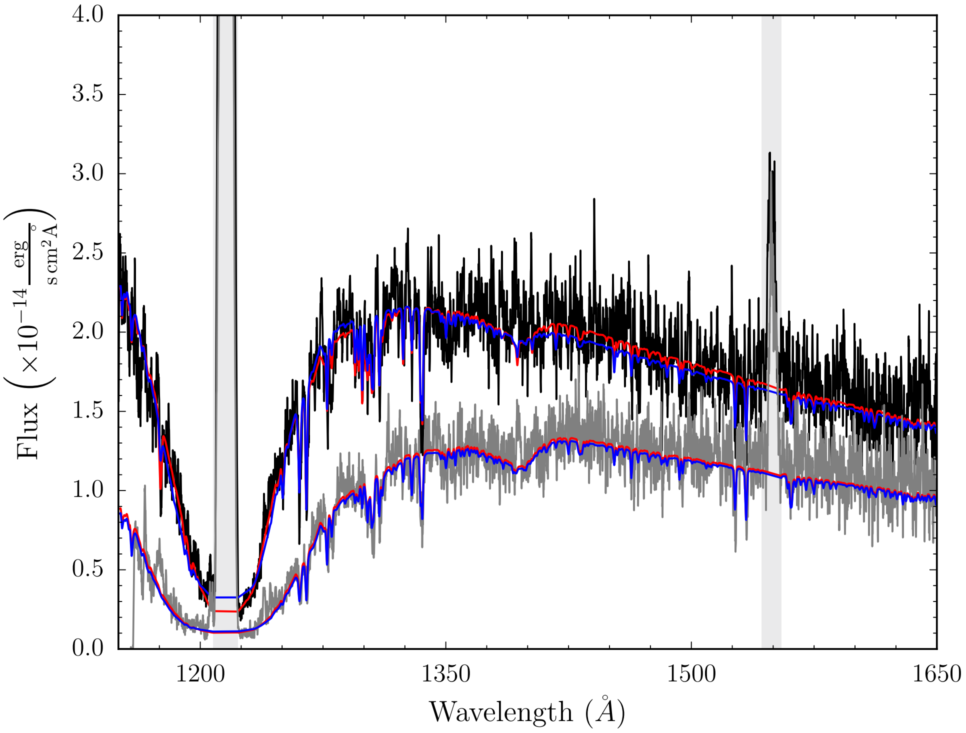

Figure 5.5: The grey and black lines display the spectra #1 and #12 defined in Fig. 5.2. I overplotted the best-MCMC fits using two-component model (blue) and three-component model (red). The spectrum #1 is well-fitted by a single white dwarf with T_{eff}=16 102$^{+37}_{-37}$ K, while spectrum #12 is better fitted by the three component model, particularly in the central region of the Lyman α absorption, using a global white dwarf at T_{eff}=15 975 K plus a hotter (22 060$^{+313}_{-303}$ K) white dwarf model covering ≃31 per cent of the visible white dwarf surface. The airglow line of Lyman α and C IV (shaded in grey) were masked during the fit. The spectra were smoothed with a 5-point boxcar for display purposes.

hot region ($T_{\mathrm{eff,spot}}$) on the white dwarf increases from the global white dwarf temperature of 15 975 K to 24 782$^{+506}_{-521}$ K. The white dwarf radius is calculated using equation 5.1, where S is the sum of the scaling factors of the T_{eff}=15 975 K underlying white dwarf and the hot region. I found that the white dwarf radius remains between 0.016−0.018R$_{\odot}$, which, I note, it is consistent with the radius estimates from the 2002, 2010, and 2011 observations (Table 5.2). In contrast to the two-component fit in Section 5.3.2, the additional flat F$_\lambda$ k component no longer shows a strong correlation with the temperature of the hot region, as the region of the core of Lyman α can be better reproduced with the inclusion of a hotter white dwarf (Fig. 5.5). In the fourth panel I show the ratio between the area of the hot region and the total visible white dwarf area. It shows that during the first seven spectra the area of the hot region is practically non-existent, explaining the large errors in the temperatures of the hot region. Once the ultraviolet flux rises and the area of this region grows, its temperature rises rapidly. Additionally, I show the flux of the C IV emission line in the bottom panel, which I discuss below.

5.4 Discussion

5.4.1 Possible scenarios explaining the change in flux of the white dwarf

In Section 5.3.2 I demonstrated that the evolution of both the total ultraviolet flux, as well as the morphology of the Lyman α profile obtained in 2013, is well-described by an increase of a few 1000 K, and subsequent decrease, in the temperature of a fraction of the white dwarf surface. The area of this hot region covers up to ≃30 per cent of the visible white dwarf area. I found this variation lasts ≃4.4 h which is close to the recurrent ≃4 h period signal reported previously (Schwieterman et al., 2010; Bullock et al., 2011; Vican et al., 2011). The three groups found that the signal wanders in phase and amplitude on time scales of days and occasionally disappears. In summary, a ≃4 h variability that is detected both in the optical and ultraviolet appears to be a recurrent feature in GW Lib and our analysis of the new *HST* observations link it to an apparent heating and cooling of a region on the white dwarf surface. Here, I discuss possible scenarios that could cause such a change in the white dwarf temperature.

An accretion spot on a magnetic white dwarf.

Accretion causes heating of the white dwarf, and non-uniform accretion of matter will result in an inhomogeneous temperature distribution over the white dwarf surface. Accretion-heated spots that exceed the temperature of the underlying white dwarf by several 1000 K are frequently observed in polars, i.e. strongly magnetic CVs, and cause a modulation of the ultraviolet flux and the width of the Lyman α profile on the spin period of the white dwarf (Gänsicke et al., 1995, 1998, 2006; Schwope et al., 2002; Araujo-Betancor et al., 2005; Szkody et al., 2010b). Assuming the presence of a weak magnetic field (B) I can calculate the minimum magnitude required by the white dwarf to decouple the electron spin and detect splitting of sharp metal lines with the spectral resolution of COS. In the case of Si II the absorption at 1260 Å and 1265 Å corresponds to electron transitions of $^2P_{1/2} \rightarrow^2 D_{3/2}$ and $^2P_{3/2} \rightarrow^2 D_{5/2}$, respectively. Under a weak magnetic field regime, the $^2D_{5/2}$ and $^2D_{3/2}$ levels of the Si II would split into six and four states, respectively. I found that necessarily $B > 1.4$ MG for $^2D_{3/2}$ (Landé factor equals to 0.8) and $B > 0.9$ MG for $^2D_{5/2}$ (Landé

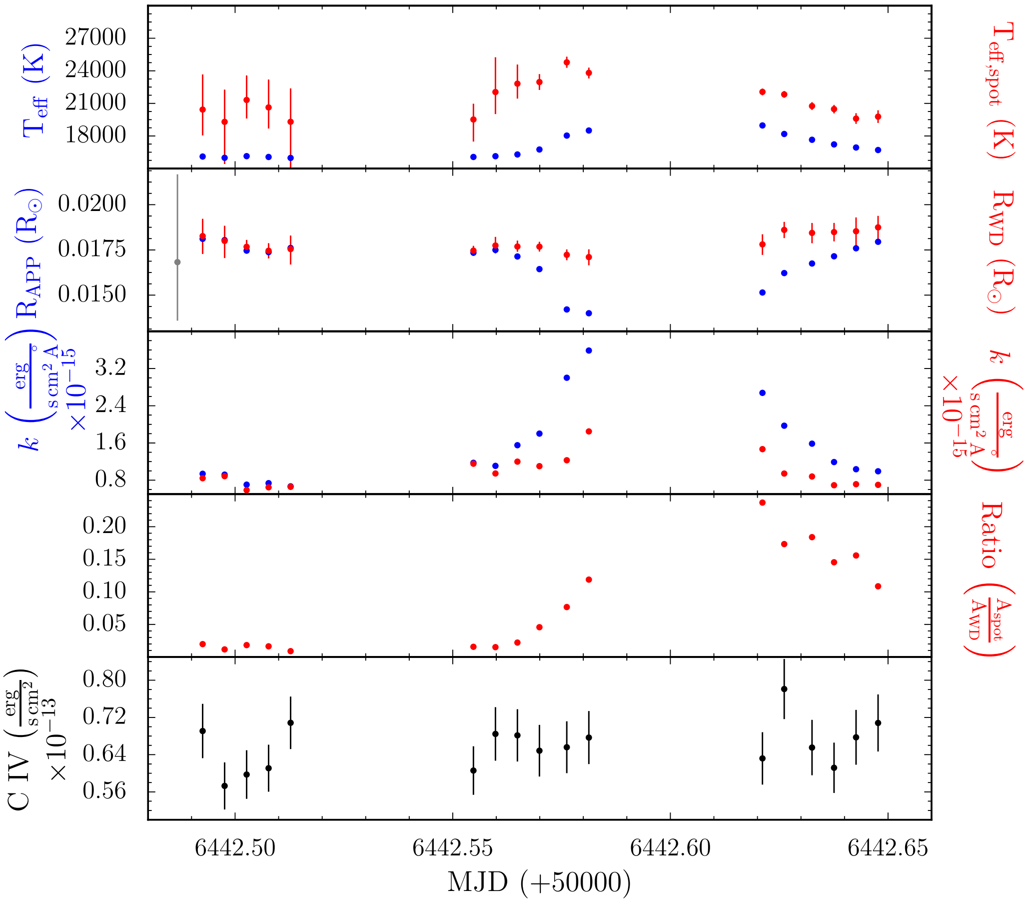

Figure 5.6: Best-fit parameters for the set of 17 spectra processed from the May 2013 observations. I fitted the set using a two-component model (blue dots): a white dwarf plus a flat F_λ (k) component, and with a three-component model (red dots): an underlying white dwarf at $T_{\rm eff}$=15 975 K, a flat F_λ component (k), and a hotter white dwarf accounting for a localised heated fraction of the white dwarf. The intrinsic uncertainties have been estimated based on the 15.87 and 84.1 percentiles of the MCMC samples in the marginalized distributions, but some of them are too small to be seen on this scale. The distance measurement used to determine the apparent white dwarf radius introduces a large systematic uncertainty (gray error bar). This systematic uncertainty affects, however, the entire sequence of apparent radii in the same way, i.e. the shape of the apparent radius variation is a robust result. The fourth panel shows the ratio between the fraction covered by the hotter white dwarf and the area of the global white dwarf. The fifth panel shows the flux of C ɪᴠ emission line at 1550 Å. See Section 5.4 for details.

factor equals to 1.2) to see such splitting. I conclude that, because I do not detect Zeeman splitting in the Si II at 1260 Å, the magnetic field of the white dwarf in GW Lib is limited to $B \leq 0.9$ MG. However, in polars, the rotation of the white dwarf is locked to the orbital period, in the range ≃1.5−8 hr, whereas the spin period of GW Lib is ≃100−200 s (van Spaandonk et al., 2010; Szkody et al., 2012). Hence, accretion onto a magnetic white dwarf would result in coherent variability on time scales of ≃100−200 s, and I therefore rule out this scenario to explain the ≃4 h variability.

A brief increase in the accretion rate.

Another possible scenario explaining the observed ≃4 h variability are quasi-periodic brief accretion events that significantly heat a fraction of the white dwarf. However, such intermittent heating needs to be extremely symmetric with respect to the spin axis of the white dwarf, as I do not observe any variability of the ultraviolet flux at the white dwarf spin period. Accretion-heating of an equatorial belt of a non-magnetic white dwarf (Kippenhahn & Thomas, 1978a) would match this constraint well.

I can estimate the excess of energy released during a hypothetical accretion episode from the excess luminosity. I derived the luminosity by integrating white dwarf models that follow the temporal evolution of the effective temperature shown as blue dots in the top panel of Fig. 5.6, scaled to the observed flux and subtracting the flat component (Fig. 5.7). The energy excess corresponds to the area above of the luminosity of the white dwarf with $T_{\rm eff} = 16\,063$ K, corresponding to spectrum #6 (blue line in Fig. 5.7) and, adopting a white dwarf mass of $0.84\,M_{\odot}$ (van Spaandonk et al., 2010) and the apparent radius of $0.018\,\mathrm{R}_{\odot}$ (See section 5.3.2), I can derive a total mass accreted during the accretion episode. The discontinuity of the data, specifically near the peak of the ≃4.4 h variability, does not allow us to accurately define the shape of the area to estimate the energy excess. The simplest interpolation is connecting the points with a straight line, which gives an energy excess of 6.2×10^{34} ergs (starred area), and a total mass of $\simeq 3.5\times10^{-16}\,M_{\odot}$, to be accreted during a hypothetical accretion episode that lasts ≃2.2 hr. However this estimate is strictly a lower limit. As an alternative, I fitted the luminosity adopting the same model I used to fit the light curve (i.e. sinusoidal function plus 2nd and 3th harmonics, red solid line). This approach gives an energy excess of 7.1×10^{34} ergs (grey area) and, consequently, an accreted mass of $4.0\times10^{-16}\,M_{\odot}$ in ≃2.2 h, i. e. the two approaches do not differ significantly, and suggest that a brief accretion episode with $1.3-1.5\times10^{-12} M_{\odot}$/yr could cause the observed heating. This rate is very low compared to the expected accretion rate for dwarf novae in quiescent states (Townsley & Gänsicke, 2009; Goliasch & Nelson, 2015).

In principle, small changes in the accretion rate onto the white dwarf could be caused by efficient irradiation of the innermost region of the disc by the slowly cooling white dwarf, keeping these regions in an ionised state while the outer disc is cooler and neutral. Instabilities in the transition region could cause quasi-periodic fluctuations of the accretion rate, resulting in heating and subsequent cooling of the white dwarf. The time scale of such cycles would depend very much on the temperature of the white dwarf.

Another possibility is that magnetic field star-disc interactions cause quasi periodic changes of the accretion rate in the inner disc. According to Uzdensky (2002), the connection between field lines of a disc and star can be periodically broken due to twisting and reconnection. One may speculate that such cycles can generate quasi-periodically occurring episodes of enhanced accretion.

If the $\simeq$4 h variability seen in GW Lib is indeed related to quasi-periodic brief accretion events, one would expect similar activity in additional CVs. Woudt & Warner (2002) and Vican et al. (2011) note that only a handful of other systems show quasi-periodic variability at periods significantly longer than their orbital periods, in particular FS Aur (Tovmassian et al., 2003). Although quasi-periodic accretion events are in principle a possible explanation for our 2013 COS observations of GW Lib, I consider this scenario unlikely because of two reasons. Firstly, I would expect an increase in the accretion rate onto the white dwarf to be accompanied with photometric stochastic flickering (which is a characteristic of FS Aur, Neustroev et al. 2013), which is not observed. Secondly, enhanced accretion activity should be linked to a variation of the C IV emission line flux, which is also not observed (Fig. 5.6).

Retrograde wave in a rapid rotating white dwarf

Schwieterman et al. (2010) speculated about unusually long pulsations modes in the white dwarf as a possible origin of the $\simeq$4 h variability. In single, slowly-rotating white dwarfs, pulsation periods can be as long as $\simeq$20 min (e.g. Mukadam et al. 2006); modes with periods of several hours are physically unlikely.

However, the white dwarf in GW Lib rotates extremely rapidly with a spin period of $\simeq$100−200 s (van Spaandonk et al., 2010; Szkody et al., 2012) compared to the slow spin periods of hours to days in single white dwarfs (Kawaler, 2004). In the case of rapid rotation, $\Omega_{\rm spin} > \Omega_{\rm mode}$, the "splitting" of g-modes by rotation is no longer a small perturbation, and the mode period can change by order unity or more. Also, modes on rotating stars are

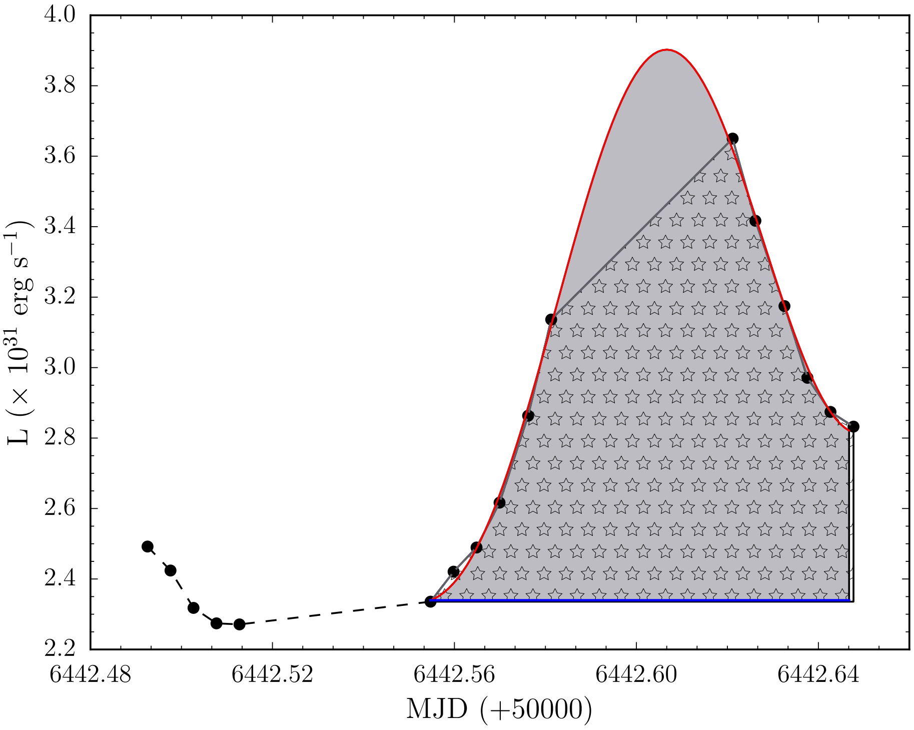

Figure 5.7: Luminosity as a function of time calculated from integrating the flux of white dwarf models with the effective temperatures given in Fig 5.6 (blue dots). The energy excess is calculated using a radius of $0.018R_\odot$ and a mass of 0.84 $M_\odot$ for the white dwarf, and subtracting the luminosity of the underlying white dwarf model with $T_{\rm eff}$= 16 063 K (area above the blue line). The starred area represents an excess of energy of 6.2×10^{34} ergs while the grey area represents 7.1×10^{34} ergs of energy excess.

sensitive to the rotation axis and the direction of rotation. As a result, for $l = 1$ modes, the modes that corresponds to the $m = -1$ spherical harmonics propagate in a prograde direction (around the star in the same direction as the spin) while the $m = +1$ mode corresponds to retrograde modes. For the retrograde modes, the frequency measured by a fixed observer is $\Omega_{\rm obs} = |\Omega_{\rm mode} - \Omega_{\rm spin}|$. The g-mode spectrum will be a sequence of modes starting at around a few hundred seconds and extending to longer periods as the radial order of the mode increases (Unno et al., 1989; Bildsten et al., 1996). As a result, for a star like GW Lib, which is rotating with a period of around 100−200 seconds, there can be a low-radial-order g-mode, $n \sim 5$, for which $\Omega_{\rm mode} \approx \Omega_{\rm spin}$ so that $\Omega_{\rm obs}$ is much closer to zero, thus giving a significantly longer period. This is a mode that, by propagating opposite to rotation on the star, ends up being almost fixed in from the observers' point of view. The excitation of this mode could give rise to the observed ≃4.4 h period (Fig. 5.8).

The model white dwarf shown in Fig. 5.8 has parameters (mass, accreted layer, accretion rate, T_{eff}) similar to those expected for GW Lib, but is not a fit (Townsley et al., 2016). The model demonstrates that an accreting white dwarf rotating at the spin rate observed for GW Lib will have low to moderate order modes that are consistent with both the observed ~4.4 h mode as well the ~280 s mode. The low order modes are those with shortest mode period in the slowly rotating GW Lib, periods at the right edge of the figure. If the white dwarf spin is near 100 s, the best candidate mode in this model for the ~4.4 h period is the retrograde ($m = +1$) $n = 6$ radial order mode. In this case the ~280 s period may correspond to either a lower radial order (shorter period, e.g. $n = 2$) mode that is short enough period to still be retrograde in the observer's frame, or one or several high order retrograde modes that have periods sufficiently longer than the spin period that the spin of the white dwarf has "dragged" them be prograde from the point of view of the observer. White dwarf models with slightly different parameters will have normal modes that are shifted up or down by up to of order 100 seconds, that will change which radial order mode matches the ~4.4 h period.

Unlike the spherically symmetric or low-spin case, rotationally modified g-modes do not extend as evenly over the entire surface of the star. Their amplitudes are larger near the equatorial regions (Bildsten et al., 1996). The equatorial band over which the mode's amplitude is large depends on the ratio between Ω_{mode} and Ω_{spin}, with lower frequency (higher radial order) modes being constrained more tightly near the equator, and higher frequency (lower radial order) having more extension to higher latitude. The moderate radial order necessary to have $\Omega_{\mathrm{spin}} \approx \Omega_{\mathrm{mode}}$ could therefore also lead to the decrease in the effective area as the mode contributes more to the flux. Some of this contribution may be blocked by the edge-on accretion disk, but if the mode extends to high enough latitude to be visible it would lead to a reduction in area like that observed.

I note that rare large-amplitude brightening episodes have also been observed in two pulsating non-accreting white dwarfs. PG 1149+057 (Hermes et al., 2015) and KIC 4552982 (Bell et al., 2015) exhibit recurrent outbursts lasting 4−40 h longer than the pulsation periods identified in these systems. PG 1149+057 and KIC 4552982 brighten overall by up to 45% and 17%, respectively, not quite as large as the observed amplitude of the 4.4 h variability in GW Lib. The recurrence time of these outbursts is ~days and, when such an event occurs, the pulsation spectrum increases in amplitude supporting the fact that the outbursts originate on the white dwarf. Hermes et al. (2015) suggest that these events are most likely related to white dwarf pulsations.

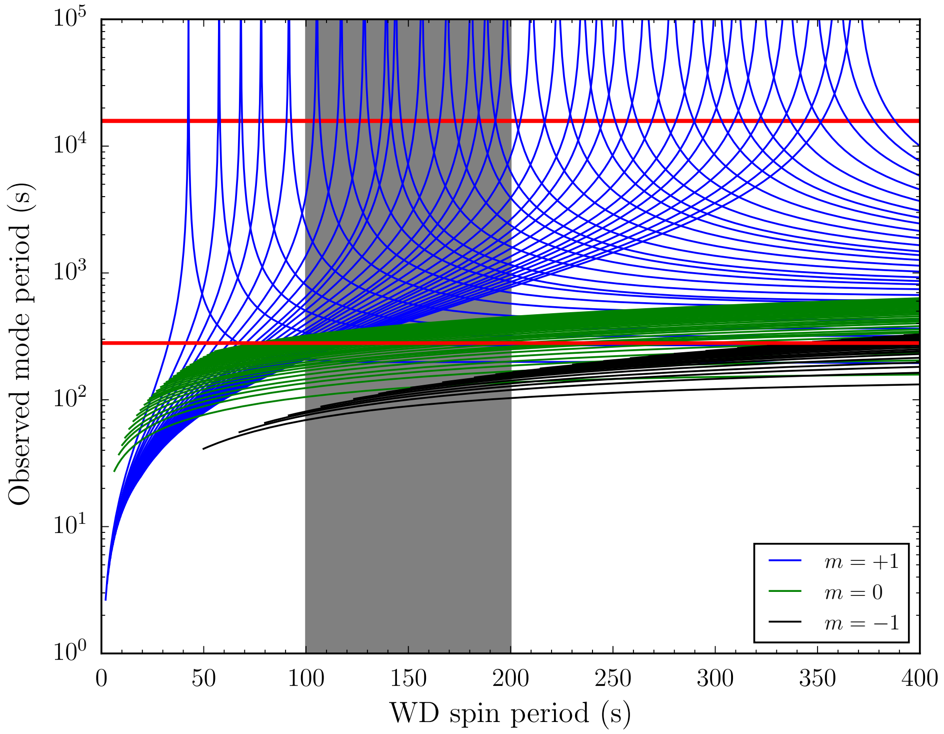

Figure 5.8: Observed mode periods produced by the splitting of the g-modes due to fast rotation of the white dwarf (Townsley et al., 2016), where $m = 1$ (retrograde, blue), $m = -1$ (prograde, black), and $m = 0$ (green). This model was computed using a total mass, $M = 0.9M_\odot$, a H-rich accreted layer mass of half of the nova ignition mass (calculated as described in Townsley & Bildsten 2004), and $T_{\text{eff}} = 15\,500\,\text{K}$ (Szkody et al., 2002). The red bands show the ≃4.4 h-period variability (top) and the ~280 s pulsation signal (bottom) identified in the 2013 observations. The light shade area represents the white dwarf spin period (van Spaandonk et al., 2010; Szkody et al., 2012).

There are two possible reasons that the mode currently responsible for the ≃4.4 h variability is not continuously detected. One is simply that it was not excited. The second is that if its period shifts by a small amount it may no longer be similar enough to the spin period to lead to long time scale variability in the observer frame. While large shifts in periods are not expected due to the stability of the overall white dwarf structure, a small shift that may arise from the heating and cooling of the outer layer due to the accretion event may be sufficient to change the match between the mode and spin period.

5.4.2 Nature of the second component

Some extra flux contribution is clearly present in the broad core of the photospheric Lyman α line. As outlined above, similar additional continuum flux components have been detected in many other dwarf nova systems (Godon et al., 2004; Long et al., 2009; Sion et al., 2003; Gänsicke et al., 2005). Under the assumption of a featureless flat F_λ model, its contribution to the total flux drops from $\simeq 8\%-26\%$ to $\simeq 7\%-13\%$, when I included a second white dwarf model representing the heated region. I find a correlation between the flux of this flat F_λ component and the effective temperature of the white dwarf in the 2013 data (Fig. 5.6). Such correlation is not quite obvious in the *HST* spectroscopy taken in 2002, 2010, 2011 (Table 5.2), where the difference in temperature between the trough and peak spectra is only a few hundred Kelvin.

To further explore the nature of this component, I repeat the fits using the three-component model but I included the second component as optically thick thermal blackbody emission instead of a flat in F_λ model, and found temperatures in the range of 18 000−28 000 K, which mimicks in an approximately a flat F_λ continuum over the wavelength range of the *HST*/COS data. However, the area of this thermally emitting region is quite small, reaching at most to $\sim 4\%$ that of the white dwarf area. Nonetheless, a blackbody model for the second component does not improve the overall fits compared to the flat F_λ model and the resulting white dwarf temperatures shown in Fig. 5.6 remain practically unchanged.

For completeness, I repeated the fits using only single white dwarfs models. Though the white dwarf temperatures are higher by $\simeq 300$ K, the overall shape of the temperature variation follows the same trend as shown in Fig. 5.6. However these fits completely fail to reproduce the observed core of the Lyman α absorption line.

While I cannot unambiguously identify the physical nature of the second component, incorporating either a flat F_λ continuum or a blackbody significantly improves the fits compared to using only single white dwarf models.

5.5 Conclusions

I have presented the analysis of new and archival *HST* observations of the dwarf nova GW Lib taken in 2013, whose UV flux in quiescence is known to be dominated by the white dwarf, and which is known to exhibit non-radial mode pulsations.

I have analysed ultraviolet *HST* observations obtained to pre-outburst in 2002, and post-outburst in 2010, and 2011, demonstrating that in fact, the non-radial pulsating signals identified in these observations lead to variations of a few hundred Kelvin over the visible white dwarf surface.

I identified the presence of short period oscillations in the new 2013 observations, with a significant detection during the the second and third orbits at periods of $\simeq$273 s and $\simeq$289 s, respectively. The amplitude is strongest in the second orbit. I suggest these oscillations are produced by pulsations of the white dwarf.

I also identified a large amplitude variability spanning the entire COS observations, with a long period of $\simeq$4.4 h, and I suggest it to be the same $\simeq$4 h signal previously detected in the ultraviolet and optical (Bullock et al., 2011; Schwieterman et al., 2010; Vican et al., 2011). I demonstrated that this $\simeq$4.4 h variability can be explained by a simultaneous increase of the white dwarf temperature and a decrease of its apparent radius. Subsequently, the white dwarf cools while the apparent radius is relaxing back to its original size. I postulate that this large temperature change occurs only over a fraction of the white dwarf surface.

A wave travelling opposite to the direction of the white dwarf rotation, with a period similar to the spin period is the most plausible explanation. This wave could be the result of a considerable splitting in the *g*-modes, caused by the rapid rotation of the white dwarf.

I identified in all STIS and COS spectra a small flux contribution of a second featureless continuum component that can be modelled by either flat F_λ model or by blackbody emission, however its origin remains unclear.

Chapter 6

Cataclysmic Variables with nuclear evolved donors

6.1 Introduction

The systematic exploitation of SNIa as excellent distance estimators was the key to successfully measure the cosmological parameters (Riess et al., 1998; Perlmutter et al., 1999). While there is a general consensus that a SNIa is the thermonuclear explosion of a CO white dwarf that surpasses the Chandrasekhar mass limit (with the exception of the double detonation model, see below), yet our understanding about the pathways that lead to the ignition remains incomplete. Different types of progenitors may result in subtle differences in the observational characteristics of SNIa, and the lack of a detailed model of the SNIa could ultimately limit the precision of SNIa based cosmology and hence our understanding of the nature of dark energy. Several models which involve mergers of white dwarfs or white dwarfs accreting from close companions are currently discussed.

The classic double degenerate channel is the result of a merger of two CO white dwarfs driven together by gravitational wave radiation, with a combined mass that exceeds the Chandrasekhar mass limit (Webbink, 1984; Iben & Tutukov, 1984). While these mergers may lead also to accretion-induced collapses rather than SNIa (Nomoto et al., 2000), they can explain the Galactic birthrates and delay time distributions of SNIa (e.g. Han, 1998; Nelemans et al., 2001; Ruiter et al., 2009; Maoz et al., 2014; Yungelson & Kuranov, 2017).

The sub-Chandrasekhar mass model consists of a CO white dwarf with a mass below 1.4 $M_{\odot}$ that accretes at a low rate from a He white dwarf companion, forming a thick layer of He which eventually ignites, propagating a shock wave that triggers the detonation in the

CO core (García-Senz & Bravo, 1999). However, some complications of this model are the observational signatures in the supernova remnant spectra which show enhancement of heavier elements (e.g. manganese), and according to theory these elements can only form in the denser conditions provided by Chandrasekhar CO white dwarfs. Hence, this model can mainly explain the formation of sub-luminous SNIa.

A less explored model is the core-degenerate scenario which is based on a Chandrasekhar or super-Chandrasekhar mass white dwarf that is formed at the termination of (or shortly after) the common envelope phase, from a merger of a white dwarf with the heated core of a massive AGB star (Livio & Riess, 2003). This model can explain the finding that more luminous SNIa occur preferentially in galaxies with active star formation (Soker, 2011).

Finally, the single degenerate channel comprises a binary system composed by a white dwarf which grows in mass by burning quasi-steadily the H accreted from a non-degenerate companion (Whelan & Iben, 1973). The major problem of this model was the lack of H in the SNIa spectra. The detection of Balmer Hα emission in the spectrum of the SNIa SN 2002ic (Hamuy et al., 2003) is a landmark discovery, since one of the characteristics to classify the SNIa is that they do not present H in their spectra. The single degenerate model predicts that nearly all SNIa present similar luminosities since they all should explode closely to the Chandrasekhar mass limit. The single degenerate model can also correctly predict the abundances of certain elements produced during the SNIa, in particular magnesium, which requires very dense conditions. Some complications are the fine-tuning of the accretion rate of H. If the white dwarf accretes matter at high rates, the material builds up an extended envelope which overflows its own Roche lobe, leading to a common envelope. In contrast, if the white dwarf accretes matter at low rates, it builds up a thin degenerate H layer, which once it gets hot enough, ignites H burning, blowing off all the accreted material, resulting in no mass gain. However, there is a regime of accretion rates which lies in between these two scenarios in which the accreted H can burn at the rate that is accreted. During this phase of shell burning on the white dwarf, the systems display strong emission in the soft-X rays (bolometric luminosities of 10^{36}–10^{38} erg s^{-1} Kahabka & van den Heuvel 1997). It has been proposed that the observed super-soft X-rays sources are excellent candidates for SNIa via the single degenerate channel. However, the number of observed nuclear burning white dwarfs may be too small to explain the rate of SNIa, and Gilfanov & Bogdán (2010) suggested that no more than about five per cent of the SNIa can form through the single degenerate channel. Nevertheless, it is important to bear in mind that during the crucial phase of mass growth, the soft-X rays emitted by the systems can be easily obscured by the interstellar medium, and therefore the number of super-soft X-rays sources may have been underestimated. Moreover, numerical simulations show that this phase is very short ($\lesssim$10 Myr) and therefore only a small number of systems will be observable during this phase. The observational study of the single degenerate channel is limited since the sample of known super-soft X-rays sources is small (<10 systems with measured orbital periods, Greiner 2000). The majority of them are distant sources in the Small and Large Magellanic Clouds and the sample reduces to only two in the Galaxy, RX J0019.8+2156 and RX J0925.7-4758. Deriving the binary parameters of these super-soft X-rays sources has been very challenging as due to their high temperatures, the white dwarfs outshine their companions. Thus since this model was proposed in the 90's, very little progress has been made.

6.1.1 White dwarf masses in CVs

Evolutionary simulations show that a significant fraction of CVs with short orbital periods (< 3 h) are expected to host low-mass (0.5 $M_{\odot}$) He-core white dwarfs (Willems et al., 2005). For high common envelope efficiencies (Section 1.2.2), He-core white dwarfs can survive the common envelope phase, whilst CO white dwarfs emerge from the common envelope phase with wider orbits complicating the formation of semi-detached systems. This is in contradiction with the white dwarf masses measured (>0.8 $M_{\odot}$) in CVs with short orbital periods (Littlefair et al., 2008). Indeed, many systematic studies of CVs have found a higher mean mass for white dwarfs (Warner, 1973; Ritter, 1976, 1987; Robinson, 1976; Smith & Dhillon, 1998; Knigge, 2006; Knigge et al., 2011; Zorotovic et al., 2011), which can not be explained as an observational bias towards the detection of CVs with high-mass white dwarfs (Zorotovic et al., 2011).

The possibility of the white dwarf growing in mass is determined by the rate of mass transfer (Nomoto, 1982; van den Heuvel et al., 1992; Zorotovic et al., 2011), but it has been very difficult to perform detailed calculations on the efficiency of mass growth as a function of the accretion rate. Theoretical simulations carried out by Wijnen et al. (2015) concluded that the observed mass distribution in CVs can not be reproduced merely as a result of mass accretion. Instead, Schreiber et al. (2016) invoke (empirical) consequential angular momentum losses (CAML) to explain the measured mass distribution as well as low observed space density of CVs compared to the theoretical predictions. The CAML mechanism causes many of the CVs with low-mass white dwarfs to become dynamically unstable and thus they merge early in their evolution. The number of CVs containing low-mass white dwarfs substantially decreases, thereby increasing the average mass of white dwarfs in CVs and, moreover, it lowers the predicted space density of CVs in the Galactic disc, resulting in a better agreement with the observations.

6.1.2 Low C/N ultraviolet emission line flux ratio as a signature of super-soft X-rays source descendants

For a failed SNIa (Section 1.2.6) to evolve to the CV stage within the Hubble time means that during the initial phase of these systems, as pre-CVs, their companions must have been more massive than our Sun. Besides that, the mass ratio of these pre-CVs needs to be larger than the critical mass ratio to undergo the thermal time scale mass transfer (Section 1.2.6), therefore the companion was powered by the CNO cycle before the onset of the mass transfer. The resulting signatures of the CNO cycle can be detected once these systems evolved into CVs after undergoing the thermal time scale mass transfer. At some point during the evolution of these CVs towards shorter orbital periods, the mass of the donor reduces to a point where it will start to develop deeper convection which dredges up the material processed in the core, and hence it results that the material that is accreted on the white dwarf surface carries the CNO signatures.

In an *HST*/STIS snapshot survey, spectroscopy of 69 CVs was obtained of which 10–15% show an extreme enhancement of nitrogen that is evident in the strong emission of N v at 1550 Å while the strength of the emission line of C iv at 1550 Å is considerable lower than seen in canonical CVs (Gänsicke et al., 2003). AE Aquarii is another observational evidence of a super-soft X-rays descendant (Schenker et al., 2002). The authors suggested that the low ultraviolet C/N emission line flux ratio observed in AE Aquarii can only be explained by accretion of material from a companion which has undergone considerable CNO nuclear burning before the onset of the mass transfer, i.e. when the companion was close to the end of the MS, and under these conditions the CV can evolve towards shorter orbital periods than the orbital period minimum (Section 1.2.3). The latter statement is supported by evolutionary simulations showing that CVs having MS donors with low H content in their cores can evolve towards ultra short orbital periods, where they join the population of AM CVn stars (Podsiadlowski et al., 2003) with few exceptions of systems having orbital period beyond the period minimum where their optical spectroscopic data show hydrogen lines (e.g Augusteijn et al., 1996; Thorstensen et al., 2002c).

In this thesis the focus is on the single degenerate channel and I pursue a different approach, studying the systems that failed the SNIa ignition, morphing into CVs. Here, I analyse COS ultraviolet spectroscopy of HS0218+3229 and QZ Serpentis which both show enhancement of the N v emission line at 1240 Å and the lack of the C iv emission line at

1550 Å, indicating that they belong to the subgroup of peculiar CVs that underwent the super-soft X-rays phase.

6.2 HS0218+3229 & QZ Ser, two failed SNIa

HS 0218+3229 is a cataclysmic variable discovered within the Hamburg Quasar Survey. A detailed analysis of data available in 2000 CCD plus 200 photographic frames taken between 1963 and 2011 revealed two outbursts with an amplitude of ≃4 magnitudes in the V and pg bands. These outbursts occurred in 1980 and 2007 (Golysheva et al., 2012). From time-resolved optical spectroscopy and R-band photometry, Rodríguez-Gil et al. (2009) measured the orbital parameters of HS0218+3229. The orbital period is found to be ≃7.13 h (Rodríguez-Gil et al., 2009; Golysheva et al., 2012). The masses of the stellar components were dynamically constrained to be $0.44\,M_\odot < M_{\rm WD} < 0.65\,M_\odot$ and $0.23\,M_\odot < M_{\rm donor} < 0.44\,M_\odot$ for the white dwarf and the secondary, respectively (Rodríguez-Gil et al., 2009).

The spectral type of the companion was found to be K5. Comparing with the masses of MS stars with the same spectral type ($\simeq 0.68\,M_\odot$ Gray, 1992), the companion star in HS 0218+3229 is undermassive. According to binary calculations, this disagreement can be explained if the secondary underwent considerable nuclear evolution before the onset of mass transfer (Schenker et al., 2002).

QZ Serpentis (QZ Ser) is a dwarf nova discovered during an outburst in 1998 (vsnet-obs 18349)[1]. A second outburst was detected in 2002 (vsnet-campaign 1281). Its orbital period was found to be 1.99 h from fits to the radial velocity of the Hα emission and absorption lines in the optical spectrum (Thorstensen et al., 2002b). They determined that the spectral type of the secondary is K4±2, this spectral class for the secondary is usually seen in dwarf novae with orbital periods around 6 h (Knigge, 2006), indicating that the companion is significantly too hot for its orbital period. It has been suggested that the secondary underwent considerable nuclear evolution and currently corresponds to the exposed helium enriched core of the originally much more massive MS star. However, atmosphere models for MS stars with temperatures hotter than ≃4000 K do not show evident features when He is enhanced, by as much as 50% of the mass fraction (Thorstensen et al., 2002b), therefore this suggestion has so far remained untested.

---

[1] http://www.kusastro.kyoto-u.ac.jp/vsnet/index.html

Table 6.1: Log of the COS observations of HS0218+3229 and QZ Ser.

Name	orbit	Date	UT time	Exposure time (s)
HS 0218	1	2012-12-22	06:31:07	1956
HS 0218	2	2012-12-22	07:49:21	1753
HS 0218	2	2012-12-22	08:20:19	853
HS 0218	3	2012-12-22	09:25:03	856
HS 0218	3	2012-12-22	09:41:14	1740
QZ Ser	1	2013-06-21	03:34:40	2317
QZ Ser	2	2013-06-21	05:10:18	2729
QZ Ser	3	2013-06-21	06:45:59	2729
QZ Ser	4	2013-06-21	08:21:40	2729

The purpose of the work presented here is to trace the CNO burning products in these systems, which can provide insight into the properties of their progenitors. Therefore, I will measure the abundances of carbon and nitrogen (i.e. the C/N ratio) from the analysis of the *HST*/COS ultraviolet spectroscopy.

6.3 COS spectroscopy

HS0218+3229 and QZ Ser were observed with COS in 2012 and 2013, respectively as part of programme 12870 in Cycle 20 (PI: B. Gänsicke). The log of the observations is shown in Table 6.1. The G140L grating was used centred at 1105 Å, which covers the wavelength range 1150 – 1800 Å with a resolution around of 0.75 Å.

6.4 Spectral fits

To measure the abundances of nitrogen and carbon, I proceed to perform fits to the COS spectroscopy. An important factor to compute the structure of the synthetic model (Section 3.1) is to know the major constituents of the atmosphere e.g. to determine whether the composition of the atmosphere is pure hydrogen (DA), pure helium (DB) or a mixture of both. Indeed, the dominant species in the atmosphere will also have crucial effects on the metal abundance determinations, since an atmosphere that is helium dominated is more transparent and therefore a lower metal abundance is required to fit the strength of the spectral metal lines (as the observations probe a larger column depth into the atmosphere). In contrast, a hydrogen atmosphere will lead to larger metal abundance determinations. However, since the interest lies on nitrogen and carbon determinations to calculate the ratio of these abundances, these effects will cancel out. Since the spectra of HS0218+3229 and

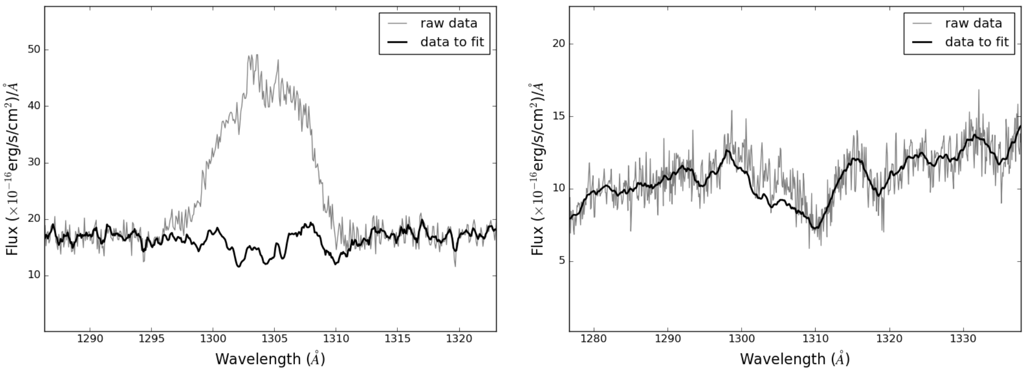

Figure 6.1: Night side extraction for HS0218+3229 (right) and QZ Ser (left). The effects of O i airglow emission at 1302 Å are highly reduced in case of HS0218+3229.

QZ Ser show the broad Lyman α absorption line which is a typical feature observed in DA white dwarfs, both systems present atmospheres with considerable amounts of H, therefore, I will use DA models to fit the spectra. In the case of HS0218+3229, the feature is narrower than in QZ Ser which indicates that the white dwarf is hotter.

Regarding the atmospheric parameters of these systems, the effective temperature and surface gravity, there are no previous estimates in the literature for these systems. In the case of HS0218+3229, I fixed $\log g$ to 8.0 ($M_{\rm WD} \simeq 0.6\,M_{\odot}$, which lies within the measured range Rodríguez-Gil et al. 2009), while for QZ Ser I fixed $\log g$=8.35 ($M_{\rm WD} \simeq 0.8\,M_{\odot}$), which corresponds to the mean mass of white dwarfs in CVs (Zorotovic et al., 2011)

Besides carbon and nitrogen with their strongest lines at C ii 1334.5,1335.7 Å and N i 1492.7,1494.7 Å, absorption lines of Si ii 1260.4,1264.7 Å, and at 1526.7,1533.5 Å, Al ii 1670,8 Å, and Mg i 1735.9,1737.6 Å are clearly identified (Figure 6.4). Therefore, I included these elements in the analysis.

A visual inspection of the bottom of the Lyman α absorption shows an additional flux from a second component, similarly as with GW Lib (Section 5.4.2), which I modelled as a constant flux in F_{λ} (k). Emission lines of He ii 1640 Å, N v 1240 Å, and Si iv 1400 Å are modelled with Gaussians. Lyman α airglow emission is masked out in the range 1200.50–1224.79 Å and 1194.08–1226.15 Å for QZ Ser and HS0218+3229, respectively. For the O i airglow emission at 1302 Å I performed the extraction from the night side of the observations (Section 2.3.4) to reduce its effects. While for HS0218+3229 there is a noticeable improvement that allows to distinguish the oxygen triplet, for QZ Ser the correction is very small, since most of the observations were taken on the night side (Figure 6.1). In both systems, the spectroscopy in the wavelength range 1290–1315 Å is replaced by their respective night side extracted spectra. I fitted these spectra in the range 1150–1850 Å using the MCMC method outlined in Section 3.2.

The parameters to fit are the effective temperature ($T_{\rm eff}$), the flux of the second component (k), and the abundances of silicon, magnesium, aluminium, carbon, and nitrogen. Hence the model is,

$$F_{\rm obs} = 4\pi S \times F_{\rm syn}(T_{\rm eff}, {\rm Si}, {\rm Mg}, {\rm Al}, {\rm Ca}, {\rm Ni}) + k. \tag{6.1}$$

There are two processes that need to be taken into account. For temperatures lower than $\sim$ 9000 K convection becomes very important, the convective flux can change by large factors even if the temperature in some layers changes by a small fraction and usually the initial computation of the structure of the white dwarf atmosphere fails to converge when the emitted flux of the model is required to have an accuracy of less than 1‰. Therefore, convection damping needs to be included, which runs the ATM code a few times until such convergence is reached, in addition the flux error accuracy needs to be increased (up to 30‰). When effective temperatures are higher than $\sim$ 25 000 K radiative levitation becomes important which requires an exhaustive choice of the frequencies in the SED to compute the structure of the atmosphere, and also requires hundreds of more lines. A visual inspection of the broad Lyman α absorption points out that neither HS0218+3229 nor QZ Ser have effective temperatures at which convection or radiative levitation are dominant. In order to confirm this prediction I fitted the spectra using a grid of pure hydrogen white dwarf models that covers 8 000–30 000 K (for the reasons mentioned above the surface gravity was fixed to 8.0 and 8.35 for HS0218+3229 and QZ Ser, respectively). From this initial fit, the effective temperatures can be constrained to be within 9 000–25 000 K. I set flat priors on the scaling factor (S) and the second component (k) to be always positive, and the logarithm of the abundances to be always negative.

Due to the large number of parameters, the procedure to fit the spectra is slightly different from the techniques used for G29-38 and GW Lib, where I could interpolate from pre-computed grids of white dwarf models. Instead, here the synthetic models are computed on the fly by running KAPPA, ATM, and SYN codes for the walkers drawn at each iteration of the MCMC. I set the mixing length of ML2/α=0.8 for the treatment of convective atmospheres.

In average the computation of a synthetic white dwarf model takes around 5–10 mins, consequently fitting the spectroscopic data of HS0218+3229 and QZ Ser with this procedure is very expensive in terms of computational time. Therefore, there is a need to improve the

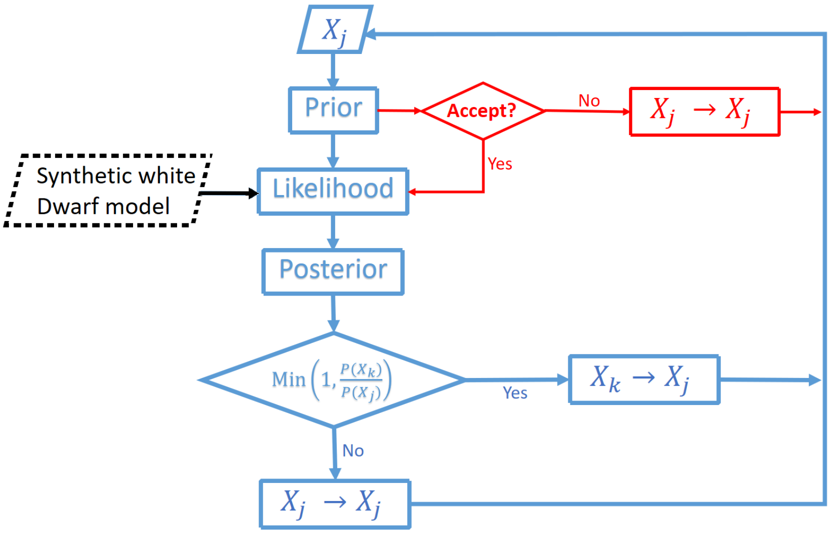

Figure 6.2: Flowchart describing the steps of the MCMC technique (see text for details).

time that the walkers spend to converge to an stationary state. The python package EMCEE, which was used to fit the ultraviolet spectroscopic data of G29-38 and GW lib, performs the steps shown in blue in Figure 6.2. If a walker contains a value that does not lie within the constraints given in the prior, the posterior probability is set to an extremely small number. As an example, if only one of the walkers, (X_1), does not satisfy the priors (e.g. contains a value for the silicon abundance $\log(\mathrm{Si/H})$ that is positive), then the posterior probability is automatically set to -10^{30}, and the synthetic spectrum needed to calculate the likelihood is not computed. Hence, running in parallel the 100 walkers that are sampling the parameter space, walker X_1, for which it is already known that the probability of being near the best solution in the parameter space is extremely low (-10^{30}), needs to wait for the remaining 99 walkers in the ensemble, which satisfied the priors, to finish their calculations (i.e.. to compute the models, and calculate the likelihood and posterior). Therefore, to make sure the walkers sample the parameter space within the constraints, I include the condition that all of them satisfy the priors before going into the likelihood which required the computation of the synthetic white dwarf models (red portion in Figure 6.2).

6.4.1 Results

Results are listed in Table 6.2, and the best fits are shown in Figures 6.3 and 6.4 for HS0218+3229 and QZ Ser, respectively.

For HS0218+3229, the effective temperature is found to be T_{eff}=$18\,462^{+221}_{-153}$ K, and the

Table 6.2: Best MCMC fit parameters for HS0218+3229 and QZ Ser for which their surface gravities were fixed to 8.0 and 8.35, respectively.

Parameters	HS0218+3229	QZ Ser
$T_{\rm eff}$ (K)	$18\,462^{+221}_{-153}$	$16\,337^{+164}_{-163}$
k ($\times 10^{-16}$ erg/s/cm^2/A)	1.6±0.2	3.4±0.2
log (C/H)	-5.9±0.5	-6.8±0.1
log (N/H)	$-3.95^{+0.17}_{-0.23}$	-3.37±0.06

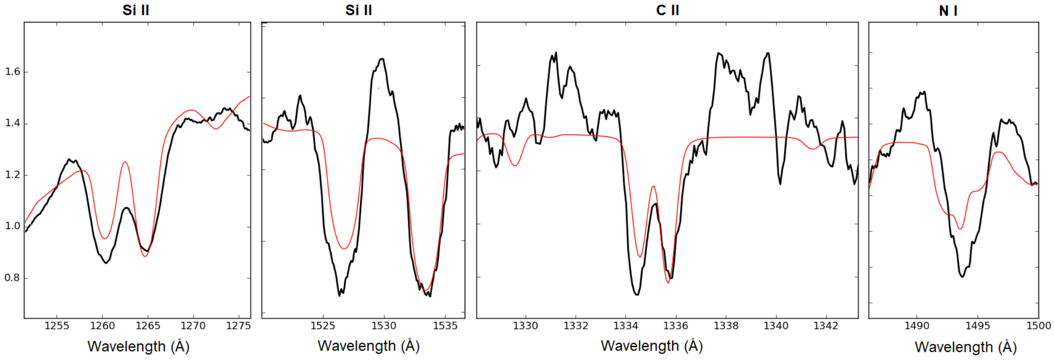

Figure 6.3: Best fit (red) to the COS spectroscopy (black) of HS0218+3229. From left to right: Si II at 1260.4,1264.7 Å, Si II at 1526.7,1533.5 Å, C II at 1334.5,1335.7 Å and N I at 1492.7,1494.7 Å.

additional flux contributed by the second component is $k = 1.6{\pm}0.2 \times 10^{-16}$ erg/s/cm^2/Å. The transition of C II at 1335.7 Å is fitted very well, however the ground state transition C II 1334.5 Å appears too strong for its statistical weight in the atmosphere of G29-38, therefore there is clear contamination by interstellar absorption lines, and interstellar contamination can also be identified in the bluer line of the two silicon doublets. The rightmost panel shows the strongest line of N I, which does not present a good fit. The overall fit is including all the nitrogen features, the next strongest lines are Ni II at 1411.9 Å which are located very close to the emission line of Si IV, and the nitrogen triplet around 1200 Å which is in the wing of Lyman α. Thus, N I 1493 Å might suffer of additional contamination, e.g. another metal transition that is not considered in the fits, such as iron or chromium, or interstellar absorption. Regardless of this systemic uncertainty, as expected the best fit provides a considerable enhancement of nitrogen (log (N/H) = $-3.95^{+0.17}_{-0.23}$) and the carbon abundance is subsolar (log (C/H) = $-5.9{\pm}0.5$), where the uncertainties are purely statistical.

As mentioned above, the effective temperature for QZ Ser is cooler than in HS0218+3229, $T_{\rm eff}$=$16\,337^{+164}_{-163}$ K. The second component contributes an additional constant flux of $k = 3.4{\pm}0.2 \times 10^{-16}$ erg/s/cm^2/Å. Similarly to HS0218+3229 there is a considerable enhance-

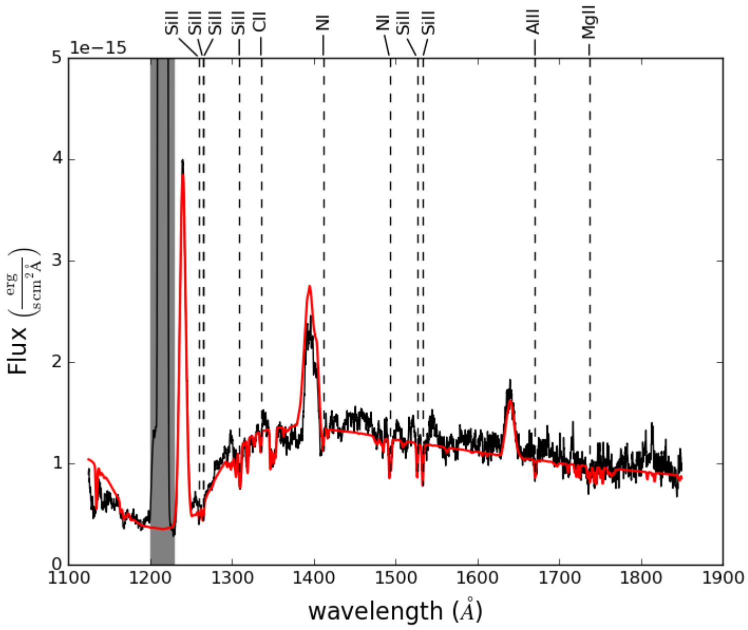

Figure 6.4: Best fit (red) to the COS spectroscopy of QZ Ser (black), corresponding to an effective temperature of T_{eff}=16 337 K (the surface gravity was fixed to log g=8.35). Additional flux from the second component was found to be $3.4 \pm 0.2 \times 10^{-16}$ erg/s/cm^2/Å. The emission lines were modelled with Gaussians. The grey band indicates the geocoronal airglow emission of Lyman α. The most prominent photospheric absoprtion lines are labelled.

ment of nitrogen ($\log(\mathrm{N/H}) = -3.3 \pm 0.06$), while the carbon abundance is subsolar ($\log(\mathrm{C/H}) = -6.8 \pm 0.1$).

A visual inspection to the blue wing of the broad Lyman α absorption line in the spectrum of QZ Ser (Figure 6.4) shows that the fit overestimates the flux level. One explanation can be the effects of helium which is deposited on the white dwarf by the accreted material. As explained above, while the CV evolves towards shorter orbital periods, the donor develops a deeper convective layer which brings up the processed material from the core, which independently of the nuclear burning that the star underwent (PP or CNO), results in the enrichment of helium. In the ultraviolet spectroscopy the only strong feature of helium is He II at 1640 Å, which is in emission, hence the main effect seen in the spectrum as a consequence of a significant helium enrichment of the atmosphere is the change of the spectral slope, which will be analysed in more detail in Section 6.6.1.

To understand the change of the C/N ratio during the evolution of CVs that undergo (or not) the thermal time scale mass transfer I will perform numerical simulations with

MESA.

6.5 Stellar evolution of the evolved companion with MESA

To calculate the chemical abundances on the surface of the companion stars in the failed SNIa, evolutionary simulations were performed with the Modules for Experiments in the Stellar Astrophysics (MESA Paxton et al., 2011, 2013, 2015). MESA is an open source code that performs stellar evolution over a wide range of stellar masses. STAR is a one-dimensional module that solves simultaneously the fundamental equations of the stellar structure (hydrostatic equilibrium, mass conservation, energy transport, and energy conservation) together with the composition profile and nuclear reactions. Therefore, the changes of the thermodynamical quantities and the structure of the star can be followed along its evolution. Here, I will describe the basic physical input that I adopted in the simulations using MESA version 9575.

6.5.1 Physical inputs

Nuclear reactions

MESA provides a large number of relevant nuclear reactions (e.g. hydrogen and helium burning) that are tabulated in the NET module. A net is defined by a set of isotopes and a set of reactions. As explained in Section 1.1.1, the nuclear reactions in the core depend on the conditions. For low central temperatures the PP chain dominates. The three branches of this chain are taken into account which includes isotopes of ^{1}H, ^{3}He, ^{4}He, ^{7}Li, ^{7}Be, and ^{8}B. If the density drops to < 1.8 g/cm^3 and the temperature in the core increases to 15×10^6 K, then the CNO cycle takes place, the four branches of the CNO cycles are included, which accounts for additional isotopes: ^{12}C, ^{13}C, ^{15}O, ^{16}O, ^{17}O, ^{13}N, ^{14}N, ^{15}N, ^{17}F, ^{18}F, and ^{19}F. For even higher temperatures and pressures, the rate of electron capture exceeds the rate of beta-decay and the hot CNO starts to breakout, therefore the isotopes of ^{18}O, ^{18}Ne and ^{19}Ne are included which are part of the reactions in the three hot CNO cycles.

Chemical elements

An important input of the stellar evolution is the initial chemical composition of the star when entering the ZAMS. They are defined by the mass fraction of hydrogen (X), helium (Y), and the rest of the elements (metals, Z), therefore $X+Y+Z=1$. The He mass fraction for creating the pre-MS is calculated as 0.24 + 2× Z_0, where Z_0 is the initial metallicity, which was set to 0.02.

Opacity

The local opacity inside the stellar structure is calculated by interpolating pre-compiled tables. These are radiative opacity tables taken from OPAL, which determine the opacity for a given chemical composition (X, Z), temperature ($\log T$, $3.75 \leqslant \log T \leqslant 8.70$) and density ($\log R = \log \rho - 3 \times \log T$, $-8 \leqslant \log R \leqslant +1$). The metal distribution is based on Grevesse & Noels (1993) solar abundances.

Mixing length for convection

The mixing length theory of convection is defined as $l = \alpha H_p$, where l is the mixing length, α is a free parameter, and H_p is the pressure scale height. It assumes that an element of fluid rises in pressure equilibrium and when it mixes with its surroundings, releases its excess heat energy. MESA includes several implementations in the MLT module, however the standard theory presented by Cox & Giuli (1968) has been set for the simulations, which assumes optically thick material. The effect of pressure from convective turbulence has been excluded.

Magnetic braking

Rappaport et al. (1983)'s prescription, which is given in equation 1.9, is used to model magnetic braking, where the gamma exponent was fixed to $\gamma = 3.0$. MESA activates the magnetic braking whenever the donor star develops a radiative core, and the mass is lower than 1.4 $M_\odot$, such that the envelope is not significantly radiative.

6.5.2 Procedure for the evolution of the donor star in the CV

Each track of a given CV is defined by the initial masses of both components ($M_{\rm WD}$ and $M_{\rm donor}$) plus the orbital period ($P_{\rm orb}$). These three parameters define the size of the Roche lobe of the donor star. The binary evolution starts with a considerably evolved MS, which is about to fill its Roche lobe, (read from a pre-computed model), plus the white dwarf which is considered as a point source. The pre-computed MS model has been prepared separately before by evolving an isolated star from the ZAMS setting the physical inputs as defined above. The evolution during the MS phase is stopped when its photospheric radius (`photosphere_r_upper_limit`) reaches 95% of the Roche radius that is defined by the binary configuration for the given track in which the pre-computed model will be used.

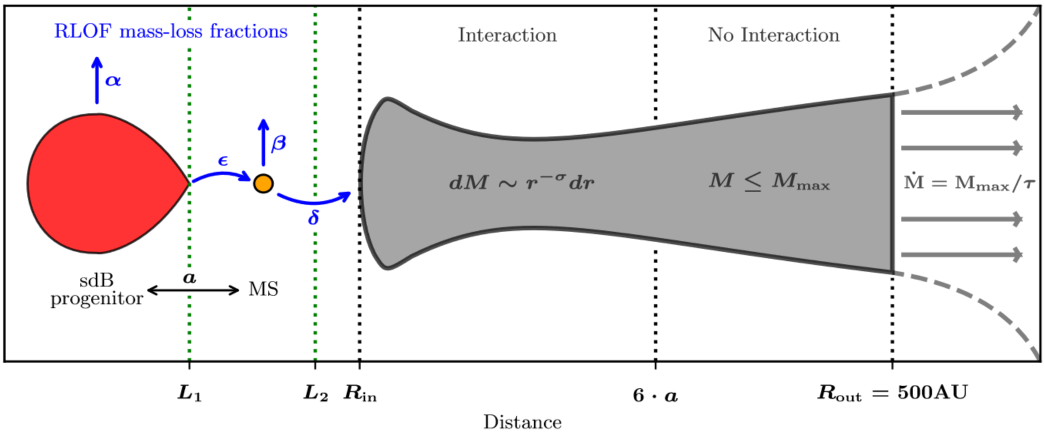

Figure 6.5: Illustration of the Roche lobe overflow model implemented in MESA, which includes the formation of a coplanar toroid. dM is the mass distribution, which depends on the mass distribution constant (σ), $\mathrm{M}_{\mathrm{max}}$ is the maximum mass of the disc, and τ is the maximum lifetime of the disc. Figure taken from Vos & Vučković (2017).

When the donor overflows its Roche lobe, the mass transfer is modelled according to two different scenarios during the evolution of the binary. In the non-conservative case the total mass of the binary system is not conserved (i.e. M_{WD} is constant). In the conservative case the total system mass is conserved and the white dwarf mass grows. Which of the two scenarios takes place is defined by the rate of mass transfer. If the mass transfer reaches the regime at which the accreted material can be steadily burnt on the white dwarf surface, then the mass transfer is conservative. For lower accretion rates ($\lesssim 10^{-7}\,M_{\odot}$/yr), it is non conservative, which translates that most, if not all, the accreted material is ejected from the system during nova eruptions (Gallagher & Starrfield, 1978; Prialnik et al., 1982; Bildsten et al., 2007). The mass transfer limit that separates the conservative and non conservative cases is given by Wolf et al. (2013), which is a function of the white dwarf mass (Figure 1.17).

The Roche lobe overflow model used in MESA includes the formation of a circumbinary disk. A visual representation of this model is shown in Figure 6.5. The mass-loss rate is calculated based on the Roche-lobe overflow fraction using the prescription of Ritter (1988) and Kolb & Ritter (1990). The amount of mass that is lost from the binary due to mass transfer can be controlled by the α, β, δ and ϵ parameters as described in Tauris & van den Heuvel (2006). Therefore, the transfer efficiency is given by 1-α-β-δ, where,

- α is the mass lost as a fast wind from the vicinity of the donor star. This is modelled as a spherically symmetric outflow.
- β corresponds to the matter transported from the donor to the vicinity of the accretor

and ejected as a fast isotropic wind.

- δ is the mass lost from the donor through the outer Lagrange point (L_2) and is modelled as a circumbinary coplanar toroid.
- ϵ is the mass transferred through the inner Lagrange point (L_1) and accreted by the white dwarf ($\epsilon = 1 - \alpha - \beta - \delta$)

Therefore, the nova eruptions are defined as α=δ=0, and β=1. In other words, this choice of values for these four parameters means that 100% of the material accreted onto the white dwarf is expelled from the white dwarf as fast wind (non-conservative scenario). In the conservative case, as mentioned above, it is not known how the growth of the white dwarf is related to the accretion rate, i.e. the fraction of the accreted material that remains on the white dwarf. Here, I take the highest value possible that MESA allows before it runs into numerical problems (90%, $\beta = 0.1$), and set $\alpha = \delta = 0$ during conservative mass transfer.

Another factor to consider when the matter is ejected is the angular momentum that the particles carry away when leaving the system. To include this angular momentum lost from the system, I use the expression of King & Kolb (1995),

$$J_{\rm spec} = M_{\rm WD}\, M_{\rm donor} \left(\frac{G\, a}{M_{\rm WD} + M_{\rm DONOR}} \right). \tag{6.2}$$

Therefore, I implement a special subroutine (`use_other_extra_jdot`) in the `src/run_binary_extras.f`

6.5.3 Evolutionary tracks for the donor

Here I will present the evolutionary simulations I ran to trace the changes in the abundances of C and N. As said before, every track depends on three parameters: the white dwarf mass ($M_{\rm WD}$), the donor mass ($M_{\rm donor}$), and the orbital period ($P_{\rm orb}$). To begin with, I will describe the range of the parameters used in the simulations.

A binary system with a mass ratio of $q_{\rm crit} = 2$ will definitively undergo thermal time scale mass transfer both in the conservative or non conservative scenarios (Figure 1.16). In addition, to ensure that the CNO cycle operates in the donor star, the initial mass has to be higher than $M_{\rm donor} = 1.3\, M_{\odot}$, therefore a good estimate for the initial white dwarf mass is $\sim 0.7\, M_{\odot}$, and the mass growth during the thermal time scale mass transfer will push the white dwarf mass into the mass regime observed among CVs (Zorotovic et al., 2011). Since my interest lies in the evolution of the chemical composition of the donor star, and due to the fact that the white dwarf is considered as a point source, it will not have any effect on the evolution of the donor apart its gravitational influence. Therefore, I fixed the white dwarf mass to 0.7 $M_{\odot}$.

The mass of the donor is chosen to be larger than the mass of the white dwarf such that it can experience unstable mass transfer ($q > 5/6$, Section 1.2.1). The upper limit is defined based on previous simulations that locate the masses of SSSs within the range 0.6 $M_{\odot} \lesssim M_{\rm donor} \lesssim 2.0\, M_{\odot}$ (Kalomeni et al., 2016), and considering the mass lost from the pre-CV phase to the SSS phase, the donor masses were chosen to be in the range 0.8–3.0 $M_{\odot}$ with steps of 0.1 $M_{\odot}$. Finally, the initial orbital periods range from 0.5–2.0 days in steps of 0.1 days.

Stopping conditions

The evolution tracks of the binaries are stopped for whichever of the following conditions is reached first:

- The mass of the white dwarf is 1.44 $M_{\odot}$, at which point the white dwarf will ignite CO burning and become a SNIa
- The accretion rate is larger than $10^{-5}\, M_{\odot}$/yr, which leads to the formation of a red giant structure, and MESA gets into numerical problems.
- The time reaches the age of the Universe (13.8×10^9 years).
- The mass of the donor reaches 0.1 $M_{\odot}$, lower masses will enter the brown dwarf regime.

6.5.4 Results

There are three main situations that can occur and I will use three tracks as examples to explain in detail the changes in the mass transfer rate, the change of the abundances of hydrogen, helium, carbon, and nitrogen on the surface of the donor, and the masses of the white dwarf and the donor. These tracks correspond to the evolution of a normal CV, a binary undergoing the thermal time scale mass transfer and then morphing into a CV and a system that explodes as a SNIa after undergoing the thermal time scale mass transfer. These evolutionary tracks are shown in blue, green, and red in Figures 6.6, 6.7, and 6.8.

Evolution as a normal CV

The evolution of a canonical CV is represented by the blue track that corresponds to a binary with initial masses of 0.7 $M_\odot$ and 1.4 $M_\odot$ for the white dwarf and the donor star, respectively, with an initial orbital period of 0.55 days (=13.2 h).

Note the mass of the donor lies in the regime to undergo the CNO burning, therefore it is expected to see the CNO products during the evolution of this system. The donor star has initially solar abundances, i.e. $\log(\mathrm{C/N}) = 0.6$ and $\log(\mathrm{He/H}) = -1.09$ (bottom panels of Figures 6.6 and 6.8, respectively). The mass transfer starts at the age of 4.26×10^6 yr and an orbital period of 13.19 h. The mass transfer quickly increases ($>10^{-8}$ $M_\odot$/yr), however it falls short of the limit required for a white dwarf mass of 0.7 $M_\odot$ to undergo a stable shell burning ($10^{-7.13}$ $M_\odot$/yr, Wolf et al. 2013 dashed line in the middle panel of Figure 6.6). At the age of 2.15×10^7 yr (P_orb = 5.05 h) the donor mass has reduced to the same mass of the white dwarf, $q \simeq 1$ (dotted line in top panel in Figure 6.6), causing a slight decrease of the mass transfer rate. The top panel in Figure 6.8 shows the depth of the convective regions in mass fraction as a function of the age, where the surface and center of the star correspond to 0 and 1, respectively. The top and the bottom of the convection zone are represented with dashed and solid lines, respectively. At the later age mentioned, the extent of the convective envelope starts to deepen, the $\log(\mathrm{C/N})$ ratio starts to invert, and the $\log(\mathrm{He/H})$ ratio begins to increase until they settle to -1.77 and -0.81, respectively. By then (8.24×10^7 yr) the mass of the donor has reduced to 0.21 $M_\odot$ becoming fully convective. Hence, the mass transfer stops and the system enters into the period gap when the orbital period is 3.8 h. The system spends most of its lifetime in the period gap and leaves the gap at the age of 1.99×10^9 yr when its orbital period is 2.08 h. The track then terminates because it reached the maximum age set as one of the stopping conditions.

SNIa

The evolution of a binary system that explodes as a SNIa is represented in red, which correspond initial masses of 0.7 $M_\odot$ and 2.3 $M_\odot$ for the white dwarf and the donor, respectively and an orbital period of 0.9 days (=21.6 h).

At the age of 4.02×10^6 yr mass transfer starts which increases drastically above the limit for stable hydrogen burning ($10^{-7.13}$ $M_\odot$/yr, Wolf et al. 2013 dashed line in middle panel of Figure 6.6). This phase is very short, as clearly seen in middle panel of Figure 6.7 it lasts only 0.54×10^6 yr. During this phase the orbital period reduces from 20.12 h to

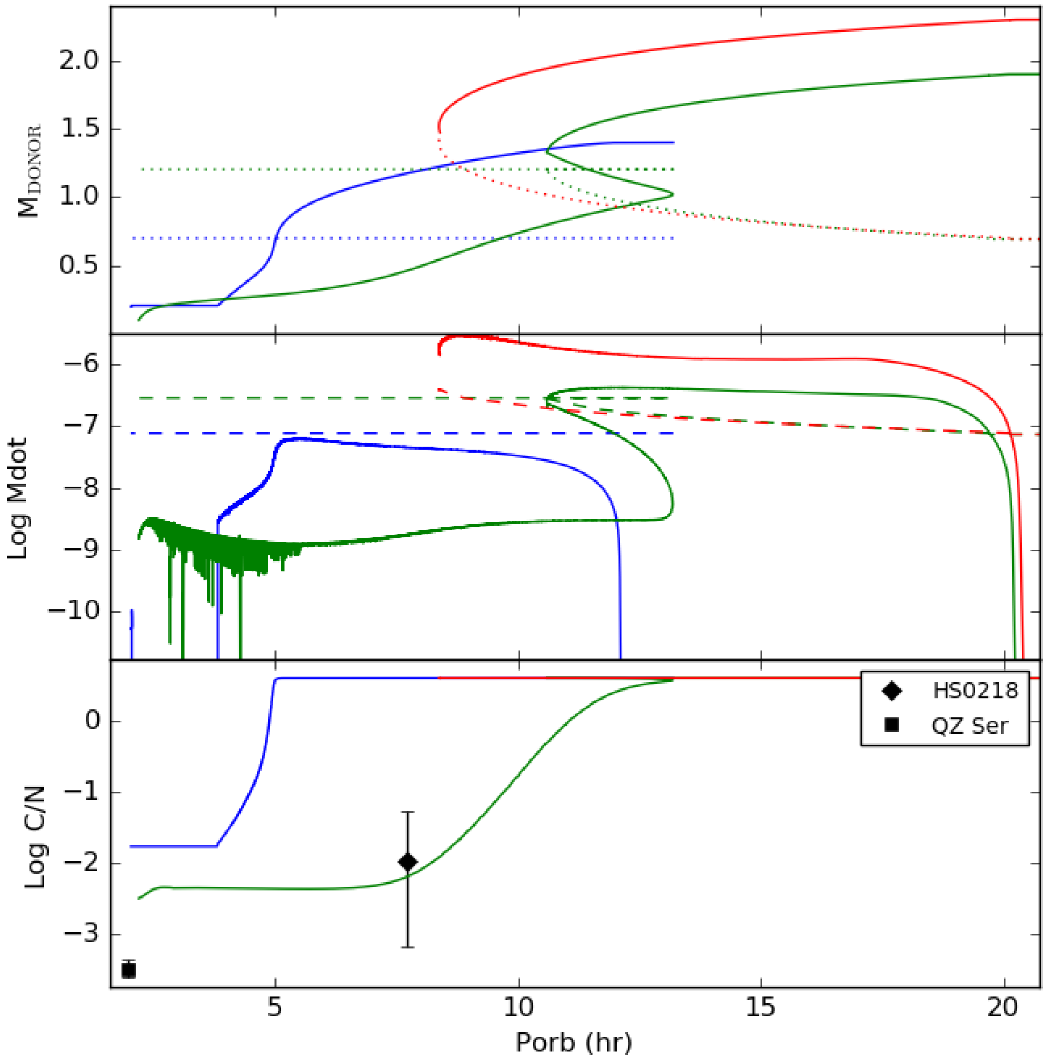

Figure 6.6: Three evolutionary simulations representing a CV (blue), a SNIa (red) and a failed SNIa (green), where their initial binary parameters are $M_{\text{donor}} = 1.4, 2.3, 1.9\, M_{\odot}$, $P_{\text{orb}} = 0.55, 0.9, 0.9$ days and $M_{\text{WD}} = 0.7, 0.7, 0.7\, M_{\odot}$. The solid lines from top to bottom correspond to the mass of the donor, the mass transfer rate, and the log (C/N) ratio as function of the orbital period, also the mass of the white dwarf (dotted line) and the mass transfer limit (dashed line) dictated by Wolf et al. (2013) are included. The bottom panel shows the log (C/N) ratio measured from fits to COS spectroscopy of HS0218+3229 and QZ Ser. In the red track ($M_{\text{WD}} = 0.7\, M_{\odot}$, $M_{\text{donor}} = 2.3\, M_{\odot}$ and $P_{\text{orb}} = 0.9$ days = 21.5 h), the white dwarf reached the Chandrasekhar limit at $P_{\text{orb}} = 8.4$ h and explodes as a SNIa.

8.4 h and when the mass ratio comes close to unity and the mass transfer start to decrease, the white dwarf mass reaches the Chandrasekhar limit, resulting in a SNIa. By the time

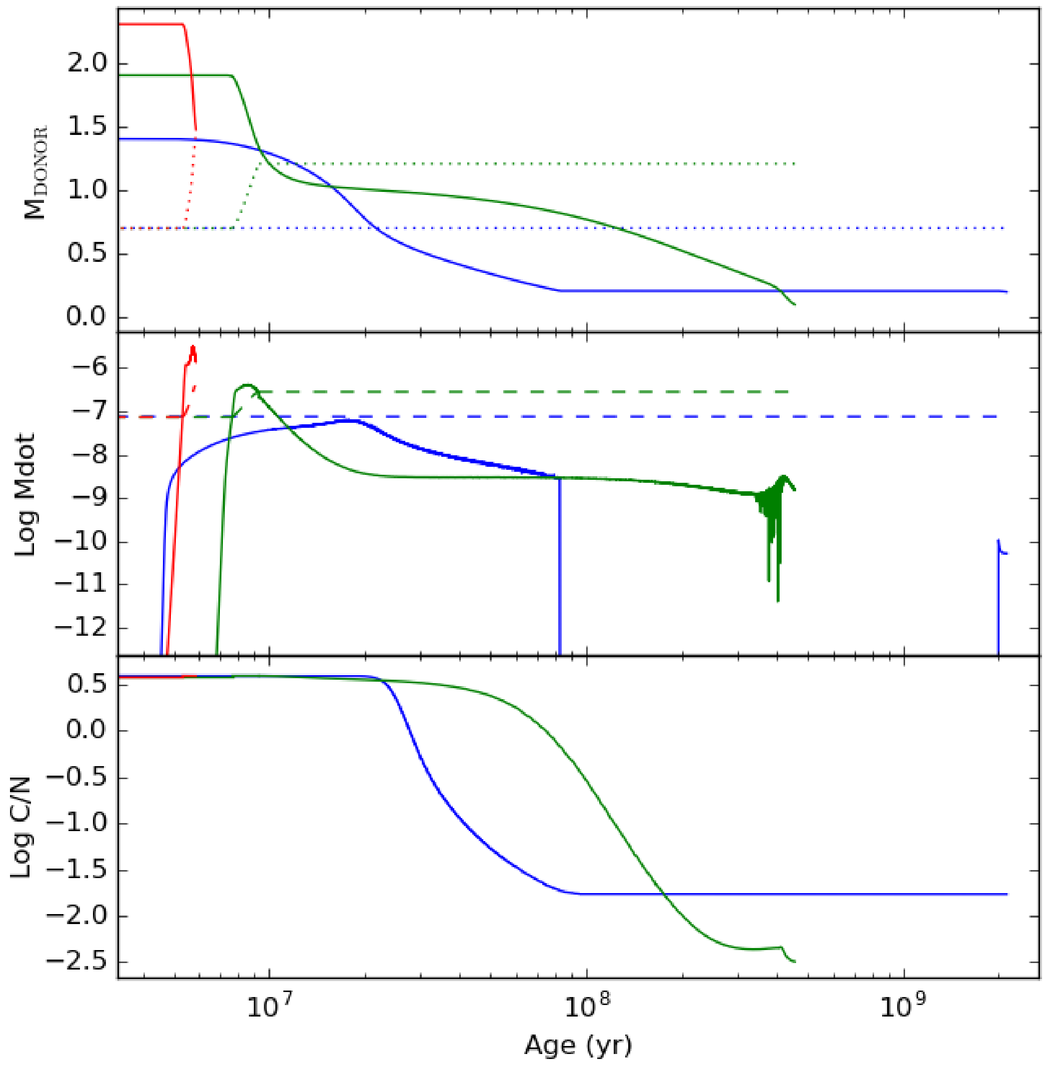

Figure 6.7: Same as Figure 6.6 but the x-axis corresponds to the age of the systems.

the white dwarf exploded, the donor did not develop a deep convective envelope, therefore the abundances remained as solar during the evolution (bottom panels in Figure 6.6 and 6.8).

Failed SNIa

This track (green) is representative of the evolutionary pathways for HS0218+3229 and QZ Ser. The track shown corresponds to the evolution of a binary composed by a white dwarf of mass 0.7 $M_\odot$ with a donor of 1.9 $M_\odot$ which have an initial orbital period of 0.9 days

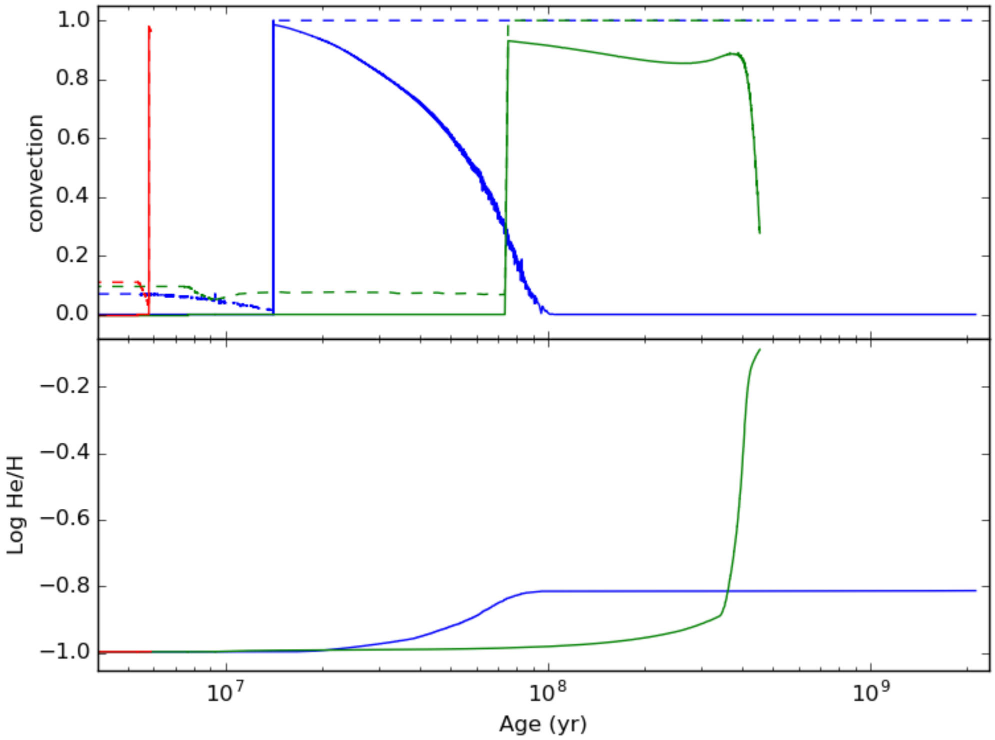

Figure 6.8: Colours are defined in the same way as in Figure 6.6. *Top:* Mass fraction of the largest convection zone ($M_{\rm conv}/M_{\rm donor}$) where the centre and the surfce correspond to 1 and 0, respectively. The top and the bottom of the convection zone are represented by dashed and solid lines, respectively. *Bottom:* Change of the helium to hydrogen abundance during the evolution.

(=21.6 h).

At an age of $5.5{\times}10^6$ yr mass transfer starts which increases rapidly to the regime at which the white dwarf can steadily burn the accreted material. During this shell burning phase, which is very short ($1.59{\times}10^6$ yr), the orbital period is significantly reduced from 19.63 h to 10.62 h. At the end of the shell burning phase the white dwarf has grown in mass to 1.2 $M_\odot$. At that moment the masses of the two stars are very similar, as a consequence the mass transfer rate drops considerably, and the system detaches, evolving slightly back towards longer periods. However, angular momentum losses (mainly magnetic braking) bring the stars close together again. Convection starts to become important and the log (C/N) ratio starts to invert until it settles to a value of −2.36, while log (He/H) continues to increase towards values larger than −0.2. This system does not enter the ≃3–2 h period gap, because at that orbital period the donor still does not become fully convective

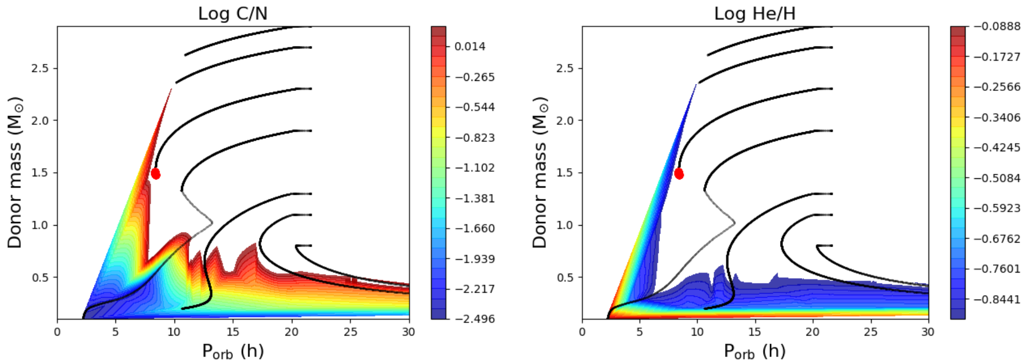

Figure 6.9: MESA simulations for binary systems composed by a white dwarf of mass $M_{\rm WD} = 0.7\,M_\odot$, with MS companions of masses 0.8–3.0 $M_\odot$ and initial orbital periods of $P_{\rm orb,i} = 0.9$ days. Overplotted for orientation are few tracks for donor masses of $M_{\rm donor} = 0.8, 1.1, 1.3, 1.9, 2.3, 2.7, 2.9\,M_\odot$ (black lines from bottom to top). The red dot represents the position in the $M_{\rm donor} - P_{\rm orb}$ plot at which the white dwarf mass in that track reaches $1.44\,M_\odot$. The colour intensity corresponds to the log C/N ratio (left) and the log He/H (right).

(top panel Figure 6.8). The track was stopped because the mass of the donor reached $0.1\,M_\odot$.

An important fact to note here is that the failed SNIa continue accreting in the period gap, indicating that a large fraction of CVs placed in the period gap are likely to be failed SNIa[2].

An important fact shown in the bottom panel in Figure 6.6 is that this track qualitatively describes the measured C/N ratio for HS0218-3229 within the uncertainties. However, with *Gaia* data release 2, I will be able use the MCMC fitting technique adding the distance as prior providing more accurate estimates of the surface gravity and the effective temperature (and consequently the mass and radius of the white dwarf). Moreover the time-averaged accretion rate is a function of the quiescent effective temperature (Townsley & Gänsicke, 2009; Townsley & Bildsten, 2003). Therefore, besides the orbital period and the C/N ratio measurements, additional knowledge of the mean accretion rate and mass of the white dwarf can constrain the progenitors of HS0218+3229 which can be extended to other post super-soft X-rays source systems.

---

[2] This was the motivation to observe the systems in the period gap. In February 2018, I obtained VLT/XShooter spectroscopy of KT Eri, AD Men, J0648+0656, V348 Pup, YZ Cnc, GZ Cnc, V351 Pup, J1128-3448, J1200-1526, V1258 Cen, TU Men, KZ Gem, AR Pic, and V1258 Cen. These observations cover from the ultraviolet to near infrared, which I will analyse these data to find the spectral type since the donor in these systems are hotter than canonical CVs for the same orbital period (Knigge, 2006)

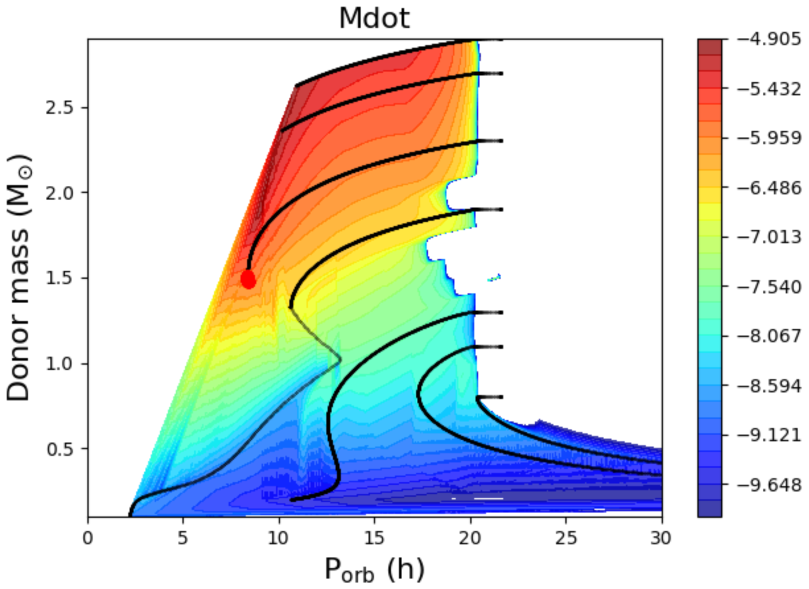

Figure 6.10: Same as Figure 6.9. The colour intensity corresponds to the log $\dot{M}$ ($M_\odot$/yr).

Constraining the parameter space for the formation SNIa and CVs

The study to estimate the formation rate of the different kind of CVs is based on population synthesis (Nelemans et al., 2001; Politano, 1996, 2004; Podsiadlowski et al., 2003; Chen et al., 2014; Goliasch & Nelson, 2015; Wijnen et al., 2015). These simulations require large coverage of the parameter space, considerable number of parameters and long evolutionary time scales, resulting in expensive computing needs. Therefore, in order to make the computations tractable, it is common to make several assumptions, e.g. to exclude the effects of the internal chemical evolution of the donor. A problem that population syntheses face is the incomplete physical description of all the relevant processes during the different pathways of evolution, starting from the birth of the primordial binaries to the long-term evolution of CVs. Here, I propose first to make a comprehensive exploration of the parameter space of different binary evolution pathways that pre-CVs can follow.

I build intensity colour diagrams for initial white dwarf mass of 0.7 $M_\odot$ together with different companions with masses $M_{\rm donor}$=0.8–3.0 $M_\odot$(in steps of 0.1 $M_\odot$) with an initial orbital period of 0.9 days for all the systems. The orbital period changes while the donor is losing mass.

Figure 6.10 shows the $M_{\rm donor} - P_{\rm orb}$ plane colour-coded by the logarithm of the mass transfer rate. In general, we can see that systems with large initial donor masses reach high mass transfer rates (exceeding $10^{-6}\,M_\odot/\mathrm{yr}$), in these situations MESA develops numerical problems since it can not handle the large amount of accretion onto the white dwarf. In contrast, lower masses for the donor lead to lower accretion rates ($< M_\mathrm{crit}$), which can evolve either towards shorter or longer orbital periods as CVs. Once the criterion for stability of mass transfer does not apply any longer (Section 1.2.1) the mass transfer drops quickly because the stars tend to detach. Whether they continue accreting will depend on the efficiency at which angular momentum is removed from the system, where magnetic braking is the dominant source at longer periods. Hence the future evolution will depend on the conditions of the donor star, e.g. having a radiative core with a thin convective envelope.

The surface chemical composition of the donor stars is shown in Figure 6.9 for carbon and nitrogen (left) and for helium and hydrogen (right). The primordial composition of the donor was set to be solar, and during the evolution towards shorter orbital periods the C/N ratio decreases. This result agrees with Kalomeni et al. (2016) who found that this ratio ranges from 0.003 to 0.03 for CVs with evolved donors. As explained above these changes in the C/N surface abundances result from the core undergoing CNO burning. The slowest reaction in the CN portion of the cycle is $^{14}\mathrm{N} + \mathrm{p} \longrightarrow {}^{15}\mathrm{O} + \gamma$ which causes ^{14}N to build up and ^{12}C to deplete. The second part, the NO portion of the cycle is more than three order of magnitudes less numerous, resulting that it can not replenish the ^{12}C to complete the second loop in the cycle. Regarding the helium abundance, helium increases however it does not become the dominant species.

In general, I find that binaries containing a white dwarf of a mass of $0.7\,M_\odot$ and having companions with masses within $\simeq 1.5 - 2.5$ experience a thermal time scale mass transfer phase with accretion rates between $10^{-7.13}\,M_\odot/\mathrm{yr}$–$10^{-6.5}\,M_\odot/\mathrm{yr}$. During this phase the orbital period decreases considerably (by few hours) in a very short period of time, $\lesssim 10\,\mathrm{Myr}$.

6.6 Discussion

6.6.1 Observable signatures of the He/H ratio

To find the C/N ratio in HS0218+3229 and QZ Ser I made use of DA models, however, as mentioned above, these two systems have been suggested to be descendants of SSSs, therefore according to the theory, at some point during the evolution of these systems towards shorter orbital periods, the mass donor will start to develop a deeper convective envelope dredging up the material processed in the core, and hence it results that at some point the material that is accreted on the white dwarf surface becomes He rich. Indeed, the optical

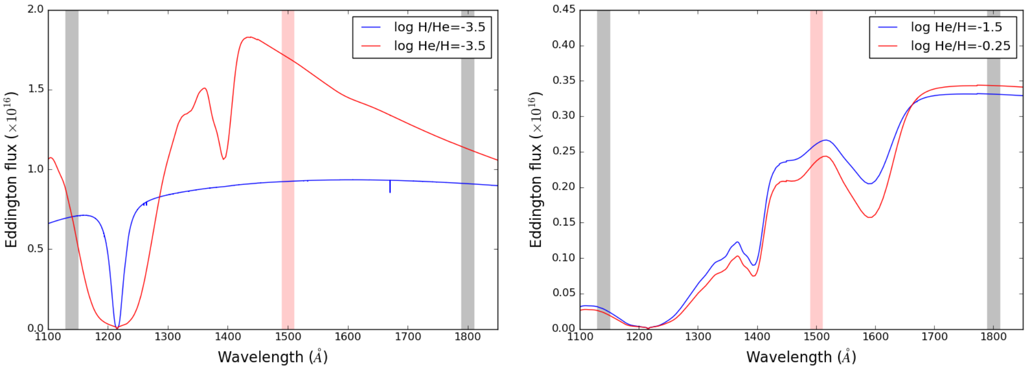

Figure 6.11: *Left:* synthetic spectra for hydrogen (red) and helium (blue) dominated atmospheres. *Right:* H/He mixed atmospheres that show very similar spectral slope behaviour, even though helium fractions differ significantly. Gray bands (1130–1150 Å and 1790–1810 Å) indicate the regions used to calculate the flux, which is normalised by the flux within the light red band (1490–1510 Å). These fluxes are used to perform the analysis of the change of the spectral slope (see text for details).

spectrum of HS0218+3229 shows strong emission lines of the Balmer series and He in its neutral and ionised states (Rodríguez-Gil et al., 2009; Golysheva et al., 2012), and while Balmer lines and He lines are more prominent in the optical (Figure 1.6), the COS spectra in both systems show clear emission of He II at 1640 Å. However, these emission lines do not provide a quantitative diagnostic on the He/H ratio.

As illustrated in the left panel in Figure 6.11, at ultraviolet wavelengths the main distinction between a DA and a DB white dwarf of the same temperature is given by the slope of the flux. Therefore, I performed an analysis of the sensitivity of the slope of the flux as a function of the H/He ratio. A direct method to analyse the slope of the spectrum is integrating the flux in a narrow wavelength ranges which are close to both ends of the spectrum, and normalise these integrated fluxes by the integrated flux in a narrow wavelength range that lies in between of these two. Following this procedure in a pure He atmosphere white dwarf, the flux in the short wavelength region will be less than one, in contrast the flux at longer wavelengths will be larger than one. In the case of the wavelength coverage of COS/G140L, which is the set up used for the observations of HS0218+3229 and QZ Ser, the two ranges chosen are 1130–1150 Å, which is in the blue wing of the broad Lyman α absorption, and 1790–1810 Å. The integrated flux in these two ranges are normalised by the flux within the 1490–1510 Å wavelength range. I performed these measurements on white dwarf models spanning a range of He/H ratios. For this purpose, I computed white dwarf models fixing the surface gravity to 8.35 (which corresponds to the average white

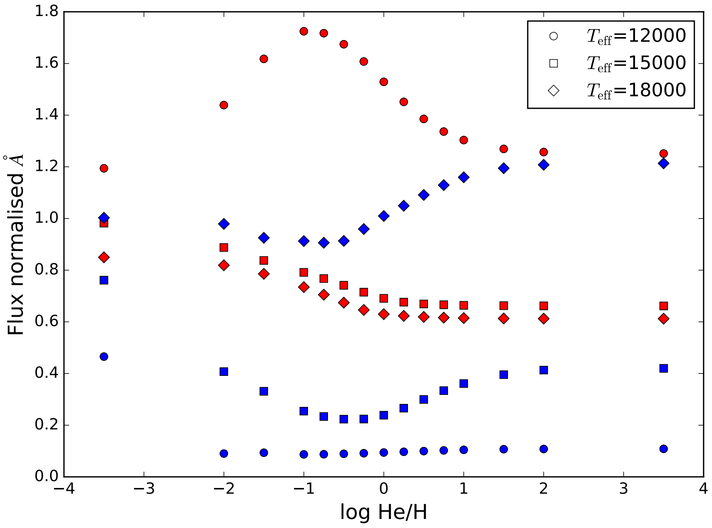

Figure 6.12: Flux ratios obtained from the wavelength ranges 1130–1150 Å/1490–1510 Å (blue) and 1790–1810 Å/1490–1510 Å (red).

dwarf mass in CVs, Zorotovic et al. 2011) and $T_{\rm eff}$=12 000, 15 000, and 18 000 K. For each effective temperature the H/He ratio is varied from a pure H ($\log(\mathrm{He/H}) = -12.00$) atmosphere to a pure He ($\log(\mathrm{H/He}) = -12.00$, note the inversion of the abundances) atmosphere. For the convective atmospheres, I set the mixing length parameter to ML2/α=1.0 .

Figure 6.12 shows these flux ratios as function of log He/H. The curves differ for the different effective temperatures, and some of the curves show an inversion which makes impossible to constrain the relative fraction of He e.g. the same flux ratio is obtained for $\log(\mathrm{He/H}) = -0.25$ and $\log(\mathrm{He/H}) = -1.5$ at longer wavelengths, in the case of $T_{\rm eff}$=12 000 K, while its counterpart at shorter wavelength is roughly flat for both log (He/H) (right panel in Figure 6.11). This analysis demonstrates that, given data of sufficient quality, it may be possible to directly measure the He/H ratio for systems with $T_{\rm eff} \gtrsim 15000$ K.

6.6.2 Side project: TYC6760-497-1, the first pre-supersoft X-rays source, (Parsons et al., 2015, MNRAS, 452, 1754)

TYC6760-497 was found during the search of white dwarf plus F, G, and K MS binary systems. This type of binary is important since, later in their evolution, they will become candidate progenitors of SNIa, either for the single of double degenerate channels, double white dwarfs or white dwarf plus evolved MS binaries, respectively (Parsons et al., 2016).

The optical spectrum of TYC6760-497-1 is totally dominated by the F8-type MS star. The existence of a white dwarf as part of this binary was suggested by the far ultraviolet excess detected in the *GALEX* (Morrissey et al., 2007) survey, and subsequently confirmed with *HST* ultraviolet observations (Parsons et al., 2015). The mass ratio of TYC6760-497 corresponds to roughly 2.1 and falls above the critical mass ratio for thermal time scale mass transfer ($q_{\rm crit}$ = 1.4–1.48), indicating that this system is likely to evolve into a super-soft X-rays source (Figure 1.16).

I performed MESA simulations following the same procedure explained above to investigate the future of TYC 6760-497-1. We assumed the initial masses of the two stars to be 1.235 $M_\odot$ and 0.63 $M_\odot$ for the donor and the white dwarf, respectively. The black line in the top panel of Figure 6.13 shows the predicted mass transfer rate for TYC 6760-497-1 versus the orbital period. At an age of around 5 Myr (corresponding to an orbital period of 11.9 h), mass transfer starts. The mass transfer rate will rapidly increase as the system is thermally unstable, but does not reach the limit for stable hydrogen burning until the system reaches an orbital period of 6.2 h (13.1 Myr from now). At this point, mass transfer becomes conservative, the mass transfer rate increases significantly, and the white dwarf mass grows due to the hydrogen shell burning (bottom panel). When the white dwarf mass reaches 0.79 $M_\odot$ (14.1 Myr from now), the mass ratio will be close to unity with a secondary mass of 0.8 $M_\odot$ (at an orbital period of 5.1 h) and the system becomes stable against (conservative) thermal time-scale mass transfer. Therefore, the accretion rate decreases below the value required for stable hydrogen burning. From this moment on, TYC 6760-497-1 will behave as a normal CV. i.e. after 105 Myr it will enter the period gap at an orbital period of 3.1 h and reinitialise mass transfer at a much lower rate at an orbital period of 2.1 h (1.5 Gyr from now). Finally, the system will reach the orbital period minimum ($\simeq$1.1 h) 4.8 Gyr from now.

The more massive secondary star will have imprinted the relative abundances of carbon and nitrogen of the accreted material as soon as the outer convection zone reaches regions containing CNO processed material, hence following the prediction of decreased values for C/N and ^{12}C/^{13}C for CVs descending from thermal time scale mass transfer systems. In Figure 6.14 I show the C/N and ^{12}C/^{13}C abundance ratios for TYC 6760-497-1 as a function of the orbital period. As soon as the secondary star starts to develop a deep convective envelope, both surface abundance ratios decrease significantly, most dramatically. C/N which drops by several orders of magnitude. TYC 6760-497-1 is therefore likely a progenitor of the CVs with decreased C/N line ratios which I called failed SNIa.

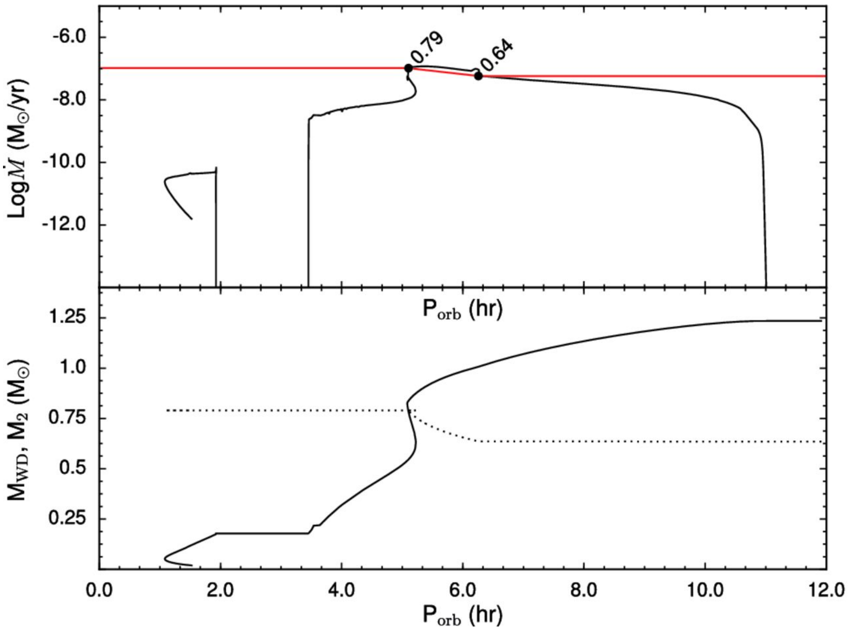

Figure 6.13: The predicted future evolution of the mass transfer rate (top panel) and the masses of the white dwarf and the donor (bottom panel, dotted line and solid line, respectively) of TYC6760-497-1 as a function of the orbital period. The horizontal red line in the top panel represents the mass transfer rate required for stable hydrogen burning for the respective mass of the white dwarf (Wolf et al., 2013). At $P_{\rm orb}$=6.5 h, TYC 6760-497-1 reaches this critical mass transfer rate. As a consequence, the white dwarf grows in mass. At $P_{\rm orb}$=5 h, the white dwarf mass has reached 0.79 $M_\odot$ and the mass transfer rate falls below the rate required for stable burning. At this moment, TYC 6760-497-1 becomes a 'normal' CV with non-conservative stable mass transfer driven by angular momentum loss only and a constant white dwarf mass. From Parsons et al. (2015).

6.7 Conclusions

The high signal-to-noise ratio in the COS ultraviolet spectroscopy of HS0218+3229 and QZ Ser allowed the measurement of the abundances of carbon ($\log({\rm C/H}) < -5$) and nitrogen ($\log({\rm N/H}) > -4$), which demonstrates that these systems underwent a very short phase of thermal time scale mass transfer in their past evolution.

Evolutionary simulations with MESA show that binary systems containing a 0.7 $M_\odot$ white dwarf which undergo thermal time scale mass transfer require companion stars with masses in the range $\simeq$1.5–2.5 $M_\odot$. The shell burning phase is very short < 10 Myr, and the orbital period is significantly reduced (by couple of hours) during this phase. The simulations show that the inversion of the C/N ratio and the increase of He/H occur towards shorter orbital periods, once the donor develops a largely convective envelope, and these ratios are

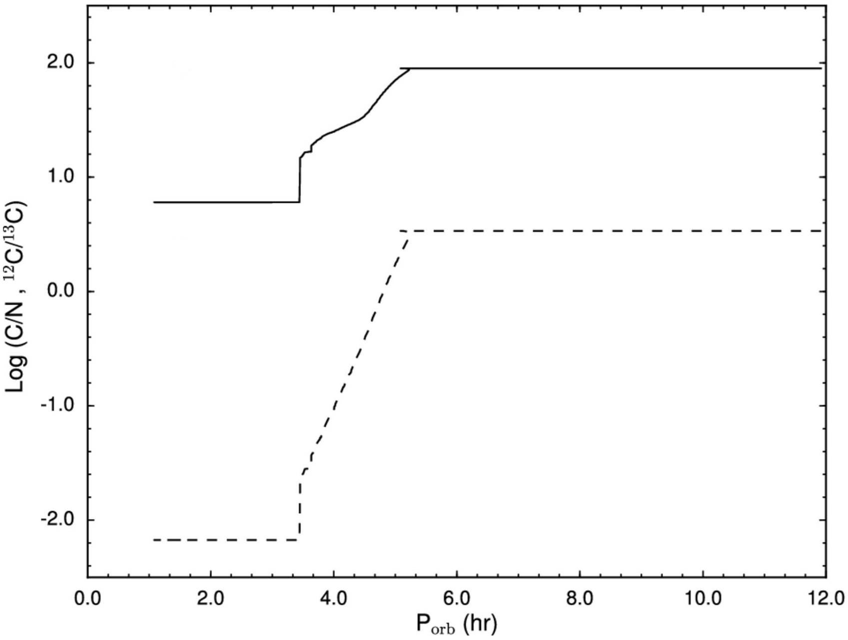

Figure 6.14: Surface abundance ratios (C/N, dashed line and ^{12}C/^{13}C, solid line) for the MS star in TYC 6760-497-1 as a function of the orbital period. Once a deep convective envelope forms ($P_{\rm orb}$ ≃5 h), both abundance ratios decrease considerably as carbon depleted material is dredged up from the core of the star where CNO burning has taken place. From Parsons et al. (2015).

very extreme ($-3 \lesssim \log{\rm (C/N)} \lesssim -2$) for those systems that underwent a phase of thermal time scale mass transfer.

When the systems are passing the 2–3 h period range, the donor still has not become fully convective, and consequently the systems continue the mass transfer, and therefore a considerable fraction of CVs in the period gap are potentially failed SNIa.

The tracks leading to SNIa are strongly dependent on the fraction of the accreted material that is retained by the white dwarf (β parameter).

Chapter 7

Concluding summary

In this thesis I have presented the work of three main projects involving the analysis of *HST* ultraviolet spectroscopy of white dwarfs, and here I will highlight the most important results.

G29-38

The geometry and the process of the accretion from the debris disc onto the white dwarf are not yet clearly understood, in particular the distribution of the metals across the white dwarf surface. The siphon model of Meyer & Meyer-Hofmeister (1994) suggests that the flow of the particles originates in a corona above the disc formed by the evaporation of the inner disc. In this scenario, the accretion of the metals would result in a homogeneous distribution over all the white dwarf surface, and so far, all abundance studies of debris-polluted white dwarfs assumed that this is the case. In contrast, accretion via a boundary layer or an accretion belt (e.g. Kippenhahn & Thomas, 1978b) would result in the deposition of metals in an equatorial belt, and hence in a inhomogeneous distribution of metals, which would affect the interpretation of the abundance analyses. G29-38 displays large amplitude variability due to non-radial pulsations. These pulsations with periods between ≃110–1250 s offer a unique opportunity to diagnose any inhomogeneity of the metals across the white dwarf surface using the pulsations as a spotlight: As a consequence of the pulsations, localised areas on the white dwarf surface are heated by a few thousand degrees, outshining the flux emitted from the unheated regions. Therefore, the ultraviolet spectroscopy is largely dominated by the flux from these heated regions. I have been analysing fast high-resolution ultraviolet spectroscopy obtained with *HST*/COS, extracting the spectra from individual pulses. Modelling the spectral absorption features of silicon and carbon in these spectra, I find that the distribution of metals across the white dwarf surface does not show large variations, arguing against an accretion geometry limited to an equatorial belt.

However, the results presented in Chapter 4 can not be conclusive due to the low signal-to-noise ratio of the minimum and peak spectra, hence in resulting large error bars of the abundances measurement. The quality of the spectra can be improved by phase-resolving the behaviour of the pulsations. Indeed, Tucker et al. (2018) accurately predicted the shape of the ultraviolet pulsations of WD 1401-147 observed with *GALEX* by modeling the quasi-simultaneous optical Whole Earth Telescope light curve. Given the brightness of G29-38 ($V = 13$), the pulsations can be fully resolved with small (20–40 cm) aperture telescopes. Therefore, we have submitted an *HST* proposal to obtain 35 orbits of COS time-tagged data of G29-38, and in case the time is awarded, we will organise a practically uninterrupted optical photometry throughout the *HST* campaign (because the equatorial location of G28-38, Dec = +05°, it is accessible from both hemispheres). These 35 orbits would allow to sample the individual pulses at least ≃70 times, providing pulse spectra with a signal-to-noise ratio ≃20. The COS data will be dissected into spectra for each individual pulse, and the corresponding metal abundances of carbon, oxygen, and silicon will be mapped onto the surface using the mode identification from the simultaneous optical photometry, which will unambiguously determine the geometry of the metal distribution on the prototype white dwarf accreting from a planetary disc.

GW Librae

Among all pulsating cataclysmic variable white dwarfs, GW Librae stands out by having a well-established observational record of three independent non-radial pulsation modes that disappeared when the white dwarf temperature rose dramatically following its 2007 accretion outburst. Therefore, GW Librae offers the unique opportunity to investigate the response of these modes to changes in the white dwarf temperature. The analysis of COS and STIS ultraviolet spectroscopy taken in 2002, 2010, and 2011, showed that pulsations produce variations in the white dwarf effective temperature, as predicted by theory. Additionally, the observations taken with COS in 2013 displayed an unexpected behaviour: besides showing variability at ≃ 275 s, which is close to the post-outburst pulsations detected with *HST* in 2010 and 2011, the white dwarf exhibits large-amplitude variability on a ≃ 4.4 h time scale. I demonstrated that this variability is produced by an increase of the temperature of a region on white dwarf covering up to ≃ 30 per cent of the visible surface. I argued against a short-lived accretion episode as the explanation of such heating, and discuss this event in the context of non-radial pulsations on a rapidly rotating star.

To further investigate the complex behaviour of the white dwarf in GW Lib, we organised in 2017 an intensive simultaneous multi-wavelength campaign using *Kepler/K2* and *HST*/COS. Here, I am presenting main preliminary result and future steps regarding the research of GW Lib.

HST/COS

Nine orbits were allocated in three visits under the programme 14912 (PI: Gänsicke) to obtain spectroscopic data in time-tag mode using same set up of the observations presented in Chapter 5. The observations were taken in July and August 2018, and the light curve extracted from the COS data is shown in black in Figure 7.1. During the first and second visits a ≃320 s-period made its appearance at different phases. In contrast, the presence of the large amplitude long-modulation is clear during the third visit, superimposed near its peak by the 275 s variability, i.e. the same period as detected in the 2013 observations.

Thanks to the work on G29-38 (Chapter 4) and QS Ser/HS0218 (Chapter 6), the tools required are partially developed to proceed straight forward with the following goals:

- The *Gaia* parallax locates GW Lib at a distance of 112.79±1.05 pc. Therefore, fits to the COS spectroscopy adding a prior on the distance will provide a strong constraint on the surface gravity and hence the mass of the white dwarf, which can be compared with measurements from the gravitational redshift ($M_{\rm WD}$=0.84±0.02 $M_{\odot}$; van Spaandonk et al. 2010, $M_{\rm WD}$=0.79±0.08 $M_{\odot}$; Szkody et al. 2012).
- Furthermore, archival COS data is available for GW Lib covering from 2010 to 2018. Therefore, changes of the effective temperature as a consequence of the pulsations can be tracked on all the COS data. In addition, the metal abundances of carbon, oxygen and silicon can be accurately measured, and changes in the abundances can provide information on changes in the accretion rate.

K2 data

The *Kepler* Space Telescope observed observed GW Lib (ID: EPIC 249251294) in short-cadence mode (58.9 s exposures) from 2017 August 22 to November 18 during Campaign 15 of its *K2* mission. Small sections of the 88 days-long *K2* light curve of GW Lib are shown in red in Figure 7.1. It shows the dominant signal at 19.5 min, and also the first (584 s) and second (389 s) harmonics are detected. The periods of these signals show drifts, and since they all drift in the same direction, we conclude that the 19.5 min signal is related to pulsations, which allows to rule out the hypothesis of an instability in the accretion disc

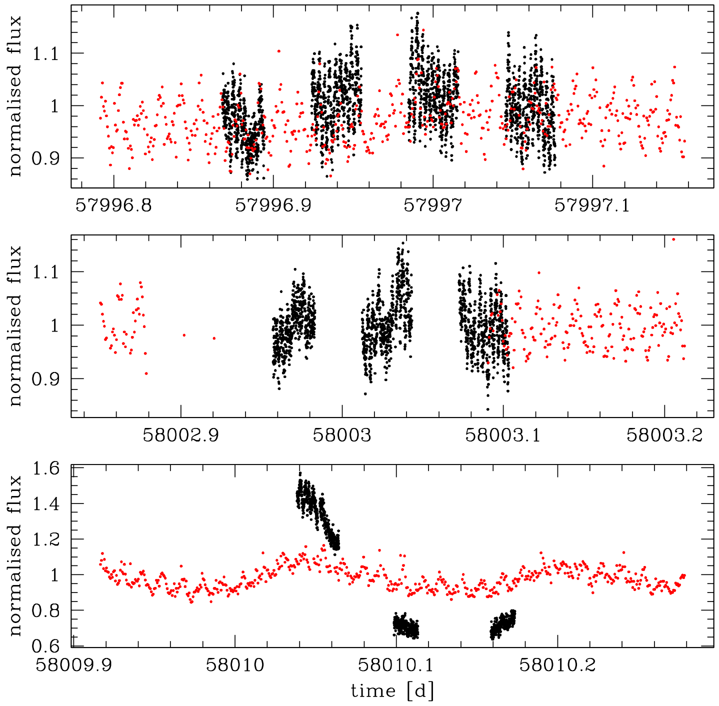

Figure 7.1: Comparison of the *K*2 and COS light curves. The 19.5 min signal has similar amplitudes in the optical and ultraviolet, in contrast, the 4 h modulation has a much larger amplitude in the ultraviolet, and the 320 s period which is strong in the ultraviolet is not detected at optical wavelengths.

proposed by Vican et al. (2011).

The short period at 320 s seen in the COS light curve is not clearly evident in the optical, however the long-modulation is also present in the simultaneous optical data in the third *HST* visit, though with a considerably lower amplitude (Figure 7.1).

The research presented in Chapter 5 suggests that the long-modulation could be the result of retrograde pulsation as result of the fast rotation of the white dwarf in GW Lib. In long term, I and my collaborators aim to understand the physics behind this modulation.

HS0218+3229 & QZ Ser

The efforts to have a unified picture to explain the relationships between the super-soft X-ray sources, cataclysmic variables and AM CVn stars in the context of the single degenerate channel are far from complete. The study of the binary configuration of super-soft X ray sources has been very challenging because (1) the sample of known super-soft X-ray sources is limited to less than a dozen systems, with only two Galactic sources, (2) the majority of the systems are far away in the Small and Large Magellanic Clouds, and (3) the spectra are dominated by the ultra hot white dwarfs outshining their companion stars. Here I developed a new method based on the observational signatures of the CNO cycle that descendants of super-soft X-ray sources present which, combined with evolutionary simulations, can constrain the binary configurations of their progenitors. I presented the analysis of *HST*/COS spectroscopic data of two post super-soft X-ray sources: HS0218+3229 and QZ Ser which exhibit extremely low C/N ratios ($\log \mathrm{C/N} < -2.0$). Moreover, I carried out MESA simulations to constrain the binary parameter space for a white dwarf of mass $0.7\,M_{\odot}$ to undergo the thermal time scale mass transfer, which requires companions with masses within $\simeq 1.5-2.5\,M_{\odot}$.

The binary systems that evolve through the super-soft X-ray channel but fail to reach the ignition mass before the thermal time scale mass transfer ends do not explode, but morph into white dwarfs accreting stably from the eroded, now lower-mass companion (e.g. Schenker 2002, MNRAS 337, 1105). Systems undergoing the super-soft X-ray phase have donors that are more massive, hence their evolution is faster. These evolved donors provide an unmistakable signatures that allows to identify them as post-super-soft X-ray sources: they are the stripped-down inner parts of initially more massive stars, which are too hot for their masses. Phrased differently, evolved donors have spectral types that are too early for their orbital period. In addition, the evolution of post-super-soft X-ray sources is not driven by angular momentum losses through magnetic braking as in normal cataclysmic variables, therefore these systems will continue accreting when evolving through the canonical period gap. I aim to obtain spectroscopy of all the cataclysmic variable systems in the period gap to obtain a statistically larger sample of failed SNIas. The immediate goals are a) accurately measure the fraction of systems within the period gap that have evolved through the super-soft X-rays phas which, together with population models, will quantify the importance of this channel, and b) determine the carbon abundances of the systems that have evolved donors.

I observed 14 non-magnetic CV donors in the period gap with Xshooter on February 2018, 16-18 (few days before thesis submission). Hence, I will now begin with the analysis of the Xshooter data, and here I am outlining how this analysis will be performed.

Normal CVs are born in the period gap with a low-mass companion have a spectral type of ≃M5 (blue in the bottom panel in Figure 7.2). In contrast, evolved donors in post-super-soft X-ray systems are significantly hotter, with spectral types around early M or

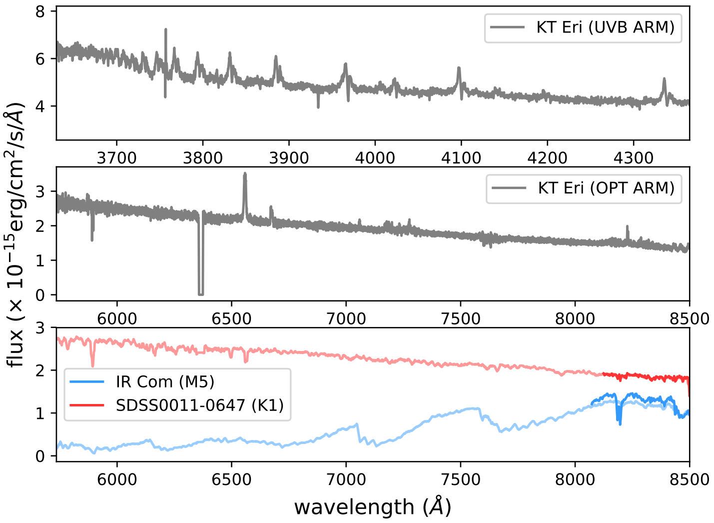

Figure 7.2: Xshooter spectrum of KT Eri (orbital period of 2.25 h) taken on February, 16, 2018 which shows emission lines from the disc (top) and that the companion has an early spectral type (second panel). As a comparison, the bottom panel shows the cataclysmic variable of IR Com and the confirmed post-super-soft X-ray system SDSSJ0011-0647 (Rebassa-Mansergas et al. 2014, ApJ, 790, 28), which have spectral type of M5 and K1, respectively, i.e. whereas the donor in IR Com is a main sequence star, the companion in SDSS0011-0647 is significantly evolved.

even mid-K (red in bottom panel in Figure 7.2). I will therefore unambiguously identify the systems with evolved donors from their spectral energy distribution. These evolved donor stars are expected to exhibit the signature of CNO burning, i.e. strongly enhanced N/C ratio with respect to solar abundances (Schenker et al. 2002, MNRAS, 337, 1105). I will measure the carbon abundances of my target stars from the CO bands in the near-IR using synthetic spectra computed with the ATLAS and SPECTRUM codes.

In the longer term, based on the derived constraints, i.e. orbital period, spectral type and mass of the companion, and carbon abundances, I will re-construct their past binary evolution using the state-of-the-art MESA code. These computations will yield an estimate of the initial mass of the companion and will inform us on the binary configurations that will enter a super-soft X-ray phase, thereby providing crucial constraints on the single-degenerate channel.

★ ★ ★

Bibliography

Abbott B. P., et al., 2017, Phys. Rev. Lett., 119, 161101

Abgrall H., Roueff E., Launay F., Roncin J. Y., Subtil J. L., 1993a, A&AS, 101, 273

Abgrall H., Roueff E., Launay F., Roncin J. Y., Subtil J. L., 1993b, A&AS, 101, 323

Aerts C., Christensen-Dalsgaard J., Kurtz D. W., 2010, Asteroseismology

Allard N. F., Koester D., Feautrier N., Spielfiedel A., 1994, A&AS, 108, 417

Allard N. F., Kielkopf J., Feautrier N., 1998, A&A, 330, 782

Allard N. F., Kielkopf J. F., Loeillet B., 2004a, A&A, 424, 347

Allard N. F., Hébrard G., Dupuis J., Chayer P., Kruk J. W., Kielkopf J., Hubeny I., 2004b, ApJ, 601, L183

Almeida L. A., Jablonski F., 2011, in Sozzetti A., Lattanzi M. G., Boss A. P., eds, IAU Symposium Vol. 276, The Astrophysics of Planetary Systems: Formation, Structure, and Dynamical Evolution. pp 495–496, doi:10.1017/S1743921311020941

Althaus L. G., Córsico A. H., Isern J., García-Berro E., 2010, A&ARv, 18, 471

Althaus L. G., Miller Bertolami M. M., Córsico A. H., 2013, A&A, 557, A19

Andronov N., Pinsonneault M., Sills A., 2003, ApJ, 582, 358

Araujo-Betancor S., Gänsicke B. T., Long K. S., Beuermann K., de Martino D., Sion E. M., Szkody P., 2005, ApJ, 622, 589

Arras P., Townsley D. M., Bildsten L., 2006, ApJ, 643, L119

Augusteijn T., van der Hooft F., de Jong J. A., van Paradijs J., 1996, A&A, 311, 889

Aviles A., et al., 2010, ApJ, 711, 389

Barstow M. A., Joyce S., Casewell S. L., Holberg J. B., Bond H. E., Burleigh M. R., 2017, in Tremblay P.-E., Gaensicke B., Marsh T., eds, Astronomical Society of the Pacific Conference Series Vol. 509, 20th European White Dwarf Workshop. p. 383

Bédard A., Bergeron P., Fontaine G., 2017, ApJ, 848, 11

Bell K. J., Hermes J. J., Bischoff-Kim A., Moorhead S., Montgomery M. H., Østensen R., Castanheira B. G., Winget D. E., 2015, ApJ, 809, 14

Benvenuto O. G., Althaus L. G., 1998, MNRAS, 293, 177

Bergeron P., Wesemael F., Fontaine G., 1991, ApJ, 367, 253

Bergeron P., Wesemael F., Lamontagne R., Fontaine G., Saffer R. A., Allard N. F., 1995, ApJ, 449, 258

Bergeron P., Fontaine G., Billères M., Boudreault S., Green E. M., 2004, ApJ, 600, 404

Bergeron P., et al., 2011, ApJ, 737, 28

Bildsten L., Ushomirsky G., Cutler C., 1996, ApJ, 460, 827

Bildsten L., Shen K. J., Weinberg N. N., Nelemans G., 2007, ApJ, 662, L95

Boss A. P., Myhill E. A., 1992, ApJS, 83, 311

Brickhill A. J., 1983, MNRAS, 204, 537

Brickhill A. J., 1991, MNRAS, 252, 334

Bullock E., et al., 2011, AJ, 141, 84

Carroll B. W., Ostlie D. A., 2006, An introduction to modern astrophysics and cosmology

Castanheira B. G., Kepler S. O., 2009, MNRAS, 396, 1709

Chandrasekhar S., 1931, ApJ, 74, 81

Charbonneau P., MacGregor K. B., 1997, ApJ, 486, 502

Chayer P., Fontaine G., Wesemael F., 1995a, ApJS, 99, 189

Chayer P., Vennes S., Pradhan A. K., Thejll P., Beauchamp A., Fontaine G., Wesemael F., 1995b, ApJ, 454, 429

Chen Y.-H., Li Y., 2013, Research in Astronomy and Astrophysics, 13, 1438

Chen A., O'Donoghue D., Stobie R. S., Kilkenny D., Warner B., 2001, MNRAS, 325, 89

Chen H.-L., Woods T. E., Yungelson L. R., Gilfanov M., Han Z., 2014, MNRAS, 445, 1912

Chote P., Sullivan D. J., 2016, MNRAS, 458, 1393

Clemens J. C., van Kerkwijk M. H., Wu Y., 2000a, MNRAS, 314, 220

Clemens J. C., van Kerkwijk M. H., Wu Y., 2000b, MNRAS, 314, 220

Copperwheat C. M., et al., 2009, MNRAS, 393, 157

Córsico A. H., Romero A. D., Althaus L. G., Hermes J. J., 2012, A&A, 547, A96

Costa J. E. S., et al., 2008, A&A, 477, 627

Cowley A. P., Schmidtke P. C., Crampton D., Hutchings J. B., 1990, ApJ, 350, 288

Cox J. P., Giuli R. T., 1968, Principles of stellar structure

Dhillon V. S., et al., 2007, MNRAS, 378, 825

Dufour P., et al., 2007, ApJ, 663, 1291

Dufour P., Fontaine G., Liebert J., Schmidt G. D., Behara N., 2008a, ApJ, 683, 978

Dufour P., Fontaine G., Liebert J., Williams K., Lai D. K., 2008b, ApJ, 683, L167

Dufour P., Béland S., Fontaine G., Chayer P., Bergeron P., 2011, ApJ, 733, L19

Dufour P., Vornanen T., Bergeron P., Fontaine A. B., 2013, in 18th European White Dwarf Workshop.. p. 167

Dziembowski W., Koester D., 1981, A&A, 97, 16

Eggleton P. P., 1976, in Eggleton P., Mitton S., Whelan J., eds, IAU Symposium Vol. 73, Structure and Evolution of Close Binary Systems. p. 209

Eggleton P. P., 1983, ApJ, 268, 368

Falcon R. E., Winget D. E., Montgomery M. H., Williams K. A., 2010, ApJ, 712, 585

Fontaine G., Brassard P., 2008, PASP, 120, 1043

Fontaine G., Lacombe P., McGraw J. T., Dearborn D. S. P., Gustafson J., 1982, ApJ, 258, 651

Fontaine G., Brassard P., Bergeron P., 2001, PASP, 113, 409

Fontaine G., Bergeron P., Billères M., Charpinet S., 2003, ApJ, 591, 1184

Foreman-Mackey D., Hogg D. W., Lang D., Goodman J., 2013, PASP, 125, 306

Gallagher J. S., Starrfield S., 1978, ARA&A, 16, 171

Gänsicke B. T., Beuermann K., de Martino D., 1995, A&A, 303, 127

Gänsicke B. T., Hoard D. W., Beuermann K., Sion E. M., Szkody P., 1998, A&A, 338, 933

Gänsicke B. T., et al., 2003, ApJ, 594, 443

Gänsicke B. T., Szkody P., Howell S. B., Sion E. M., 2005, ApJ, 629, 451

Gänsicke B. T., Long K. S., Barstow M. A., Hubeny I., 2006, ApJ, 639, 1039

Gänsicke B. T., et al., 2009, MNRAS, 397, 2170

Gänsicke B. T., Koester D., Farihi J., Girven J., Parsons S. G., Breedt E., 2012, MNRAS, 424, 333

García-Senz D., Bravo E., 1999, in Miyama S. M., Tomisaka K., Hanawa T., eds, Astrophysics and Space Science Library Vol. 240, Numerical Astrophysics. p. 281, doi:10.1007/978-94-011-4780-4_88

Giammichele N., Bergeron P., Dufour P., 2012a, ApJS, 199, 29

Giammichele N., Bergeron P., Dufour P., 2012b, ApJS, 199, 29

Giammichele N., Charpinet S., Brassard P., Fontaine G., 2017, A&A, 598, A109

Gianninas A., Bergeron P., Fontaine G., 2006, AJ, 132, 831

Gianninas A., Bergeron P., Ruiz M. T., 2009, in Journal of Physics Conference Series. p. 012021 (`arXiv:0810.5324`), doi:10.1088/1742-6596/172/1/012021

Gianninas A., Bergeron P., Ruiz M. T., 2011, ApJ, 743, 138

Gianninas A., Dufour P., Kilic M., Brown W. R., Bergeron P., Hermes J. J., 2014, ApJ, 794, 35

Gilfanov M., Bogdán Á., 2010, Nature, 463, 924

Godon P., Sion E. M., 2003, ApJ, 586, 427

Godon P., Regev O., Shaviv G., 1995, MNRAS, 275, 1093

Godon P., Sion E. M., Cheng F. H., Szkody P., Long K. S., Froning C. S., 2004, ApJ, 612, 429

Godon P., Sion E. M., Barrett P. E., Hubeny I., Linnell A. P., Szkody P., 2008, ApJ, 679, 1447

Godon P., et al., 2016, ApJ, 833, 146

Goliasch J., Nelson L., 2015, ApJ, 809, 80

Golysheva P. Y., Antipin S. V., Zharova A. V., Katysheva N. A., Chochol D., Shugarov S. Y., 2012, Astrophysics, 55, 208

Goodman J., Weare J., 2010, Communications in Applied Mathematics and Computational Science, Vol.~5, No.~1, p.~65-80, 2010, 5, 65

Graham J. R., Matthews K., Neugebauer G., Soifer B. T., 1990, ApJ, 357, 216

Gray D. F., 1992, Science, 257, 1978

Greiner J., 2000, New Astron., 5, 137

Greiner J., Hasinger G., Kahabka P., 1991, A&A, 246, L17

Grevesse N., Noels A., 1993, Physica Scripta Volume T, 47, 133

Hōshi R., 1979, Progress of Theoretical Physics, 61, 1307

Hamuy M., et al., 2003, Nature, 424, 651

Han Z., 1998, MNRAS, 296, 1019

Hansen B. M. S., et al., 2004, ApJS, 155, 551

Hansen B. M. S., et al., 2013, Nature, 500, 51

Heger A., Fryer C. L., Woosley S. E., Langer N., Hartmann D. H., 2003, ApJ, 591, 288

Hellier C., 2001, Cataclysmic Variable Stars

Hermes J. J., et al., 2015, ApJ, 810, L5

Hilton E. J., Szkody P., Mukadam A., Mukai K., Hellier C., van Zyl L., Homer L., 2007, AJ, 134, 1503

Holberg J. B., Bergeron P., 2006, AJ, 132, 1221

Holberg J. B., Barstow M. A., Bruhweiler F. C., Cruise A. M., Penny A. J., 1998, ApJ, 497, 935

Holberg J. B., Bergeron P., Gianninas A., 2008, AJ, 5, 137

Holberg J. B., Oswalt T. D., Barstow M. A., 2012, AJ, 143, 68

Horner J., Wittenmyer R. A., Hinse T. C., Marshall J. P., Mustill A. J., Tinney C. G., 2013, MNRAS, 435, 2033

Howell S. B., Nelson L. A., Rappaport S., 2001, ApJ, 550, 897

Huang S.-S., 1966, Annales d'Astrophysique, 29, 331

Hubeny I., Lanz T., 1995, ApJ, 439, 875

Hurley J. R., Pols O. R., Tout C. A., 2000, MNRAS, 315, 543

Iben Jr. I., 1982, ApJ, 259, 244

Iben Jr. I., 1991, ApJS, 76, 55

Iben Jr. I., Tutukov A. V., 1984, ApJS, 54, 335

Iben Jr. I., Ritossa C., García-Berro E., 1997, ApJ, 489, 772

Ishioka R., et al., 2001, PASJ, 53, 905

Istrate A. G., Tauris T. M., Langer N., Antoniadis J., 2014, A&A, 571, L3

Ivanova N., Taam R. E., 2003, ApJ, 599, 516

Jeans J. H., 1902, Royal Society of London Philosophical Transactions Series A, 199, 1

Jura M., 2003, ApJ, 584, L91

Kahabka P., van den Heuvel E. P. J., 1997, ARA&A, 35, 69

Kalomeni B., Nelson L., Rappaport S., Molnar M., Quintin J., Yakut K., 2016, ApJ, 833, 83

Kato T., Maehara H., Monard B., 2008, PASJ, 60, L23

Kato T., Hambsch F.-J., Oksanen A., Starr P., Henden A., 2015, PASJ, 67, 3

Kawaler S. D., 1988, ApJ, 333, 236

Kawaler S. D., 2004, in Maeder A., Eenens P., eds, IAU Symposium Vol. 215, Stellar Rotation. p. 561

Kawaler S. D., Bradley P. A., 1994, ApJ, 427, 415

King A. R., Kolb U., 1995, ApJ, 439, 330

Kippenhahn R., Thomas H.-C., 1978a, A&A, 63, 265

Kippenhahn R., Thomas H.-C., 1978b, A&A, 63, 265

Kippenhahn R., Weigert A., 1990, Stellar Structure and Evolution

Kippenhahn R., Weigert A., Weiss A., 2012, Stellar Structure and Evolution, doi:10.1007/978-3-642-30304-3.

Kleinman S. J., et al., 1998, ApJ, 495, 424

Kleinman S. J., et al., 2013, ApJS, 204, 5

Knigge C., 2006, MNRAS, 373, 484

Knigge C., Baraffe I., Patterson J., 2011, ApJS, 194, 28

Koester D., 1987, ApJ, 322, 852

Koester D., 2009, A&A, 498, 517

Koester D., 2010, Mem. Soc. Astron. Italiana, 81, 921

Koester D., 2013, White Dwarf Stars. p. 559

Koester D., Allard N. F., 2000, Baltic Astronomy, 9, 119

Koester D., Provencal J., Shipman H. L., 1997, A&A, 320, L57

Koester D., et al., 2001, A&A, 378, 556

Koester D., Rollenhagen K., Napiwotzki R., Voss B., Christlieb N., Homeier D., Reimers D., 2005, A&A, 432, 1025

Koester D., Voss B., Napiwotzki R., Christlieb N., Homeier D., Lisker T., Reimers D., Heber U., 2009, A&A, 505, 441

Koester D., Provencal J., Gänsicke B. T., 2014, A&A, 568, A118

Kolb U., Baraffe I., 1999, in Hellier C., Mukai K., eds, Astronomical Society of the Pacific Conference Series Vol. 157, Annapolis Workshop on Magnetic Cataclysmic Variables. p. 273 (`arXiv:astro-ph/9810315`)

Kolb U., Ritter H., 1990, A&A, 236, 385

König M., Beuermann K., Gänsicke B. T., 2006, A&A, 449, 1129

Kowalski P. M., Saumon D., 2006, ApJ, 651, L137

Kraft R. P., 1967, ApJ, 150, 551

Kroupa P., 2001, MNRAS, 322

Kuiper G. P., 1938, ApJ, 88, 472

Lajoie C.-P., Bergeron P., 2007, ApJ, 667, 1126

Landolt A. U., 1968, ApJ, 153, 151

Lenz P., Breger M., 2005, Communications in Asteroseismology, 146, 53

Liebert J., Bergeron P., Holberg J. B., 2005, ApJS, 156, 47

Linnell A. P., Szkody P., Plotkin R. M., Holtzman J., Seibert M., Harrison T. E., Howell S. B., 2010, ApJ, 713, 1183

Littlefair S. P., Dhillon V. S., Marsh T. R., Gänsicke B. T., Southworth J., Baraffe I., Watson C. A., Copperwheat C., 2008, MNRAS, 388, 1582

Livio M., Riess A. G., 2003, ApJ, 594, L93

Long K. S., Helfand D. J., Grabelsky D. A., 1981, ApJ, 248, 925

Long K. S., Gänsicke B. T., Knigge C., Froning C. S., Monard B., 2009, ApJ, 697, 1512

Longa-Peña P., Steeghs D., Marsh T., 2015, MNRAS, 447, 149

MacGregor K. B., Charbonneau P., 1997, ApJ, 486, 484

Maoz D., Mannucci F., Nelemans G., 2014, ARA&A, 52, 107

Marsh T. R., et al., 2016, Nature, 537, 374

Massa D., et al. 2013, COS Data Handbook v. 2.0

Matranga M., Drake J. J., Kashyap V., Steeghs D., 2012, ApJ, 747, 132

McGraw J. T., Robinson E. L., 1975, ApJ, 200, L89

McGraw J. T., Liebert J., Starrfield S. G., Green R., 1979, in van Horn H. M., Weidemann V., eds, IAU Colloq. 53: White Dwarfs and Variable Degenerate Stars. pp 377–381

Mestel L., 1968, MNRAS, 138, 359

Mestel L., Spruit H. C., 1987, MNRAS, 226, 57

Metcalfe T. S., 2001, in Provencal J. L., Shipman H. L., MacDonald J., Goodchild S., eds, Astronomical Society of the Pacific Conference Series Vol. 226, 12th European Workshop on White Dwarfs. p. 324 (`arXiv:astro-ph/0008516`)

Meyer F., Meyer-Hofmeister E., 1981, A&A, 104, L10

Meyer F., Meyer-Hofmeister E., 1994, A&A, 288, 175

Montgomery M. H., 2005, ApJ, 633, 1142

Montgomery M. H., Williams K. A., Winget D. E., Dufour P., DeGennaro S., Liebert J., 2008a, ApJ, 678, L51

Montgomery M. H., Thompson S. E., von Hippel T., 2008b, ApJ, 685, L133

Morin J., Donati J.-F., Petit P., Delfosse X., Forveille T., Jardine M. M., 2010, MNRAS, 407, 2269

Morrissey P., et al., 2007, ApJS, 173, 682

Mukadam A. S., Montgomery M. H., Winget D. E., Kepler S. O., Clemens J. C., 2006, ApJ, 640, 956

Nelemans G., Tout C. A., 2005, MNRAS, 356, 753

Nelemans G., Verbunt F., Yungelson L. R., Portegies Zwart S. F., 2000, A&A, 360, 1011

Nelemans G., Yungelson L. R., Portegies Zwart S. F., Verbunt F., 2001, A&A, 365, 491

Neustroev V. V., Tovmassian G. H., Zharikov S. V., Sjoberg G., 2013, MNRAS, 432, 2596

Nomoto K., 1982, ApJ, 253, 798

Nomoto K., Umeda H., Kobayashi C., Hachisu I., Kato M., Tsujimoto T., 2000, in Holt S. S., Zhang W. W., eds, American Institute of Physics Conference Series Vol. 522, American Institute of Physics Conference Series. pp 35–52 (`arXiv:astro-ph/0003134`), doi:10.1063/1.1291694

Nomoto K., Saio H., Kato M., Hachisu I., 2007, ApJ, 663, 1269

O'Donoghue D., Koen C., Kilkenny D., Stobie R. S., Koester D., Bessell M. S., Hambly N., MacGillivray H., 2003, MNRAS, 345, 506

Osaki Y., 1974, PASJ, 26, 429

Østensen R. H., Bloemen S., Vučković M., Aerts C., Oreiro R., Kinemuchi K., Still M., Koester D., 2011, ApJ, 736, L39

Paczyński B., 1965, Acta Astron., 15, 89

Paczyński B., 1967, Acta Astron., 17, 287

Paczyński B., 1971, ARA&A, 9, 183

Paquette C., Pelletier C., Fontaine G., Michaud G., 1986, ApJS, 61, 197

Parsons S. G., Marsh T. R., Copperwheat C. M., Dhillon V. S., Littlefair S. P., Gänsicke B. T., Hickman R., 2010a, MNRAS, 402, 2591

Parsons S. G., et al., 2010b, MNRAS, 407, 2362

Parsons S. G., Marsh T. R., Gänsicke B. T., Tappert C., 2011, MNRAS, 412, 2563

Parsons S. G., et al., 2012, MNRAS, 420, 3281

Parsons S. G., et al., 2015, MNRAS, 452, 1754

Parsons S. G., et al., 2016, MNRAS, 458, 2793

Parsons S. G., et al., 2017, MNRAS, 470, 4473

Patterson J., et al., 2005, PASP, 117, 1204

Pauli E.-M., Napiwotzki R., Heber U., Altmann M., Odenkirchen M., 2006, A&A, 447, 173

Paxton B., Bildsten L., Dotter A., Herwig F., Lesaffre P., Timmes F., 2011, ApJS, 192, 3

Paxton B., et al., 2013, ApJS, 208, 4

Paxton B., et al., 2015, ApJS, 220, 15

Perlmutter S., et al., 1999, ApJ, 517, 565

Piro A. L., Bildsten L., 2004, ApJ, 616, L155

Piro A. L., Arras P., Bildsten L., 2005, ApJ, 628, 401

Podsiadlowski P., Han Z., Rappaport S., 2003, MNRAS, 340, 1214

Politano M., 1996, ApJ, 465, 338

Politano M., 2004, ApJ, 604, 817

Postnov K. A., Yungelson L. R., 2014, Living Reviews in Relativity, 17, 3

Prialnik D., 2000, An Introduction to the Theory of Stellar Structure and Evolution

Prialnik D., Livio M., Shaviv G., Kovetz A., 1982, ApJ, 257, 312

Provencal J. L., Shipman H. L., Hog E., Thejll P., 1998, ApJ, 494, 759

Provencal J. L., Shipman H. L., Koester D., Wesemael F., Bergeron P., 2002, ApJ, 568, 324

Provencal J. L., et al., 2009, ApJ, 693, 564

Pylyser E. H. P., Savonije G. J., 1989, A&A, 208, 52

Rappaport S., Joss P. C., Webbink R. F., 1982, ApJ, 254, 616

Rappaport S., Verbunt F., Joss P. C., 1983, ApJ, 275, 713

Reid I. N., 1996, AJ, 111, 2000

Reiners A., Basri G., 2008, ApJ, 684, 1390

Renzini A., et al., 1996, ApJ, 465, L23

Ribeiro T., Kafka S., Baptista R., Tappert C., 2010, AJ, 139, 1106

Riess A. G., et al., 1998, AJ, 116, 1009

Riley A., et al. 2018, STIS Instrument Handbook, Version 17.0

Ritter H., 1976, MNRAS, 175, 279

Ritter H., 1987, Mem. Soc. Astron. Italiana, 58, 133

Ritter H., 1988, A&A, 202, 93

Robinson E. L., 1976, ApJ, 203, 485

Robinson E. L., Kepler S. O., Nather R. E., 1982, ApJ, 259, 219

Robinson E. L., et al., 1995, ApJ, 438, 908

Rodríguez-Gil P., Torres M. A. P., Gänsicke B. T., Muñoz-Darias T., Steeghs D., Schwarz R., Rau A., Hagen H.-J., 2009, A&A, 496, 805

Rodríguez-Gil P., Schmidtobreick L., Long K. S., Gänsicke B. T., Torres M. A. P., Rubio-Díez M. M., Santander-García M., 2012, MNRAS, 422, 2332

Romero A. D., Córsico A. H., Althaus L. G., Kepler S. O., Castanheira B. G., Miller Bertolami M. M., 2012, MNRAS, 420, 1462

Ruiter A. J., Belczynski K., Fryer C., 2009, ApJ, 699, 2026

Saio H., 2013, in European Physical Journal Web of Conferences. p. 05005, doi:10.1051/epjconf/20134305005

Salpeter E. E., 1955, ApJ, 121, 161

Schatzman E., 1962, Annales d'Astrophysique, 25, 18

Schenker K., King A. R., Kolb U., Wynn G. A., Zhang Z., 2002, MNRAS, 337, 1105

Schmidtobreick L., Rodríguez-Gil P., Long K. S., Gänsicke B. T., Tappert C., Torres M. A. P., 2012, MNRAS, 422, 731

Schreiber M. R., Gänsicke B. T., 2002, A&A, 382, 124

Schreiber M. R., Zorotovic M., Wijnen T. P. G., 2016, MNRAS, 455, L16

Schwieterman E. W., et al., 2010, Journal of the Southeastern Association for Research in Astronomy, 3, 6

Schwope A. D., Hambaryan V., Schwarz R., Kanbach G., Gänsicke B. T., 2002, A&A, 392, 541

Shapley H., 1914, ApJ, 40, 448

Shara M. M., Prialnik D., Shaviv G., 1977, A&A, 61, 363

Shipman H. L., Provencal J. L., Hog E., Thejll P., 1997, ApJ, 488, L43

Shulyak D., Reiners A., Engeln A., Malo L., Yadav R., Morin J., Kochukhov O., 2017, Nature Astronomy, 1, 0184

Sion E. M., Szkody P., Cheng F., Gänsicke B. T., Howell S. B., 2003, ApJ, 583, 907

Sion E. M., Holberg J. B., Oswalt T. D., McCook G. P., Wasatonic R., 2009, AJ, 138, 1681

Smak J., 1983, ApJ, 272, 234

Smale A. P., et al., 1988, MNRAS, 233, 51

Smith D. A., Dhillon V. S., 1998, MNRAS, 301, 767

Soker N., 2011, preprint, (`arXiv:1109.4652`)

Starrfield S., Timmes F. X., Hix W. R., Sion E. M., Sparks W. M., Dwyer S. J., 2004, ApJ, 612, L53

Subasavage J. P., et al., 2017, AJ, 154, 32

Szkody P., Gänsicke B. T., Howell S. B., Sion E. M., 2002, ApJ, 575, L79

Szkody P., et al., 2010a, ApJ, 710, 64

Szkody P., et al., 2010b, ApJ, 716, 1531

Szkody P., et al., 2012, ApJ, 753, 158

Szkody P., et al., 2017, AJ, 153, 123

Tassoul M., Fontaine G., Winget D. E., 1990, ApJS, 72, 335

Tauris T. M., van den Heuvel E. P. J., 2006, Formation and evolution of compact stellar X-ray sources. pp 623–665

Templeton M., Stubbings R., Waagen E. O., Schmeer P., Pearce A., Nelson P., 2007, Central Bureau Electronic Telegrams, 922, 1

Thompson S. E., van Kerkwijk M. H., Clemens J. C., 2008, MNRAS, 389, 93

Thompson S. E., et al., 2010, ApJ, 714, 296

Thorstensen J. R., 2003, AJ, 126, 3017

Thorstensen J. R., Patterson J., Kemp J., Vennes S., 2002a, PASP, 114, 1108

Thorstensen J. R., Fenton W. H., Patterson J., Kemp J., Halpern J., Baraffe I., 2002b, PASP, 114, 1117

Thorstensen J. R., Fenton W. H., Patterson J. O., Kemp J., Krajci T., Baraffe I., 2002c, ApJ, 567, L49

Toonen S., Nelemans G., 2013, A&A, 557, A87

Tovmassian G., et al., 2003, PASP, 115, 725

Townsley D. M., Bildsten L., 2002, in Gänsicke B. T., Beuermann K., Reinsch K., eds, Astronomical Society of the Pacific Conference Series Vol. 261, The Physics of Cataclysmic Variables and Related Objects. p. 31 (`arXiv:astro-ph/0112267`)

Townsley D. M., Bildsten L., 2003, ApJ, 596, L227

Townsley D. M., Bildsten L., 2004, ApJ, 600, 390

Townsley D. M., Gänsicke B. T., 2009, ApJ, 693, 1007

Townsley D. M., Arras P., Bildsten L., 2016, preprint, (`arXiv:1601.02046`)

Tremblay P.-E., Ludwig H.-G., Steffen M., Bergeron P., Freytag B., 2011, A&A, 531, L19

Tremblay P.-E., Kalirai J. S., Soderblom D. R., Cignoni M., Cummings J., 2014, ApJ, 791, 92

Tremblay P.-E., Cummings J., Kalirai J. S., Gänsicke B. T., Gentile-Fusillo N., Raddi R., 2016, MNRAS, 461, 2100

Trümper J., et al., 1991, Nature, 349, 579

Tucker M. A., et al., 2018, MNRAS, 475, 4768

Tutukov A., Yungelson L., 1979, in Conti P. S., De Loore C. W. H., eds, IAU Symposium Vol. 83, Mass Loss and Evolution of O-Type Stars. pp 401–406

Unno W., Osaki Y., Ando H., Saio H., Shibahashi H., 1989, Nonradial oscillations of stars

Uzdensky D. A., 2002, ApJ, 572, 432

Van Grootel V., Dupret M.-A., Fontaine G., Brassard P., Grigahcène A., Quirion P.-O., 2012, A&A, 539, A87

Van Grootel V., Fontaine G., Brassard P., Dupret M.-A., 2013, ApJ, 762, 57

Van Grootel V., Fontaine G., Brassard P., Dupret M.-A., 2015, A&A, 575, A125

Verbunt F., Zwaan C., 1981, A&A, 100, L7

Vican L., et al., 2011, PASP, 123, 1156

Vos J., Vučković M., 2017, preprint, (`arXiv:1711.05555`)

Voss B., 2006, Universität Kiel, 000

Warner B., 1973, MNRAS, 162, 189

Webbink R. F., 1984, ApJ, 277, 355

Whelan J., Iben Jr. I., 1973, ApJ, 186, 1007

Whyte C. A., Eggleton P. P., 1980, MNRAS, 190, 801

Wijnen T. P. G., Zorotovic M., Schreiber M. R., 2015, A&A, 577, A143

Willems B., Kolb U., 2004, A&A, 419, 1057

Willems B., Kolb U., Sandquist E. L., Taam R. E., Dubus G., 2005, ApJ, 635, 1263

Wilson D. J., Gänsicke B. T., Koester D., Toloza O., Pala A. F., Breedt E., Parsons S. G., 2015, MNRAS, 451, 3237

Winget D. E., 1995, Baltic Astronomy, 4, 129

Winget D. E., Kepler S. O., 2008, ARA&A, 46, 157

Winget D. E., Robinson E. L., Nather R. D., Fontaine G., 1982, ApJ, 262, L11

Wolf W. M., Bildsten L., Brooks J., Paxton B., 2013, ApJ, 777, 136

Wood M. A., 1992, ApJ, 386, 539

Wood M. A., 1995, in Koester D., Werner K., eds, Lecture Notes in Physics, Berlin Springer Verlag Vol. 443, White Dwarfs. p. 41, doi:10.1007/3-540-59157-5_171

Woudt P. A., Warner B., 2002, Ap&SS, 282, 433

Woudt P. A., et al., 2012, MNRAS, 427, 1004

Wu Y., Goldreich P., 1999, ApJ, 519, 783

Xu S., Jura M., Koester D., Klein B., Zuckerman B., 2013, ApJ, 766, L18

Xu S., Jura M., Koester D., Klein B., Zuckerman B., 2014, ApJ, 783, 79

Yungelson L. R., 2005, in Burderi L., Antonelli L. A., D'Antona F., di Salvo T., Israel G. L., Piersanti L., Tornambè A., Straniero O., eds, American Institute of Physics Conference Series Vol. 797, Interacting Binaries: Accretion, Evolution, and Outcomes. pp 1–10 (`arXiv:astro-ph/0412635`), doi:10.1063/1.2130209

Yungelson L. R., Kuranov A. G., 2017, MNRAS, 464, 1607

Zorotovic M., Schreiber M. R., Gänsicke B. T., 2011, A&A, 536, A42

Zuckerman B., Becklin E. E., 1987, Nature, 330, 138

Zuckerman B., Reid I. N., 1998, ApJ, 505, L143

Zuckerman B., Koester D., Reid I. N., Hünsch M., 2003, ApJ, 596, 477

Zuckerman B., Koester D., Melis C., Hansen B. M., Jura M., 2007, ApJ, 671, 872

van Altena W. F., Lee J. T., Hoffleit E. D., 1994, in Morrison L. V., Gilmore G. F., eds, Galactic and Solar System Optical Astrometry. p. 50

van Spaandonk L., Steeghs D., Marsh T. R., Parsons S. G., 2010, ApJ, 715, L109

van Zyl L., Warner B., O'Donoghue D., Sullivan D., Pritchard J., Kemp J., 2000, Baltic Astronomy, 9, 231

van Zyl L., et al., 2004, MNRAS, 350, 307

van den Heuvel E. P. J., 1976, in Eggleton P., Mitton S., Whelan J., eds, IAU Symposium Vol. 73, Structure and Evolution of Close Binary Systems. p. 35

van den Heuvel E. P. J., Bhattacharya D., Nomoto K., Rappaport S. A., 1992, A&A, 262, 97

von Hippel T., Thompson S. E., 2007, ApJ, 661, 477